Speleothem climate capture of the Neanderthal demise

Laura Melanie Charlotte Deeprose

BSc (Hons), MSc

June 2018

This thesis is submitted in partial fulfilment of the requirements for the degree of Doctor of Philosophy.

Abstract

The Iberian Peninsula is a region of climatic and archaeological interest as it lies upon the boundary between the North Atlantic and Mediterranean climatic zones and was the last refuge of the Neanderthals. The influence of climate changes on Neanderthal populations remains a mystery due to the lack of independently-dated high-resolution terrestrial records of past climate and environmental change from the Iberian Peninsula. The primary aim of this project was to construct a palaeoclimate record using speleothems from Matienzo, northern Iberia, across the period encapsulating the Neanderthal demise.

Contemporary cave monitoring of Cueva de las Perlas has demonstrated the potential for speleothems to be used as indicators of past climate and environmental conditions. Assessment of cave dynamics through a comprehensive monitoring programme has classified the karst hydrology, cave ventilation, processes influencing speleothem growth and proxies preserved within speleothem calcite.

Three speleothems were used to develop records of past climate and environmental variability between 90,000 and 30,000 years ago. A long-term aridity trend was evident throughout the record which is interpreted as a response to orbital-forcing. Sub-orbital climate instability was superimposed onto this long-term trend as evidenced through wet-dry proxies ($\delta^{18}O$, $\delta^{13}C$, Mg and Sr). Millennial-scale events coincident with the timing of North Atlantic Heinrich Events have been identified and the sub-orbital climate variability resembles that of North Atlantic Dansgaard-Oeschger cycles. Therefore, evidence from the speleothems demonstrates a tight coupling of the North Atlantic Ocean-Atmosphere system throughout MIS3. The Cueva de las Perlas speleothems have established that the period of the Neanderthal demise was characterised by climate instability involving abrupt shifts and millennial-scale events, thereby adding climatic pressures at a time of anatomically modern human appearance.

Declaration

I hereby declare that the work presented in this thesis is my own, except where acknowledged, and has not been submitted for the award of a higher degree or other qualification at this or any other institution.

Signed:

Date:

Name: Laura Melanie Charlotte Deeprose

Acknowledgements

First and foremost, I would like to say a massive thank you to my supervisor Peter Wynn for his endless support and advice about cave monitoring and speleothem science. I am also grateful to Phil Barker for his supervisory support and positivity. Thank you both for your continued enthusiasm throughout the project.

This project would not have been possible without the financial input from the NERC Envision Doctoral Training Partnership, BGS University Funding Initiative (BUFI) and NERC Isotope Geoscience Facilities Steering Committee (NIGFSC).

Thank you to the NERC Isotope Geosciences Laboratory (NIGL) team for your analytical support and advice. I would like to extend a special thank you to Melanie Leng, Andi Smith, Stephen Noble and Diana Sahy for sharing their knowledge and encouragement during my visits to Keyworth.

I would like to show my appreciation to those who have provided analytical support at Lancaster University. To Montse Auladell-Mestre for your support and encouragement in the earliest stages of laboratory work. To Debbie Hurst and Catherine Wearing for their technical laboratory assistance. To Dave Hughes for his extensive commitment to isotope analysis and continuous analytical support. To Andy Stott and the Centre of Ecology and Hydrology (CEH) for their analytical support throughout the project. I would like to extend my thanks to Wlodek Tych for his timeseries expertise and MatLab knowledge and to Gemma Davies for her GIS support. Additionally, I would like extend my gratitude to Christina Manning for her analytical support during the trace element analysis and help with the data processing.

A big thank you to the Matienzo caving community who have supported the project at all stages. A special thanks to Andy Quin for field support and logistics and to Pete Smith for his continued commitment by visiting the cave monthly throughout the course of the project. Cave monitoring and speleothem sampling in Cueva de las Perlas was undertaken with the kind permission from Gobierno de Cantabria, Consejería de Educación Cultura y Deporte.

To my fantastic field assistants Joanna Houska for her infectious enthusiasm, Charlotte Clarke for our hilarious fieldwork shenanigans and to Alex Chapman for his willingness to come on fieldwork at such short notice!

Throughout my PhD I have met some amazing people and have really grown with them as we have ventured along this PhD journey together. I would like to say a special thank you to Ceri Davies and Emma Gray for the endless coffees and chats. To Kirsty Forber and Rachel Efrat for their emotional support and friendship, frequently over a burrito or two. To Alistair MacDonald for his sense of humour and encouragement through our first year at Lancaster. To Rob Larson for his culinary expertise and willingness to sample the majority Lancaster's restaurants. Also, a huge thank you to all those who have been a member of the B46 office during my time there, particularly Ann Kretzschmar, Tamsin Blayney and Runmei Wang along with many others who have come and gone during the years.

To all those at St. Thomas' Church Lancaster, Christ Church Alsager and St. Matthew's Yiewsley who have given me more strength than I could have ever imagined. To my amazing Heysham life group for your encouragement and for all the discussions we have shared together.

Without the support of my family and friends this would not have been possible. Thank you all for your love, support, inspiration and prayers over the past few years. Your enthusiasm for speleothems has never ceased to amaze me!

And finally, I would like to thank my husband Jonty Warren for his care and passion for knowledge which has inspired me over the past three and a half years. I will be forever grateful!

Contents

Lists of figures

List of tables

1. Introduction

Between 90,000 – 30,000 years before present (BP) the North Atlantic region was subject to dramatic oscillations in climate and environment (Bond *et al.,* 1993; Rasmussen *et al.,* 2014). This time period encapsulates the Neanderthal population decline and eventual extinction. The demise of the Neanderthals has been attributed at least in part to changes in climate, with the Iberian Peninsula acting as the last refuge of the Neanderthals (d'Errico and Sánchez Goñi, 2003; Finlayson and Carrion, 2007; Tzedakis *et al.,* 2007; Wolf *et al.,* 2018). In order to attribute the influence of climate change on Neanderthal populations, long-term high-resolution records of past climate variability are required. Although numerous marine records from the North Atlantic have been used to determine past environmental variability (Roucoux *et al.,* 2005; Sánchez Goñi *et al.,* 2008, 2018), there remains a lack of high-resolution independently dated terrestrial climate records from the Iberian Peninsula.

The Iberian Peninsula lies upon the boundary between two climatic zones: the North Atlantic and the Mediterranean. Consequently, the region is highly sensitive to short- and long-term variations in atmospheric circulation (Martín-Chivelet *et al.,* 2011). Evidence from a variety of proxy archives has demonstrated a tight coupling of the North Atlantic Ocean-Atmosphere system throughout MIS3 and variations in atmospheric and oceanic conditions have been identified as driving mechanisms behind widespread abrupt millennial-scale variability (Bond *et al.,* 1993; Rasmussen *et al.,* 1996; Roucoux *et al.,* 2005). The sensitivity of the Iberian Peninsula to variations in climate demonstrates the potential of the region to provide long-term palaeoclimate records.

Speleothems are becoming increasingly utilised as valuable terrestrial archives of palaeoclimate and palaeoenvironment. Calcareous speleothems preserve a record of climatic and environmental conditions through incorporation of stable isotopes and trace elements into the calcite crystal lattice (McDermott, 2004, Fairchild and Baker, 2012). The chemical signal preserved within speleothem calcite can be influenced by the atmosphere, soil, vegetation, karst and cave system. Therefore, variability in chemical proxies can be used to infer changes in past climate and environment

(Fairchild and Baker, 2012). A key advantage to speleothem records is their ability to be independently dated through uranium-series methods (McDermott, 2004; Fairchild and Baker, 2012).

Prior to speleothem analysis, cave systems must be understood as each cave system is unique and will behave individually. Hydrological routing through the karst (Miorandi *et al.,* 2010; Bradley *et al.,* 2010; Baker and Bradley, 2010), karst-water interactions (Fairchild *et al.,* 2000; Fairchild and McMillan, 2007) and cave ventilation (Spötl *et al.,* 2005; Mattey *et al.,* 2010; James *et al.,* 2015; Smith *et al.,* 2015) can influence chemical signatures in speleothem calcite. Understanding cave environments in which speleothems are depositing is critical in order to accurately interpret geochemical signals in speleothems in relation to climate and environmental variability.

This thesis will present a cave monitoring study and subsequent speleothem reconstruction from Cueva de las Perlas, Northern Spain. The primary aim of the project is to reconstruct palaeoclimate from Matienzo (Northern Iberia) during the period of the Neanderthal Demise; which in this study will encompass 90,000-30,000 years BP. This aim can be broken down into two sub-aims:

1. Understand the internal cave dynamics of Cueva de las Perlas
2. Collect and produce a climatic record from Cueva de las Perlas

An extensive cave monitoring programme has been undertaken within Cueva de las Perlas to determine how the external climate signal is transferred into the speleothem calcite and provide insight into the various processes which may act to modify the climate and environmental signal. The results and discussion of the cave monitoring programme are presented in chapters 4 (cave air characteristics) and 5 (drip water chemistry).

Dating of the selected speleothems from Cueva de las Perlas was undertaken to determine periods of growth and identify speleothems suited to the present study. Further uranium-series dating of these speleothems was used to produce an independent chronology to constrain speleothem growth. Speleothems were used to

produce records of past climate and environmental change through stable isotope and trace element analyses and the results are presented in chapter 6.

The speleothem records from Matienzo have been compared to others across the North Atlantic region in order to determine whether any detected shifts in climate and environment are apparent only at a local scale or can be linked to other records from the wider region (chapter 7). The impact of changes in climate and environment on declining Neanderthal populations is also examined in chapter 7.

2. Literature review

The primary aim of this project was to reconstruct climate and environmental variability during the period of the Neanderthal demise. This literature review will therefore discuss the key topics of Neanderthals, climate change and cave monitoring in order to meet the primary aim. This chapter will first introduce possible mechanisms for the Neanderthal extinction and highlight the complexities involved in dating the timing of the Neanderthal demise. A primary theory invokes climate change as the mechanism driving the extinction of Neanderthal populations and section 2.2 will provide an overview of climate and environmental variability between 90-25ka which encapsulates the Neanderthal population decline and extinction. Caves hold clues to reconstructing the environment and landscapes in which the Neanderthals were living and section 2.3 will discuss how speleothems can be used as archives for palaeoclimate and palaeoenvironmental reconstruction. In order to interpret speleothem records accurately it is important to understand the cave system in which they are growing and section 2.4 will present an overview of cave monitoring and its significance. Section 2.5 will discuss speleothem growth whilst the final section (2.6) will discuss speleothem geochemistry with respect to stable isotope analyses, trace element composition and dating through U-series.

2.1 The Neanderthal demise

2.1.1 Overview

The Neanderthals, *Homo neanderthalensis*, were a hominin species found throughout Eurasia between 300-30ka BP (Harvati, 2010). The reasons why the Neanderthals went extinct have long fascinated scientists, however even today it is not fully understood why this species disappeared. Two key hypotheses have emerged; the first proposes climatic change during MIS3 led to the Neanderthal extinction (d'Errico and Sánchez Goñi, 2003; van Andel and Davies, 2003; Finlayson and Carrion, 2007; Bradtmöller *et al.,* 2012; Wolf *et al.,* 2018) while the second proposes the arrival of Anatomically Modern Humans (AMH) led to the disappearance of Neanderthals (Banks *et al.,* 2008; Roebroeks, 2008) either through competitive exclusion or interbreeding. This section

will explore the key points of each argument, particularly in light of recent dating which has challenged the exact timing of the Neanderthal disappearance (Higham *et al.,* 2011, 2014).

The replacement of Neanderthals by Anatomically Modern Humans is complex and diachronous across Europe. The scarcity of fossil remains hinders understanding of this transition which is primarily identified through the succession of stone tool assemblages (Hoffecker, 2009; Hublin, 2015; Staubwasser *et al.,* 2018). The Middle-Upper Palaeolithic Transition is characterised by a shift from Mousterian technologies associated with Neanderthals to Aurignacian technologies associated with modern humans and often "transitional" technologies will be associated with specific regions (Staubwasser *et al.,* 2018). The Châtelperronian technology is an example of a transitional technology which has been associated with Neanderthals (Bailey and Hublin, 2006). Key archaeological sites from the northwestern Iberian Peninsula which have recently been re-dated by Higham *et al.* (2014) include: La Viña, El Sidrón, La Güelga, Esquilleu, Morín, Arrillor, Labeko Koba, Lezetxiki. Within the Matienzo depression, Cueva de Cofresnedo is a site of archaeological interest. An Aurignacian layer has been dated to 31,360yr BP and this most likely overlies sediments associated with the Mousterian (Smith, 2006).

2.1.2 Climate

2.1.2.1 Climatic variability

Orbitally-forced climate changes throughout the Late Pleistocene have been proposed as the driving mechanism for the migration of *H. sapiens* out of Africa (Timmerman and Friedrich, 2016; de Menocal and Stringer, 2016) strengthening the argument for a dynamic relationship between hominin migration and climate change. Although the evidence for this hypothesis is not empirical, such long-term changes in climate may have influenced Neanderthal populations or potentially it was the unprecedented climatic variability during Marine Isotope Stage 3 (MIS3) which triggered the Neanderthal demise. MIS3 encompasses the period between 57-29ka and is characterised by rapid climate oscillations. Ice core records show a series of rapid

warming events known as Dansgaard-Oeschger (DO) events within MIS3 and these are expressed as abrupt shifts from stadial climatic conditions to milder interstadial climatic conditions, followed by a gradual return to colder stadial conditions (Dansgaard *et al.,* 1993). Another key feature of MIS3 is the presence of Heinrich events which are periods marked by significantly reduced sea surface temperatures and large releases of icebergs from the Laurentide ice sheet. Each Heinrich event marks the coldest period of a DO event and is followed by a rapid increase in temperature (Bond *et al.,* 1993). Further information about Heinrich events and DO variability can be found in section 2.2.

Recent work by Staubwasser *et al.* (2018) has shown archaeological sterile layers coincide with Greenland Stadial 12 (GS12), GS11 and GS10. These periods document cold and arid conditions at the time of the transition between Neanderthals and Anatomically Modern Humans. Additionally, the study highlights the diachronous nature of the Middle-Upper Palaeolithic Transition across Europe.

It has been suggested that climatic variability can place a significant amount of stress on mammalian populations (Barnosky *et al.,* 2004) and various authors have proposed the Neanderthals became extinct in relation to climatic instability during MIS3 (Finlayson and Carrion, 2007; Tzedakis *et al.,* 2007). Stewart (2005; 2007) has proposed that the Neanderthal extinction should be included in the wider Late Pleistocene extinction of the megafauna related to climatic deterioration during MIS3 towards the Last Glacial Maximum (LGM). These papers have identified the Neanderthals as part of a non-analogue environment incorporating a mixture of boreal, steppic and temperate faunas and environments. A fall in temperatures and carrying capacity of the landscape due to climatic deterioration towards the LGM has been determined by Stewart (2005) to have led to the spread of AMH, a fall in the number of carnivore numbers on the landscape including the cave bear, extinction of numerous animals including the mammoth, straight-tusked elephant, the Merck's rhinoceros and crucially the demise of the Neanderthals. Additionally, other authors have highlighted the importance of the non-analogue environment which was home to the Neanderthals and the vulnerability of such landscapes to the climatic instability which dominated MIS3 (Burjachs *et al.,* 2012; Magniez and Boulbes, 2014). During

MIS3 the shift towards cooler and drier conditions, especially during Heinrich events and towards the LGM, may have led to shifts in vegetation communities and extinctions of specific taxa (Burjachs *et al.,* 2012). It was these changes, combined with an increase in habitat fragmentation also related to climatic deterioration (Magniez and Boulbes, 2014) which may have placed Neanderthal populations under increased environmental stress and later contributed to their demise.

2.1.2.2 Heinrich events

Heinrich events are evident in a variety of records from across Europe, particularly the Iberian Peninsula. These events appear to cause an overall reduction in temperature and an increase in aridity in these regions. Stalagmites from Villars Cave, SW France (Wainer *et al.,* 2009; Genty *et al.,* 2010) and Sofular Cave, NW Turkey (Fleitmann *et al.,* 2009) have used stable isotope variations to identify Heinrich events 4 (H4) and 5 (H5) as periods of increased aridity and cooling. Evidence from a variety of marine cores from the Iberian margin (Roucoux *et al.,* 2005; Salgueiro *et al.,* 2010) have used various different proxies including pollen, stable isotopes and planktonic foraminifera identification to demonstrate periods of climate cooling across the North Atlantic. The marine cores from this region have identified the Heinrich events as periods of reduced sea surface temperatures. Additionally, Roucoux *et al.* (2005) indicated shifts in land pollen associated with Heinrich events, particularly a decrease in *Pinus* related to H4, implying dry and cooler conditions during the H4 event. Finally, lake records from Western Europe have shown through geochemical analysis and pollen identification, that Heinrich events are represented by cool temperatures and increased aridity on land. For example, at Fuentillejo maar, Spain, cold and arid conditions are thought to have dominated H4 due to lower lake levels, reduced total organic carbon and an increase in *Juniperus* and steppic-vegetation (Vegas *et al.,* 2010). Additionally, the lake record from Les Echets, France exhibits a hiatus around the timing of H4, suggesting a cold and dry period (Veres *et al.,* 2009).

2.1.2.3 H4

In the past, studies have often linked the disappearance of Neanderthals with the dramatically reduced temperatures and enhanced aridity which spread across Europe during H4 (Mellars, 1998; Bratmöller *et al.,* 2012). H4 in Iberia was characterised by

cooler and more arid conditions which saw the expansion of semi-desert vegetation in the western Mediterranean and the expansion of grasslands in the North (Sánchez Goñi *et al.,* 2008). Adaptation to the severe extremes of H4 would have forced changes in Neanderthal subsistence strategies and ability to cope with severe winters, and perhaps the Neanderthals could not adapt to these abrupt changes. AMH on the other hand appear to have had several prior adaptations such as complex tools and a social capacity which may have given them an advantage over Neanderthal groups (Mellars, 1998).

Alternative theories have argued for H4 leading to a later extinction of Neanderthals in southern Iberia associated with the expansion of semi-desert in this region (d'Errico and Sánchez Goñi, 2003; Sepulchre *et al.,* 2007). It is argued that aridification associated with H4 prevented the migration of AMH into southern Iberia until after H4. Model simulations have estimated a maximum vegetation of just 25% combined with a vast expansion of semi-desert environments across Iberia during H4 (Sepulchre *et al.,* 2007) and pollen evidence has justified this model (d'Errico and Sánchez Goñi, 2003). The enhanced aridity across central and southern Europe has led to the proposal that Neanderthal populations declined in density during this period due to a reduction in ungulate biomass (Sepulchre *et al.,* 2007). However, in spite of the population decrease during H4, the spread of semi-desert environments appears to have allowed the Neanderthals to occupy southern Iberia by slowing the advance of AMH (d'Errico and Sánchez Goñi, 2003).

The Campanian Ignimbrite (CI) eruption at 40ka is known as one of the most explosive events in Europe and its impact on the Neanderthals has also been debated (Fedele *et al.,* 2008; Lowe *et al.,* 2012). The volcanic event is proposed to have significantly impacted the ecology of the Mediterranean region and caused a 'volcanic winter' coincident with the onset of the H4 event resulting in widespread and rapid cooling (Fedele *et al.,* 2008). These factors may have impacted Neanderthal populations by causing them to contract or by leading to evolutionary and cultural development in AMH populations, giving them an advantage over Neanderthals (Fedele *et al.,* 2008; Lowe *et al.,* 2012). Models of the CI eruption have simulated the environmental effects associated with the eruption cannot in isolation explain the Neanderthal extinction.

Although, the authors do specify the immediate impact of climatic cooling as a consequence of the eruption would have had a significant influence on Neanderthal lifestyles and survival (Black *et al.,* 2015). Additionally, recent work by Davies *et al.* (2015) presented strengthened chronological frameworks to investigate the response of Neanderthal and AMH populations to abrupt climate shifts and environmental disasters. The paper concluded that it remains difficult to attribute the Neanderthal demise to a specific abrupt environmental transition or an environmental disaster such as the Campanian Ignimbrite.

2.1.2.4 Recent re-dating

Significant improvements to the radiocarbon dating technique have recently revised interpretation of the Neanderthal extinction (Higham *et al.,* 2014; Wood *et al.,* 2014). These improvements include: the selection of more material for dating e.g. bone and artefacts, more effective removal of contamination and an extended calibration curve covering the past 50ka (Davies, 2014). Sites from across Eurasia have been re-dated and calibrated using Bayesian age modelling and the results have indicated the disappearance of the Mousterian culture associated with the Neanderthals at around 42ka BP (Higham *et al.,* 2014; Wood *et al.,* 2014).

2.1.2.5 H5

In light of recent re-dating some authors have begun to identify H5 as a key factor which led to the extinction of the Neanderthals (Galvan *et al.,* 2014; Garralda *et al.,* 2014). The study by Galvan *et al.* (2014) dated and analysed the archaeological sequence at El Salt, Spain and found that the site was occupied by Neanderthals until ~45ka. Importantly, at ~45ka there was evidence of increased aridity and grassland expansion related to the H5 event and at El Salt this climatic event is associated with the last presence of the Neanderthals. Teeth from El Salt have been studied and represent the last occupation of the site between 47.2±4.4 and 45.2±3.4ka. The overlying unit which does not contain any archaeology, represents abandonment of the site potentially due to a climatic shift to arid conditions as shown through the sediments (Garralda *et al.,* 2014; Galvan *et al.,* 2014).

Alternatively, prior to the re-dating of Neanderthal sites, Müller *et al.* (2011) postulated that the severe climatic conditions associated with H5 led to the

abandonment of Neanderthal sites across Europe which allowed AMH to colonise and spread into the abandoned eastern Mediterranean, after H5. Müller *et al.* (2011) argued that the shift from desert-steppe to open forest associated with the climatic amelioration after H5, as shown by pollen records from Tenaghi Philipon, NE Greece, permitted the rapid spread of AMH into and across Europe before the Neanderthals could reoccupy this region.

2.1.3 Competition with AMH

2.1.3.1 Extinction through competitive exclusion

The role of AMH in the Neanderthal extinction has led to extensive debates. The model of Banks *et al.* (2008) combined palaeoclimate data with archaeological and chronological data and the results have suggested that Neanderthals contracted their range during Greenland Interstadial 8 following H4 due to the expansion of AMH and any climatic causes can be rejected. The use of cryptotephra as an isochronous marker horizon has argued the technological transition between the Middle and Upper Palaeolithic occurred prior to the H4 event and the Campanian Ignimbrite eruption (Lowe *et al.,* 2012). Therefore, the authors have suggested competition with AMH was the driving factor leading to the Neanderthal demise.

D'Errico and Sánchez Goñi (2003) have argued for a combined influence of both AMH competition and climate change. The authors have suggested the climatic amelioration after H4 led to the expansion of AMH across the Iberian Peninsula and the arrival of AMH in the southern Iberian Peninsula and associated competition ultimately resulted in the extinction of the Neanderthals (d'Errico and Sánchez Goñi, 2003). Additionally, Müller *et al.* (2011) argued that a combination of the severe climatic conditions associated with H5 combined with increased competition with AMH led to the demise of the Neanderthals.

2.1.3.2 Problems with dating

The key problem for determining the causes of the Neanderthal extinction is dating. As shown in section 2.1.2.4, recent dating has changed our view of when the Neanderthals became extinct. Authors have recently argued for the earlier arrival of

AMH in Europe with key findings from Kent's Cavern, UK, dated to 44.2-41.5ka (Higham *et al.,* 2011) and Grotta del Cavallo, Italy, dated to 45-43ka (Benazzi *et al.,* 2011). The earlier arrival of AMH complicates the causes for Neanderthal extinction as the two species may have overlapped in areas of Europe. Recent work by Higham *et al.* (2014) has identified a potential overlap between Neanderthals and AMH of 2,600-5,400yrs, which is enough time for cultural and genetic overlap between the two species.

2.1.4 Genetic evidence

In recent years, technological advances have allowed improved and detailed understanding of Neanderthal genetics (Green *et al.,* 2010). Genetic evidence has identified Neanderthal populations were small and isolated which led to inbreeding (Castellano *et al.,* 2014; Prüfer *et al.,* 2014). The pro-longed population bottle-neck as a consequence of inbreeding reduced the genetic diversity of the Neanderthal population (Prüfer *et al.,* 2014). Subsequently, Neanderthals were 40% less fit than the AMH who were migrating across Eurasia (Harris and Nielsen 2016; 2017). If the fitness disadvantage was passed down to Neanderthal-AMH hybrid offspring, Neanderthal genes are proposed to be selected against leading to a reduction in Neanderthal ancestry over time as a consequence of natural selection (Juric *et al.,* 2016; Harris and Nielsen, 2016; 2017). Genetic evidence may therefore imply Neanderthals did not truly become extinct but were assimilated into the genomes of AMH (Harris and Nielsen, 2017).

On the other hand, genetic evidence has led some authors to link population bottlenecks and extinction of Neanderthals with climate changes. Analysis of recent western Neanderthal mtDNA, i.e. the mitochondrial DNA of Neanderthals present in Western Europe since 48ka, has revealed a reduced amount of genetic variation when compared to eastern and older Neanderthals (Dalén *et al.,* 2012). The paper has proposed the genetic turnover in recent western Neanderthals was most likely a result of the climatic variability during MIS3. The authors speculate North Atlantic cold periods associated with H5 and H6 influenced the terrestrial environment which led to the bottleneck or localised extinction of Neanderthals in western Europe (Dalén *et al.,* 2012).

2.1.5 Summary

It is apparent that the demise of the Neanderthals is a complicated issue and the numerous factors which may have been responsible are still debated. Primary problems include dating issues in addition to the sparse resolution of the archaeological record and the diachronous nature of the transition between Neanderthals and AMH. Important to this project is the role of climate but as d'Errico and Sánchez Goñi (2003) pointed out, there remains a lack of high resolution, independently dated and continuous palaeoclimate records from the Iberian Peninsula and this remains true today. Therefore, there is a need to create such records from across the Iberian Peninsula before the role of climate change in the Neanderthal extinction can be addressed.

2.2 Climate change 90-25ka

2.2.1 Introduction

Recent improvements in the independent dating of ice core, marine and terrestrial records have permitted the correlation of these records across the globe and in particular the northern hemisphere. The correlation of these various records has begun to identify leads and lags in the climate system as well as enhancing current understanding of the forcing factors behind these abrupt changes (Blockley *et al.,* 2012). Between 90-25ka the climate of the North Atlantic was influenced by orbital forcing but it was also driven by sub-orbital mechanisms. Evidence from different archives from across the northern hemisphere will be presented in this section as well as a summary of the forcing mechanisms.

2.2.2 Orbitally-driven climate change

Orbital forcing was long hypothesised to influence the Earth's climate (Croll, 1864; Milankovitch, 1941) and support for the orbital forcing theory later came from the oxygen isotope records of planktonic foraminifera preserved within marine sediments (Emiliani, 1955, Emiliani, 1966, Shackleton, 1967). Shifts in the isotopic composition of

foraminifera within deep-sea cores were identified as a proxy for global ice volume (Shackleton, 1967). This finding led to the development of the SPECMAP astronomical timescale which tuned stacked oxygen isotope records from planktonic foraminifera to orbital forcing, producing a single global marine $\delta^{18}O$ record (Imbrie *et al.,* 1984; Martinson *et al.,* 1987). The development of the SPECMAP timescale permitted comparison of marine $\delta^{18}O$ records with other proxies from around the world and contributed to understanding climatic processes which operate over Glacial-Interglacial timescales (Bassinot, 2009). The development of the LR04 stack increased the resolution of the SPECMAP timescale and extended it back to 5.3Myr (Lisiecki and Raymo, 2005). It is important to note that there are issues associated with tuning any record to orbital forcing (Blaauw, 2012) and recent work has also highlighted the chronological limitations associated with marine cores (Austin and Hibbert, 2012). Nevertheless, these long records of changes in the $\delta^{18}O$ composition of foraminifera led to the definition of Marine Isotope Stages (MIS) which correspond to Glacial-Interglacial cycles driven by orbital forcing (Imbrie *et al.,* 1984; Martinson *et al.,* 1987; Lisiecki and Raymo, 2005).

Ages for the onsets of different marine isotope stages relevant to this study are shown in table 2.1. Glacial marine isotope stages are represented by even numbers whilst Interglacial marine isotope stages are represented by odd numbers. However, MIS3 is an anomaly as it is characterised by a high degree of climate instability in comparison to the relatively stable glacial conditions of MIS 4 and MIS2 (Bond *et al.,* 1993; Shackleton *et al.,* 2000; Lisiecki and Raymo, 2005).

Table 2.1: Onset ages for MIS5-2 (as defined by Lisiecki and Raymo, 2005).

Marine Isotope Stage	**Onset age (ka)**
MIS2	29
MIS3	57
MIS4	71
MIS5	130

Marine sediment cores spanning MIS3 have identified a period of terrestrial tree decline (Roucoux *et al.,* 2005; Fletcher and Sánchez Goñi, 2008), lowered SST (Cacho *et al.,* 1999) and ice sheet growth (Thomson *et al.,* 1999; Shackleton *et al.,* 2000;

Schönfeld *et al.,* 2003; Roucoux *et al.,* 2005). It has been argued that these proxies indicate a long-term aridity and cooling trend throughout MIS3 on the Iberian Peninsula and this period corresponds to a reduction in Northern Hemisphere Summer Insolation.

2.2.3 Sub-orbital climate variability

2.2.3.1 Ice cores

The identification of abrupt millennial-scale climatic events in the Greenland ice cores (Dansgaard *et al.,* 1993; Grootes *et al.,* 1993) has led to numerous studies which have focussed on identifying these climatic patterns in terrestrial and marine records (Voelker*,* 2002).

Ice core records from Greenland have demonstrated an unstable climate dominated the Last Glacial Period, characterised by a sequence of abrupt climatic shifts known as Dansgaard-Oeschger (DO) events. During DO events climate abruptly switched from cold conditions to mild interstadial conditions (Dansgaard *et al.,* 1993; Johnsen *et al.,* 1992; Rasmussen *et al.,* 2014). The chronology of the DO events is represented in Greenland by Greenland Interstadials (GI) and Greenland Stadials (GS) with GI periods defined by warm conditions and GS periods defined by cold conditions (figure 2.1) (Rasmussen *et al.,* 2014). Across the Last Glacial Cycle 25 DO events (GI periods) have been identified and are defined by a sharp increase in temperature followed by a gradual return to stadial conditions (GS periods) (NGRIPmembers, 2004; Kindler *et al.,* 2014; Rasmussen *et al.,* 2014). The temperature increase associated with the DO events varies between 5°C to 16.5°C (Kindler *et al.,* 2014).

The chronology of these events (GI and GS) has recently been redefined through comparison of the oxygen isotope compositions and calcium ion concentrations in three ice-core records (NGRIP, GRIP, GISP2) from Greenland on the same timescale. The time period examined herein (90-25ka) spans GI-22 to GS-3. It is evident from the Greenland ice core records that the period between 90-25ka, similar to the rest of the Last Glacial Period, was characterised by rapid increases in temperature at the onset of interstadial conditions (DO events) followed by a gradual decline in temperatures

back to stadial conditions (Dansgaard *et al.,* 1982; Johnsen *et al.,* 1992; Dansgaard *et al.,* 1993; NGRIP members, 2004; Rasmussen *et al.,* 2014).

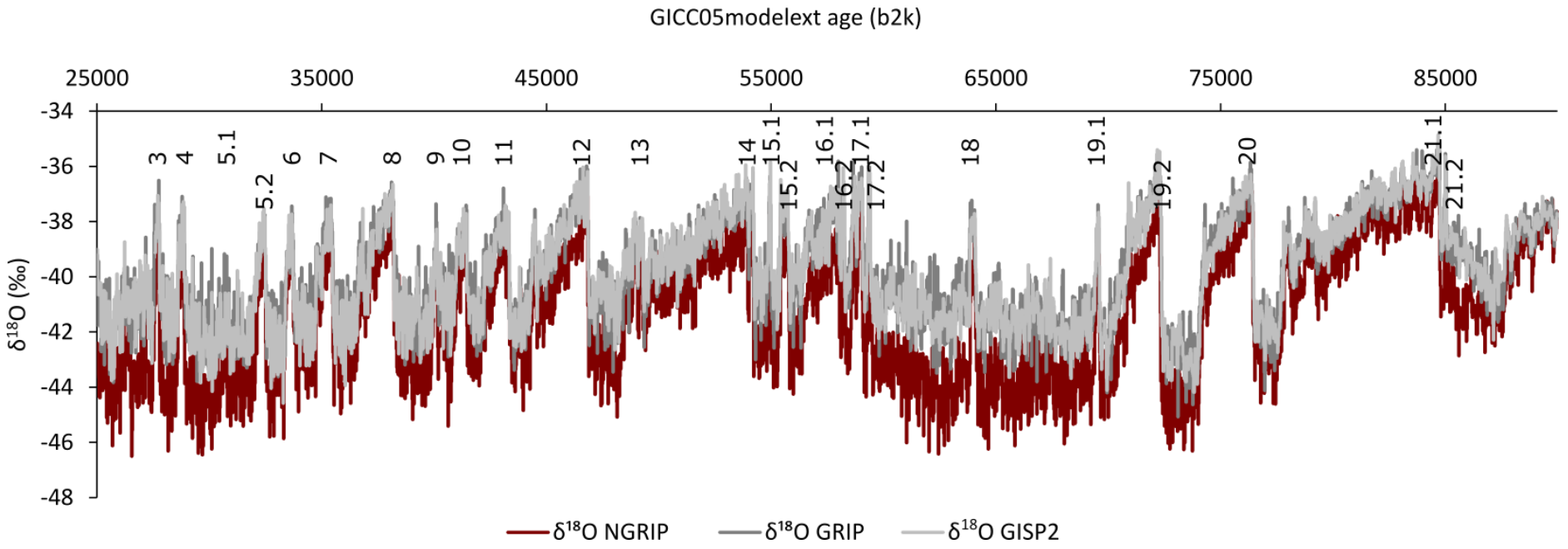

Figure 2.1: Oxygen isotope records from three Greenland ice cores (Rasmussen et al. 2014) using the chronological framework developed by Seierstad et al. (2014). Numbers express Greenland Interstadial onsets as defined by Rasmussen et al. (2014). Data available from: http://www.iceandclimate.nbi.ku.dk/data/

2.2.3.2 Marine

Evidence from a series of marine cores from the North Atlantic demonstrated a pattern of millennial-scale abrupt increases in temperature followed by gradual cooling, similar to the DO cycles in Greenland (Bond *et al.,* 1993). A key finding of Bond *et al.* (1993) was the identification of a series of 'saw-toothed' cooling cycles (now known as Bond cycles) composed of numerous DO cycles, gradually becoming colder and culminating in a Heinrich event. The Heinrich events mark the coldest point of a Bond cycle where large numbers of icebergs were released into the North Atlantic (Bond *et al.,* 1993). Heinrich events 5, 4 and 3 occurred during the time period studied in this thesis (86-27ka) with dates of 45,000, 38,000 and 31,000 respectively (Hemming, 2004).

Evidence from marine records across Europe express similar climatic variability during MIS3. For example marine core MD99-2281 from south of the Faroe Islands expressed climatic instability throughout MIS3 as a result of the dynamic behaviour of the European ice sheets during this time (Zumaque *et al.,* 2012). The multi-proxy record studied by Zumaque *et al.* (2012) identified a series of oscillations matching the GI and GS events; GI events were milder while stronger ice sheet calving occurred during GS events. Comparably, the Eastern Mediterranean pollen records from marine core 9509 have indicated a reduction in forests and an increase in arid herbaceous flora between 43.5-16.2ka (Langgut *et al.,* 2011). Furthermore, Heinrich events 6-2 have been identified in marine core 9509 based upon short-lived reductions in arboreal vegetation suggestive of a decline in moisture availability and thus Langgut *et al.* (2011) have demonstrated the expression of North Atlantic climate events in the Eastern Mediterranean.

Marine core MD95-2042, taken from off the coast of the Iberian Peninsula, has demonstrated through planktonic $\delta^{18}O$ analyses, stadial-interstadial climate variability correlating with DO cyclicity in Greenland (Shackleton *et al.,* 2000). Further work on MD95-2042 by Sánchez Goñi *et al.* (2000) identified a pattern of DO cycles and Heinrich events through a combination of dinocyst, pollen, foraminifera and coarse lithic analyses as well as the $\delta^{18}O$ profile. The study demonstrated a three-phase sequence of Heinrich events 5 and 4 with only the middle phase characterised by cold

and dry conditions. In contrast, the first and final phases exhibited milder and more humid climates. The pollen record from MD95-2042 highlighted several periods corresponding to DO stadials characterised by steppic taxa such as *Artemisia* and Chenopodiaceae (Sánchez Goñi *et al.,* 2000). However, caution should be applied when trying to link these events in southwest Europe to DO cyclicity in the Greenland ice cores, as the MD95-2042 record has been tied to the GISP2 timescale on the basis that rapid warming was synchronous between the two regions (Sánchez Goñi *et al.,* 2000, Shackleton *et al.,* 2000).

However, despite the dating issues and alternative influences, numerous cores from around the Iberian Peninsula have shown a similar pattern of DO cyclicity and Heinrich events. Sánchez Goñi *et al.* (2018) discuss the significant contribution of pollen studies in the identification of DO variability and Heinrich events on the Iberian Peninsula. A pollen record from the Alboran Sea (MD95-2043) showed an alternation between semi-desert vegetation such as *Artemisia* and Chenopodiaceae during stadials and Heinrich events and mixed oak forest during interstadials (Fletcher and Sánchez Goñi, 2008). Two cores off the Iberian margin have demonstrated variations in productivity are coincident with DO variability and Heinrich events (Pailler and Bard, 2002). The combined pollen and planktonic $\delta^{18}O$ data from marine core MD95-2039 has provided evidence for millennial-scale variability. Fluctuations in thermophilous tree populations correspond to shifts in SSTs with warmer SST synchronous with expanding thermophilous tree populations (Roucoux *et al.,* 2005). In addition, Heinrich events in the Roucoux *et al.* (2005) study are demonstrated to have been more severe than DO stadials due to the greater reduction in *Pinus*. Interestingly, the fire regime of western France has been shown in marine core MD04-2845 to exhibit DO variability and Heinrich events through multiproxy analysis of microcharcoal, pollen and organic carbon in conjunction with analysis of ice rafted debris and isotopic analyses of foraminifera (Daniau *et al.,* 2009). Key records of climate change from the Iberian Margin are presented in figure 2.2 alongside the Greenland ice core record (NGRIP).

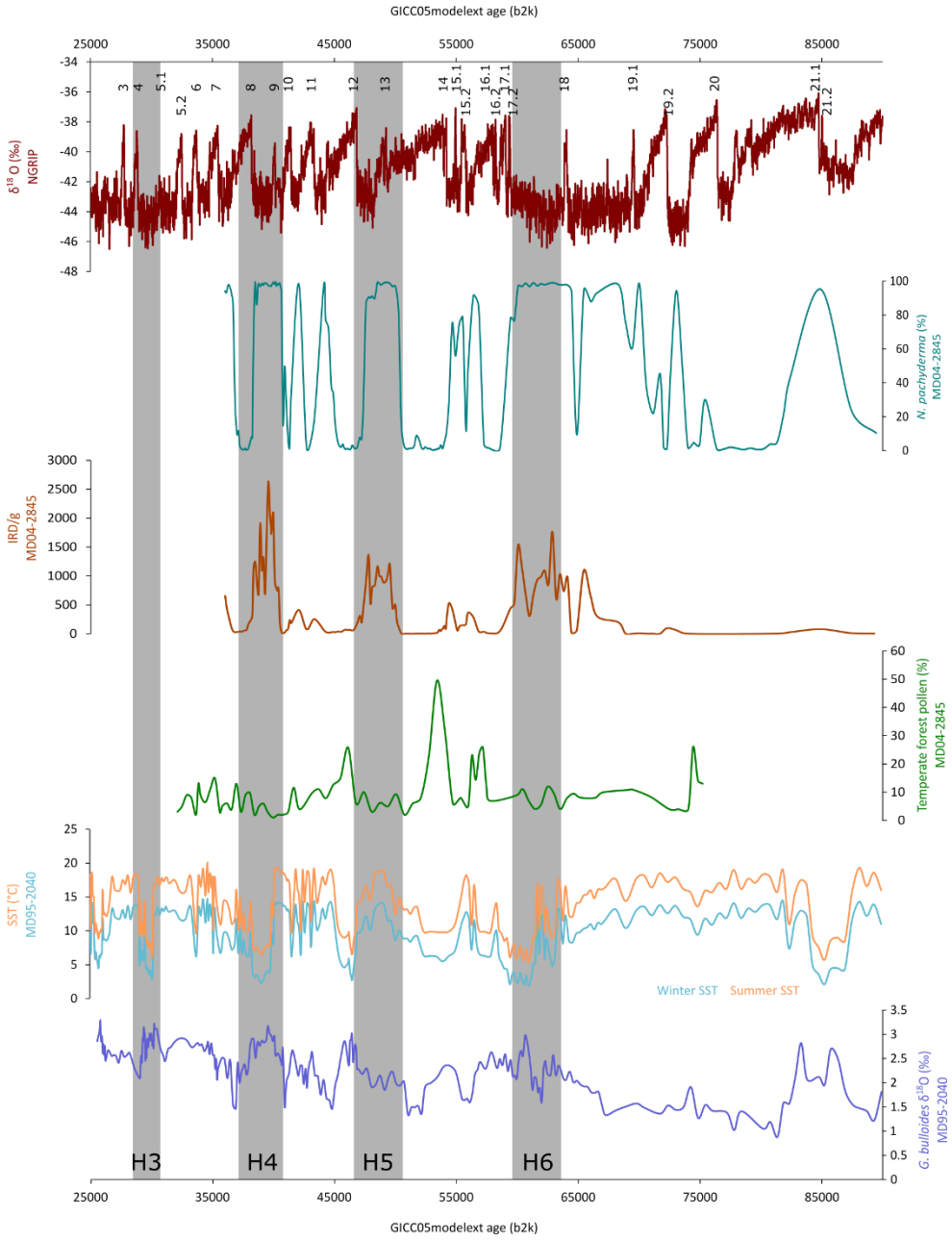

Figure 2.2: Marine sediment proxy data from the North Atlantic and the Greenland Ice core record. The oxygen isotope record from NGRIP is from Rasmussen et al. (2014) and uses the chronological framework developed in Seierstad et al. (2014). Numbers at the top refer to onset ages of Greenland Interstadials as defined by Rasmussen et al. (2014). N. pachyderma data (data source: Sánchez Goñi, 2013) and IRD (data source: Sánchez Goñi 2013) from core MD04-2845 are from Sánchez Goñi et al., (2013). Temperate pollen data from MD04-2845 is from Daniau et al. (2009) (data source: ACER Project members, 2017a). SST (data source: Voelker et al., 2011b) and G. bulloides $\delta^{18}O$ (data source: Voelker et al., 2011c) are from Voelker et al., 2011a. Heinrich events are also shown and correspond to the dates of Hemming (2004).

2.2.3.3 Speleothems

Evidence for climatic instability during MIS3 has been shown from oxygen and carbon stable isotope records from speleothems across Europe (Spötl and Mangini, 2002; Genty *et al.,* 2003; Wainer *et al.,* 2009; Fleitmann *et al.,* 2009; Genty *et al.,* 2010; Moseley *et al.,* 2014). Stalagmites from Hölloch Cave, northern Alps, exhibited millennial-scale increases in $\delta^{18}O$ values of up to 3‰ which were correlated to DO events in the Greenland ice cores, higher sea surface temperatures in the NE Atlantic Ocean and strengthening of the East Asian Summer Monsoon across Asia (Moseley *et al.,* 2014). A similar correlation was found in the oxygen isotope profile from Solfular Cave, Turkey (Fleitmann *et al.,* 2009). Additionally, carbon isotope records have been used to infer climate changes across MIS3 from speleothem records with shifts in $\delta^{13}C$ values reflecting varying vegetation cover and soil microbial activity directly related to temperature and precipitation (Wainer *et al.,* 2009, Fleitmann *et al.,* 2009, Genty *et al.,* 2003, Genty *et al.,* 2010). During periods of climatic amelioration microbial activity in the soil zone increases, as does the amount of overlying vegetation and as a result the $\delta^{13}C$ values in the soil become lowered (Wainer *et al.,* 2009). Carbon and oxygen profiles from terrestrial speleothems have therefore provided crucial evidence for the response of these areas to North Atlantic climate events and have identified key leads and lags within the climate system. For example, Moseley *et al.* (2014) demonstrated that the DO events in the Greenland ice cores lagged the large amplitude millennial-scale increases in $\delta^{18}O$ values preserved within stalagmites from Hölloch Cave. Throughout MIS4-2, speleothem growth was rare in NW Spain as a result of reductions in temperature and humidity (Stoll *et al.,* 2013). Sporadic periods of growth in MIS3 appear to coincide with warmer SST (>13.7°C) associated with DO interstadials.

2.2.3.4 Lacustrine

Lake records which have been precisely and accurately dated through a combination of radiocarbon dating, tephrochronology and varve counting, can provide important terrestrial archives of palaeoenvironment (Hayashi *et al.,* 2010; Nakagawa *et al.,* 2012). The Les Echets palaeolake, eastern France has provided a vital record of palaeoclimate during MIS3 through analysis of geochemistry (Veres *et al.,* 2009; Wohlfarth *et al.,* 2008), pollen (Wohlfarth *et al.,* 2008) and diatoms (Ampel *et al.,*

2008). Studies from Les Echets have revealed a similar pattern of stadial-interstadial climate variability during MIS3 as well as the identification of Heinrich events 4, 3 and 2, similar to those recorded in marine and ice core records. Interstadial periods are characterised by, silty gyttja sediments rich in organics (Veres *et al.,* 2009), reduced erosion and high arboreal pollen (Wohlfarth *et al.,* 2008) and a diverse assemblage of planktonic diatoms (Ampel *et al.,* 2008). Conversely, stadials are characterised by minerogenic sediments and increased clastic sedimentation (Veres *et al.,* 2009; Wohlfarth *et al.,* 2008), increased erosion and high non-arboreal pollen (Wohlfarth *et al.,* 2008), and a low diversity assemblage of benthic diatoms such as *Fragilaria* suggestive of periods of protracted ice cover (Ampel *et al.,* 2008). Additionally, Heinrich events are defined by periods of significantly lowered lake level productivity (Veres *et al.,* 2009), limited diatoms (Ampel *et al.,* 2008) and increased erosion (Wohlfarth *et al.,* 2008). Heinrich event 4 was identified by Wohlfarth *et al.* (2008) as a hiatus between 36.3-40.3ka at Les Echets due to reduced lake levels related to the extreme cold and arid conditions.

Lacustrine records from Lago Grande di Monticchio, southern Italy, have revealed a pattern of climate instability over the past 102ka based upon pollen analysis (Allen *et al.,* 1999). Last glacial interstadials were dominated by wooded steppe environments whilst stadials were dominated by steppe environments and shifts between vegetation types were demonstrated to have occurred within 200 years. Thus, evidence of abrupt climatic oscillations from Lago Grande di Monticchio supports the coupling of the Northern Hemisphere ocean-atmosphere system during the Last Glacial cycle. Tzedakis *et al.* (2004) discussed the evidence for vegetation response to stadial-interstadial climate variability and Heinrich events from Greek lacustrine records. The three records analysed from across Greece responded to these events, however the individual responses were site specific due to local factors.

In contrast to the substantial amount of marine records spanning MIS3 from the Iberian Peninsula, the number of lacustrine sequences remains relatively minor (Moreno *et al.,* 2012). The production of lake records from the Iberian Peninsula is limited by the challenges in producing a chronology and a relatively high sampling resolution (Moreno *et al.,* 2012). A key sequence does exist from Lake Banyoles, NE

Spain, and pollen was initially reported from this sequence by Pèrez-Obiol and Julià (1994) extending back to 30ka BP. Since then, Höbig *et al.* (2012) have studied the sedimentological properties and produced a palaeoclimate reconstruction of Lake Banyoles through a multi-proxy approach. Of particular reference to the present study is the geochemical analysis carried out by Höbig *et al.* (2012) which has shown evidence for past climatic variability extending possibly down to MIS4 and through to the Holocene. Shifts in element ratios from Lake Banyoles, especially K/Ca, are suggestive of variations in humidity; tentatively assigned to Heinrich events 5-0. Further work on Lake Banyoles sediments has demonstrated MIS3 as a period of high climate and environmental instability shown through isotope excursions ($\delta^{18}O$ and $\delta^{13}C$), total organic carbon and benthic diatom abundance (Lacey *et al.,* 2016).

The Fuentillejo Maar record, central Spain, was analysed using a multi-proxy approach and identified periods of aridity associated with Heinrich events and DO stadials (Vegas *et al.,* 2010). However, the FUENT-1 record demonstrated that H4, 2, 1 and the YD have a different climatic signal (cold and arid) to H5 and 3 (warm and arid) indicating the influence of regional processes over North Atlantic climate variability. The lake sequence from Lake Enol contained a series of laminated rhythmic sediments associated with variations in carbonate content, suggestive of slight climatic ameliorations between Heinrich events. However, further work is needed to derive a record of palaeoclimate from the Lake Enol sequence during MIS3 and tighter chronological control is also required (Moreno *et al.,* 2010). It is apparent that there is a gap in the concentration of lacustrine sequences from the Iberian Peninsula and only further studies can contribute to understanding how rapid climatic oscillations during MIS3 affected terrestrial landscapes (Moreno *et al.,* 2012). Furthermore, the recent extension to the IntCal calibration curve (IntCal13) (Reimer *et al.,* 2013) will help to constrain the chronologies of future lacustrine records from the Iberian Peninsula.

2.2.3.5 Additional archives

Mammal assemblages from Iberia have demonstrated MIS3 was a period of climatic instability, as shown through the coexistence of cold-adapted and temperate taxa occupying the region (Álvarez-Lao, 2014). *Mammuthus primigenius* (woolly

mammoth), *Coelodonta antiquitatis* (woolly rhino), *Rangifer tarandus* (reindeer) and *Alopex lagopus* (arctic fox) are used as key cold-climate indicator species on the Iberian Peninsula during MIS3 and appear to be associated with the expansion of steppe-environments corresponding to Heinrich events (Álvarez-Lao and García, 2010). Specifically, evidence from the Jou Puerta site demonstrates a mixture of cold and temperate taxa, suggesting a mosaic of habitats composed of steppe-environments, forests and rocky mountains (Álvarez-Lao, 2014). Overall, mammalian evidence from cold-climate taxa suggests occupation and cohabitation with local temperate taxa in the Iberian Peninsula during episodes of extreme cold and aridity across Eurasia.

Travertine pollen assemblages from caves or rock shelters on the Iberian Peninsula have provided key terrestrial pollen sequences spanning the Last Glacial period (Burjachs and Julià, 1994; Carrión *et al.,* 1998). Due to the relatively low resolution and poor chronological controls, these records do not provide information regarding millennial-scale shifts during MIS3. Furthermore, despite the presence of long peat sequences in the Iberian Peninsula, particularly the Padul sequences (Pons and Reille, 1988, Ortiz *et al.,* 2004), millennial-scale variability during MIS3 has not been identified.

A loess record from Nussloch, Germany, exhibited DO variability through changes in grain-size index with H3 and H4 being defined in the sequence by maxima in grain-size indicating arid conditions (Rousseau *et al.,* 2007). Additionally, evidence from central Spanish loess sequences identified a period of aridity at 42ka and an even harsher period of aridity between 28.4±2.4ka and 32.2±2.7ka (Wolf *et al.,* 2018). Due to dating and resolution complexities, loess deposition from the central Spanish sequence cannot be assigned to a specific stadial or Heinrich Event.

2.2.4 Driving mechanisms for sub-orbital variability

2.2.4.1 Pacing of DO events

The recurrence time between DO warming events was shown to vary significantly between 1-12ka over the past 90ka (Bond *et al.,* 1999). The work of Bond *et al.* (1997)

derived a periodicity of 1470±500yrs for abrupt climate shifts during the Holocene and Last Glacial period using North Atlantic marine sediments. Solar forcing has been proposed to drive this cyclicity during the Holocene (Bond *et al.,* 2001). In the interval 12-50ka, $\delta^{18}O$ values from the GISP2 ice core identify a significant periodicity peak at 1470yrs which has been interpreted to reflect the pacing of DO events (Grootes and Stuvier, 1997). The validity of the ~1500yr cycles has been questioned (Wuncsh, 2000; Ditlevsen *et al.,* 2007). Although recent studies suggest a periodic forcing mechanism cannot be rejected (Schulz, 2002; Ditlevsen and Ditlevsen, 2009; Woillez *et al.,* 2012). Statistical analysis by Schulz (2002) indicated that between 13 and 46ka the pacing of DO events varied by ±20% around the 1470yr periodicity. The study postulated it was unlikely that variations in North Atlantic Deep Water formation forced the DO cyclicity during the Last Glacial period.

2.2.4.2 Forcing mechanisms of climate variability

The Iberian Peninsula demonstrated a shift to extreme aridity and cooling during Heinrich Events and DO stadial periods. It has been hypothesised that these periods were associated with a reduction in Atlantic Meridional Overturning Circulation (AMOC) (Rasmussen *et al.,* 1996; Stocker, 2000; Roucoux *et al.,* 2005). A weakened AMOC resulted in lowered sea surface temperatures (SST) and strengthening of westerly winds which shifted to the North. During Heinrich Events aridity and cooling were intensified relative to DO stadials as a result of lowered SST, offshore ice and the close proximity of the polar front (Roucoux *et al.,* 2005).

The identification of abrupt warming events in the North Atlantic and across Europe coincident with Greenland interstadial periods has discerned the presence of a tightly coupled ocean-atmosphere system prior to and throughout MIS3 (Bond *et al.,* 1993; Roucoux *et al.,* 2001; Vegas *et al.,* 2010). The onsets of DO events have been proposed to link to abrupt reorganisation of atmospheric circulation (Bond *et al.,* 1993) as they were rapid, occurring within decades, and involved a warming of 9±3°C (Severinghaus and Brook, 1999). High-resolution analysis of Greenland ice cores revealed polar atmospheric circulation can shift within 1 to 3 years. Southern Hemisphere/tropical warming has been hypothesised as the trigger for mid-to-high latitude warming

associated with DO events due to northward migration of the Intertropical Convergence Zone (ITCZ) (Steffensen *et al.,* 2008).

2.2.5 Summary

Various records across the Northern Hemisphere have shown that DO cycles and Heinrich events in the North Atlantic were propagated as far as Eastern Asia during MIS3 and further work will continue to reveal leads and lags in the climate system and forcing mechanisms. The European records presented appear to record climate and environmental responses to DO variability and Heinrich events as do the marine records from the Iberian Peninsula. However, as discussed, the Iberian marine records exhibit latitudinal and longitudinal variability with sites in the NW most influenced by subpolar waters (Salgueiro *et al.,* 2010). This section has highlighted the present lack of terrestrial records spanning 90-25ka from the Iberian Peninsula, particularly from speleothems. It is possible that during this period conditions may have been too cold and arid to permit speleothem growth. However, very few speleothem studies from the Iberian Peninsula have focussed on this time period and speleothems dating to this period may have been overlooked.

2.3 Speleothems as recorders of climate and environmental processes

Speleothems preserve a range of proxies for climate and environmental variability such as stable isotopes (primarily O and C) and trace elements. The variability of these proxies over time can be interpreted with respect to past climate and environmental changes (Fairchild and Baker, 2012). The chemical signal evolves from precipitation infiltrating soil, bedrock and into the cave void where it is subsequently preserved in speleothem calcite. This sequence is explained in detail below and summarised in figure 2.3.

The chemical signature preserved in precipitation is a function of atmospheric moisture which in turn can vary over time dependent on variable atmospheric

circulation patters, temperature and precipitation amount (Fairchild *et al.,* 2006a). Precipitation infiltrates into the soil zone upon which CO_2 is assimilated into the solution resulting in the generation of a weak carbonic acid (eq. 2.1).

$$\mathrm{H_2O} + \mathrm{CO_2} \rightarrow H_2CO_3 \qquad \text{Eq. 2.1}$$

Carbonic acid dissolves the underlying karstic bedrock which leads to a solution which is supersaturated in calcium carbonate ($CaCO_3$) (eq. 2.2).

$$\mathrm{H_2CO_3} + \mathrm{CaCO_3} \rightarrow Ca^{2+} + 2HCO_3^{-} \qquad \text{Eq. 2.2}$$

As drip waters enter the cave void, CO_2 is lost from the solution through degassing. As a consequence, $CaCO_3$ is precipitated as speleothem deposits (eq. 2.3)

$$Ca^{2+} + 2\mathrm{HCO_3}^{-} \rightarrow CaCO_3 + H_2O + CO_2 \qquad \text{Eq. 2.3}$$

Throughout this sequence from the atmosphere to the speleothem, climatic and environmental signals within the precipitation and subsequent infiltrating waters can be generated or modified (Fairchild *et al.,* 2006a; Fairchild and Baker, 2012). Five realms have been defined by Fairchild *et al.,* 2006a where signals may be modified:

- Atmosphere
- Soil and upper epikarst
- Lower epikarst and cave
- $CaCO_3$ precipitation
- Secondary alteration of calcite

Therefore, the geochemical signal preserved in speleothems represents a combined signal derived from the realms listed above (Fairchild *et al.,* 2006a). Speleothem records have a vast potential to provide a unique perspective regarding a variety of processes such as karst and cave evolution, vegetation dynamics and climate changes.

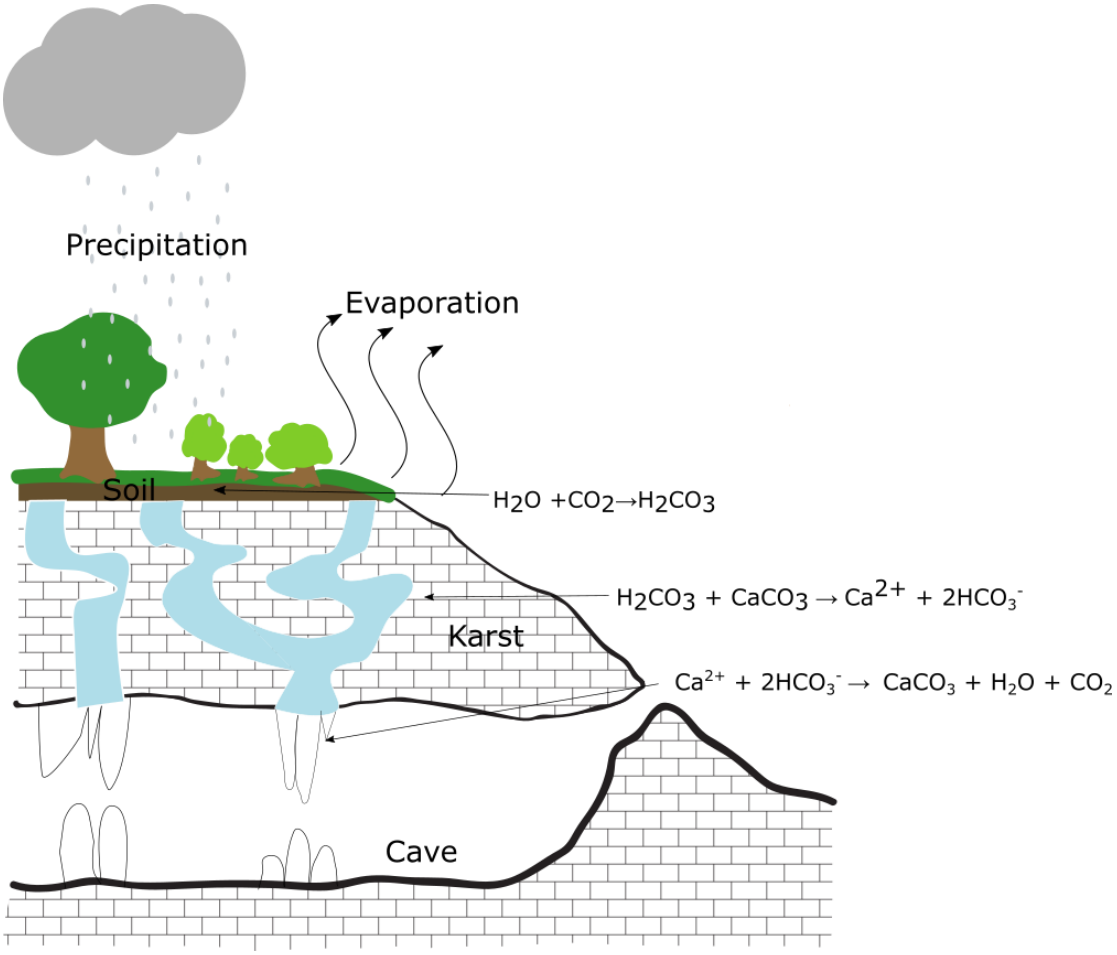

Figure 2.3: Schematic diagram adapted from Fairchild et al. (2006a) (originally adapted from Tooth, 2000) illustrating dissolution and precipitation processes within the karst system.

2.4 Understanding the dynamics of cave systems

2.4.1 Introduction

Caves are typically thought to be relatively stable environments which act to preserve speleothem archives. The climate signal preserved in chemical signatures of precipitation and dripwaters are modified as they move through the atmosphere, soil, karst and into the cave where it is preserved in speleothem calcite (Fairchild *et al.,* 2006a). As a consequence, hydrological routing, karst-water interactions and cave ventilation are examples of such processes which may act to modify the palaeoclimate signal preserved in dripwaters. Through cave monitoring, these processes can be

classified and the palaeoclimatic proxies within the speleothems can be correctly interpreted and any local effects which may act to modify the palaeoclimate record can be identified (Mattey *et al.,* 2010; Fairchild and Baker, 2012). This section will discuss the three processes mentioned above and review current techniques for monitoring these processes within cave environments.

2.4.2 Processes acting to modify speleothem signals

2.4.2.1 Hydrological routing

Karst systems are dynamic environments with a variety of different storage and flow conditions occurring in numerous different geological contexts. However, characterising the karst hydrology poses a challenge due to the heterogenous nature of the karst environment (Ford and Williams, 2007; Bradley *et al.,* 2010). Understanding the nature of the karst hydrology is critical to understanding induced uncertainty in speleothem palaeoclimate proxies through the relationships between the chemistry of infiltrating waters, surface and sub-surface climatology, and speleothem proxy values such as $\delta^{18}O$ (Bradley *et al.,* 2010).

Dissolution of carbonate rocks such as limestone and dolomite through surface precipitation and surface-water inflows results in the development of karst. The karst landscape is characterised by an extensive system of underground water movement and cave systems (Ford and Williams, 2007; Bradley *et al.,* 2010; Fairchild and Baker, 2012). Three levels of porosity can be distinguished within karst and these are primary, secondary and tertiary (Ford and Williams, 2007).

Primary porosity in bedrock is associated with inter-granular pore space (Fairchild and Baker, 2012). In Mesozoic (as well as Palaeozoic and Cenozoic) carbonates porosity is typically less than 10% (Fairchild and Baker, 2012) and the process of dolomitization of limestone initially reduce porosity due to infilling but then porosity will increase as a result of the smaller dolomitic rhombs (Ford and Williams, 2007). Water movement associated with primary porosity is known as matrix flow and can be very slow moving (Fairchild and Baker, 2012). Smart and Friedrich (1987) classified matrix flow drip sites

as having a low coefficient of variation in drip rate as a result of consistently low discharge.

Secondary porosity is related to joints and fractures within the karst (Ford and Williams, 2007; Bradley *et al.,* 2010). Fractures within the karst encourage rapid transmission of infiltrating drips following recharge events resulting in a significant increase in drip discharge (Miorandi *et al.,* 2010).

Finally, tertiary porosity is associated with dissolution along penetrable fissures by groundwaters which develop into conduits and caves (Ford and Williams, 2007). Conduit flow discharge varies significantly in response to external rainfall patterns and conduit drip sites are classified by a high coefficient of variation based upon intermittent and often high levels of discharge (Smart and Friedrich, 1987).

The ways in which water moves through the karst system will vary depending on water delivery into the karst system. In turn this may reflect the internal void connectivity within the karst, the extent to which permeability has developed and the configuration of water reservoirs either within the matrix or structural voids within the karst (Bradley *et al.,* 2010). A combination of different flow pathways may occur and there may be numerous individual water stores within the karst. Percolating waters between these stores may be routed via flow pathways which are slow and diffuse through the karst matrix or rapid, turbulent preferential flows through fissures and conduits (Bradley *et al.,* 2010). The properties of individual speleothems will therefore be influenced by dripwater routing (Fairchild and Baker, 2012). The heterogenous nature of karst makes modelling hydrological pathways complicated to predict (Baker and Brunsdon, 2003) with numerous studies documenting the presence of different flow regimes (Baker *et al.,* 1997; Baldini *et al.,* 2006; Miorandi *et al.,* 2010).

2.4.2.2 Karst-water interactions

Interactions between bedrock and percolating waters can act to modify the trace element composition of dripwaters and subsequently speleothems (Fairchild *et al.,* 2000; Sinclair, 2011; Sinclair *et al.,* 2012). Two relevant karst-water interactions processes are prior calcite precipitation and incongruent calcite dissolution. These

processes should be understood and monitored prior to interpretation of signals in speleothem calcite.

Prior Calcite Precipitation

Calcite deposition may occur within air pockets in the karst with a lowered PCO_2. Prior calcite precipitation (PCP) is the term used to describe the process of up-flow deposition of calcite relative to a drip site or speleothem (Fairchild and McMillan, 2007). This process removes Ca^{2+} ions from solution as $CaCO_3$ is precipitated causing an increase in the trace element to Ca ratio. PCP is typically enhanced under dry conditions (Fairchild *et al.,* 2000; Fairchild and Treble, 2009). Numerous studies have identified a positive correlation between Mg and Sr as well as $\delta^{13}C$ values (Johnson *et al.,* 2006; Griffiths *et al.,* 2010; Hori *et al.,* 2013) and this correlation has been suggested to result from enhanced PCP under dry conditions. Thus, these studies among others, have implied the co-variation of trace elements, primarily Mg and Sr, as an aridity indicator.

Incongruent calcite dissolution

Incongruent calcite dissolution (ICD) refers to the process involving the preferential release of minor ions (e.g. Mg and Sr) into solution relative to Ca during calcite dissolution (Sinclair, 2011). McGillen and Fairchild (2005) identified Mg and Sr enrichment relative to Ca in $CaCO_3$ samples from glacial environments and invoked ICD as the responsible process. Two models of ICD are presented by Sinclair (2011). The first involves the incongruent leaching of Mg and Sr ions at freshly exposed calcite crystal surfaces. The second proposes ICD is a combined process of congruent dissolution of $CaCO_3$ followed by incongruent reprecipitation of $CaCO_3$. Mathematical models have identified the signatures of PCP and ICD expressed in Mg/Ca and Sr/Ca ratios are similar and therefore, the relationships between Mg/Ca and Sr/Ca can be used to inform about karst-water interactions (covering both PCP and ICD) (Sinclair, 2011; Sinclair *et al.,* 2012).

2.4.2.3 Cave ventilation

Movement of air within caves, referred to herein as cave ventilation, plays a critical role in modulating PCO_2 within the cave atmosphere and can significantly influence speleothem proxies such as growth rates and trace element and stable isotope

geochemistry (Wynn *et al.,* 2014; Baker *et al.,* 2014; James *et al.,* 2015; Vieten *et al.,* 2016). Temperature-controlled density-driven ventilation has been identified in numerous different cave systems (see 2.4.3.5 Cave Temperature for case studies). The 'typical' seasonal ventilation cycle sees the predominance of low PCO_2 air in the cave during the winter. Low PCO_2 air is drawn into the cave when external air temperatures fall below cave temperatures, inducing a flow of dense, cooler CO_2-poor air into the cave. During winter low PCO_2 encourages $CaCO_3$ precipitation within the cave. Conversely in summer, external temperatures exceed those within the cave and as a consequence CO_2 builds up within the cave and limits $CaCO_3$ precipitation (Spotl *et al.,* 2005; Sebela and Turk, 2011; Ravbar and Kostunik, 2013; James *et al.,* 2015; Vieten *et al.,* 2016). Global model predictions of cave ventilation have demonstrated speleothem proxies in temporal and boreal regions may exhibit a seasonal bias as a function of seasonal cave ventilation. In contrast, model predictions indicate no such bias in speleothems from tropical and boreal regions (James *et al.,* 2015).

2.4.3 Understanding karst hydrology and cave ventilation through cave monitoring parameters

In order to interpret speleothems as palaeoclimatic records it is vital to understand the cave environment in which they are growing. In the past it was frequently thought that speleothems grew in equilibrium conditions, however cave monitoring studies have demonstrated caves are often not in equilibrium and this may impact the palaeoclimatic indicators used in speleothem studies (Mattey *et al.,* 2008; Fairchild and Baker, 2012). Therefore, it is important to monitor the cave environments so that the palaeoclimatic proxies within the speleothems can be correctly interpreted and any local effects which may act to modify the palaeoclimate record can be identified (Mattey *et al.,* 2010; Fairchild and Baker, 2012). This section will provide an overview of different cave monitoring techniques and how they can reveal information into the processes discussed in section 2.4.2.

2.4.3.1 Drip rates

As discussed in section 2.4.2.1, drip rates can play a role in influencing the chemical composition of infiltrating waters. It is crucial to understand the hydrological response of changing rainfall and subsequent movement of water through the karst as these factors control the dripwater chemistry which feeds the speleothems in the cave (Mattey and Collister, 2008; Fairchild and Baker, 2012). Therefore, monitoring of drip rates has important implications when examining the palaeoclimate record, especially when interpreting $\delta^{18}O$ values and growth rate (Mattey and Collister, 2008).

Drip rates within caves are monitored through acoustic drip counting (Collister and Mattey, 2005; Hu *et al.,* 2008; Mattey *et al.,* 2010; Miorandi *et al.,* 2010) or through infra-red led counters (Genty, 2008). These methods provide high resolution continuous monitoring of drip rates and the acoustic drip rate logging systems, commonly referred to as Stalagmates, can provide high resolution records of drip rates over 1 to 2 years without human involvement (Collister and Mattey, 2005).

Monitoring of drip rates at Crag Cave, SW Ireland has identified spatial variability in drip rates and also has shown that different drip rates can influence the interpretation of stalagmites as palaeoclimate archives with the key trends shown in table 2.2 (Baldini *et al.,* 2006). Spatial variability in drip rates related to different flow pathways has been identified at numerous other cave sites including New St. Michael's Cave (Mattey *et al.,* 2008), Villars Cave, SW France (Genty, 2008) and at Grotta di Ernesto, NE Italy (Miorandi *et al.,* 2010) .

Table 2.2: A summary of the different drip regmines in Crag Cave (Baldini et al., 2006). The table has been included to demonstrate how different drips respond differently to climate and will therefore influence the palaeoclimate signal preserved in speleothem calcite.

Drip rate	**Palaeoclimate reconstruction**	**Justification**
Slow (<0.1 ml/min)	Decadal/Millennial	Minimal recharge produces a record of long-term variability without the influence of individual meteorological events
Intermediate (0.1-2 ml/min)	Seasonal	Related to external conditions and responds to water excess
Rapid (>2 ml/min)	Not suitable	High recharge may lead to hiatuses or re-dissolution of calcite

2.4.3.2 Electrical conductivity

Karst hydrology is thought to control variations in electrical conductivity with the key driving mechanisms being soil CO_2 dissolution (Fairchild *et al.,* 2006a; Miorandi *et al.,* 2010), dilution effects (Borsato, 1997), variations in the degree of mixing and dissolution of the bedrock (Genty and Deflandre, 1998; Fernadez-Cortes *et al.,* 2007) and prior calcite precipitation (Fairchild *et al.,* 2006a; Miorandi *et al.,* 2010). Relationships between drip rates and EC have previously been identified. Positive correlations between drip rate and EC have been proposed to be related to high hydraulic pressure during a period of water excess leading to the release of stored waters in pores and microfissures which have become supersaturated. Consequently, a simultaneous increase in drip rate and EC is observed (Genty and Deflandre, 1998; Fernandez-Cortes *et al.,* 2007). On the other hand, some authors have reported a negative correlation between drip rate and EC. Studies at Grotta Di Ernesto (GDE) (Italy) have found distinctive reductions in EC correlate to increases in drip rates during rainfall events (Borsato, 1997; Miorandi *et al.,* 2010). The pattern identified at GDE has been proposed to relate to dilution effects during infiltration events which leads to undersaturation of the dripwaters and an overall reduction of dripwater EC.

Recent research at Asiul Cave (Northern Iberia) has demonstrated EC responses to seasonal variations in external air pressure, karst hydrology and drip rate at event

timescales (Smith *et al.,* 2015). Throughout the winter, hydrological events lead to increased CO_2 values in the cave as a consequence of higher drip rates and subsequent dripwater degassing; this leads to a rise in EC. However, in summer, hydrological events reduce the atmospheric pressure within the cave which in turn results in soil and/or karst air being drawn down into the cave. The addition of air with a higher CO_2 content limits degassing of cave dripwaters and enhances EC (Smith *et al.,* 2015).

2.4.3.3 Oxygen and deuterium isotopes in precipitation and cave waters

A linear relationship exists between $\delta^{18}O$ and δD values in precipitation as they are controlled by the same processes and it is this linear correlation that defines the Global Meteoric Water Line (GMWL) (Clark and Fritz, 1997; Sharp, 2007; Lachniet, 2009) (see section 2.6.2.2 for more information). Each precipitation event will have a distinct isotopic signature dependent on source evaporation and condensation. Measurements of local precipitation are crucial in establishing a Local Meteoric Water Line which can differ from the GMWL as a result of local processes such as vapour source, re-evaporation and mixing (Clark and Fritz, 1997). Understanding the isotopic composition of cave drip waters in relation to the LMWL will permit assessment of the degree of evaporation relative to precipitation in the soil and drip waters, seasonality of precipitation in the drip waters and estimations of moisture recycling which can significantly influence the interpretation of speleothem proxies (Lachniet, 2009).

2.4.3.4 Trace element chemistry

Studies have shown that it is important to monitor dripwater chemistry in order to accurately interpret speleothem records in terms of palaeoclimate, particularly variations in trace elements such as Mg and Sr (Baker *et al.,* 2000). Section 2.4.2.2 identified the influence of karst-water interaction processes on infiltrating drip waters, primarily through analysis of Ca, Mg and Sr. A study of dripwater chemistry at Villars Cave has shown evidence of seasonal variation in Mg and Sr related to enhanced prior calcite precipitation during the summer months. Overall, the study identified the need to interpret each site individually with extensive monitoring at each site (Baker *et al.,* 2000). Seasonal variations in Mg concentration have also been identified in Crag Cave, SW Ireland with increases in Mg reflecting drier conditions associated with PCP during the summer (Baldini *et al.,* 2006).

2.4.3.5 Cave air temperature

Measurement of cave air temperatures can enhance understanding of cave ventilation dynamics. Cave air temperatures are typically monitored using a range of temperature sensors with a resolution of ~0.1°C and studies have frequently used these to continuously record variations in temperature over extended periods of time (Hu *et al.,* 2008; Mattey *et al.,* 2010; Ravbar and Kosutnik, 2013; Fairchild and Baker, 2012). Speleothems used in palaeoclimate studies are frequently taken from caves which exhibit minimal seasonal variation in cave air temperature and reflect the average annual external air temperature (Mattey *et al.,* 2010; Genty, 2008; Verheyden *et al.,* 2008). However, variation in seasonal cave air temperature is often evident between sites within the cave, with larger amplitude fluctuations exhibited closer towards the cave entrance (Mattey *et al.,* 2010; Genty, 2008; Středa *et al.,* 2012; Spötl *et al.,* 2005). In chambers close to the entrance of Obir Cave, Austria, there is a seasonal variation of 5°C related to the seasonal switch in air currents. Conversely, sites further from the entrance exhibit a reduced or minimal seasonal variation in temperature, for example at 75m from the cave entrance in Obir Cave the seasonal variation in cave air temperature is reduced to 1°C (Spötl *et al.,* 2005).

Seasonal variations in cave air temperature of 5-6°C have been identified at Heshang Cave China (Johnson *et al.,* 2006; Hu *et al.,* 2008). Johnson *et al.* (2006) identified that seasonal variations in cave air temperature contribute to the $\delta^{18}O$ composition in speleothem calcite; higher cave air temperatures combined with low drip-water $\delta^{18}O$ during the summer and autumn result in lower $\delta^{18}O$ values in the calcite. Hence the $\delta^{18}O$ signal preserved within the speleothem calcite at Heshang Cave is influenced by both drip-water $\delta^{18}O$ composition and cave air temperature variations.

2.4.3.6 Cave carbon dynamics

The concentration of PCO_2 within caves is frequently measured through infra-red spectroscopy (Spötl *et al.,* 2005; Mattey *et al.,* 2010). Understanding of PCO_2 variations in cave air is important as cave air PCO_2 controls calcite growth rates by influencing the rate of degassing between the dripwaters and the cave air (Baldini, 2010). The key sources of carbon dioxide in caves are derived from: 1) root respiration and the decay of organic matter within the epikarst, 2) degassing of dripwaters with CO_2 from soils,

3) decay of organic matter within the cave, 4) respiration of organisms living within the cave, 5) geothermal activity (James, 1977; Baldini, 2010; Fairchild and Baker, 2012). Various caves have shown dynamic variations in PCO_2 on different scales (Spötl *et al.,* 2005; Banner *et al.,* 2007; Baldini *et al.,* 2008; Mattey *et al.,* 2010), however some caves have identified homogeneous atmospheres with minimal seasonal variation in PCO_2 (Riechelmann *et al.,* 2011).

At Obir Cave monitoring of PCO_2 and dripwater has shown geochemical variability across a year related to changing air circulation within the cave (Spötl *et al.,* 2005). The ventilation at Obir Cave is characterised by chimney-type ventilation, as shown through the PCO_2 monitoring. Chimney-type ventilation is characterised by seasonal reversals in circulation forced by differences in temperature between the cave air and the outside atmosphere and as a result Obir Cave exhibits high PCO_2 in summer and low PCO_2 in winter (Spötl *et al.,* 2005). When PCO_2 levels are lowered there is a higher PCO_2 gradient between the cave air and the dripwaters which results in faster degassing and increased calcite precipitation (Mattey *et al.,* 2010; Spötl *et al.,* 2005). Consequently, drip waters exhibit seasonal variations in electrical conductivity, alkalinity, pH and $\delta^{13}C$ values (Spötl *et al.,* 2005). Forced degassing under low PCO_2 concentrations has been shown to kinetically fractionate ^{13}C which will ultimately influence the interpretation of $\delta^{13}C$ values within speleothems (Spötl *et al.,* 2005; Mattey *et al.,* 2010; Frisia *et al.,* 2011).

2.4.3.7 Pressure

Differences between external and internal pressure have been demonstrated to induce air movement known as pressure induced ventilation. Such a phenomenon was evidenced in Asiul cave (Smith *et al.,* 2015), where ventilation was induced when low external pressures (frequently associated with storm activity) enhanced the pressure gradient between cave and external atmospheric air. As a consequence, air moved out the cave resulting in karst air being drawn down into the cave void increasing cave air PCO_2. This signal is expressed in cave drip waters as an increase in EC and will also act to limit $CaCO_3$ precipitation (Smith *et al.,* 2015).

2.4.4 Summary

This section has examined a range of cave monitoring parameters and how they can be used to provide insight into karst hydrology and cave dynamics. Measurement of speleothem drip rates can provide a deeper understanding of the karst hydrology overlying the individual drip site. Additional study of chemical proxies within speleothem drip waters can enhance interpretation of karst hydrology, within karst processes and internal cave dynamics. Monitoring of cave air can develop an understanding of cave air dynamics and their role over speleothem carbonate formation. A key conclusion from the studies presented in this section is that cave monitoring of various parameters can permit a greater understanding of cave ventilation dynamics.

2.5 Speleothem growth rates

Speleothem growth occurs when infiltrating waters from the karst come into contact with an atmosphere with a lower pCO_2. The interaction between the high pCO_2 waters and the lower pCO_2 atmosphere results in degassing of the waters. The resultant solution becomes supersaturated with respect to calcium carbonate which forces the precipitation of $CaCO_3$ (Frisia and Borsato, 2010) as shown in equation 2.3. Speleothem growth is dependent on the specific conditions of water availability and air circulation which supply the components for growth and remove waste CO_2 from the cave atmosphere (Fairchild and Baker, 2012). The growth rate of speleothems is therefore a function of degassing rate, Ca^{2+} ion availability and flow conditions to the drip-site (Genty and Deflandre, 1998; Dreybrodt, 1999; Dickinson *et al.,* 2002; Spötl *et al.,* 2005; Frisia and Borsato, 2010; Boch *et al.,* 2011).

Drip-waters with a low supersaturation will precipitate calcite under quasi-equilibrium conditions and increases in saturation will lead to increased growth rate (Frisia *et al.,* 2000; Frisia and Borsato, 2010). In cave environments, variations in flow rate, transport and concentration of impurities are normal. Thus, growth rate will vary throughout the period of speleothem deposition (Frisia and Borsato, 2010).

Cave ventilation has been identified as a factor influencing speleothem growth. Lower pCO_2 under periods of strong ventilation will enhance degassing. The study of Obir Cave demonstrated that growth rates are enhanced, and carbon isotope values are fractionated in winter due to the seasonal ventilation regime (Spötl *et al.,* 2005).

The growth of speleothems is a result of degassing of CO_2 from cave drip waters upon entering the cave void. This reaction can occur under equilibrium or kinetic conditions, both of which impart a different chemical signature which is preserved in the speleothem calcite. Under slow equilibrium conditions crystal growth forms large, uniform columnar crystals (Frisia *et al.,* 2000; Frisia and Borsato, 2010). In contrast, dendritic fabrics composed of calcite crystals arranged in branches have been associated with disequilibrium conditions and form as a result of prolonged outgassing and extremely low drip rates (Frisia *et al.,* 2000; Frisia and Borsato, 2010).

In summary, speleothem formation is a function of degassing of CO_2 from drip waters entering the cave. The growth of speleothems is dependent on specific conditions of water delivery and air circulation and the reaction may occur under equilibrium or kinetic conditions (Fairchild and Baker, 2012). The crystal structure of speleothems can provide insight into changes in speleothem growth conditions and techniques such as microstratigraphic logging of calcite fabrics can act to complement the interpretation of speleothem geochemical records (Frisia, 2015).

2.6 Speleothem geochemistry

2.6.1 Uranium-series dating

2.6.1.1 Introduction

The application of uranium-series dating to speleothems is critical when assessing records of palaeoclimate and palaeoenvironment, an argument summarised by Henderson (2006). There has been an abundance of speleothem studies which have employed U-series dating e.g. Kaufman *et al.* (1998); Wang *et al.* (2001); Fleitmann *et al.* (2003); Spötl *et al.* (2006), to name a few. This review section will focus on the principles, methods and required conditions necessary for U-series dating.

2.6.1.2 Background

Speleothems are commonly dated by the U-series disequilibrium method and as a consequence there has been an abundance of published U-Th speleothem dates (Dorale *et al.,* 2004). Uranium in cave drip waters is derived from dissolution of the overlying bedrock (Scholz and Hoffmann, 2008). In oxidising environments, uranium is easily oxidised to the U^{6+} state, typically in the form of the UO_2^{2+} ion, which is highly soluble and easily mobilized in groundwaters (Langmuir, 1978, Langmuir, 1997, White, 2004, Dorale *et al.,* 2004). In contrast, under oxidising conditions, thorium remains in the quadrivalent state (Th^{4+}), where it is insoluble and immobile (Langmuir and Herman, 1980, White, 2004, Zhao *et al.,* 2009, van Calsteren and Thomas, 2006, Dorale *et al.,* 2004, Scholz and Hoffmann, 2008). Therefore, speleothems may be formed with U incorporated into the calcite but will contain negligible amounts of Th and as a consequence any Th measured in the speleothem is assumed to be a product of the radioactive decay of U. Hence, measurement of the Th and U concentrations in the speleothem can determine the time since deposition (White, 2004, van Calsteren and Thomas, 2006, Zhao *et al.,* 2009, Dorale *et al.,* 2004). Equation 2.4 is used to state that the number of atoms disintegrating (dN) per unit time (dT) is equivalent to λN where λ is the decay constant and N is the number of atoms:

$$dN/dT = \lambda N \qquad \text{Eq. 2.4}$$

(Scholz and Hoffmann, 2008, Dorale *et al.,* 2004, van Calsteren and Thomas, 2006).

The half-life of a particular radioactive nuclide is equal to (ln 2)/λ (Dorale *et al.,* 2004). The U-series dating technique uses the decay of ^{238}U which has a half-life of 4.469×10^9 and in this decay chain ^{234}U and ^{230}Th are longest-lived isotopes which are utilised in the method (White, 2004; Zhao *et al.,* 2009). Cheng *et al.* (2000) used high-precision thermal ionisation mass spectrometry to re-define the half-lives of ^{234}U and ^{230}Th as 245,250±490yrs (2σ) and 75,690±230yrs (2σ) respectively. The two equations below (eq. 2.5 and 2.6) are used to calculate the ages of a speleothem:

$$\frac{U^{234}}{U^{238}} = 1 + \left[\left(\frac{U^{234}}{U^{238}}\right)_0 - 1\right] e^{-\lambda_4 t} \qquad \text{Eq. 2.5}$$

$$\frac{Th^{230}}{U^{234}} = \frac{\left(1-e^{-\lambda_0 t}\right)}{\left(U^{234}/U^{238}\right)} + \frac{\lambda_0}{\lambda_0+\lambda_4}\left[\left(\frac{U^{234}}{U^{238}}\right)_0 - 1\right]\left(e^{-\lambda_4 t} - e^{-\lambda_0 t}\right) \qquad \text{Eq. 2.6}$$

Where λ_0 and λ_4 represent the decay constants for ^{230}Th and ^{234}U respectively (White, 2004). Within the equations there are two unknowns, time (t) and the initial $^{234}U/^{238}U$ ratio. Through measuring the isotopic ratios defined in the equations above, the age of a speleothem sample can be determined (White, 2004).

Thus, speleothems which form with measurable amounts of U, negligible amounts of Th and remain closed-systems, can provide accurate ages over the past 500,000yrs (White, 2004; Dorale *et al.,* 2004; Zhao *et al.,* 2009).

2.6.1.3 Methods

There are primarily two methods to calculate U-Th ages and these are alpha spectrometry and mass spectrometry (Van Calsteren and Thomas, 2006; Scholz and Hoffman, 2008); the latter of these was used in the present study. There are predominantly two mass spectrometry techniques employed to measured U and Th isotopes and these are thermal ionisation mass spectrometry (TIMS) and multi-collector inductively coupled plasma mass spectrometry (MS-ICP-MS) (Scholz and Hoffman, 2008). The advancements in mass spectrometry have led to a reduction in sample size, increased precision of ^{230}Th ages and extended the age range to which U-Th dating could be applied (Dorale *et al.,* 2004).

2.6.1.4 Required conditions necessary for U-series dating

In order for a sample to be successfully dated by U-Th methods, it must meet three conditions. Firstly, the sample must have formed with appreciable U in order to measure the isotopes accurately (White, 2004; Dorale *et al.,* 2004; Lauritzen, 2014). The amount of U in speleothems can vary between <0.01 to >120ppm depending on bedrock geology (Lauritzen, 2014). Mass spectrometry techniques require at least 0.6µg of ^{238}U to date a 100ka sample; younger samples or samples with low U concentrations will require larger amounts of ^{238}U (Lauritzen, 2014).

Secondly, the speleothem must have formed with negligible ^{230}Th (White, 2004; Dorale *et al.,* 2004; Scholz and Hoffman, 2008). ^{230}Th may be incorporated into the speleothem through detrital matter and in order to determine the initial ^{230}Th content, the $^{230}Th/^{232}Th$ ratio is measured (Dorale *et al.,* 2004). The crustal isotope ratio of $^{230}Th/^{232}Th$ is ~5 x 10^{-6} and initial ^{230}Th within speleothems will typically be

accompanied by a greater amount of ^{232}Th (Hellstrom, 2006, Scholz and Hoffmann, 2008). Therefore, if it is assumed that detrital ^{232}Th is associated with ^{230}Th in a given ratio, samples with high initial ^{230}Th can be identified (Scholz and Hoffman, 2008). Due to the variability of the ^{230}Th/^{232}Th ratio between source materials, two correction procedures have been proposed (Scholz and Hoffman, 2008). The first uses isochron techniques to measure the isotopic composition of the detrital material whilst the second uses an estimation of the isotopic composition of the detrital material and an estimation of the associated error (see Hellstrom, 2006).

Thirdly, the speleothem calcite must remain a closed-system (White, 2004; Dorale *et al.,* 2004; Lauritzen, 2014) whereby there is no exchange between the parent and daughter isotopes and the environment (van Calsteren and Thomas, 2006). Speleothems are commonly assumed to be closed-systems as they are unlikely to be subject to diagenesis (through meteoric water) after formation (Scholz and Hoffman, 2008). However, there are exceptions and speleothems have been shown to exhibit open-system behaviour. Speleothems may lose or gain radionuclides as a consequence of prolonged exposure to the cave atmosphere (Richards and Dorale, 2003) such as during a hiatus.

2.6.1.5 Age modelling

High-resolution proxy analysis requires a high-resolution chronology. Uranium-series dating at high-resolution is impractical due to the large volumes of material required (100mg) and associated costs of analyses (Smith, 2014). Each speleothem within a study should have a robust independent chronology as even coeval stalagmites cannot be chronologically constrained on the basis of stratigraphic correlation (Benson *et al.,* 2018). Therefore, it is important to establish an independent chronology for high-resolution proxy records and this can be done through creation of an age-depth model. An age-depth model will establish the age between two adjacent U-series dates and can be used to infer the timing of proxy changes. This model is calculated using the relationship between ages and proxies from specified distances along the speleothem growth axis (Scholz *et al.,* 2012). Age modelling is a recurring problem across different archives. A literature analysis by Blaauw (2010) revealed that 65 (out

of 93) papers published in 2008 did not specify the errors associated with the age-models constructed and 71 did not specify the age modelling software used.

Linear point-to-point interpolation is the most frequently used method for speleothem age-depth modelling (e.g. McDermott *et al.,* 1999; Wang *et al.,* 2005). Recent models such as StalAge (Scholz and Hoffmann, 2011), COPRA (Breitenbach *et al.,* 2012) and OxCal (Bronk-Ramsey, 2008) allow for improved age-depth modelling incorporating age uncertainties, age reversals and hiatuses as well as direct proxy-record age reconstruction.

2.6.1.6 Summary

U-series dating, based upon the decay of U to Th, can provide accurate and precise ages of speleothem calcite. The introduction of mass spectrometry techniques led to high precision ages, decreased sample size and increased the applicable age range of the method (Dorale *et al.,* 2004). In order to apply U-Th dating the speleothem must have formed with enough U, contained no or minimal initial Th and remained a closed-system (White, 2004; Dorale *et al.,* 2004; Lauritzen, 2014). If these conditions are met, then an independently dated chronology can be constructed for a speleothem and this can be used alongside palaeoclimate and palaeoenvironmental indicators to provide a key archive of past climate and environmental change. It is important that an independent robust chronology is constructed for each speleothem and appropriate age modelling software is used to construct age-depth models.

2.6.2 Assessing palaeoclimate and palaeoenvironment using stable isotope analyses of speleothems

2.6.2.1 Overview of isotope systematics

The most frequently used isotopes in speleothem-based climate studies are oxygen and carbon. Hydrogen is also measured in rainfall and cave drip waters and is predominantly controlled by the same processes as oxygen. This review will discuss the factors which influence the oxygen (and hydrogen) isotope composition of water as it moves through the hydrological cycle, into the soil and the karst and finally into

the cave. Organic and inorganic processes which influence the carbon isotope composition will also be discussed.

Oxygen and hydrogen isotopes measured within waters are reported relative to Standard Mean Ocean Water (SMOW) (Craig, 1961b; Clark and Fritz, 1997; Sharp, 2007). Carbon isotopes measured within carbonates are reported relative to Pee Dee Belemnite (PDB) (Craig, 1957; Clark and Fritz, 1997; Sharp, 2007). Oxygen isotopes within carbonates can be reported relative to SMOW or PDB (Clark and Fritz, 1997). The prefix 'Vienna' (i.e. VSMOW and VPDB) has been used in recent years as the supply of standards has been exhausted (Sharp, 2007; Lachniet, 2009).

Stable isotope measurements are reported using the delta (δ) notation, introduced by McKinney *et al.* (1950) (eq. 2.7):

$$\delta = \left(\frac{R_x - R_{std}}{R_{std}}\right) x\ 1000 \qquad \text{Eq. 2.7}$$

Where:

- R = the ratio of the abundance of the heavy to light isotope
- x = the sample
- std = standard (Sharp, 2007)

The δ value is reported as per mil (‰) or as parts per thousand (Sharp, 2007). The δ value for both VSMOW and VPDB is 0.0‰ and therefore the sample $^{18}O/^{16}O$ ratio represents the difference relative to the standard (Sharp, 2007; Lachniet, 2009). A negative δ value means the ratio of the heavy to light isotope in the sample is lower than that of the standard (Sharp, 2007).

2.6.2.2 Oxygen isotopes

Hydrological cycle

The primary influence over the $\delta^{18}O$ value of water at the beginning of the hydrological cycle is the $\delta^{18}O$ value of the ocean and the oxygen isotope composition of meteoric waters is primarily controlled by evaporation of ocean waters (Clark and Fritz, 1997; Lachniet, 2009). Equilibrium fractionation during evaporation of ocean waters will lead to preferential evaporation of ^{16}O. The resulting vapour will be depleted in ^{18}O relative

to the ocean waters and consequently have a reduced $\delta^{18}O$ value. Although not necessarily the case, if evaporation of ocean water has occurred in equilibrium, the isotopic composition of the resulting vapour and precipitation may be determined. For example, the equilibrium isotopic composition of water vapour (for oceans at 25°C) should be:

$\delta^{18}O_{vapour} = \delta^{18}O_{seawater} + \varepsilon^{18}Ov\text{-}w = 0.0 + (-9.3) = -9.3‰$ (Clark and Fritz, 1997) Eq.2.8

Kinetic (or non-equilibrium) fractionation may occur during evaporation of ocean waters and this is primarily related to humidity (Gonfiantini, 1986; Clark and Fritz; 1997, Lachniet, 2009). Low humidity will reduce water-vapour exchange and permit net diffusion between the boundary layer and the atmosphere. Therefore, as a result of evaporation the $\delta^{18}O$ values of the water surface and in the boundary layer will become progressively enriched in ^{18}O (Clark and Fritz, 1997).

In contrast to evaporation, condensation is an equilibrium process. Rainfall will have an increased $\delta^{18}O$ value relative to the vapour from which it formed due to preferential removal of ^{18}O during condensation (Dansgaard, 1964; Clark and Fritz, 1997; Lachniet, 2009). Condensation is a function of temperature and in order for condensation to occur, there must be a reduction in temperature. Along an air mass trajectory, an air mass will cool and condensation in the form of precipitation will occur. As the air mass moves further from the moisture source, the vapour becomes progressively depleted in ^{18}O. This is known as Rayleigh-type distillation (Lachniet, 2009; Clark and Fritz, 1997; Dansgaard, 1964).

The global meteoric water line (GMWL) describes the linear correlation which exists between $\delta^{18}O$ and δD values in meteoric waters (Craig, 1961a; Clark and Fritz, 1997; Sharp, 2007). Craig (1961a) defined the GMWL as (eq. 2.9):

$$\delta D = 8 * \delta^{18}O + 10‰ \text{ SMOW} \qquad \text{Eq. 2.9}$$

The work of Rozanski *et al.* (1993), using the GNIP network has refined Craig's equation (eq. 2.10):

$$\delta D = 8.20\ (\pm 0.07)\ \delta^{18}O + 11.27\ (\pm 0.65)‰ \text{ VSMOW} \qquad \text{Eq. 2.10}$$

The Rozanski *et al.* (1993) equation is based on precipitation and provides a weighted annual mean of precipitation.

As oxygen and hydrogen isotopes are controlled by the same processes, they produce a strong linear correlation, with a slope of ~8 (Dansgaard, 1964; Clark and Fritz, 1997; Lachniet, 2009). The intercept of this slope is known as the deuterium excess, *d*, and can be calculated using eq. 2.11:

$$d = \delta D - 8\delta^{18}O \text{ (Dansgaard, 1964).} \qquad \text{Eq. 2.11}$$

d is primarily controlled by kinetic effects during the evaporation of waters from the ocean or land (Sharp, 2007; Lachniet, 2009). Hydrogen is more readily fractionated than O, hence the excess. Evaporation will result in an increase in $\delta^{18}O$ and δD values in the remaining waters. As a consequence, the $\delta D/\delta^{18}O$ slope would be <8, plotting to the right of the GMWL and *d* values would be low. Conditions of high evaporation and low humidity will result in vapour and condensation plotting to the left of the GMWL in order to maintain mass-balance and the *d* values would be high (Clark and Fritz, 1997; Lachniet, 2009; Sharp, 2007).

The GMWL is a global average of local meteoric water lines which may be individually driven by local climatic mechanisms (Sharp, 2007; Clark and Fritz, 1997). Clark and Fritz (1997) highlighted that different locations will possess a distinctive local meteoric water line relating to the vapour source and the effects of secondary processes such as re-evaporation and mixing. In addition, Lachniet (2009) stressed the importance of establishing a LMWL when using speleothems to reconstruct palaeoclimate as this will permit assessment of the degree of evaporation relative to precipitation in the soil and drip waters, seasonality of precipitation in the drip waters and estimations of moisture recycling.

Isotope effects

As the water moves through the hydrological cycle it can be modified by a series of isotope 'effects'. These are related to: temperature, latitude, continentality, amount of precipitation, altitude, moisture source, seasonality and ice volume. Each of these is discussed separately below.

Temperature effect

The temperature effect refers to the positive correlation between mean annual surface air temperature at a site (dT) and the mean oxygen isotope composition of precipitation ($\delta^{18}O_p$), noted as $\delta^{18}O_p$/dT (Lachniet, 2009; Rozanski *et al.,* 1993). The temperature effect was initially studied by Dansgaard (1964) who used data from the IAEA/WMO network to study the relationship between site-specific surface air temperature and the $\delta^{18}O$ value of precipitation. Dansgaard (1964) suggested the positive correlation between the two variables plotted along a slope of ~0.7‰ per °C for locations in the mid- to high-latitudes. Further work by Rozanski *et al.* (1993) verified this relationship; however, the slope of best fit (representing the temperature range 0-20°C) plotted as 0.58‰ per °C. Rozanski *et al.* (1993) highlighted a stronger relationship (>0.58‰ per °C) was evident in the Polar Regions, while no correlation was evident in the tropics. Nevertheless, the slope of the $\delta^{18}O_p$/dT relationship ranges between +0.17‰ to +0.90‰ per °C increase across the globe (Rozanski *et al.,* 1993; Dansgaard, 1964). This relationship has demonstrated non-linear temporal and spatial variability between regions (Lachniet, 2009) and is supported by water isotope modelling through an ocean-atmosphere system (Schmidt *et al.,* 2007).

Studies within North America have illustrated the complexity with the globally implemented Dansgaard (1964) $\delta^{18}O_p$/dT figure of 0.69‰ per °C. Precipitation in central Kentucky has reported a $\delta^{18}O_p$/dT relationship of 0.38‰ per °C (Harmon, 1979) while Stuiver (1968) reported a value of 0.3‰ °C in Chicago. The temperature effect on precipitation was also identified by Ayalon *et al.* (1998) at Soreq Cave, Israel. Ayalon *et al.* (1998) found a distinctive correlation between $\delta^{18}O$ values of precipitation and surface air temperatures, with lower $\delta^{18}O$ values associated with lower temperatures. The oxygen isotope composition of precipitation is also dependent on seasonal temperature with higher $\delta^{18}O$ values in summer and lower $\delta^{18}O$ values in winter (Lachniet, 2009).

Rozanski *et al.* (1993) proposed that the IAEA/WMO network has identified three types of isotope dependence on temperature. Firstly, the spatially variable relationship between annual $\delta^{18}O_p$ averages and surface air temperature at different sites. Secondly, the temporal relationship between seasonal $\delta^{18}O_p$ changes and

surface air temperature for a station or a group of stations. Finally, the temporal relationship between inter-annual $\delta^{18}O_p$ changes and surface air temperature at a single site.

Latitude effect

The global pattern of $\delta^{18}O_p$ values has been shown to vary with latitude and this is known as the latitude effect. Data has shown highest $\delta^{18}O_p$ values at the tropics with values decreasing towards the higher latitudes (Rozanski *et al.,* 1993; Bowen and Wilkinson, 2002, Lachniet, 2009). The main reason for this pattern is related to the large amount of global evaporation (65%) which occurs in tropical oceans between 30°S and 30°N. As this vapour is transported to higher-latitudes, precipitation leads to a decrease in the $\delta^{18}O$ values due to an overall reduction in the amount of water available within the airmass (Rozanski *et al.,* 1993).

However, data presented by Rozanski *et al.* (1993) exhibit a spread of data around the broad latitudinal pattern. It has been proposed that this spread of data can be related to anomalies in regional temperature, the continental effect, the amount effect and the altitude effect. The model of (Bowen and Wilkinson, 2002) also incorporates altitude and atmospheric vapour transport pathways and these factors account for variations away from the latitudinal gradient (e.g. the western coast of South America).

Rozanski *et al.* (1993) demonstrated temperature plays a key role in creating the latitudinal gradient in $\delta^{18}O_p$. A decrease in lower atmosphere temperature in winter results in a reduction in the amount of total precipitable water in the atmosphere. As a consequence, there is a significant increase in effective rain-out and depletion of the oxygen isotope composition of the water vapour and any subsequent precipitation.

Continental effect

The relative decrease in $\delta^{18}O_p$ values related to increasing distance from the ocean is known as the continental effect. The continental effect is the result of progressive removal of moisture and preferential removal of heavy isotopes from an airmass as it moves further inland (Dansgaard, 1964; Rozanski *et al.,* 1993; Lachniet, 2009). Continental moisture may be returned to the atmosphere via evaporation of lakes,

rivers or soil waters and this may oppose the continental effect (Koster *et al.,* 1993; Lachniet, 2009). In addition, transpiration from plants may also recycle moisture to the atmosphere but will not fractionate the isotopes in the water (Gat *et al.,* 1994; Lachniet, 2009)

The maps produced by Bowen and Revenaugh (2003) demonstrated a pattern of lower $\delta^{18}O_p$ values with increasing distance from the coastal regions and this effect was found to be strongest across Northern Eurasia and North America. Rozanski *et al.* (1993) quantified the continental gradient across Europe and reached a value of -2‰ per 1000km. Similarly, Welker (2000) identified a continental gradient in $\delta^{18}O_p$ values of -1.2‰ per 100km across the North American Pacific NW.

Amount effect

The amount effect refers to the inverse correlation between $\delta^{18}O_p$ values and rainfall amount, with lower $\delta^{18}O_p$ values associated with periods of increased rainfall (Dansgaard, 1964; Rozanski *et al.,* 1993; Lachniet, 2009). Tropical regions which exhibit deep vertical convection are predominantly influenced by the amount effect (Lachniet, 2009; Dansgaard, 1964). The amount effect was proposed to be related to evaporation of falling raindrops and also to isotopic exchange between falling raindrops and atmospheric moisture (Dansgaard, 1964; Rozanski *et al.,* 1993). Therefore, relatively low $\delta^{18}O_p$ values in tropical regions can be related to significant cooling of the air with minimal modification by other processes such as evaporation and isotope exchange. On the other hand, relatively high $\delta^{18}O_p$ values in tropical regions represent raindrops which have been enriched in ^{18}O through evaporation and isotopic exchange (Dansgaard, 1964). Lachniet and Patterson (2006) illustrated the significant influence of the amount effect on $\delta^{18}O_p$ values in Panama (Central America). A negative correlation (r= -0.89) was found to exist between $\delta^{18}O_p$ values and rainfall amount with a $\delta^{18}O_p$ -rainfall amount slope of -2.85±0.05‰ per 100mm of rainfall. Variations in the oxygen isotope composition of speleothems have been interpreted to reflect changes in rainfall amount in the tropics (Fleitmann *et al.,* 2003; Neff *et al.,* 2001; Burns *et al.,* 2002; Griffiths *et al.,* 2009; Griffiths *et al.,* 2010) and also outside of the tropics (Treble *et al.,* 2005a; Bar-Matthews *et al.,* 2003).

Altitude effect

The altitude effect refers to the decrease in $\delta^{18}O_p$ values with increasing altitude (Dansgaard, 1964; Rozanski *et al.,* 1993; Lachniet, 2009). This effect is the result of declining temperatures of condensation with increasing altitude and progressive Rayleigh distillation associated with uplifting of an airmass over an orographic barrier (Rozanski *et al.,* 1993; Lachniet, 2009). Kendall (2004) stated that typical altitude gradients vary between -0.15 to -0.5‰ per 100m. The map produced by Bowen and Wilkinson (2002) takes into account the altitude effect on $\delta^{18}O_p$ values and highlighted key mountainous regions such as the Andes and the Tibetan Plateau which are characterised by relatively low $\delta^{18}O_p$ values.

Source effect

Different moisture sources have different $\delta^{18}O$ values and this is known as the source effect (Rozanski *et al.,* 1993; Clark and Fritz, 1997; Lachniet, 2009). Variations in air mass trajectories and temperature of the vapour source areas as well as differential $\delta^{18}O$ values of the oceans between regions are the mechanisms which cause the source effect (LeGrande and Schmidt, 2006; Lachniet, 2009). Studies from North America have identified four moisture source areas, and these are: the Gulf of Mexico and subtropical Atlantic, the Arctic, the North Pacific and the subtropical Pacific (Rozanski *et al.,* 1993; Friedman *et al.,* 2002; Clark and Fritz, 1997; Lachniet, 2009; Bryson and Hare, 1974). Each of these source regions has a distinct oxygen isotope composition and it has been proposed that in the mid-continental USA, moisture originating from the Pacific or the Arctic will have lower $\delta^{18}O$ values relative to moisture from the Gulf of Mexico as it has been transported over a greater distance (Clark and Fritz, 1997; Denniston *et al.,* 1999; Lachniet, 2009).

In South America, the oxygen isotope composition of precipitation south of 20°S has been shown to be controlled by seasonal shifts in moisture source (Cruz *et al.,* 2005). During winter and early spring $\delta^{18}O_p$ values are higher due to extratropical winter precipitation from the Atlantic. In contrast, during the austral summer, $\delta^{18}O_p$ values are lower due to subtropical precipitation originating from the Amazon Basin (Cruz *et al.,* 2005). Maher and Thompson (2012) have proposed changes in $\delta^{18}O$ values in speleothems across China are related to different moisture sources. Maher and

Thompson (2012) suggested that Indian-monsoon sourced $\delta^{18}O_p$ values occurred during periods of high boreal summer insolation whilst during periods of low insolation Pacific moisture sources were dominant.

Seasonality

There is a distinct pattern of $\delta^{18}O_p$ values at mid- to high-latitudes exhibiting seasonal variability (Dansgaard, 1964; Rozanski *et al.,* 1993; Lachniet, 2009). Seasonal variations in $\delta^{18}O_p$ values are related to three driving mechanisms. Firstly, seasonal temperature variations at mid- to high-latitudes leads to seasonal variability in the total amount of precipitable water available in the atmosphere and this is associated with different amounts of effective rain-out. Consequently, this alters the oxygen isotope composition of precipitation (Rozanski *et al.,* 1993). Secondly, seasonal shifts in evapotranspiration on the continents acts to modify the atmospheric water balance (Rozanski *et al.,* 1982; Rozanski *et al.,* 1993) Finally, seasonal changes in the vapour source areas and/or storm trajectories can result in seasonal fluctuations in $\delta^{18}O_p$ (Rozanski *et al.,* 1993).

Ice volume

The ice volume effect has been shown to alter the oxygen isotope composition of the ocean on glacial-interglacial timescales (Lachniet, 2009). During glacial periods $\delta^{18}O$ values of the ocean will increase due to preferential evaporation of ^{16}O and an increase in the proportion of freshwater locked up in ice sheets (Lachniet, 2009). Schrag *et al.* (2002) identified a glacial-interglacial shift in $\delta^{18}O$ values of 0.7-0.8‰ from the deep Atlantic Ocean and an average shift of 1.0±0.1‰ in the global oxygen isotope composition of seawater. As highlighted by Lachniet (2009), shifts in the oxygen isotope composition of the oceans over glacial-interglacial timescales will cause subsequent shifts in the $\delta^{18}O$ value of precipitation and cave drip waters.

Soil

The amount of precipitation which infiltrates soil pores lies between 5-25% in temperate climates as the processes of runoff, interception by vegetation, transpiration and evaporation limit the amount of precipitation infiltration (Clark and Fritz, 1997; Lachniet, 2009). Of these processes, only evaporation acts to modify $\delta^{18}O$

values in soil water. Evaporation of water from soil will lead to enrichment in ^{18}O (Zimmerman *et al.,* 1967; Allison, 1982; Gat, 1996; Clark and Fritz, 1997; Tang and Feng, 2001; Lachniet, 2009). A negative relationship exists between isotopic enrichment and humidity (Tang and Feng, 2001). The enrichment of ^{18}O will be greater than deuterium as a result of the kinetic effects of evaporation (Tang and Feng, 2001) and this kinetic fractionation can lead to a $\delta D/ \delta^{18}O$ slope as low as 2 (Allison, 1982). In addition, Tang and Feng (2001) identified the isotopic composition of precipitation was significantly more variable than that of soil water. The authors suggested that the soil water was composed of different meteoric waters from different precipitation events, potentially over different seasons, which have become mixed within the soil zone.

Epikarst

Drip water $\delta^{18}O$ values may be modified within the epikarst zone by the timing and amount of recharge (Lachniet, 2009). Jones *et al.* (2000) demonstrated the aquifer in Barbados was only recharged by 10-20% of mean annual precipitation which predominantly occurred during the wettest period. As a consequence, the groundwater $\delta^{18}O$ values are lower relative to those of precipitation. The transit time of waters through the karst has also been shown to influence the oxygen isotope composition of drip waters (Baldini *et al.,* 2006; Lachniet, 2009). Slow drips (<0.1ml/min) within cave environments have been proposed to be applicable to studies examining decadal- to millennial-scale variability due to longer transit times in the karst permitting mixing (Baldini *et al.,* 2006). In contrast, Baldini *et al.* (2006) have suggested intermediate drips (0.1-2ml/min) will have a shorter transit time and may be used in studies examining seasonal timescales. McDonald *et al.* (2007) identified that drip discharge at drip sites with overlying bedrock thickness of 12 and 22m responded rapidly to precipitation events. It was suggested the speleothem geochemical records fed by these drips may provide high-resolution trends of palaeo-rainfall. In contrast, drip discharge at drip sites at 45m did not correspond to precipitation events and may provide records of longer-term rainfall trends. Variations in the saturation state of drip waters have been shown to influence the timing of calcite deposition which will impact the oxygen isotope composition of speleothems

(Baldini *et al.,* 2006; Lachniet, 2009; Cai *et al.,* 2011). Seasonal variations in pCO_2 of the drip waters and cave air will influence the rates of degassing and this may result in a seasonal calcite deposition bias (Baldini *et al.,* 2006; Mattey *et al.,* 2008; Lachniet, 2009; Cai *et al.,* 2011). For example, at Shihua Cave (China) less calcite is deposited during the summer (rainy) season due to higher drip rates and cave air pCO2 which act to limit degassing and consequently limit calcite precipitation (Cai *et al.,* 2011).

Cave

The oxygen isotope composition of cave drip waters and any precipitated speleothems is related to recharge patterns and processes which modify the $\delta^{18}O$ value in the soil and karst (Fairchild et al., 2006a; Lachniet, 2009). Speleothems used in palaeoclimate studies must be shown to have formed in isotopic equilibrium with the cave drip waters from which they formed (Hendy, 1971; Fairchild and Baker, 2012). Isotopic equilibrium is likely to be achieved when the rate of drip water degassing is slow (Hendy, 1971). Equilibrium isotope fractionation is temperature dependent and is determined by the differential bond strength of isotopes in an element. Under equilibrium isotope fractionation between water and calcite, ^{18}O will be preferentially incorporated into the speleothem calcite (Sharp, 2007; Lachniet, 2009). An equilibrium fraction factor relationship for synthetic calcite was defined by Kim and O'Neil (1997) as:

$$1000ln\ \alpha_{(calcite-water)} = 18.03\ (10^3 T^{-1}) - 32.42 \qquad \text{Eq. 2.12}$$

Where $1000\ln \alpha_{(calcite\text{-}water)}$ is the fractionation between calcite and water and T is the temperature in Kelvin. A combined analysis using laboratory, theoretical and cave studies by Tremaine *et al.* (2011) led to a new equation defining the empirical isotope-temperature fractionation relationship for inorganic calcite (eq. 2.13).

$$1000ln\ \alpha_{(calcite-water)} = 16.1\ (10^3 T^{-1}) - 24.6 \qquad \text{Eq. 2.13}$$

Equation 2.13 defines a temperature-dependent oxygen isotope fractionation of -0.177‰/°C.

When rapid degassing occurs, kinetic fractionation may act to modify the isotopic composition of the drip waters. Calcite precipitated from kinetically fractionated

waters may show enrichment in both ^{18}O and ^{13}C (Hendy, 1971). The Hendy Test is used to determine whether calcite deposition occurred in equilibrium with cave drip waters and is carried out by analysing $\delta^{18}O$ and $\delta^{13}C$ values along a single growth layer. Kinetic fractionation is confirmed if $\delta^{18}O$ and $\delta^{13}C$ values positively co-vary along a single layer and/or along the growth axis and if $\delta^{18}O$ values are variable along a single growth layer (Hendy, 1971). However, the Hendy Test has been criticized and Dorale and Liu (2009) concluded the Hendy Test is not an accurate determination of whether calcite has formed in isotopic equilibrium with cave drip waters. Dorale and Liu (2009) argued that kinetic fractionation could be occurring along the flanks of the speleothem while equilibrium fraction is occurring at the centre, sampling along a single growth layer is impractical, climatic factors may cause the co-variation of $\delta^{18}O$ and $\delta^{13}C$ values depending on the timescale being examined and finally, replication is a better method to identify kinetic effects in speleothems.

2.6.2.3 Carbon isotopes

Open vs. Closed system models

The carbon isotope composition ($\delta^{13}C$) within speleothems has been suggested to predominantly reflect the carbon isotope composition of the percolating drip waters (Fairchild *et al.,* 2006a). Percolating waters acquire carbon from the following sources: CO_2 from the soil, CO_2 from the atmosphere and dissolution of carbonate minerals within the karstic host rock (Fairchild *et al.,* 2007). Two end-member systems have been used to describe the processes through which percolating waters accumulate calcium carbonate from the soil and epikarst (Hendy, 1971; McDermott, 2004; McDermott *et al.,* 2005). The first is the open-system model; under these conditions there is continuous equilibration between the percolating water and an unlimited supply of CO_2 within the soil (Hendy, 1971; McDermott, 2004; McDermott *et al.,* 2005). The result of the continuous equilibration is an increase in the amount of limestone dissolution, consequently leading to a higher proportion of bicarbonate within the seepage water. Under the open-system model, the $\delta^{13}C$ of percolating waters and subsequently speleothems, is largely influenced by the soil $\delta^{13}C$ with a minimal influence from the epikarst (McDermott, 2004; McDermott *et al.,* 2005). The second model is that of a closed-system. When carbonate dissolution begins to occur in a

closed-system, the percolating waters become isolated from the reservoir of CO_2 in the soil (Hendy, 1971; McDermott, 2004; Fairchild *et al.,* 2006a). The resulting carbon isotope composition of the water therefore reflects the $\delta^{13}C$ of the host rock (McDermott, 2004; McDermott *et al.,* 2005) and overall the total dissolved Ca and DIC are greatly reduced in comparison to open-systems (Fairchild *et al.,* 2006a). However, these two models represent extreme situations (Hendy, 1971) and the majority of natural systems are most likely to be somewhat open and therefore will have a dissolved inorganic carbon $\delta^{13}C$ value which lies between the two models (McDermott 2004; McDermott *et al.,* 2005).

Organic processes

Variations in the carbon isotope ratio from speleothems forming in arid environments have often been inferred to reflect changes in vegetation type (McDemott, 2004; Fairchild *et al.,* 2006a). Plants which utilize the C3 pathway typically have a $\delta^{13}C$ value between -26‰ to -20‰ while plants utilizing the C4 pathway tend to have a $\delta^{13}C$ value between -16‰ to -10‰ (McDermott, 2004; McDermott *et al.,* 2005). These different vegetation types are recorded in speleothem carbonate through the $\delta^{13}C$ values. When carbonate $\delta^{13}C$ values lie between -14‰ to -6‰, it is frequently inferred that the carbonate formed in equilibrium with CO_2 respired from C3 vegetation. Conversely, carbonates which have been deposited in equilibrium with CO_2 respired from C4 vegetation typically have $\delta^{13}C$ values within the range of -6‰ to +2‰ (McDermott, 2004).

In regions which lack C4 vegetation, the interpretation of the carbon isotope record can be complicated. However, stalagmites from Villars Cave, France, have provided a record of carbon isotope measurements related to variations in biogenic soil CO_2 production (Genty *et al.,* 2003). Between 83,000 – 32,000yr BP, the $\delta^{13}C$ values from Villars Cave stalagmites are significantly lower during warm periods due to a larger amount of biogenic CO_2 becoming incorporated into the percolating waters. In contrast, under cold conditions, vegetation and soil become degraded and as a result there is a reduction in biogenic CO_2 production and a rise in the proportion of atmospheric CO_2. Due to the increased proportion of atmospheric (heavy) carbon, the

percolating waters and speleothems will have higher $\delta^{13}C$ values when conditions are colder (Genty *et al.,* 2003).

Inorganic processes

The precipitation of calcite in the karst above a cave has often been used to explain high carbon isotope ratios (McDermott, 2004). This process, referred to as PCP, is related to degassing of CO_2. During degassing, carbon is preferentially released as ^{12}C and this leaves the percolating waters with a higher proportion of ^{13}C (Fairchild and Baker, 2012). Baker *et al.* (1997) identified PCP as one of three possible mechanisms which may have led to high $\delta^{13}C$ values in speleothems from Stump Cross Caverns, UK. Baker *et al.* (1997) proposed that degassing of percolating waters within the karst would result in calcite deposition and elevated $\delta^{13}C$ values within the waters and subsequently any calcite precipitated from the waters. Degassing (and subsequent kinetic fractionation effects) between stalactite and stalagmite as well as disequilibrium with soil CO_2 were proposed in addition to PCP to explain the high $\delta^{13}C$ values of speleothems studied by Baker *et al.* (1997).

Trace elements have the potential to support the interpretation of the $\delta^{13}C$ value in speleothems (McDermott, 2004). Assessment of the relationships between Mg/Ca, Sr/Ca and $\delta^{13}C$ values from speleothems has frequently identified a significant positive co-variation, indicative of a common forcing mechanism (Griffiths *et al.,* 2010; Regattieri *et al.,* 2014). The driving mechanisms has been proposed as PCP within the karst which is enhanced under dry conditions.

Within cave processes - kinetic fractionation

Drip rate is known to control kinetic (disequilibrium) fractionation during calcite precipitation (Mühlinghaus *et al.,* 2009). Mühlinghaus *et al.* (2009) identified that under fast drip regimes, the carbon isotope composition of the resulting calcite forms in isotopic equilibrium with the drip waters. Conversely, extensive degassing of CO_2 and calcite precipitation will lead to a progressive increase in the $\delta^{13}C$ values of the solution and any further precipitated calcite (Mickler *et al.,* 2006) and these processes are promoted under slow drip regimes (Mühlinghaus *et al.,* 2009). Another control over kinetic fractionation, which is closely related to drip rate, is the residence time of the solution on the stalagmite surface (Mühlinghaus *et al.,* 2009). If residence times

are longer, the amount of calcite precipitation will increase whilst the amount of bicarbonate in the solution will decrease. This will result in a progressive rise in the carbon isotope ratio of the bicarbonate in solution and this will ultimately lead to isotopic equilibrium between the bicarbonate in solution and the cave PCO_2 (Mühlinghaus *et al.,* 2009).

Kinetic fractionation of carbon isotopes has been shown to occur under strong cave ventilation regimes (Spötl *et al.,* 2005; Mattey *et al.,* 2008; Frisia *et al.,* 2011) as discussed in section 2.4.3.6. Enhanced degassing results in kinetic fractionation of the carbon isotopes and enrichment of ^{13}C in the solution and precipitating stalagmites (Spotl *et al.,* 2005; Mattey *et al.,* 2008; Frisia *et al.,* 2011). These studies have demonstrated the complexity of the carbon isotope composition in speleothems and have highlighted the importance of cave monitoring studies (Spotl *et al.,* 2005; Mattey *et al.,* 2008; Frisia *et al.,* 2011).

2.6.2.4 Summary

Isotopes are fractionated by an array of processes. Oxygen (and hydrogen) isotopes are modified throughout the hydrological cycle. The initial isotopic composition of meteoric waters is controlled by the $\delta^{18}O$ value of ocean water and is modified by evaporation and condensation (Dansgaard, 1964; Clark and Fritz, 1997; Lachniet, 2009). Meteoric water can be modified by the following isotope 'effects': temperature, latitude, continentality, amount of precipitation, altitude, moisture source, seasonality and ice volume (Rozanski *et al.,* 1993; Lachniet, 2009). In the soil zone, evaporation has been shown to influence $\delta^{18}O$ values within soil water (Clark and Fritz, 1997; Lachniet, 2009). The timing and amount of recharge may further modify the oxygen isotope composition of water in the epikarst (Lachniet, 2009). Finally, kinetic fractionation within the cave will change the isotopic composition of drip waters and any speleothems precipitated from these waters (Hendy, 1971; Lachniet, 2009).

Drip waters can accumulate carbon from the soil and epikarst via an open or closed system (Hendy, 1971; McDermott, 2004; McDermott *et al.,* 2005). Carbon isotope ratios in speleothems have been interpreted to reflect changes in vegetation type (McDermott, 2004; Fairchild *et al.,* 2006a) and vegetation productivity (Genty *et al.,*

2003). Additionally, inorganic processes such as PCP (Baker *et al.,* 1997; McDermott *et al.,* 2004), and within-cave kinetic fractionation (Muhlinghaus *et al.,* 2009; Mickler *et al.,* 2006; Spotl *et al.,* 2005; Mattey *et al.,* 2008; Frisia *et al.,* 2011) have been shown control the carbon isotope composition of drip waters and speleothems.

2.6.3 The application of trace elements to speleothem studies

2.6.3.1 Introduction

Increasingly, trace elements are being used in speleothem studies aiming to reconstruct palaeoclimate (Fairchild and Treble, 2009). As identified in section 2.3 geochemical signals within speleothems can be controlled and modified by many different processes within the atmosphere, vegetation and soil, karst and cave, during speleothem crystal growth and during secondary alteration of calcite (Fairchild *et al.,* 2006a; Fairchild and Treble, 2009). Therefore, the concentrations of different elements in speleothems can be used to interpret variations in different processes and have the potential to become powerful high-resolution proxies of palaeoclimate and palaeoenvironment (Borsato *et al.,* 2007; Fairchild and Treble, 2009). Furthermore, seasonal cycles in trace elements have recently been used in conjunction with other dating techniques to constrain speleothem chronologies (Smith *et al.,* 2009; Ban *et al.,* 2018). Nonetheless, the complexity of the cave environment complicates the interpretation of trace element profiles and therefore understanding the trace element sources and influencing processes is vital to decode the chemical signal preserved within the speleothem (Fairchild *et al.,* 2000, Fairchild and Treble, 2009).

2.6.3.2 Sources of trace elements

As a result of the individual tectonic and depositional processes operating at each site, trace element composition is highly site-specific and often individual speleothems within a cave system may each possess a distinct trace element signature (Fairchild and Treble, 2009).

Atmosphere

Although the atmosphere provides the primary source for the stable oxygen isotope signal preserved in speleothem calcite, it is remains a minor source for trace element.

However, some trace element signals have been shown to relate to dry deposition of aeolian dust (Goede *et al.,* 1998; Frumkin and Stein, 2004; Fairchild and Treble, 2009) and others have identified the contribution of sea-salt aerosols in wet atmospheric deposition as a source of trace element species (Baker *et al.,* 2000; Fairchild *et al.,* 2000). Anthropogenically and volcanically sourced sulphur emitted into the atmosphere can also be transferred and preserved into speleothem calcite and therefore speleothems may act as an archive of modern pollution or volcanic activity (Frisia *et al.,* 2005; Wynn *et al.,* 2008, 2010). Although, work by Borsato *et al.* (2015) demonstrated the variable transmission time between S deposition and incorporation into the stalagmite which can significantly influence interpretation of S as a proxy.

Vegetation

Vegetation productivity and decay have been demonstrated to control elemental concentrations of P (Huang *et al.,* 2001; Fairchild and Treble, 2009; Treble *et al.,* 2003). A study at Ernesto Cave, Italy, identified the supply of P to the karst and cave was related to vegetation decay in the autumn and this was expressed by peaks in P within the speleothem records (Huang *et al.,* 2001). Analysis of P within speleothems was confirmed to be a useful proxy for palaeo-rainfall by Treble *et al.* (2003). Within the study, P was demonstrated to be a reliable indicator of surface bioproductivity which is ultimately related to rainfall.

The die-back of vegetation in autumn combined with increased infiltration may result in an increase in speleothem P during the autumn-winter (Borsato *et al.,* 2007; Treble *et al.,* 2003). Seasonal variations in speleothem P concentrations have been identified and express the annual distinction between different seasonal hydrological regimes (Borsato *et al.,* 2007). In summary, P has frequently been applied in speleothem studies as a proxy for rainfall resulting in variations in vegetation productivity and seasonal die-back of vegetation during the autumn (Huang *et al.,* 2001; Treble *et al.,* 2003; Borsato *et al.,* 2007; Fairchild and Treble, 2009; Fairchild *et al.,* 2010; Orland *et al.,* 2014; Webb *et al.,* 2014).

Soil and karst processes

The largest source of calcium and most trace elements which occur in speleothems is the karst bedrock and overlying soil. The factors which control the transfer of trace

elements into karst are two-fold: 1) the degree of chemical mobilization of the trace elements in the soil and epikarst; 2) the hydrological processes which influence infiltration rates of water into the epikarst (Fairchild and Treble, 2009). Chemical mobilization behaviours include rapid entrainment of solutes, particles and colloids combined with dissolution of salts and leaching of weakly-sorbed species; intermediate calcite dissolution and slow release of ions through chemical weathering (Fairchild and Treble, 2009).

Infiltrating waters which form speleothems may contain characteristic trace element compositions due to dissolution and hydrological processes as a function of flow conditions. High flow conditions can lead to the enrichment of some trace element species, in particular those associated with colloidal transport (Fairchild and Treble, 2009). Zn has been shown to be associated with colloids and distinct peaks in Zn have been identified in Obir Cave related to autumnal infiltration maxima (Fairchild *et al.,* 2010; Wynn *et al.,* 2014). Wynn *et al.* (2014) identified annual peaks in Zn were associated with natural organic matter and ultimately controlled by water excess, pH of the soil in relation to microbial activity and the variability of the overlying snowpack. The study has demonstrated the significance of Zn event laminae related to hydrological flushing of Zn from the soil during the autumn and has provided support for other models which have proposed various trace elements are transported into speleothems through Natural Organic Matter (NOM).

Under conditions of low flow and reduced effective precipitation on the surface, rock-water residence times increase. As a consequence, the bedrock is subjected to enhanced dissolution and trace element release (Hellstrom and McCulloch, 2000). Additionally, increased water-rock residence times in the aquifer combined with the presence of a porous bedrock, encourages degassing of waters and precipitation of $CaCO_3$ along the flowpath (Fairchild *et al.,* 2000; McMillan *et al.,* 2005).

Prior calcite precipitation has been shown to have a critical influence over Mg in speleothems. Precipitation of calcite up-flow of the precipitating speleothem is related to degassing of the karstic waters due to contact with a different PCO_2 which ultimately results in supersaturation of $CaCO_3$ in the karstic waters and calcite precipitation (Fairchild and Treble, 2009). As a result, more Ca is removed from the

solution than the trace elements, leading to enrichment of the trace element to calcium ratio (Fairchild and Treble, 2009). Fairchild *et al.* (2000) proposed that under dry conditions there will be an increase in PCP due to the reduction in water availability within the karst overlying the cave. Similar to Mg, prior calcite precipitation can influence the Sr composition in dripwaters and subsequently speleothems (Fairchild and Treble, 2009). The positive correlation between Mg/Ca and $\delta^{13}C$ (Fohlmeister *et al.,* 2012; Regattieri *et al.,* 2014) or Mg/Ca, Sr/Ca and $\delta^{13}C$ values (Johnson *et al.,* 2006; Griffiths *et al.,* 2010; Cruz *et al.,* 2007) has frequently been used to indicate PCP as a forcing mechanism for variations in Mg/Ca, Sr/Ca and $\delta^{13}C$ and has subsequently be inferred as an aridity proxy. However, the chemical covariance between Mg/Ca and Sr/Ca has been shown to be nearly identical for PCP and ICD processes and Sinclair *et al.* (2012) expressed the difficulties in separating the chemical signatures of these processes.

Numerous studies have used a combination of Ba/Ca, Mg/Ca and Sr/Ca ratios alongside $\delta^{18}O$ and $\delta^{13}C$ measurements to suggest variations in Ba/Ca relate to PCP upstream of the stalagmite (Wu *et al.,* 2012; Hori *et al.*, 2013; Johnson *et al.,* 2006). For example, Johnson *et al.* (2006) measured Mg, Sr and Ba at Heshang Cave, China and identified that co-variation between the trace elements was related to enhanced degassing and subsequent PCP due to dry conditions above the cave. Hori *et al.* (2013) highlighted the co-variation between Sr/Ca, Ba/Ca and $\delta^{13}C$ in a stalagmite from Maboroshi cave, Japan, was related to drier conditions during the Lateglacial and Holocene leading to an increased amount of PCP.

2.6.3.3 Partition coefficient

Section 2.6.3.2 indicated that analysing speleothem trace element concentrations can provide high-resolution records of vegetation dynamics and karst-water interactions. However, the incorporation of elements into the speleothem crystal lattice may complicate the interpretation of speleothem records. A distribution or partition coefficient can be used to define the incorporation of an element from a solution into a speleothem (Fairchild and Treble, 2009).

Frequently speleothem studies use trace elements such as Mg, Sr and Ba which are known to form divalent cations when in solution and substitute for Ca within the

crystal lattice of carbonate (Fairchild and Treble, 2009). A relationship between solution and mineral trace element compositions can be defined using a distribution or partition coefficient through the following equation (Eq. 2.14) of Morse and Bender (1990):

$$(Tr/Ca_{CaCO3}) = K_{Tr}\,(Tr/Ca)_{solution} \qquad \text{Eq. 2.14}$$

Where Tr = trace element and K_{Tr} = distribution coefficient

The distribution coefficient may be controlled by various factors including crystal morphology, temperature, precipitation rate as well as different aspects of the solution composition (Fairchild and Treble, 2009).

2.6.3.4 The influence of growth kinetics

In some cave environments, Sr concentration in speleothems has been suggested to be predominantly controlled by growth rate (Fairchild *et al.,* 2001; Fairchild and Treble, 2009). When growth rates are higher, a higher concentration of Sr is expected to be found in speleothems (Lorens, 1981; Gabitov and Watson, 2006; Fairchild and Treble, 2009).

Co-variation between Sr and Ba has been used as an indicator of growth kinetics, particularly growth rates, in both dripwaters and speleothems (Treble *et al.,* 2003; Treble *et al.,* 2005b; Webb *et al.,* 2014). Treble *et al.* (2003) concluded that Ba was controlled by growth rate on intra- and inter-annual scales but identified that the inter-annual behaviour of Sr differed from Ba, suggesting that Sr concentrations were moderated by PCP. Further work by Treble *et al.* (2005b) produced a series of trace element maps and demonstrated that Sr and Ba were controlled by annual changes in precipitation resulting in a seasonally variable growth rate. Additionally, the trace element maps produced by Treble *et al.* (2005b) suggested a correspondence between U and annual growth layering within the stalagmites from SW Australia. Treble *et al.* (2005b) concluded by suggesting that U variation within stalagmites corresponds to the annual growth layering and demonstrated that speleothem growth was complex, ultimately impacting the interpretation of annual trace element cycles.

2.6.3.5 Summary

This section has demonstrated the sources of trace elements found in speleothem calcite and the complex chemical interactions between the source, transport and preservation in the speleothem crystal lattice. Speleothem trace element composition can be modified by processes operating in the atmosphere, the soil and upper epikarst, the lower epikarst and cave and during $CaCO_3$ precipitation (Fairchild *et al.,* 2006a). In order to fully understand the mechanisms forcing changes observed in speleothem trace element records, they must be used in conjunction with stable isotope records and in-depth hydrological monitoring (Fairchild *et al.,* 2000; Fairchild and Treble, 2009; Fairchild and Baker, 2012). When used in this way, trace elements have a vast potential to investigate past environmental and climatic variability.

3. Site description and methodology

3.1 Location and regional geology

The site of Cueva de las Perlas (43°19'02.0"N, 003°35'33.3"W, 336m a.s.l.) is situated in the village of Matienzo located in the north of the Iberian Peninsula, ~45km southeast of Santander (figure 3.1). Cueva de las Perlas lies within a 28km^2 enclosed karstic depression within the Cantabrian Cordillera which is the western most extension of the Pyrenees mountain range (Waltham, 1981, Quin, 2010).

The depression has a characteristic Y-shape, which is made up of three distinctive 'arms': La Secada to the north, La Vega to the west and Ozana to the south east (figure 3.2) (Quin, 2010). Orogenic pressure from the formation of the Pyrenees led to anticline/syncline development in the early to mid-Tertiary period (Quin, 2010; Ruiz Cobo N.D). The Matienzo depression developed through preferential erosion of the anticline running E-W between La Vega and Ozana.

The primary geology of the area is Early Cretaceous sedimentary strata (Mills and Waltham, 1981; Quin, 2010). The valley floor is composed of impermeable Barremian (Early Cretaceous) sandstones and marls. Overlying these beds are Aptian limestones (Early Cretaceous) which are thinly bedded with sandstone lenses. Massive beds of Albian (Early Cretaceous) limestone lie above the Aptian limestones. The youngest beds represent the thinly bedded Albian limestones. Recently a stratabound hydrothermal dolomite (HTD) within the Aptian carbonates in the Matienzo valley was identified (Dewit *et al.,* 2014) and the positioning of the HTD body covers the site of Cueva de las Perlas. Therefore, it is proposed that Cueva de las Perlas lies within a coarsely crystalline dolomite bedrock with calcite inter-grown.

A key feature of the Matienzo depression is the extensive network of cave systems, with 386.6km of mapped passages as of Mar-18 (Corrin, 2018). Waltham (1981) proposed a minimum age for cave development of 1.8Ma. These caves are formed through karstic dissolution which exploits weaknesses in the limestone. The principle behind this process is that calcium carbonate, the primary component of limestone,

can be dissolved by weak acids and this process is expressed by equation 3.1 (Quin, 2010).

$$CaCO_3 + CO_2 + H_2O \Leftrightarrow Ca^{2+} + 2HCO_{3-} \quad \text{Eq. 3.1}$$

Cave altitudes within the Matienzo depression represent progressive lowering of the valley floor. Subsequently, the oldest cave systems are located at the highest altitudes with modern active cave formation occurring on the valley floor.

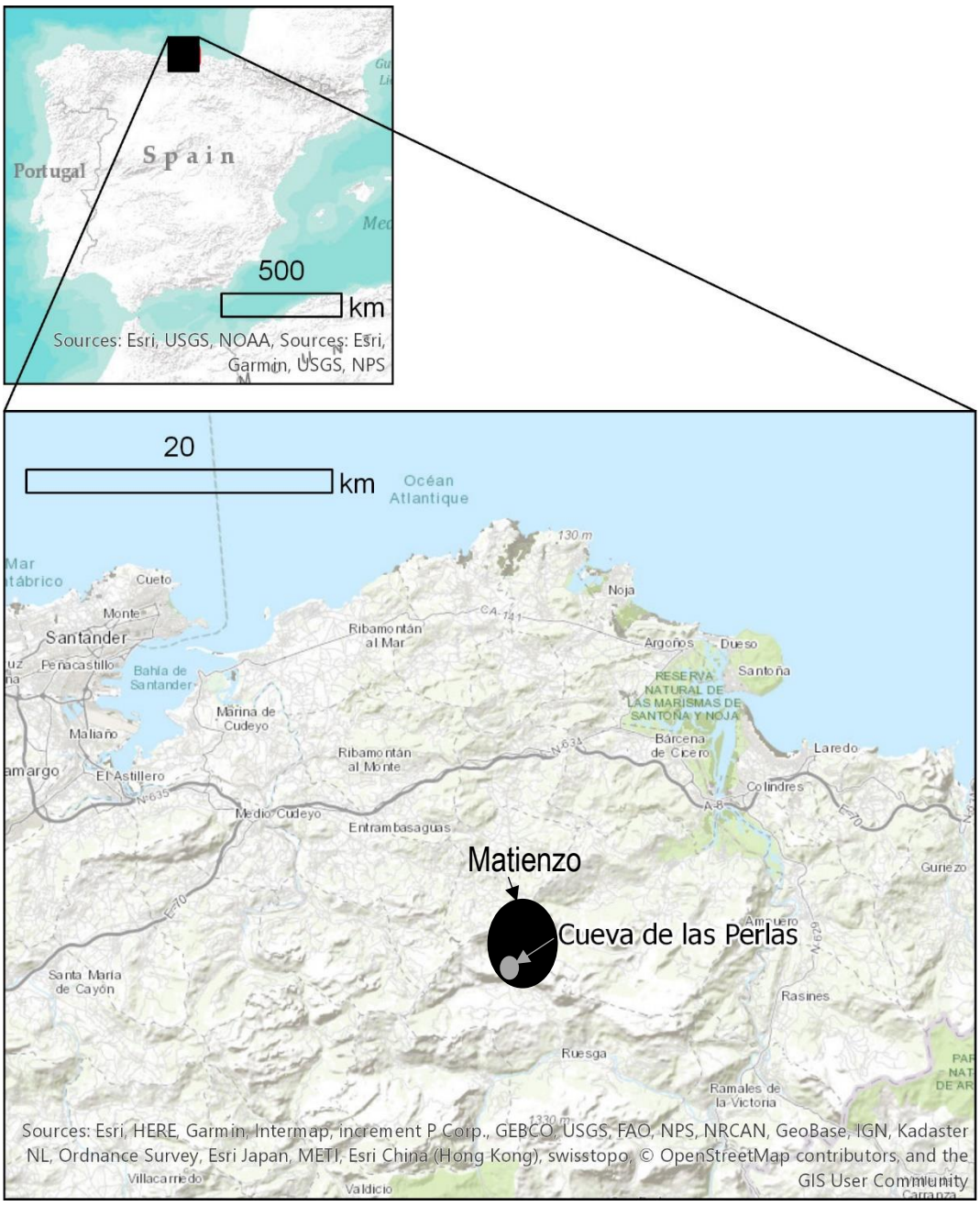

Figure 3.1: Matienzo maps. ArcGIS software by Esri was used to create the maps. Copyright © Esri.

Figure 3.2: Map of the Matienzo valley. ArcGIS software by Esri was used to create the map. Copyright © Esri.

3.2 Modern environment

The Matienzo depression has an oceanic climate (Corrin, 2004; Ruiz Cobo N.D.) which leads to a mean annual rainfall >1500mm occurring throughout the year. The climate of Matienzo can be described as temperate to warm (Corrin, 2004). Due to the positioning of the Matienzo depression in Northern Iberia, the climate is directly influenced by the North Atlantic which makes this region unique compared to southern Spain which has the additional Mediterranean climate influence (Smith *et*

al., 2016a). The marginal location of this region to key oceanic circulation regimes heightens its sensitivity to oscillatory climatic behaviour throughout the Quaternary.

The North Atlantic Oscillation is the primary control over the modern-day climate of the Iberian Peninsula (Trigo *et al.,* 2004; Naughton *et al.,* 2009). Under negative NAO conditions, a weak Azores high and/or Icelandic Low (Hurrell, 1995) leads to a reduction in the strength of westerly winds from the eastern North Atlantic. As a result, during negative NAO conditions, Iberia experiences increased winter precipitation and river flow (Trigo *et al.,* 2004; Naughton *et al.,* 2009). Positive NAO conditions are the result of an enhanced pressure gradient between the Azores high and Icelandic low (Hurrell, 1995). Under positive NAO conditions, the westerlies are strengthened and shift northwards resulting in arid conditions across the Iberian Peninsula (Trigo *et al.,* 2004). Therefore, the positioning of Matienzo in the northern Iberian Peninsula makes the region particularly sensitive to changes in air mass movements over long timescales.

Rocky limestone outcrops are abundant on the hillslopes within which Cueva de las Perlas is situated and are shown in figure 3.3. Soils on these slopes are poorly developed and thin (15-100cm). Consequently, the vegetation overlying the cave consists of shrubs such as heaths (*Erica arborea, Daboecia cantabrica, Erica vagans*), brambles (*Rubus ulmiformis*) and heather (*Calluna vulgaris, Ulex europaeus*) (Ruiz Cobo, N.D.). Land use on the valley sides is low intensity with occasional animal grazing. In contrast, the valley base is rich in flora and fauna and is used by the local community for agriculture.

Figure 3.3: Images of the hillslope on which Cueva de las Perlas is located. Photos used are included with the kind permission of J. Houska.

3.3 Cave description

3.3.1 Cave environment

Cueva de las Perlas is a horizontal cave site with two entrances. The eastern entrance is relatively large but narrows into a crawl before joining the main chamber. In contrast, the western entrance involves a 2m drop onto a sloping floor which opens into the main chamber. For this study, the western entrance was used as the primary entrance. A 14.95m passage along a bearing of 295° links the entrance to the 'cave monitoring chamber' and it was in this chamber where the majority of monitoring for this study was undertaken. A survey of the cave is shown in figure 3.4 and the locations of different cave monitoring sampling sites are marked on the survey. The monitoring chamber is 10.9m across and primarily three drip sites were monitored at 4.75m (P1), 6.8m (P2) and 7.5m (P3) from the western chamber wall. The cave extends a further 12.3m where it narrows and ends in a boulder choke. Rock overburden was estimated through basic trigonometry to be 4.01m based upon an angle of slope of 15° and a measured distance into the cave of 14.95m. At the back of the cave the overburden is calculated to 7.3m based upon same angle of slope but a distance of 27.25m

The cave is highly decorated with abundant straws, columns and stalagmites. Images from the inside of Cueva de las Perlas are shown in figure 3.5. The cave is home to many cave pearls which is where the name Cueva de las Perlas originates. In the western section of the cave behind the monitoring chamber there is evidence for a sediment collapse and this has left the stalagmites at different angles. It was from this collapsed flowstone and sediment section that the speleothems analysed in this study were collected.

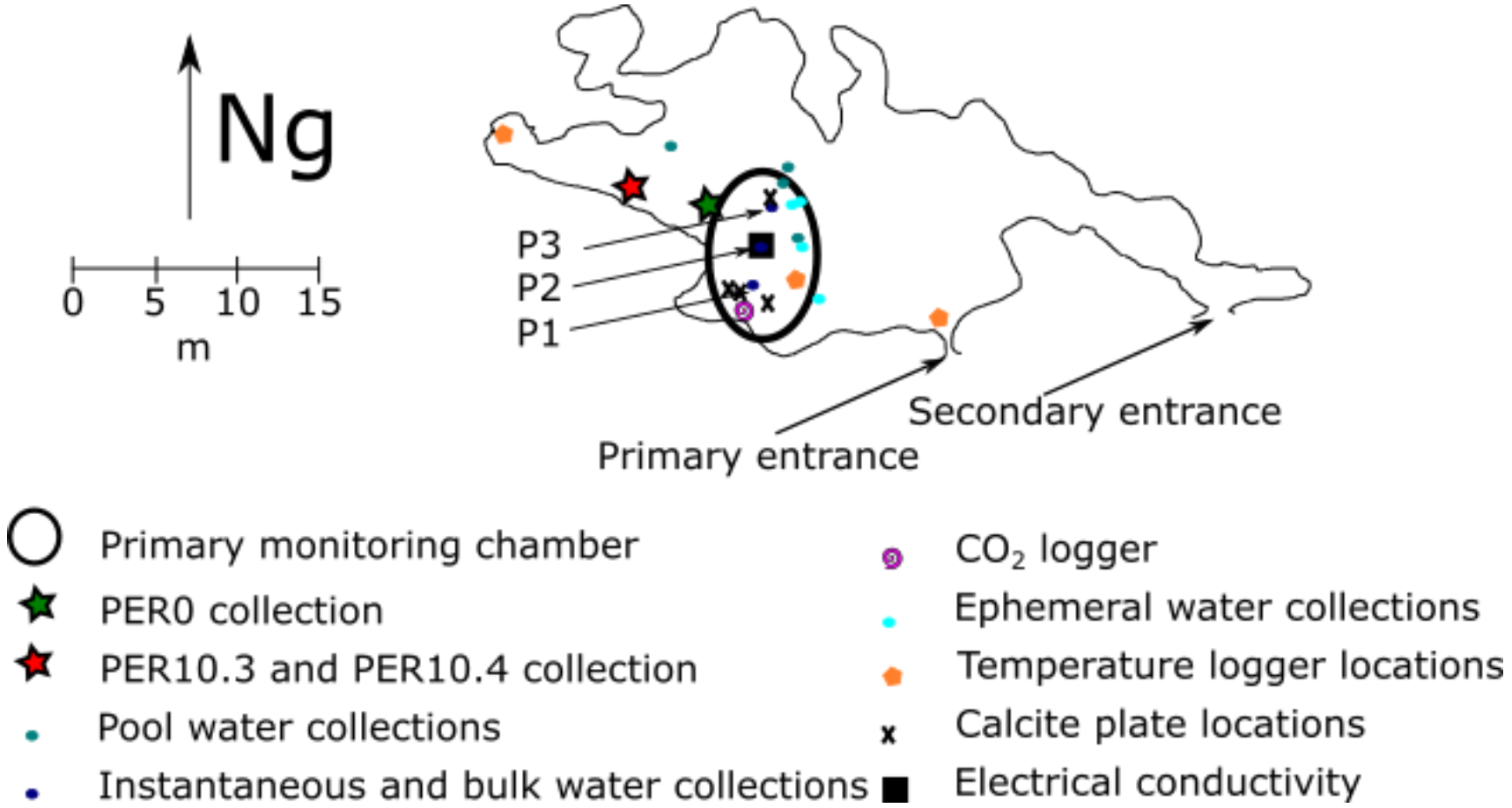

Figure 3.4: Cave survey (plan view) showing the primary logging sites. The survey has been redrawn based upon Smith (1998) and is drawn to magnetic north and rotated 3° W to align with grid north.

Figure 3.5: Photos from Cueva de las Perlas. The site from which PER0 was taken (A), the drip water collection set-up (B), the cave entrance (C) and the collapsed flowstone section (D). Photos included with the kind permission of J. Houska.

3.3.2 Identifying speleothem material in Cueva de las Perlas

In order to identify appropriate material for the present study, a number of basal cores were drilled from speleothems in 2015. The ages were placed onto the cave survey shown in figure 3.6. The cores collected from the monitoring chamber were primarily Holocene with the exception of a MIS5e speleothem and a MIS5a/MIS4 speleothem located towards the collapsed section at the rear of the monitoring chamber.

Samples for palaeoclimate reconstruction were taken from the collapsed section as there were no actively dripping stalagmites in this area, the candle-shaped stalagmites each possessed a thick outer coating and were not translucent (a sign of active deposition) and finally the stalagmites were found to be at a series of different angles representing varying periods of sediment and flowstone collapse. An initial stalagmite (PER0) was taken from the collapsed section and was found to have a basal age of ~85ka and cessation of growth at ~65ka. This allowed an approximate date of flowstone collapse and relative dating of other speleothem samples according to the angle of repose on the flowstone slab. A cluster of candle-shaped speleothems, also

from the collapsed section, was found and each of the speleothems appeared to be resting at a series of different angles as a result of gradual tilting of the flowstone slab since 65ka. Thereby covering the period of interest for this study. PER0 visually had the highest angle of tilt and therefore the cluster of speleothems shown in figure 3.7 were assumed to represent phased growth from <65ka based on the varying angles of tilt.

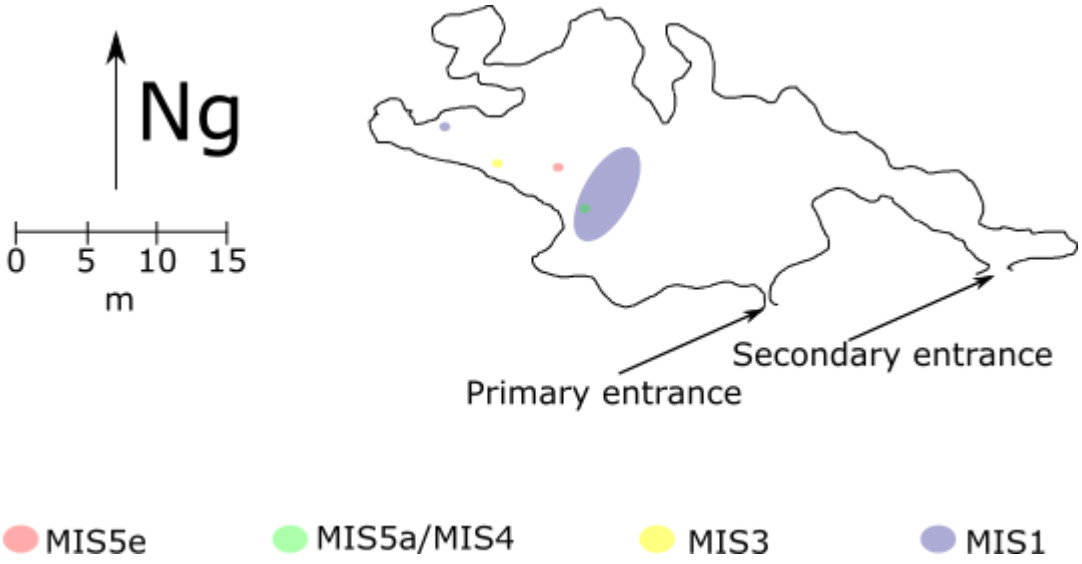

Figure 3.6: Schematic illustrating the basal drilling results from 2015. The MIS5a/MIS4 and MIS3 speleothems were used in the present study. The survey has been redrawn from Smith (1998).

Figure 3.7: PER10.3 and PER10.4 in-situ (a) and schematic diagram with basal ages (B).

3.4 Speleothem samples for palaeoclimate reconstruction

3.4.1 PER0

PER0 (figure 3.8) was collected from the sediment/flowstone collapse section towards the rear of the monitoring chamber. The sample is 390mm in length and consists of white columnar calcite. Clear growth bands can be seen within the sample. The sample was covered in a 1-5mm thick 'skin' and was not actively dripping at the time of collection.

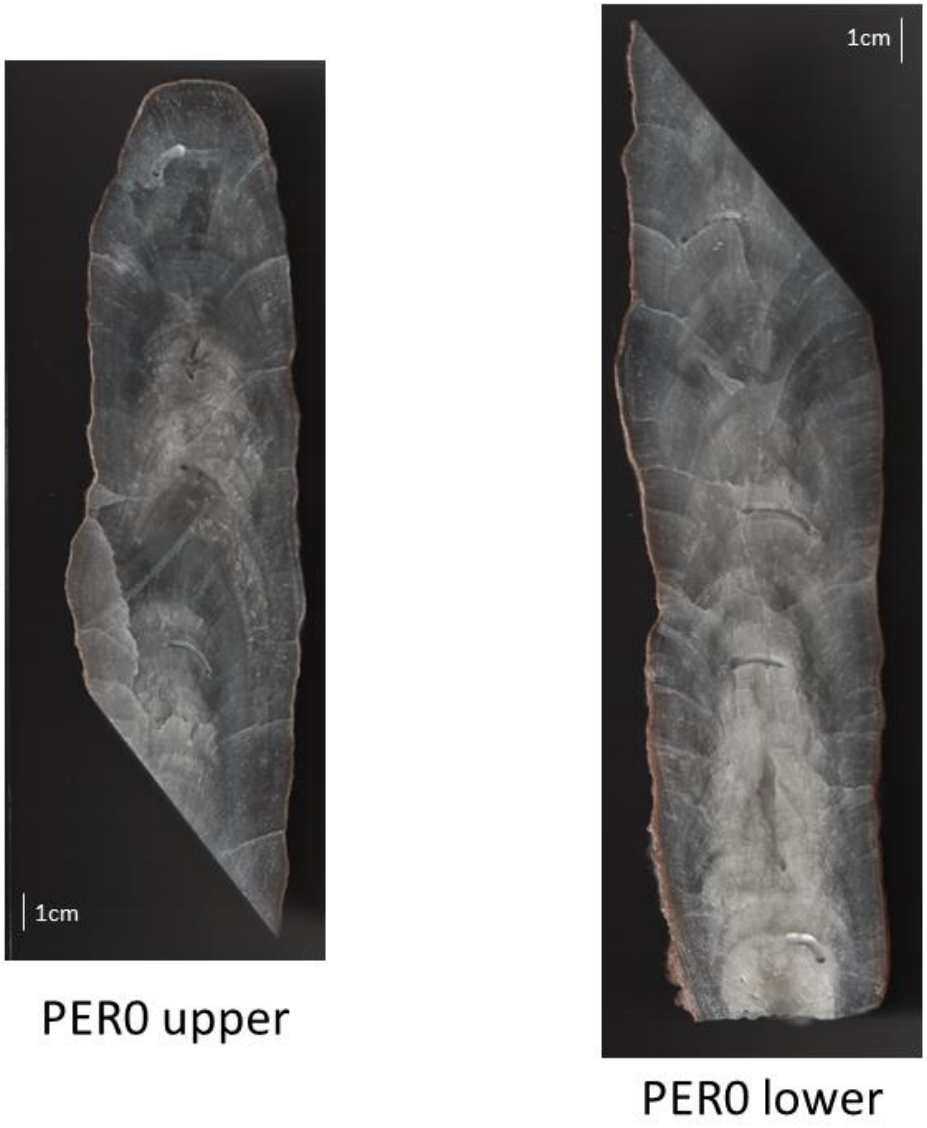

Figure 3.8: PER0 sample from Cueva de las Perlas.

3.4.2 PER10.3 and PER10.4

Samples PER10.3 and PER10.4 were taken from the cluster of speleothems shown in figure 3.7 on the western collapse section behind the PER0 sample site. PER10.3 is 203.1mm in length and PER10.4 is 236.8mm in length. Both speleothems consist of white columnar calcite and show distinct growth bands (figure 3.9). Hiatuses are indicated in both speleothems by a colour change from white calcite to brown layer. Neither of the samples were actively dripping at time of collection and, similar to PER0, each possessed an outer 'skin' consisting of a darker coloured calcite.

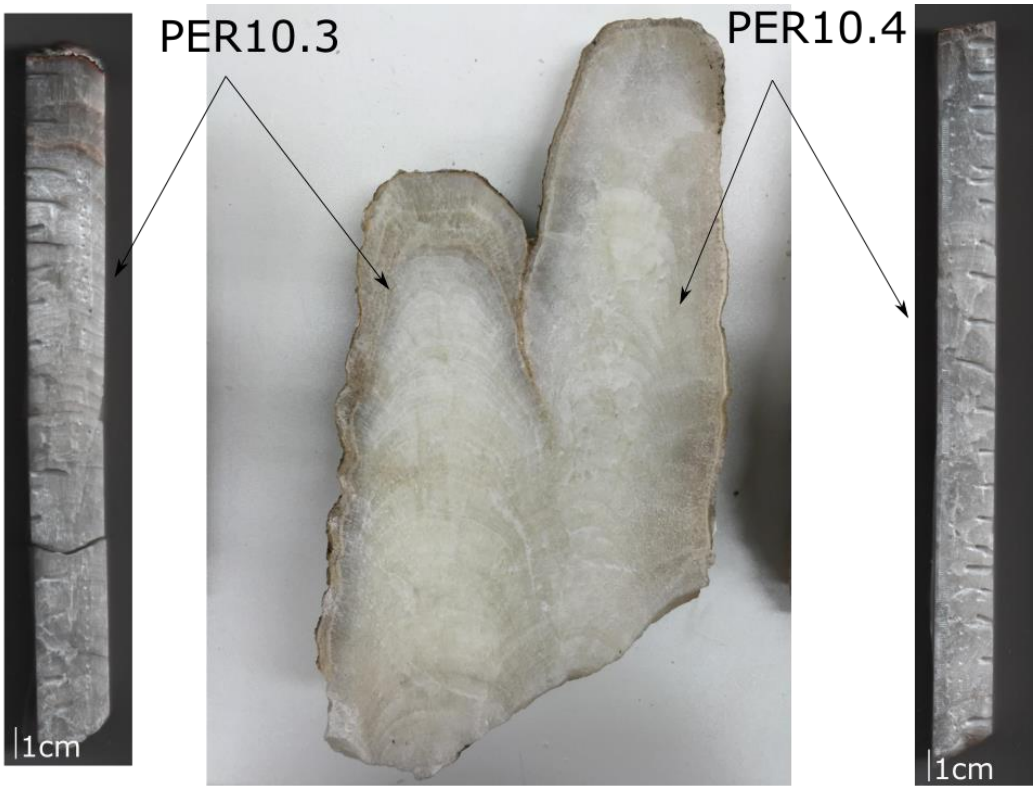

Figure 3.9: PER10.3 and PER10.4 samples from Cueva de las Perlas.

3.5 Climate and cave monitoring

3.5.1 Overview

External climate and environmental monitoring and cave monitoring for this project began in Feb-15 and built on the work of Smith (2014). Monitoring of the external climate, soil and cave was undertaken in order to gain an understanding into the cave dynamics and investigate the processes within the air, soil, karst and cave which may influence speleothem chemistry. Field visits were made to Matienzo and in addition to these visits, monthly visits were made by members of the Matienzo Caving Community. The following section will describe the techniques and equipment used in the monitoring programme.

3.5.2 External climate monitoring

External temperature has been measured on the same hillslope as (500m from) Cueva de las Perlas at N 43º19'00.1" W 003º35'40.1 at 293m (a.s.l.) in the same location detailed in Smith *et al.* (2016a). Temperature has been continuously logged by a Tinytag Plus 2 Dual Channel Temperature/Relative Humidity TGP-4500 logger since Apr-10. Measurements were logged at 30-minute intervals and are accurate to within ±0.01°C. External air pressure has been measured using a baro-diver at 10-minute intervals since Apr-15 in the same location as the external temperature logging. The baro-diver has a quoted accuracy of ±0.5cmH_2O.

Rainfall amount was measured using a Pluvimate logger situated in a rain gauge in the village of Matienzo located approximately 1km from Cueva de las Perlas from Feb-11 (43°19'00.1"N, 003°35'23.4"W). The logging interval was set to 10 minutes and sensitivity is 0.006mm per hour. In addition, monthly samples were monitored for rainfall volume and subsampled by a member of the Matienzo Caving Community for chemical analysis. Samples were later analysed for stable isotopes (oxygen and hydrogen), cations and anions in the laboratories at Lancaster University using the methods described in section 3.6.

Carbon dioxide measurements of the external air were taken during fieldwork visits by the PI using a hand-held Vaisala GMP221 probe attached to an MI70 indicator. The unit

measurement range is 0-10,000ppm and has a measurement uncertainty of 2% and an observed working uncertainty of 10% (Smith *et al.,* 2015). Monthly samples for carbon isotope analysis were taken from the external air by injecting 20ml of air into a 12ml evacuated exetainer.

3.5.3 Soil monitoring

A soil sampling device was placed in the same hillslope as Cueva de las Perlas in Jan-12 (described in Smith, 2014 and Smith *et al.* 2016a). The device was positioned at a soil depth of 50cm which marked the transition between the soil and karst zones (figure 3.10). The soil sampling tube was a distinctive L-shape and a series of holes were drilled into the base in order to allow for air exchange. A silicone tubing was placed into the piping and taped to the top of the horizontal pipe section (figure 3.10B). This tubing was used to extract soil gas samples. Soil gas samples were taken using a 20ml syringe and inserted into a 12ml evacuated exetainer. Analysis of soil CO_2 was undertaken by inserting the hand-held Vaisala (described in section 3.5.2) into the soil tube. The location of the soil sampler was not moved closer to Cueva de las Perlas due to thinner soils (15-30cm). The homogeneous nature of the vegetation and soil cover on the hillslope is thought to reduce any potential spatial variations in soil productivity. Soil temperature has been logged continuously by a Tinytag Plus 2 Dual Channel Temperature/Relative Humidity TGP-4500 logger buried next to the soil sampling device since Apr-15.

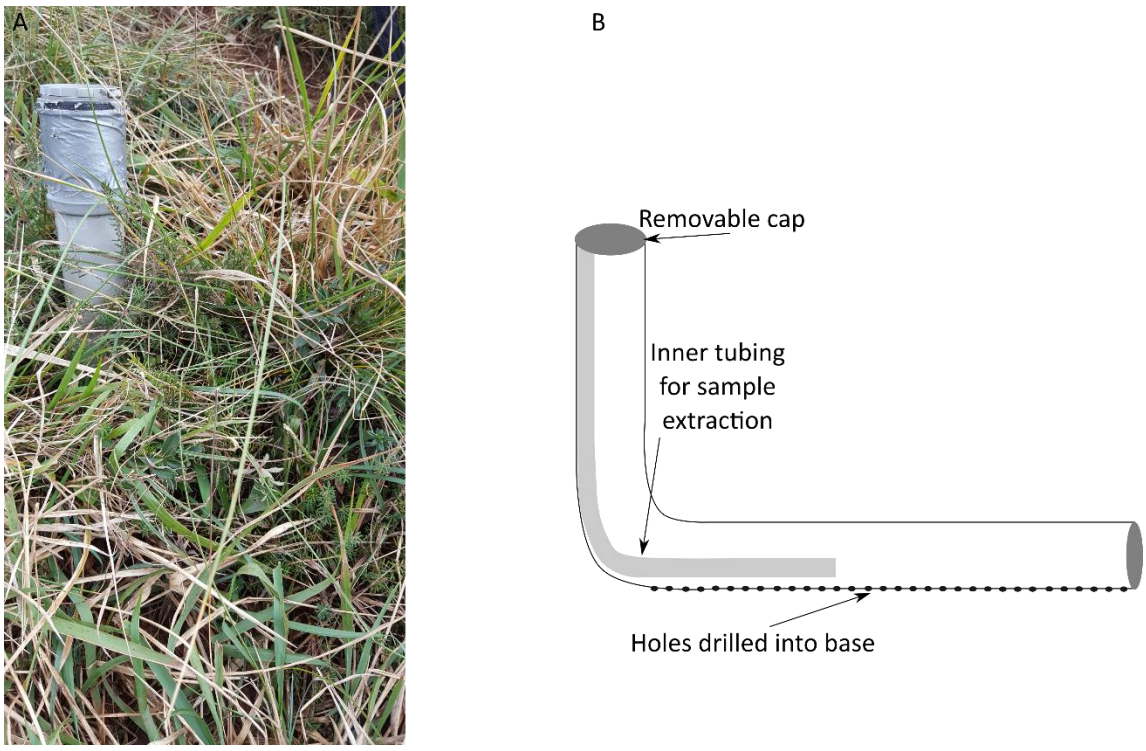

Figure 3.10: Soil sampling device. A: Image of soil sampling device above ground. B: Schematic of the soil sampling device.

3.5.4 Internal cave monitoring

3.5.4.1 Cave air

Temperature has been continuously logged at 30-minute intervals by a Tinytag Plus 2 Dual Channel Temperature/Relative Humidity TGP-4500 logger. Cave temperatures have been logged since Apr-10 with additional loggers placed within Cueva de las Perlas in Feb-15 (see figure 3.4 for locations).

Carbon dioxide has been measured within the cave since Feb-15 using a Vaisala GMP221 probe attached to an MI70 indicator (section 3.5.2). Continuous logging has been undertaken at hourly intervals with spot measurements taken during visits by the PI. Two Vaisala indicators were used and these were switched monthly. An alternative method was trialled to log CO_2 concentrations within Cueva de las Perlas using a Tinytag TGE-011-SPK CO_2 logger attached to a 12v battery via a transformer (J. Gunn, Pers. Comm,

2016). The Tinytag CO_2 logger has an accuracy of <± (50ppm +3% of the measured value). However, due to technical complications, the data from the Tinytag was not comparable to that of the Vaisala and has therefore been excluded from the analysis herein.

Cave air samples of 20ml were injected into evacuated 12ml exetainers on a monthly basis and during visits by the PI. Samples were then later analysed for carbon isotope composition at the Life Sciences Mass Spectrometry Facility within CEH Lancaster through IRMS (section 3.6).

3.5.4.2 Cave water

Cave water collection set-up

Water was collected from four different water types within the cave: pools, bulk water collections, instantaneous drips and ephemeral drips (figure 3.4 shows the locations). Samples from the pool waters were only collected on visits from four pool locations within the cave. Ephemeral drips represent samples of water collected over a maximum 24-hour period during visits by the PI. These drips have an ephemeral nature and therefore collection was only possible when the sites were actively dripping. Three drip sites (P1, P2 and P3) in the monitoring chamber were used to investigate drip rates and water chemistry. Bulk collectors were set up on these stalagmites by attaching a funnel and tubing to the top of the stalagmite. A jerry can was connected to the tubing and acted as the bulk water collection vessel. Samples for chemical analyses and spot measurements of temperature, electrical conductivity and pH were taken from these bulk waters on a monthly basis by a member of the Matienzo caving community. During visits by the PI or by the Matienzo Caving Community, bottles were placed within the funnels underneath the three drip sites. These water samples were collected within 24-hr and therefore represent 'instantaneous' collections.

Speleothem drip rates

Speleothem drip rates were measured using three Stalagmate acoustic drip loggers (Mattey and Collister, 2008) which were set to log at 10-minute intervals. Loggers were placed on three selected stalagmites (P1, P2 and P3, figure 3.4) in the monitoring chamber in an effort to understand contemporary hydrological routing through the karst in response to external climatic parameters. Initial logging began in Mar-14 with further

loggers placed in the cave in Feb-15. Stalagmate factory settings record 0.15ml drops at a maximum drip rate of 5 drops per second.

Drip water electrical conductivity

Drip water electrical conductivity, pressure and temperature measurements were logged continuously at 10-minute intervals between Jun-15 to Sep-17 using a CTD diver positioned at the P2 drip site. Measurements for electrical conductivity were recorded as specific conductance at 25^{o}C with an accuracy of ±1% of the reading. The CTD diver pressure measurements are accurate to ±0.5cmH_2O and temperature to ±0.1°C. The CTD diver was set-up using the housing system described in Smith *et al.* (2015) and shown in figure 3.11. The probe relies on a drip-in drip-out syphon system to ensure continuous water movement within the housing. Calibrations were undertaken before and after deployment to ensure any drift in analytical readings could be accounted for.

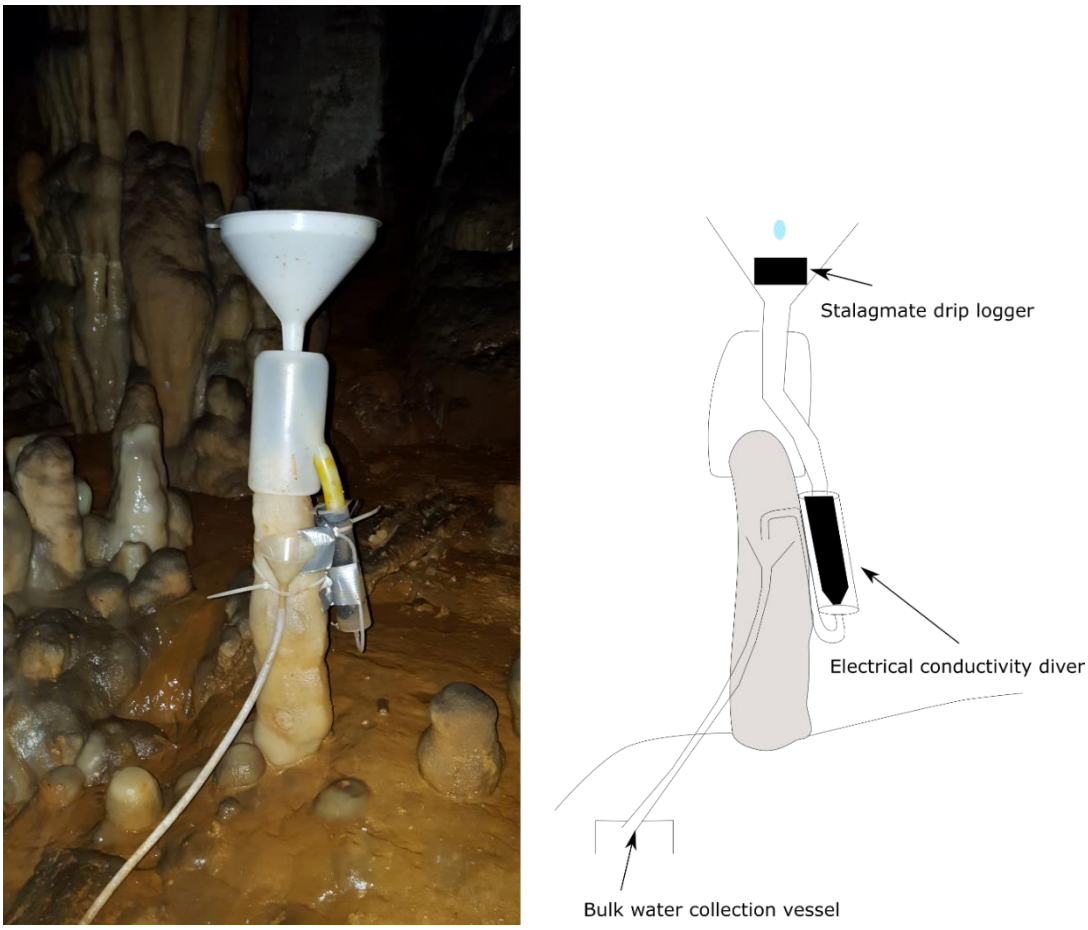

Figure 3.11: Diver set-up image and schematic diagram.

Monthly water measurements

Samples were taken from the bulk water vessels by a member of the Matienzo Caving Community each month between Feb-15 to Sep-18. Temperature, pH and electrical conductivity were measured monthly from the bulk water using a Hanna probe HI 98129. The probe is accurate to 0.1°C, 0.05 pH and ±80µS/cm for electrical conductivity. During visits by the PI bulk waters, instantaneous waters (collected over maximum period of 24hours), pool waters and ephemeral waters were measured for electrical conductivity, pH and temperature using a WTW multi 340i. A Tetracon 325 probe was used to measure electrical conductivity and a Sentix 41 probe to measure pH. The probes have an accuracy of 0.5°C, 0.1µS/cm and 0.01 for pH. In addition, where possible, water sample alkalinity was measured during fieldwork using a Hach alkalinity test kit with an accuracy of 0.1mg/l.

Water sampling

Bulk and instantaneous drip waters were sampled monthly whilst pool waters and ephemeral drips were only sampled during fieldwork visits when there was sufficient water available. Samples for isotopic analysis were placed in 2ml glass vials with a plastic septa screw cap. Samples for cations and anions were placed in 60ml Nalgene bottles. Collection vessels were filled to prevent isotopic exchange between water and any air within the bottle. For DIC sampling 175µl of orthophosphoric acid was added to 12ml exetainers and each one was evacuated to remove atmospheric gases following the methodology of Waldron *et al.* (2007) and Webb *et al.* (2016). Water samples were injected into the exetainer using a syringe and the reaction between the sample water and phosphoric acid liberated DIC as CO_2 gas into the exetainer headspace for later isotopic analysis. Sample volumes were typically 4ml which were sufficient to produce a CO_2 volume for accurate isotopic analysis by IRMS (section 3.6.3.4).

Calcite plates

Since 2010, modern calcite has been collected by placing glass plates underneath actively dripping stalactites (figure 3.12). Some calcite plates were left to precipitate calcite for over a year, whilst others, in particular those from the 2016-2017 season, were monitored and used to understand seasonal calcite precipitation (further detail in section 5.5). The curved surface of the plates reflects the curvature of the stalagmites

and avoids water-pooling on the plate surface. Plates were delicately removed and left to dry within the cave for a few hours. Calcite was sampled from the plates and used for stable isotope analyses described in section 3.6.4.2.

Figure 3.12: Images of calcite plates in situ.

3.6 Laboratory work

Modern samples collected from Matienzo were transported to Lancaster University for chemical analysis. The following section describes the laboratory methodologies for the analyses undertaken on the air samples (carbon isotope analysis), soil samples (carbon isotope analysis), cave and rain water samples (cations, anions and stable isotope analyses). Analyses of modern carbonate was undertaken at Lancaster University. Speleothem U-series dating, and stable isotope analyses were undertaken at the NERC Isotope Geosciences Laboratory (NIGL) and trace element analysis at Royal Holloway Earth Sciences LA-ICP-MS laboratory, these methods are also described below.

3.6.1 Air

3.6.1.1 Determination of the carbon isotope composition of air

Carbon isotope analyses of external, soil and cave air were undertaken at the NERC Life Sciences Mass Spectrometry Facility, CEH Lancaster. $\delta^{13}C$ values of CO_2 were measured using an Isoprime Tracegas Preconcentrator coupled to an Isoprime Isotope ratio mass spectrometer. Between 100 to 600µl of headspace air was introduced into the injection port of the Preconcentrator whereupon water was removed using a drying agent (magnesium perchlorate) and CO_2 was cryogenically focussed before entering into the IRMS via an open split. The isotope ratio of the CO_2 is compared to known reference gas pulses. Prior to each analytical batch, the instrument was calibrated, and blanks were run. A duplicate after every fourth sample was run during each analysis. Precision was equal to or better than ±0.1‰. During each run, quality control NIST reference standards of known isotopic composition (RM8562 Palaeomarine origin and RM8564 Modern biomass origin) were used within the calibration. All $\delta^{13}C$ values are expressed relative to the international standard Pee Dee Belemnite.

3.6.2 Soil

3.6.2.1 Determination of the organic carbon isotope composition of soil

Soil samples from above the cave site were collected for carbon isotope analysis of the organic component. Prior to $\delta^{13}C$ analysis, soil samples were dried and then washed with

10% HCl to remove any inorganic carbonate. The solution was left overnight and washed with deionised water multiple times until the sample was neutralised. During this stage the soils were split into two batches, one batch was centrifuged, and one batch was filtered. Samples were then dried and stored prior to analysis. Soil samples were analysed on an Elementar Vario Micro Cube Elemental Analyser linked to a VisION mass spectrometer at Lancaster University. 3.3mg of soil was weighed out into tin boats and these were placed in the autosampler. Sample analysis was undertaken using a catalytic combustion temperature of 950°C. The samples fall into the furnace and O_2 is added on top to combust the sample, the liberated CO_2 was then analysed for carbon isotope composition, known standards were run alongside the unknown samples and these were cornflour (-11.26‰), and a high C standard (-26.27‰). The cornflour standard was an in-house standard traceable to IAEA CH6. The high C standard was from Elemental Microanalysis and is traceable to IAEA CH6. Internal precision based on calibration and reference materials was better than 0.11‰. Sample replicates were also run to ensure sample precision.

3.6.3 Cave and rain water

3.6.3.1 Cations

Cation analysis was undertaken using inductively coupled plasma optical emission spectrometry (ICP-OES). Prior to analysis, samples were acidified to 0.1M using an ultra-pure (Primar grade) HNO_3. Cations (Ca, Mg, K, Na and Sr) were measured using a Thermo Scientific iCAP 600 series at Lancaster University. Standard solutions were made using 1000ppm elemental standards which were diluted to the predicted cave water concentration range shown in table 3.1. Standards were used to create a five-point calibration curve from which the trace element concentrations in the unknown samples were derived (table 3.1). During each run a check standard made to 1000ppb for all elements was run every 10 samples to ensure machine stability. Limits of detection (LOD) were calculated by using three times the standard deviation of the blanks run alongside each sample batch.

Table 3.1: Cation standard information. Calibration standard ranges and limits of detection for each of the elements analysed using ICP-OES.

Element	**Calibration standard range (ppb)**	**LOD (ppb)**
Ca	0 - 80000	88
K	0 - 25000	90
Mg	0 - 25000	30
Na	0 - 25000	214
Si	0 - 1000	9
Sr	0 - 1000	1

3.6.3.2 Anions

Water samples were analysed for sulphate (SO_4^{2-}), chloride (Cl) and nitrate (NO_3) using Dionex Ion Chromatography at Lancaster University. The samples were run alongside two Spex Certiprep water standards, one undiluted (WR1) and one diluted by two times the original Spex Certiprep standard (WR2). Chromeleon software was used for data processing. Standard deviations and LODs are shown in table 3.2.

Table 3.2: Anion standard information. Standard deviation for reference materials and limits of detection based on blanks for different elements during anion analysis calculated from blank samples run throughout each analysis.

Analyte	**Stdev**	**LOD (ppb)**
Cl	0.43	117
SO_4	0.41	287
NO_3	0.5	14

3.6.3.3 Oxygen and deuterium isotope analyses

Samples collected prior to Oct-16 were analysed for $\delta^{18}O$ using an equilibration method using an IsoPrime100 mass spectrometer attached to an IsoPrime Multiflow inlet. Samples of 200µl were heated to 40°C and left to equilibrate with an equilibration CO_2 gas. The gas in the headspace was then analysed for $^{18}O/^{16}O$ ratios and results were

calibrated to VSMOW using laboratory standards of -15‰ (LEC LIGHT) and -1.5‰ (LEC HEAVY). In order to check for drift within an analysis run, a separate internal standard (TAP) was run before, within and after the run and if necessary, drift corrections were applied. Precisions for this method are shown in table 3.3. From Oct-16 oxygen isotopes in waters were analysed by direct EA injection via a liquid autosampler (see method below).

Table 3.3: Standard deviations for different standards used in the equilibration method.

Standard	**Std value (‰)**	**Maximum standard deviation**	**Average standard deviation**	**Number of runs**
LEC Light	-15	0.21	0.14	11
LEC Heavy	-1.5	0.21	0.11	11
TAP	-6.22	0.45	0.31	11

Samples for deuterium and oxygen isotope analyses (from Oct-16) were analysed in the Lancaster stable isotope facility using an Elementar Pyrocube elemental analyser coupled with an Isoprime 100 mass spectrometer, following the method of Wynn *et al.* (2015). For the deuterium analyses, 0.3µl of sample was injected and passed over a chromium metal catalyst at a combustion temperature of 1080°C. For oxygen isotope analyses, 0.4µl of sample was injected and passed over glassy carbon chips at a combustion temperature of 1450°C. Both oxygen and deuterium isotope values are reported relative to VSMOW based upon calibration to external standards. Standard values and precisions are shown in table 3.4.

To measure for machine drift within a run, an internal standard was used and if required a drift correction was applied to the unknown samples. Unknown sample waters were analysed in triplicate to determine accurate replication.

Table 3.4: Standard values and precisions for oxygen and deuterium stable isotope analyses. The total number of runs for oxygen analyses was ten and the total number of runs for deuterium analyses was 15. The fourth column shows the number of runs where the standard was used.

Standard	**Std value**	**Maximum standard deviation**	**Average standard deviation**	**Number of runs**
Light (O)	-33.57	0.28	0.16	10
Med (O)	-12.34	0.34	0.18	7
Heavy (O)	-0.41	0.28	0.21	7
LEC TAP (O)	-6.22	0.43	0.27	10
VSMOW2 (O)	0	0.10	0.09	3
Zero water (H)	11.26	0.80	0.35	11
GISP (H)	-189.5	0.33	0.33	1
Low water (H)	-269.07	0.73	0.42	12
LEC TAP (H)	-40.28	0.67	1.29	15
VSMOW2 (H)	0	0.35	0.20	2

3.6.3.4 Determination of the carbon isotope composition of cave water

Analysis of carbon isotope composition from the gas evolved from the reaction between 4ml of cave water and 175µl of orthophosphoric acid was undertaken in the Lancaster University stable isotope facility. Carbon isotope values were measured using a multiflow prep line interfaced to an Isoprime 100 isotope ratio mass spectrometer in continuous flow mode. The CO_2 was analysed against international standards LSVEC (-46.6‰), NBS-18 (-5.01‰) and CO-1 (2.49‰). Samples were standardised based on calibration to international reference materials and results are given relative to VPDB. Standard precision was better than 0.10‰.

3.6.4 Carbonates

3.6.4.1 Uranium-series dating

Carbonate samples for uranium-series dating were drilled across calcite growth layers using a hand drill with a diamond encrusted drill bit. This method of drilling aimed to produce between 100-200mg of carbonate per sample.

Chemistry

Chemical preparation of samples for uranium-series dating was undertaken at NIGL (BGS) and followed the protocol summarised in the supplementary material of Prouty *et al.* (2016) and Smith (2014). Carbonate powders (~100-150mg) were weighed out and dissolved in 8M HNO_3. After dissolution, samples were centrifuged in order to separate the dissolved carbonate from the insoluble detrital silicate fraction. The silicate fraction was dissolved in a solution of 11M $HClO_4$: 29M HF: 16M HNO_3 (1:2:8) using 50µl of HF per estimated mg of material, evaporated to dryness, re-dissolved in 8 M HNO_3, and added back to the respective carbonate fractions. To reduce the risk of sample contamination during the chemical preparation procedure, all evaporation steps took place in a closed Evapoclean device. Samples were spiked with a ^{229}Th-^{236}U tracer and left to equilibrate overnight and evaporated to dryness. Samples underwent two overnight oxidation steps in 2 ml 16M HNO_3 and ~ 0.2 ml 30% H_2O_2 (hydrogen peroxide), each followed by evaporation to dryness. Following this, samples were dissolved in 8 ml 1M HCl, and a high-purity iron chloride solution was added. Fe, U and Th were co-precipitated through the addition of ammonia. Samples were then centrifuged and washed in Milli-Q water three times to isolate the precipitate and remove any potential contaminants from the sample matrix.

After re-dissolution in 8M HNO_3, samples were placed on 0.6ml ion exchange columns containing Eichrom anion exchange resin (AG-1 x8). The columns were washed with additional 8M HNO_3 to remove residual matrix elements and iron, after which Th and U were eluted in 8M HCl and 0.2M HCl respectively. Th fractions were dried down, dissolved in 8M HNO_3, passed through the ion exchange columns a second time to ensure complete removal of iron, and filtered through a 0.22 µm PTFE membrane to remove any resin particles. The U and Th fractions were dried and oxidised twice using 2ml 16M HNO_3 and 0.2ml 30% H_2O_2 to remove any residual organic impurities and were finally

dissolved in 1ml 0.1M HCl and 0.035M HF. All samples were filtered through syringe filters with a 0.22 µm PTFE membrane prior to mass spectrometry in order to remove any particulate matter from the solution, which may have been derived from the sample preparation process.

Analysis

Isotope ratio measurements were made using a Thermo Neptune Plus multi-collector ICP-MS at NIGL, BGS. Samples were introduced into the system through a Cetac Aridus II desolvating nebulizer. Measurements for U and Th were undertaken separately with U measurements made using normal Ni-sample and X-skimmer cones and Th measurements made using JET-sample and X-skimmer cones. ^{234}U and ^{230}Th were measured on an axial secondary electron multiplier whereas Faraday cups with 10^{11} Ω resistors were used to measure the other isotopes (^{233}U, ^{235}U, ^{236}U, ^{238}U, ^{229}Th and ^{232}Th) (Prouty *et al.,* 2016).

Hydride formation and down mass tailing were monitored at the beginning of each analytical session based on measurements at mass 237 and 239 using CRM 112a certified reference solution, and the resulting corrections were applied to all sample and standard data during off-line data processing. The contribution of U and Th from the sample introduction system was corrected for by using ^{234}U-^{235}U-^{236}U-^{238}U or ^{229}Th-^{230}Th-^{232}Th axial SEM measurements on clean acid with the same composition of that added to the samples. Background ^{234}U-^{235}U-^{236}U-^{238}U or ^{229}Th-^{230}Th-^{232}Th were measured prior to each sample and standard and were subtracted during off-line data processing. A sample-standard bracketing approach was used to account for SEM/Faraday gain and exponential mass fractionation. U fractions were measured in groups of five bracketed by a pair of measurements on CRM 112a solution, the $^{234}U/^{235}U$ ratio of which was used to derive SEM/Faraday gain, and CRM 112a with added IRMM 3636 reference material, the $^{233}U/^{236}U$ ratio of which was used to monitor mass fractionation. Th fractions were measured in groups of 10, bracketed by clusters of five measurements of an in-house Th reference solution which was calibrated against CRM 112a for Th (Smith, 2014; Prouty *et al.,* 2016) to derive correction factors which encompass both mass fractionation and, where appropriate, SEM/Faraday gain for $^{230}Th/^{229}Th$, $^{232}Th/^{229}Th$ and $^{230}Th/^{232}Th$ ratios.

Data reduction

In-house Excel spreadsheets were used to process raw data generated from mass spectrometry. Corrections for hydride formation, down-mass tailing and blank corrections (on-peak zeroes) were applied to raw ion beam intensities from the samples. These ion beam intensities were then used to calculate isotope ratios which were then corrected for SEM/Faraday gain and mass fractionation. These ratios were then used to calculate mean and standard errors for the following isotope ratios: $^{236}U/^{235}U$; $^{234}U/^{235}U$; $^{229}Th/^{230}Th$ and $^{230}Th/^{232}Th$. U and Th blanks were monitored for each sample batch and were on the order of 20 pg for ^{238}U, 2.5 pg for ^{232}Th and 1.5 fg for ^{230}Th. Blanks were negligible compared to the U-Th concentrations of the samples for all isotopes except ^{230}Th, of which the samples contained on average 50 fg. To address this, a blank correction was applied to all samples, based on subtracting the measured average ^{230}Th intensity of a set of unspiked Th blanks from the ^{230}Th signal of the samples.

U and Th concentration (ppm), U and Th activity ratios, $^{230}Th/^{234}U$ ages and uncertainties were calculated using and in-house Matlab Excel add-in. A correction for initial detrital ^{230}Th was applied to all samples assuming a detritus isotope composition of $(^{232}Th/^{238}U) = 1.2$, $(^{230}Th/^{238}U) = 1$ and $(^{234}U/^{238}U) = 1$, with ± 50% 2σ uncertainties on each activity ratio. An additional uncertainty component of 0.1 % for U isotope ratios and 0.2 % for Th isotope ratios was propagated on all activity ratios and ages to account for external reproducibility.

3.6.4.2 Determination of the oxygen and carbon isotope compositions of carbonate

Samples for low-resolution isotope analysis were drilled across calcite growth layers in speleothems using a hand drill whilst samples for high-resolution isotope analysis were drilled using an automated micromill at the NERC stable isotope facility at the British Geological Survey (NIGL). Drill bits used for sampling speleothem carbonate were diamond encrusted and generated 50-100µg of carbonate powder per sample. Speleothem carbonate powders were run for isotopic analyses (oxygen and carbon) using an IsoPrime dual inlet mass spectrometer plus Multiprep device. Samples are placed into glass vials and sealed with septa. The automated system evacuates the vials and delivers anhydrous phosphoric acid to the carbonate at 90°C. The evolved CO_2 is cryogenically cleaned and then moves into the mass spectrometer. Isotope values ($\delta^{18}O$

and $\delta^{13}C$) are reported as per mille (‰) deviations of the isotopic ratios ($^{18}O/^{16}O$ and $^{13}C/^{12}C$). Values are calculated to the VPDB scale using a within-run laboratory standard calibrated against NBS-19. A Craig correction (Craig, 1957) was also applied to account for ^{17}O. Analytical reproducibility of the standard calcite (KCM) is <0.1‰ for both $\delta^{18}O$ and $\delta^{13}C$. Samples were run alongside laboratory standard (KCM) with a standard deviation better than 0.06‰ and 0.05‰ for $\delta^{18}O$ and $\delta^{13}C$ values respectively. All values are reported relative to the VPDB international standard.

Calcite plates were sampled by gently scraping 1cm by 1cm squares of calcite off the plate using a scalpel. Rock samples were drilled using a hand drill with a diamond encrusted drill bit. Calcite plate samples and rock samples were placed into 12ml exetainers and a small amount (5-6 drops) of 103% phosphoric acid was added. Samples were left to react at 90°C for 1 hour. The CO_2 exsolved from the reaction was then analysed at the Lancaster University stable isotope facility using a multiflow prep line interfaced to an Isoprime 100 isotope ratio mass spectrometer in continuous flow mode. Samples were analysed alongside external standards (LSVEC, NBS-18 and CO1) and internal standards ($CaCO_3$) with a standard deviation better than 0.07‰ and 0.12‰ for carbon and oxygen isotope values respectively.

3.6.4.3 Laser ablation ICP-MS

Prior to analysis for trace elements the speleothem samples were cut into ~5cm by ~2.5cm pieces. The LA-ICPMS facility in the Department of Earth Sciences at Royal Holloway allows for a flexible sample size, quick analysis time and high sensitivity. The set-up uses a custom-made 193nm excimer laser-ablation system which is coupled to an Agilent 7500ce/cs quadrupole ICPMS (Müller *et al.,* 2009). Transects were pre-ablated using a scan speed of 2mm/minute, a 20Hz repetition rate and no delay. Laser data acquisition used a 10µm width by 140µm length rectangular rotating slit and samples were ablated using a scan speed of 12µm/second, a 15Hz repetition rate and a third and fourth delay time of 30 seconds. Twenty-five elements were analysed with the most useful being Mg25, Ca43, Sr88, and Ba138. Each sample was run alongside NIST610, NIST612, ATHO-G and MACS3 external standards. Calcium was used as the internal standard and sample concentrations (ppm) were calculated based upon a stoichiometric

Ca concentration in $CaCO_3$ of 40% mol mol^{-1} (Jochum *et al.,* 2011). The raw data was converted using equation 3.2.

$$C^x{}_{sample} = C^r{}_{sample} \times \frac{C^x{}_{std}}{C^r{}_{std}} \times \frac{i^x{}_{sample}}{i^r{}_{sample}} \times \frac{i^r{}_{std}}{i^x{}_{std}} \quad \text{Eq. 3.2}$$

In equation 3.2 $C^r{}_{sample}$ is the concentration of the reference element (Ca) in the sample, this value was 400,000. $C^x{}_{std}$ represents the isotopic correction in ppm due to the abundance of the isotope in the total standard, for the analysis herein NIST612 and MACS3 were employed as the standards. $C^r{}_{std}$ is the concentration of the reference element (Ca) in the external standard in ppm. $I^x{}_{sample}$ is the intensity of the unknown element in the sample. $I^r{}_{sample}$ is the intensity of the reference element in the sample, taken as an average. $I^r{}_{std}$ is the intensity of the reference element in the standard, taken as an average. $I^x{}_{std}$ is the intensity of the unknown element in the standard.

3.6.4.4 Trace element analysis of rock carbonates by ICP-OES

Rock samples were taken from the cave roof, cave entrance and outside the cave. Around 4mg of rock powder per sample was drilled out using a como hand drill. The powder was acidified by adding 1ml of 1M HNO_3 and left to react overnight. Samples were made up to 0.1M HNO3 by adding 10ml of deionised water and 7ml of the solution was pipetted into a sample tube for analysis by ICP-OES. Rock powders were analysed in solution for calcium (Ca), potassium (K), Magnesium (Mg), Sodium (Na) and Strontium (Sr) and standard deviations and limits of detection for the solutions are shown in table 3.5.

Table 3.5: Standard deviations and limits of detection for ICP-OES analysis of rock powders in solution.

Element	**Standard deviation (ppb)**	**LOD (ppb)**
Ca	8	25
K	15	44
Mg	2	7
Na	19	56
Sr	0	1

Calcium concentrations measured in solution were converted to rock Ca concentrations (ppm) using a stochastic distribution of 400,000ppm (mg/kg) in calcite. The other rock trace elements were then calculated to this stochastic Ca concentration (Jochum *et al.,* 2011).

3.6.5 Summary

This section has provided a description of the laboratory methods used within this thesis. A summary of the laboratory methods is shown in table 3.6.

Table 3.6. Summary of laboratory methods.

Sample type		Analysis	Method	Location
Air		$\delta^{13}C$	Isoprime Tracegas Preconcentrator coupled to an Isoprime Isotope ratio mass spectrometer	NERC Life Sciences Mass Spectrometry Facility, CEH Lancaster
Soil		$\delta^{13}C$	An Isoprime100 IRMS coupled with a VARIO PYROcube Elemental Analyser	Lancaster Environment Centre
Water		Cations	ICP-OES	Lancaster Environment Centre
		Anions	Dionex Ion Chromoatography	Lancaster Environment Centre
		$\delta^{18}O$	Prior to Oct-16: Isoprime100 IRMS coupled with an Isoprime Multiflow inlet Post Oct-16: Isoprime100 IRMS coupled with a VARIO PYROcube Elemental Analyser	Lancaster Environment Centre
		δD	Isoprime100 IRMS coupled with a VARIO PYROcube Elemental Analyser	Lancaster Environment Centre
		$\delta^{13}C$	Isoprime100 IRMS coupled with an Isoprime Multiflow inlet	Lancaster Environment Centre
Carbonates	Speleothem material	U-series	Thermo Neptune Plus multi-collector ICP-MS	NERC Isotope Geosciences Laboratories
		$\delta^{18}O$ and $\delta^{13}C$	Isoprime dual inlet mass spectrometer plus Multiprep Device	NERC Isotope Geosciences Laboratories
		Trace elements	Laser-ablation ICP-MS	Royal Holloway Earth Sciences department
	Modern calcite	$\delta^{18}O$ and $\delta^{13}C$	Isoprime100 IRMS coupled with an Isoprime Multiflow inlet	Lancaster Environment Centre
	Bedrock	$\delta^{18}O$ and $\delta^{13}C$	Isoprime100 IRMS coupled with an Isoprime Multiflow inlet	Lancaster Environment Centre
		Trace elements	ICP-OES	Lancaster Environment Centre

4. Cave monitoring: Cave air characteristics

4.1 Introduction

Cave monitoring can significantly improve understanding of the cave environment and ensure palaeoclimate records are accurately interpreted. Monitoring studies of cave air temperature (section 2.4.3.5) and cave carbon dynamics (section 2.4.3.6) have identified cave ventilation patterns and their significant influence on speleothem growth (Spötl *et al.,* 2005; James *et al.,* 2015) and stable oxygen isotope composition (Johnson *et al.,* 2006). This chapter will present data characterising the cave air composition and air flow dynamics, with a view to explore the influence this may have on speleothem calcite chemistry. Temperature records from the Matienzo region (external climate), the soil (soil climate) and Cueva de las Perlas (cave climate) will presented to determine the relationship between air density and ventilation dynamics within Cueva de las Perlas. Records of external and internal pressure will be presented as they have been shown to influence cave carbon dynamics (Smith *et al.,* 2015). Data assessing the carbon dynamics from the atmospheric air, soil and Cueva de las Perlas will also be presented in this chapter in order to further investigate the patterns of ventilation and identify the driving processes. Although the behaviour of the cave in the contemporary situation is no guarantee of the behaviour of the cave in the past, it does in part aid understanding of the broader cave characteristics and the influence these may have on speleothem environmental records.

4.2 Temperature

4.2.1 External atmosphere

External temperatures have been recorded close to Cueva de las Perlas (43°19’00.1”N 003°35’40.1”W, 293m a.s.l) between Apr-10 to Jan-18. Data were recorded using a Tinytag (Apr-10 to Apr-16) and a baro-diver (Apr-15 to Jan-18). Data collected for this study have been used to extend the record of Smith (2014). Logging was paused between Mar-13 and Apr-14 within the Matienzo valley, representing the monitoring gap between research projects.

Seasonal cycles are evident within the external temperatures (figure 4.1). The hottest months are typically July, August and September (with average monthly temperatures exceeding 19.5°C) and the coldest months are typically December, January and February (with average monthly temperatures below 8.5°C).

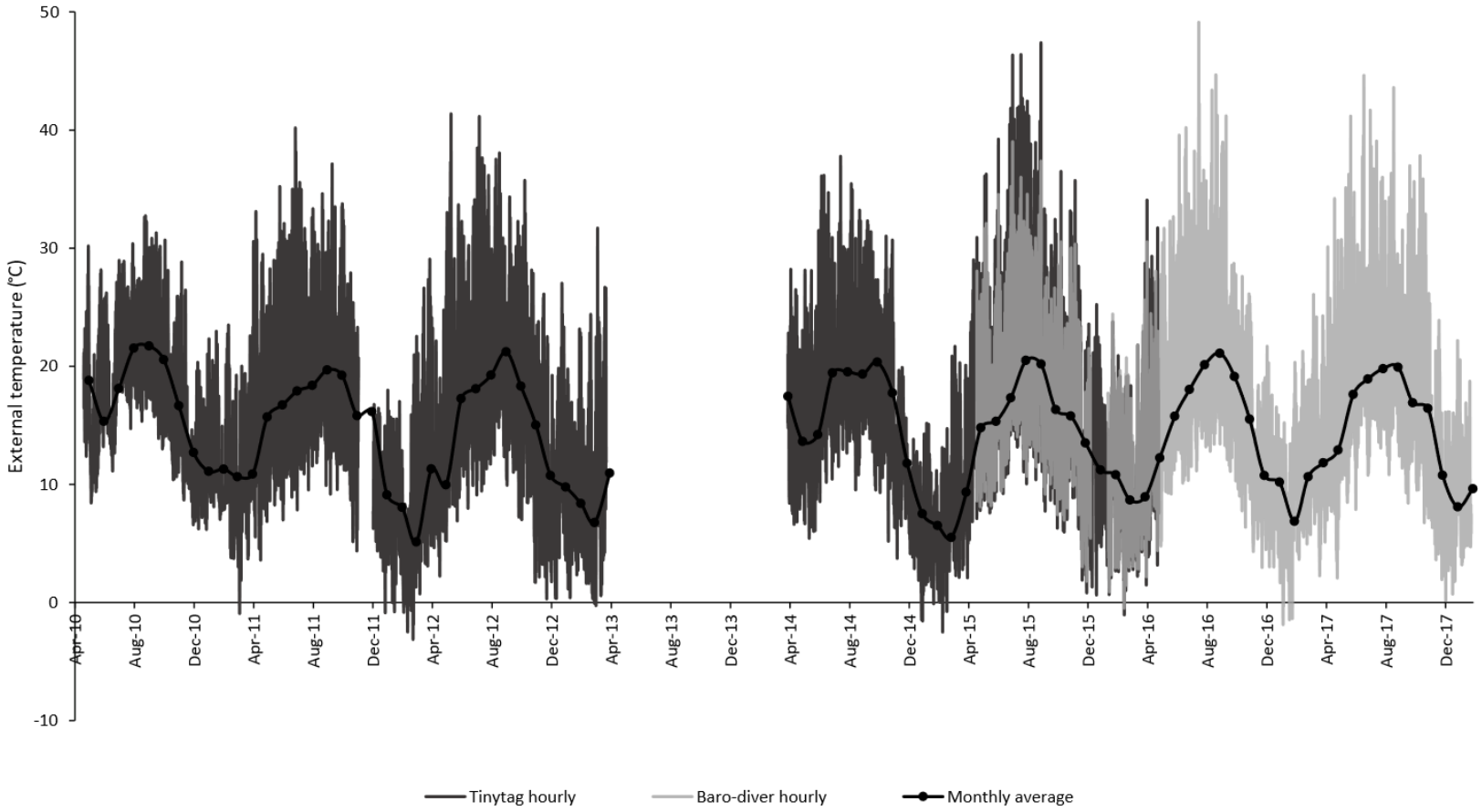

Figure 4.1: External hourly and monthly average temperatures. The external loggers were placed on the same slope as Cueva de las Perlas located at 43°19'00.1"N 003°35'40.1"W, 293m a.s.l.

4.2.2 Soil

4.2.2.1 Temperature

Soil temperatures play a major role in determining productivity and microbial activity and therefore soil monitoring was undertaken in the shallow soils on the same slope as the entrance to Cueva de las Perlas.

Soil temperatures vary seasonally year-round (figure 4.2). The hottest soil temperatures occur in summer (Jul-15 and Aug-17) characterised by temperatures in excess of 20.5°C. The coldest soil temperatures occur in winter (Dec-15, Jan-16 and Mar-17) and average monthly temperatures fall below 8.5°C. The gap between Apr-16 to Oct-16 was related to a logger malfunction. Variability within soil temperatures is reduced between Oct-16 and Jan-18 when compared to Apr-15 to Apr-16. This is most likely a reflection of the logger being buried deeper in the soil profile in Oct-16.

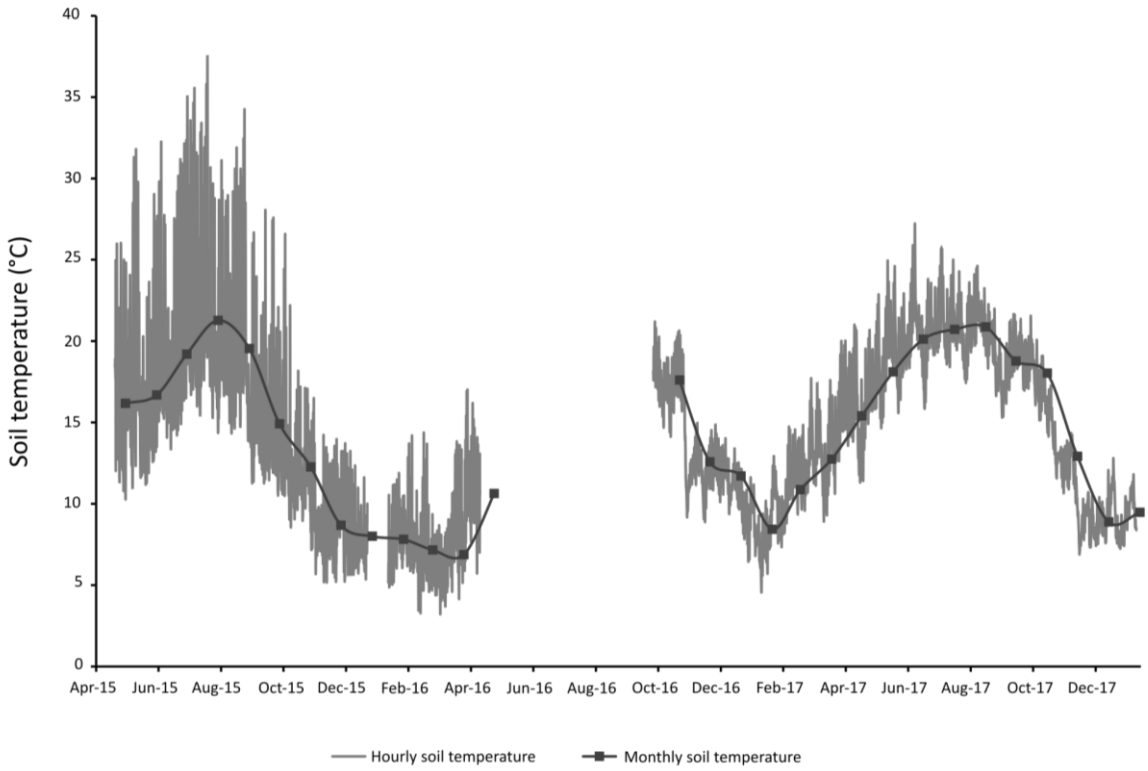

Figure 4.2: Hourly averaged soil temperature. The soil sampling device was placed on the same slope as Cueva de las Perlas located at 43°19'0.63''N, 3°35'28.32''W, 285m a.s.l.

4.2.2.2 Soil lag times

The shallow depth of the soils should mean that the lag time between peak atmospheric temperature and peak soil temperature is relatively short. Hourly soil temperature data were compared to hourly external air temperature to calculate daily lag times between maximum external and maximum soil temperatures (table 4.1). A total of 514 days were analysed with an average lag time between external and soil temperature of 2.27 hours with 50% of analysed days (257 days) with a lag time of an hour or less.

The record from 2017 is the most representative of the soil system. In Oct-16, the logger was reburied deeper which is reflected in the soil temperatures by reduced variability (figure 4.2). Additionally, the data collected in 2017 represent the longest undisturbed logging period between Oct-16 and Jan-18. This undisturbed period of logging allowed vegetation to develop within the soil and therefore is most likely to accurately portray the natural soil regime.

Table 4.1: Lag times between maximum external temperatures and maximum soil temperatures.

Year	**Average lag time (hours)**	**Lag time for 50% of days (hours)**	**Lag time for 75% of days (hours)**	**Number of available days**
2015	3.89	6	7	88
2016	2.50	1	2	127
2017	1.56	1	2	280
2018	2.15	3	4	19
All years	2.27	1	4	514

4.2.3 Cave temperature

Internal cave temperatures were recorded at three locations within the cave. These were positioned at the cave entrance (P1), in the monitoring chamber located 15m from the cave entrance (P3) and at 27.3m which marks the back of the cave (P2). Gaps within the dataset relate to delays downloading the logger or logger malfunctions.

4.2.3.1 Records of cave temperature

Cave entrance

The cave entrance temperature was collected between Apr-14 to Oct-16 (figure 4.3). In 2016, a full 12 months of data were recorded and the annual temperature of 14.05°C lies close to the external annual average temperature of 14.27°C. The coldest months occur during winter/early spring (Dec-14 = 6.73°C, Mar-16 = 3.14°C and Apr-17 = 1.24°C) whilst the warmest months occur late summer/early autumn (Oct-14 = 12.7°C, Aug-15 = 14.05°C, Sep-16 = 12.29°C). The cave entrance record exhibits a significant range in hourly temperature of 5.97°C, 10.91°C and 11.05°C for 2014 (number of months (n) = 9), 2015 (n = 12) and 2016 (n=9) respectively.

Monitoring chamber

Temperature within the monitoring chamber was recorded between Apr-10 and Jan-18 (figure 4.3). Annual cave temperatures are presented in table 4.2. Data from years when a full dataset of internal and external temperatures is available (2015, 2016 and 2017) show internal cave temperatures lie close to annual external average temperatures of 13.28°C, 13.38°C and 14.49°C for 2015, 2016 and 2017 respectively. Over the last three years annual cave temperature has increased. For example, between 2016 and 2017 the average temperature in the monitoring chamber rose by 0.81°C. However, this does not follow the external trend where temperatures exhibited minimal change between 2016 and 2017.

Table 4.2: Annual average temperatures and standard deviations from the monitoring chamber and external environment.

Year	Average annual cave temperature (°C)	Cave std dev.	Average annual external temperature (°C)	External std dev.	Number of months in average
2010	13.62	1.05	17.28	5.31	9
2011	12.99	0.93	15.10	6.09	3
2012	13.39	1.11	13.71	7.15	11
2013					
2014	13.62	1.21	15.95	6.04	10
2015	13.28	1.22	14.13	7.04	12
2016	13.68	1.27	14.26	6.36	12
2017	14.49	1.58	14.27	6.46	12

Annual temperature minima and maxima vary between years with minima occurring in winter/early Spring (Jan-Apr) and maxima occurring in late summer/early autumn (Sep-Nov). Seasonal variations in temperature are recorded within the monitoring chamber and values for 2015, 2016 and 2017 were 3.80°C, 4.35°C and 4.72°C respectively.

Cave back

A logger was set recording hourly temperature at the back of the cave between Feb-15 and Jan-18 (figure 4.3). Annual average temperatures at the cave back were 13.54°C, 13.96°C and 14.5°C in 2015, 2016 and 2017. These temperatures lie close to the external annual averages with differences <0.3°C between external annual average and cave back annual average temperatures.

Seasonal variability is apparent within the rear of the cave with variations of 2.25°C, 2.84°C and 2.53°C for 2015, 2016 and 2017 respectively. Temperature minima occur in the spring (Mar/Apr) and temperature maxima occur in late autumn (Oct/Nov).

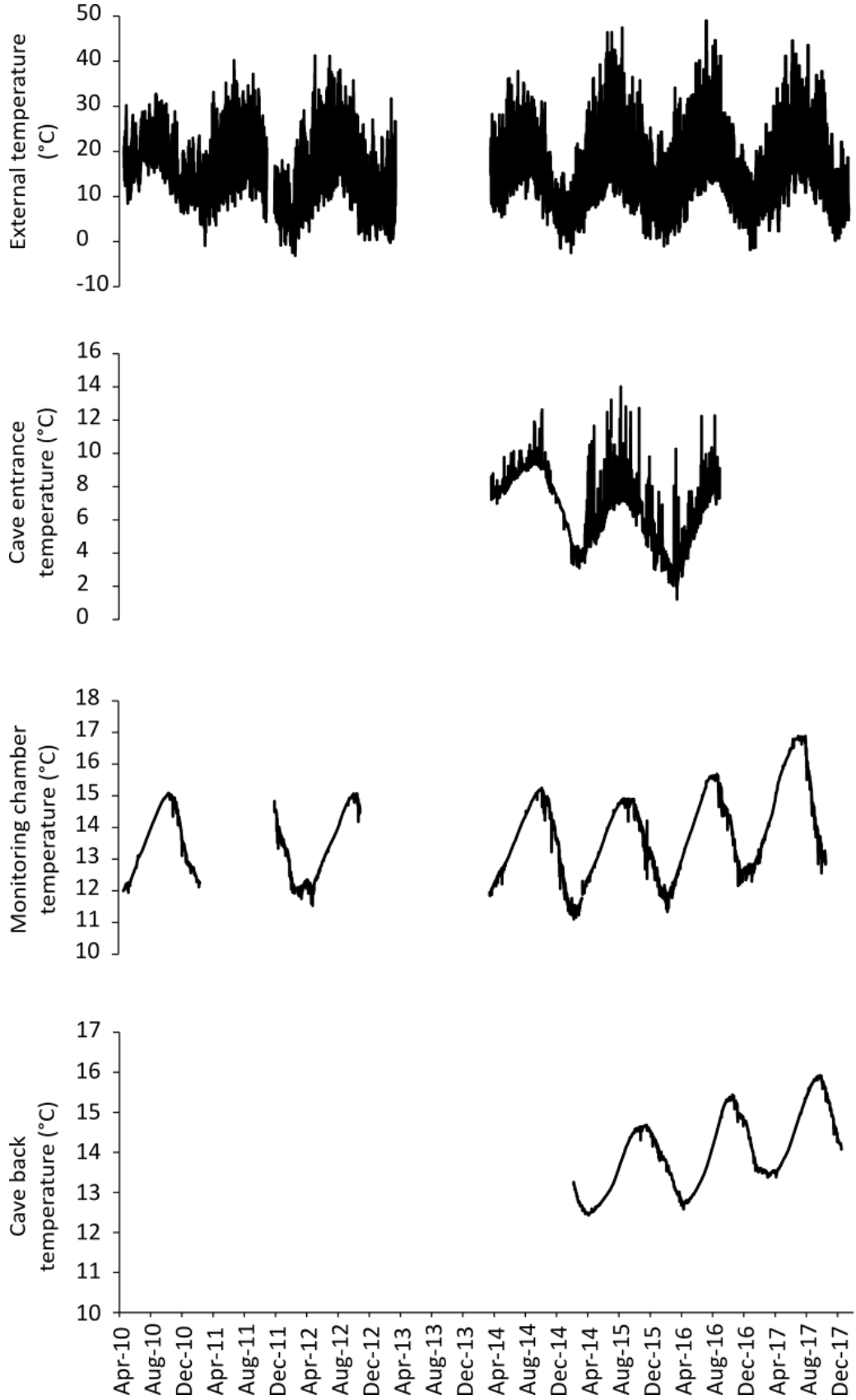

Figure 4.3: External and internal cave temperatures.

4.2.3.2 Cave temperature interpretation

Temporal variability in cave temperature

External and internal temperature dynamics drive ventilation according to air density differences. This subsequent seasonal ventilation of the cave is demonstrated through the cave temperature record which results in seasonal cave temperature cycles. Two modes of ventilation, summer and winter, are proposed to influence cave temperature and are displayed on figure 4.4.

The summer (weak) ventilation mode begins in April when external average daily temperature rises above the cave temperature. During this mode there is a continuous steady rise in cave temperature as daily external temperature is consistently higher than cave temperature. Minimal temperature variation during the summer mode is evidenced by the smooth rise in temperature. The cave is poorly ventilated during this period with an increase in air drawn down from the karst.

At the end of September, the steady rise in summer cave temperature stops and cave temperature stabilises and begins to fluctuate as a consequence of daily external temperature occasionally falling below cave internal temperature. During this period there is an offset between peak summer external temperature and peak summer cave temperature. The lag times vary but are typically >1 month. The delay may relate to the ongoing release of heat into the cave atmosphere from the surrounding bedrock, long after the external temperature has passed its peak. The manifestation of this release of latent bedrock heat is apparent in figure 4.4 expressed by the delay in peak cave temperatures relative to external air temperatures. Due to the large thermal inertia of rock, rock temperatures can control cave temperature. Heat is transferred from the atmosphere into the soil and then into the bedrock. The bedrock will then transmit the heat via conduction to the cave. Although the soil temperature signature will be transmitted to the cave, variability may be attenuated and there may be a phase lag related to depth (Fairchild and Baker, 2012).

The transmission of heat will be lagged in relation to soil temperature and studies from soil boreholes have shown heat transfer can take days or even months to propagate through the soil (Smerdon *et al.,* 2006; Fairchild and Baker, 2012). Lag times through rock are expected to be longer due to the reduced thermal diffusivity of rock relative to soil

(Fairchild and Baker, 2012). Monitoring undertaken at Eagle Cave identified a six-month offset between peak external and peak cave temperatures related to inter-annual variability transmitted through conduction. Bedrock overburden at Eagle Cave, central Spain, has been calculated as 20m and the phase lag has been estimated to represent a period of several years rather than half a year (Fairchild and Baker, 2012; Domínguez-Villar *et al.,* 2013). Due to the shallow nature of Cueva de las Perlas within the bedrock, it is proposed the phase lag between peak external and internal cave temperatures is related to prolonged transmission of heat through the karst bedrock via conduction.

The winter (strong) ventilation mode is initiated when external temperature falls below cave internal temperatures. As a consequence, cold, dense external air flows into the cave which lowers the cave temperature. This phase is characterised by a decline in cave internal temperature and an enhanced diurnal variability. The temperature in Cueva de las Perlas is variable during the winter mode over short-timescales (daily/hourly) and this is related to external temperatures crossing the internal cave temperature threshold, thereby driving an influx of cold external air into the cave. The seasonal cycle in temperature driven by density-induced ventilation has also been identified at numerous other cave sites (Spötl *et al.,* 2005; Šebela and Turk, 2011; Ravbar and Kosutnik, 2013; Smith *et al.,* 2016a; Vieten *et al.,* 2016) and will be explored further in section 4.5.

Spatial variability in cave temperature

The cave temperature records demonstrate spatial variability as expressed by differences in seasonal temperature oscillations. The logger situated towards the cave entrance records the highest degree of seasonal cave temperature variability and tracks changes in external temperature. The monitoring chamber records a reduced variability relative to the cave entrance, and temperature logging from the back of the cave shows the lowest variability. Therefore, the influence of seasonal ventilation cycles driven by density-differences between internal and external temperatures is attenuated with distance from the cave entrance. At Obir Cave, Austria, a similar pattern was identified, showing a lessened influence of the seasonal ventilation regime as cave depth increased (Spötl *et al.,* 2005).

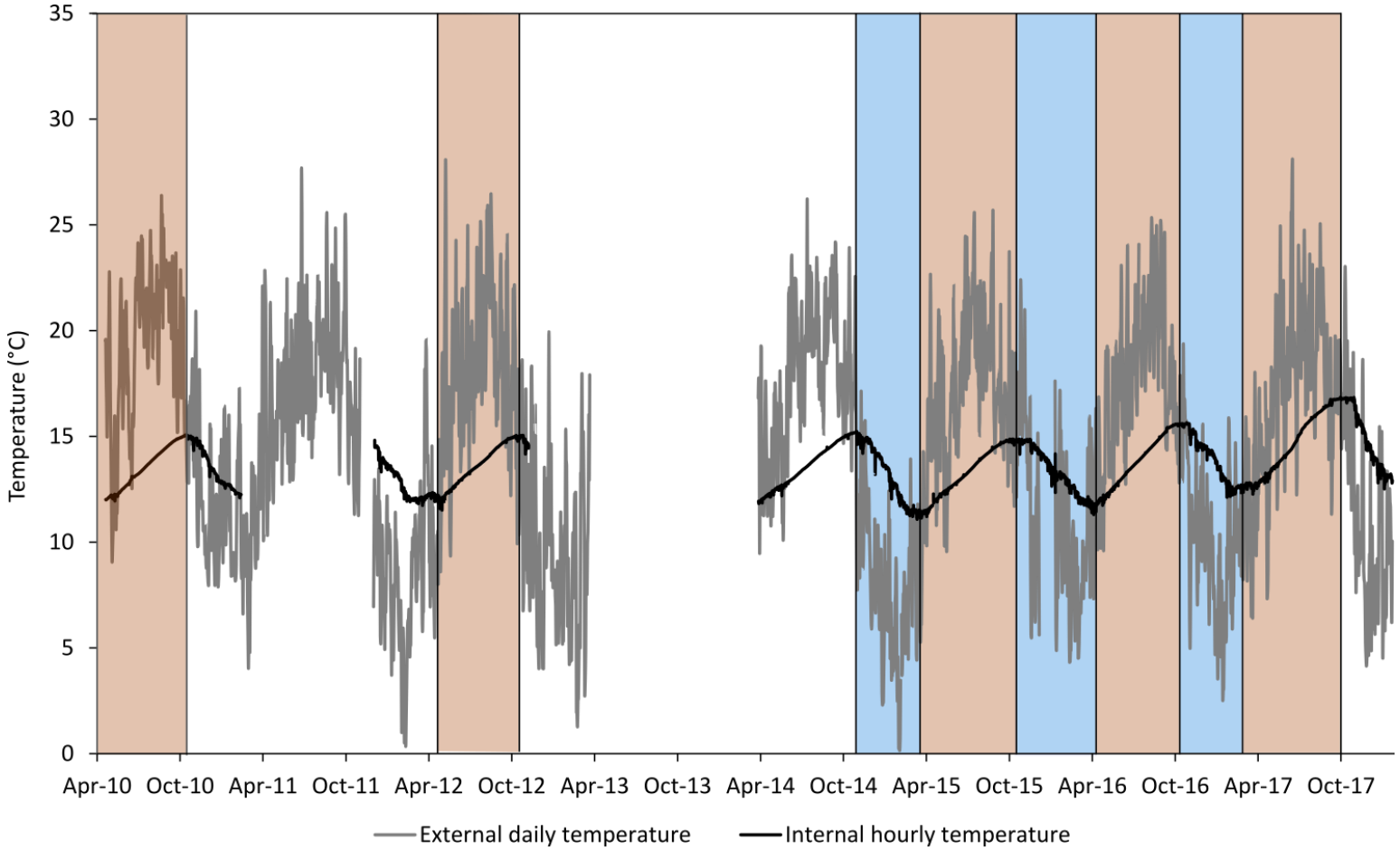

Figure 4.4: Seasonal ventilation phases in temperature. The internal hourly temperature record is from the monitoring chamber. Blue shaded periods represent winter/strong ventilation and orange shading represents summer/weak ventilation.

4.3 Pressure

4.3.1 External pressure

Pressure was measured between Apr-15 and Jan-18 (figure 4.5). Annual external pressure averages were 1003cm H_2O, 1001cm H_2O and 1004cm H_2O for 2015, 2016 and 2017. For 2015 and 2017 pressure varies by 48cm H_2O and 61cm H_2O. In 2016, pressure values exhibit a higher range of 247cm H_2O due to a large oscillation in June and July (see section 4.3.3 for a detailed description).

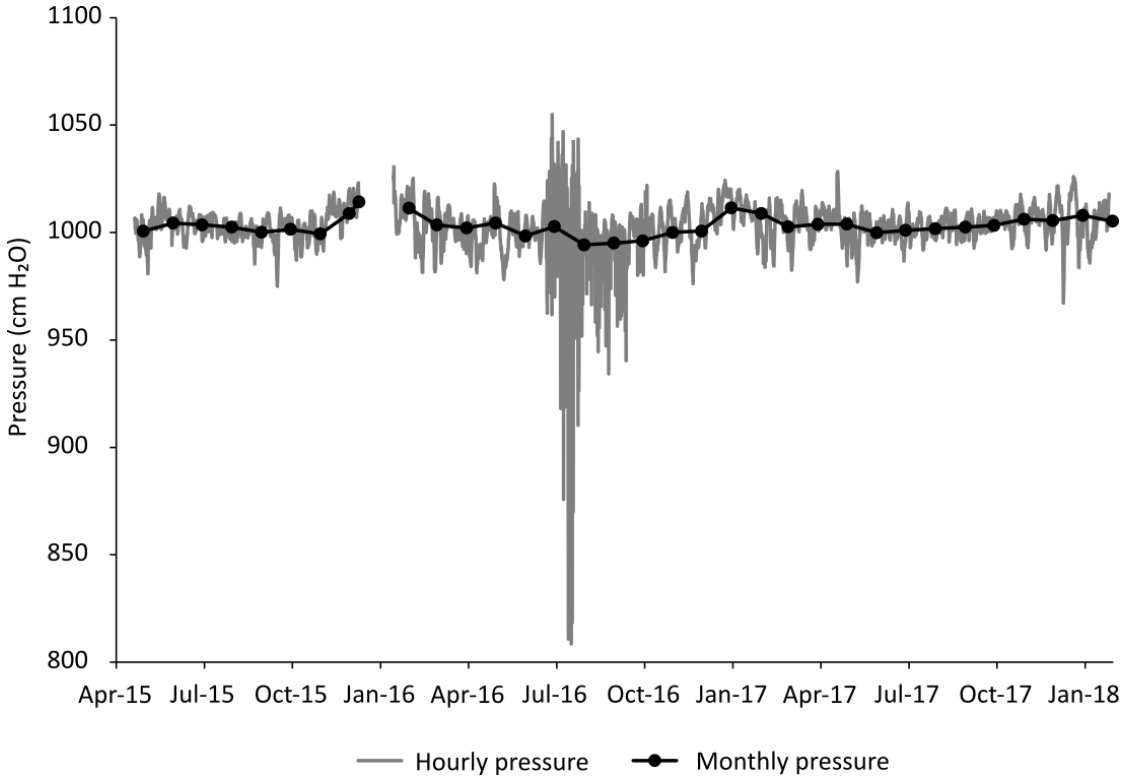

Figure 4.5: External pressure.

4.3.2 Internal pressure

Cave pressure was measured between Apr-14 and Sep-17. Average annual cave pressures were 1010cm H_2O, 1014cm H_2O, 1010cm H_2O and 1010cm H_2O for 2014, 2015, 2016 and 2017. Each year pressure exhibited a variability between 40-60cm H_2O. Values are relatively high during the summer months. The winter months are characterised by relatively lower values with the lowest values recorded in October/November prior to pressure maxima values which are recorded each year in December (2014- 2016).

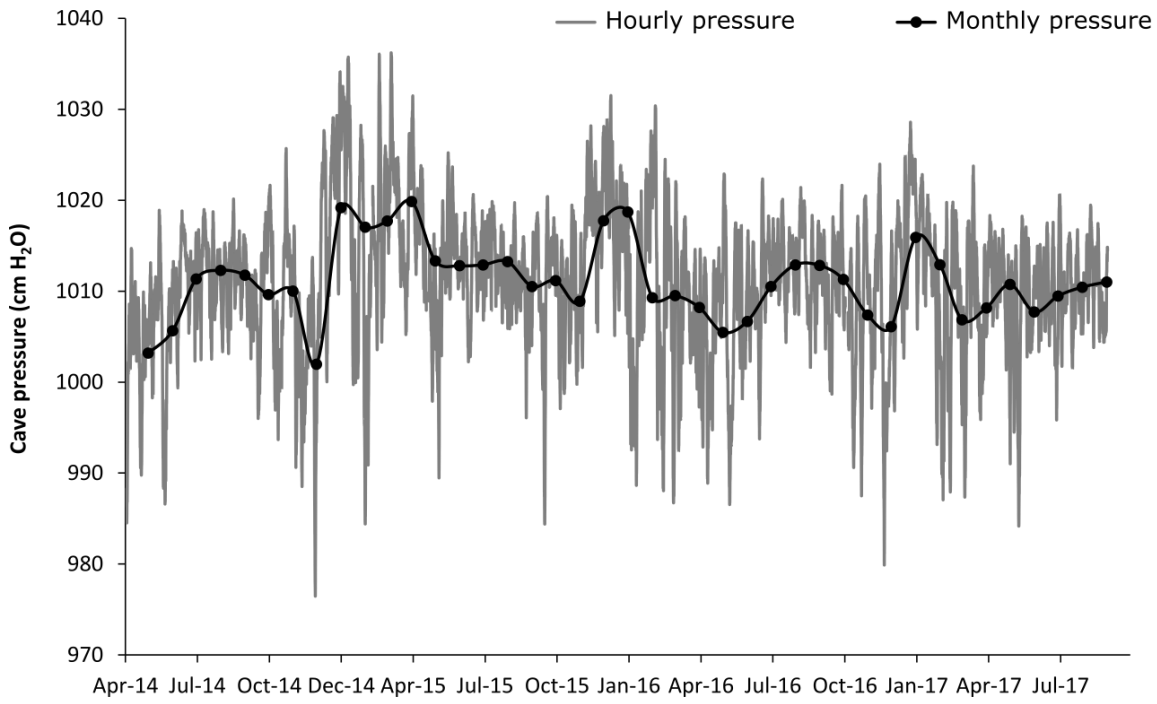

Figure 4.6: Cave pressure.

4.3.3 Pressure comparison

Internal and external hourly pressure are compared in figure 4.7 and appear to correlate throughout the majority of the monitoring period and values overlap within error. However, it is apparent that the internal and external loggers are significantly different between Jun-16 and Oct-16. Hourly internal and external pressure for the full dataset are plotted against each other (figure 4.7) and have an r^2 value of 0.35 (figure 4.7 B). However, when the data between Jun-16 and Oct-16 is removed, the r^2 value increases significantly to 0.92 (figure 4.7 C). Temperature data and field evidence indicate that during this period the hillslope was subject to fires. Therefore, external data between Jun-16 and Oct-16 will be excluded from further analysis.

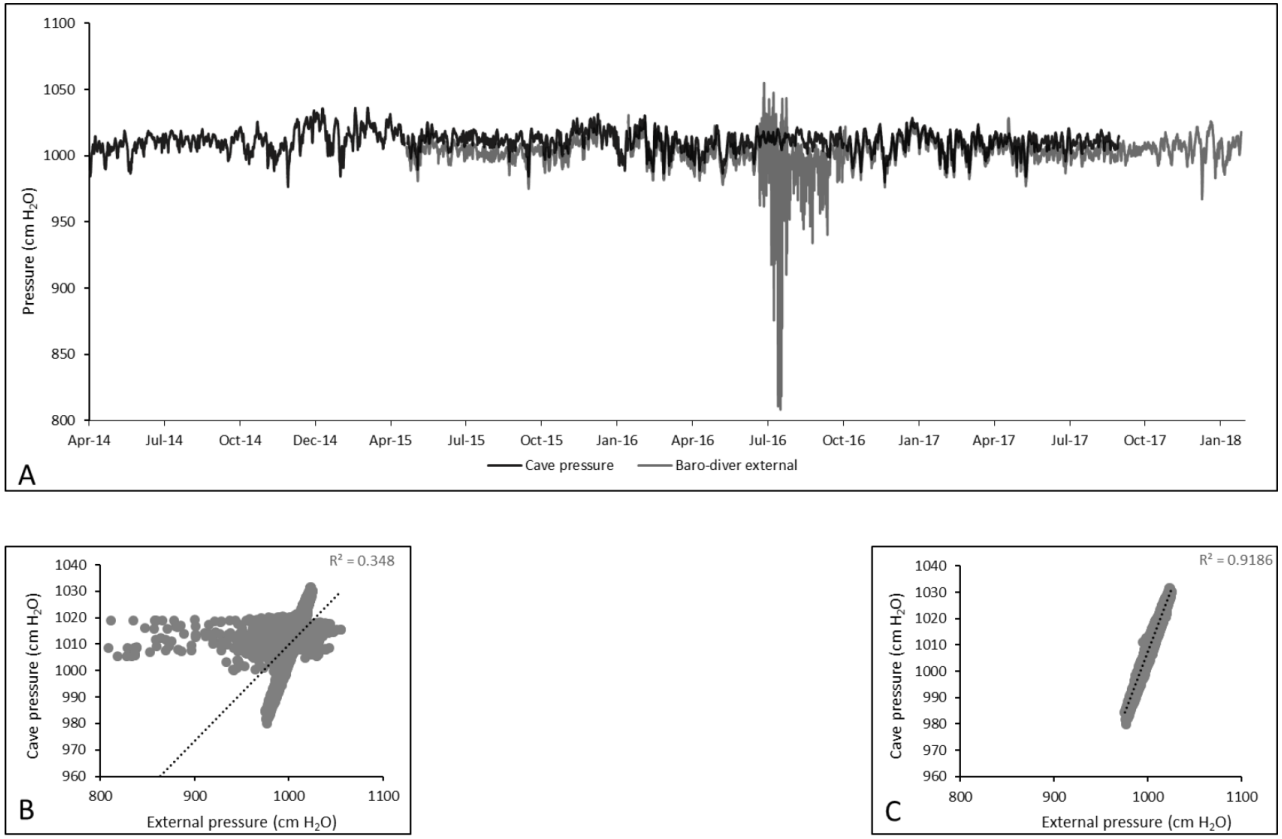

Figure 4.7: Comparison of internal and external pressure. A presents the complete records from both internal and external pressure with temperature also shown. B is a comparison between hourly internal and external values for the full dataset. C is a comparison between hourly internal and external values with the data between Jun-16 and Oct-16 removed.

The high correlation between internal and external pressure indicates that the cave is responding to changes in external pressure rapidly (figure 4.7 C). Decreases in external pressure relate to storm activity and increase the pressure gradient between the cave and external atmosphere. A case example from Jul-15 is shown in figure 4.8 and further demonstrates changes in cave pressure respond instantaneously to changes in external pressure. Due to the shallow depth of Cueva de las Perlas and the close proximity of the monitoring chamber to the cave entrance, oscillations in external pressure are transmitted rapidly into the cave system. Oscillations in cave pressure can induce air flow within a cave which can subsequently alter cave atmosphere CO_2 concentrations (Denis *et al.,* 2005; James *et al.,* 2015; Smith *et al.,* 2015). The potential influence of pressure-induced ventilation on cave carbon dynamics will be considered further in sections 4.4.3 and 4.4.4.

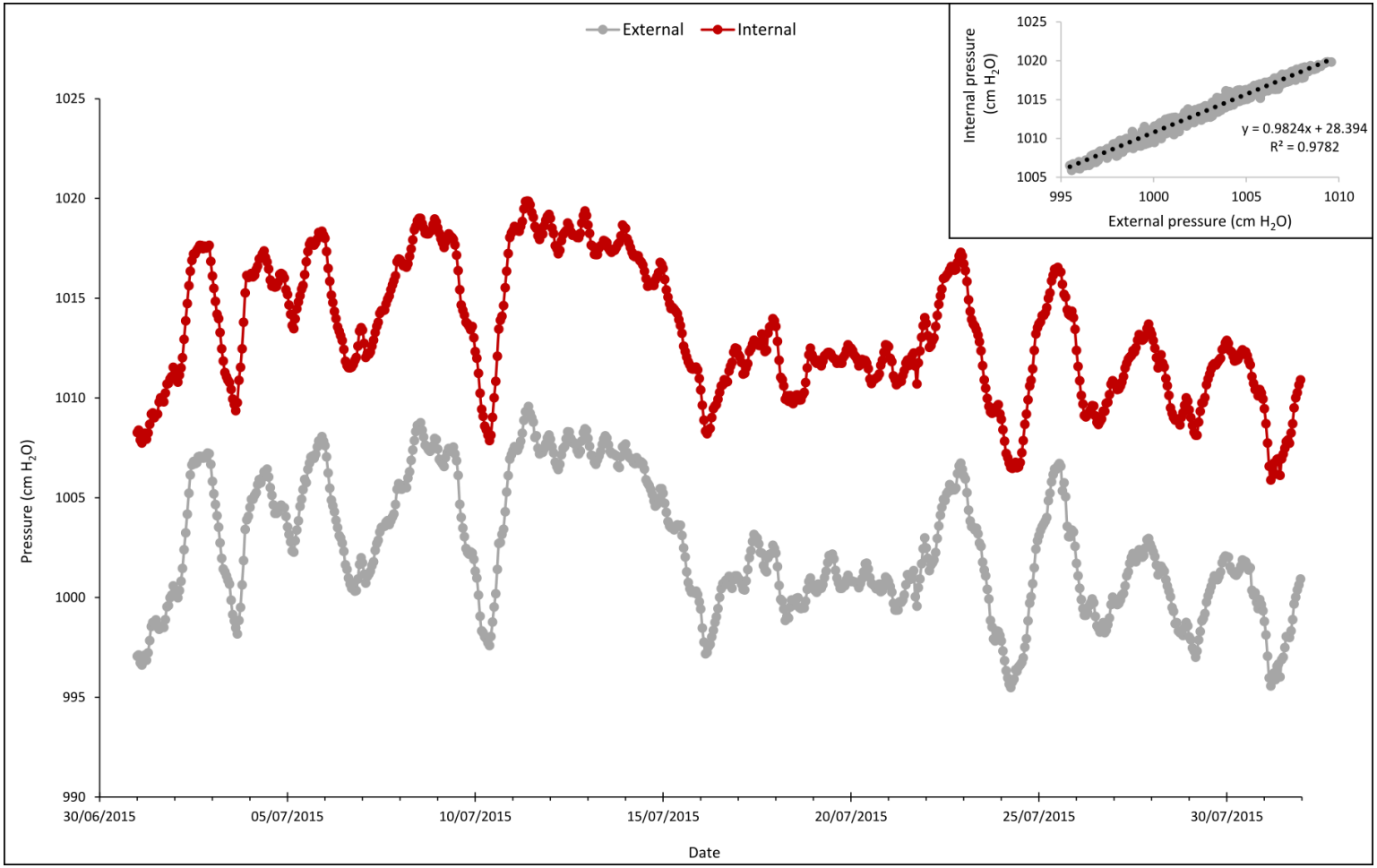

Figure 4.8: External and internal hourly pressure during Jul-15. Inset is the direct comparison of hourly external and internal pressure.

4.4 Carbon dynamics

4.4.1 External air carbon dynamics

External air CO_2 concentrations were only measured during field visits between Feb-15 and Jan-18 and results are presented in figure 4.9. Average concentrations were 375ppm and 378ppm and ranges were 10ppm and 120ppm for 2015 and 2016. Only one measurement was taken during 2017 and one during 2018 and these were 360ppm and 420ppm.

External air samples were collected between Feb-15 and Jan-18 for determination of carbon isotope composition and results are shown in figure 4.9. External air annual carbon isotope averages were -10.34‰, -10.77‰ and -10.93‰ and annual ranges were 1.9‰, 2.65‰ and 1.69‰ for 2015 (n= 15), 2016 (n= 22) and 2017 (n= 8) respectively. Carbon isotope values in external air do not demonstrate seasonal cycles.

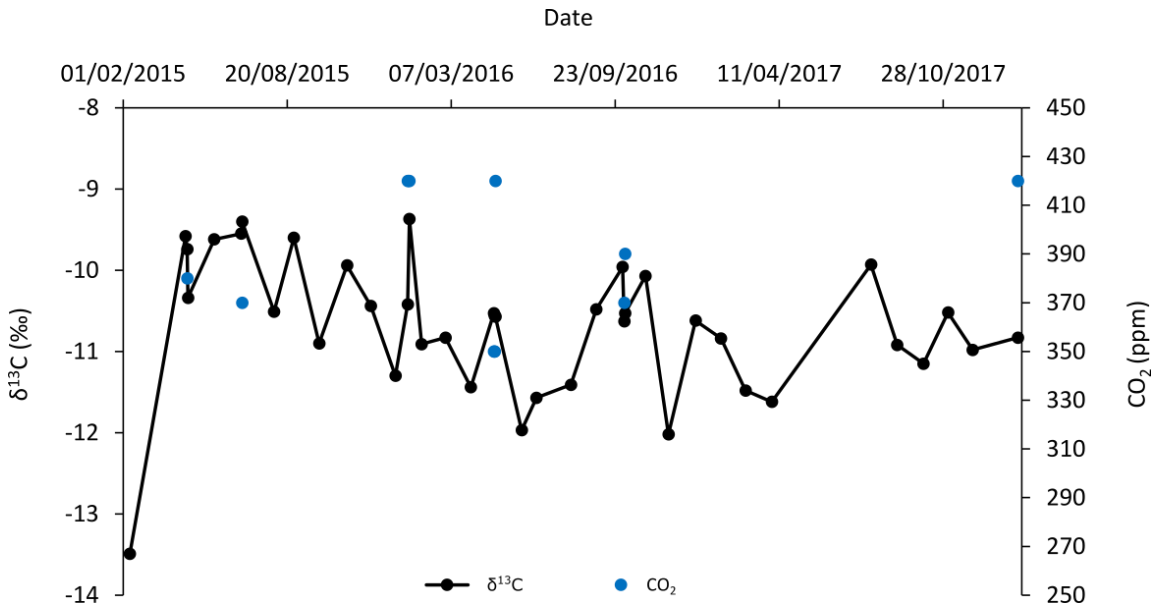

Figure 4.9: CO_2 concentrations and carbon isotope values from external air.

4.4.2 Soil carbon dynamics

4.4.2.1 Soil air carbon

Soil air samples were taken between Apr-15 and Jan-18 to determine carbon isotope composition and are compared to CO_2 spot measurements in figure 4.10. Annual

averages of soil CO_2 were 2643ppm, 2439ppm and 2375ppm for 2015, 2016 and 2017 respectively. CO_2 concentrations are higher in summer with an average of 2857ppm (2016 value) compared to the winter average of 1712ppm. Annual average soil carbon isotope compositions were -20.55‰, -21.64‰ and -21.65‰ for 2015 (number of samples (n) = 4), 2016 (n= 18) and 2017 (n= 5). Soil air carbon isotope values are isotopically more enriched in ^{13}C during winter than in summer (table 4.3).

Table 4.3: Summary of soil air carbon isotope values.

Year	Annual average $\delta^{13}C$ (‰)	Annual range $\delta^{13}C$ (‰)	Number of samples	Summer average $\delta^{13}C$ (‰)	Number of samples	Winter average $\delta^{13}C$ (‰)	Number of samples
2015	-20.55	2.24	4	-21.03	3	-19.1	1
2016	-21.63	7.5	16	-22.17	11	-20.44	5
2017	-21.65	2.79	5	-22.56	2	-21.04	3

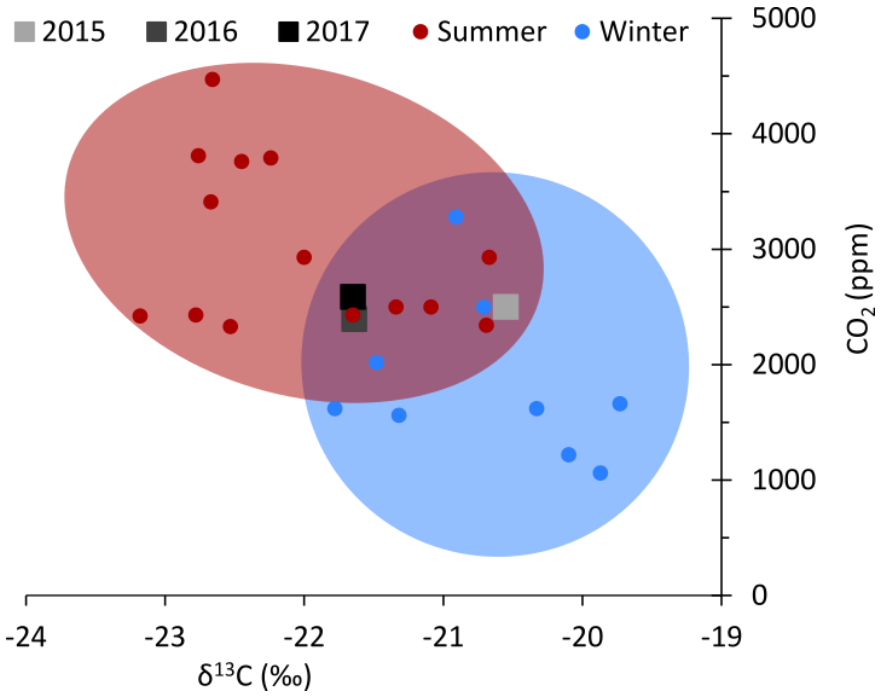

Figure 4.10: CO_2 concentrations and carbon isotope values from soil air. Values are grouped by season and annual averages are also presented.

4.4.2.2 Soil organic carbon isotope composition

Soil was sampled from four different depths in Apr-16. Two methods were used to process the samples, one batch was filtered prior to carbon isotope analysis and the other was centrifuged (section 3.6.2.1). The results from both methods are presented in table 4.4. Carbon isotope values ranged between -27.63 and -26.58‰. It must be noted that soil samples were only taken once and therefore any seasonal variation cannot be determined.

Table 4.4: Carbon isotope values from soil organic matter.

Soil depth	**$\delta^{13}C$ (‰) centrifuged samples**	**$\delta^{13}C$ (‰) filtered samples**
0	-27.74	-27.48
5	-27.63	-27.00
10	-26.97	-26.66
15	-26.58	-26.72

4.4.2.3 Soil interpretation

In order to understand the carbon dynamics within the cave, it is critical to understand the carbon dynamics of the overlying soil. Monthly CO_2 concentrations and carbon isotope measurements from the soil air samples are presented in figure 4.11 in addition to the soil temperature record (from section 4.2.2.1). Figure 4.11 demonstrates a seasonal variation in soil carbon dynamics. During the winter months (Oct-Mar) CO_2 concentrations are lower, temperatures are lower and $\delta^{13}C$ values are higher. In contrast, during the summer months (Apr-Sept), CO_2 levels rise, temperatures rise and $\delta^{13}C$ values are lower.

Section 4.4.2.1 identified seasonal variation in CO_2 concentration and $\delta^{13}C$ values and it is proposed this seasonal variability is related to variations in productivity. During the summer, productivity is higher driven by warmer temperatures. The CO_2 spot measurements and $\delta^{13}C$ values may be biased to 'good weather days' and therefore may not provide a full indication of the seasonality operating within the soil carbon system.

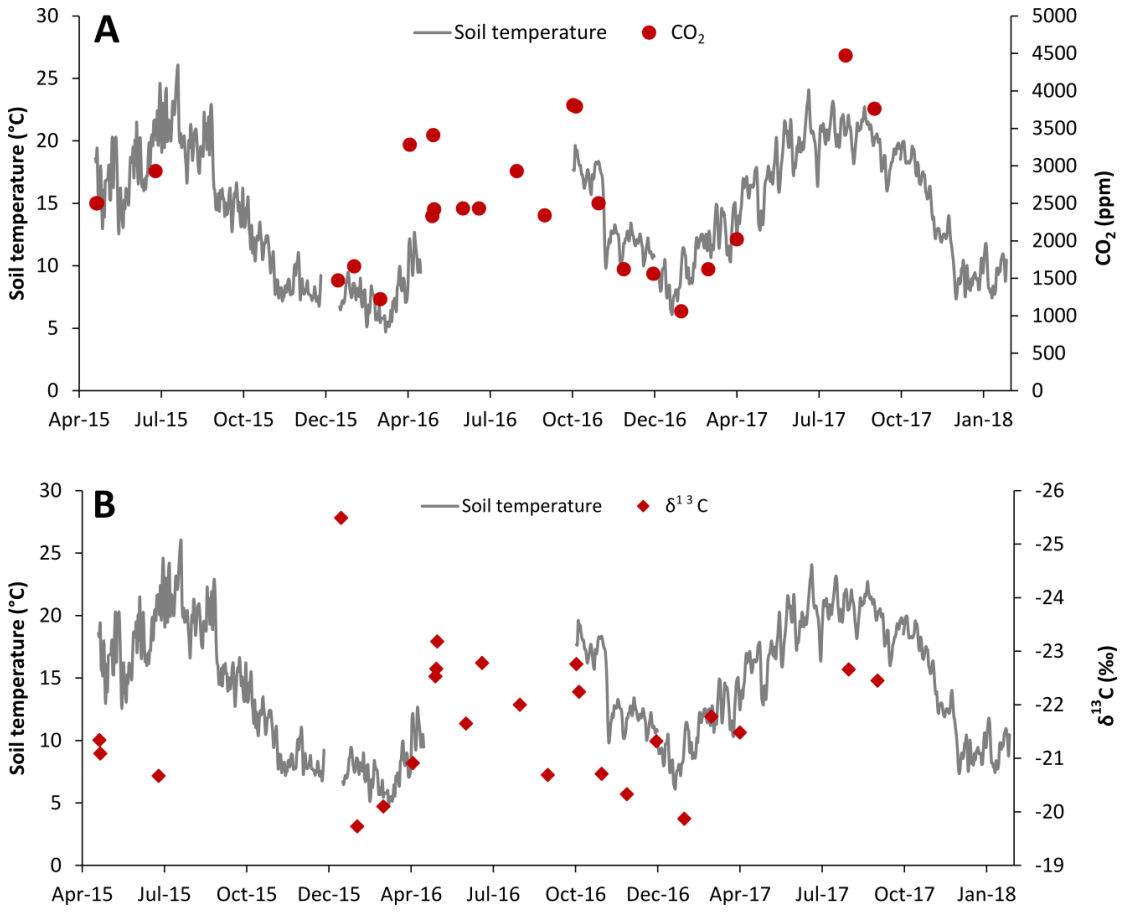

Figure 4.11: Relationships between soil carbon and temperature. A: Soil CO_2 concentration spot measurements and soil temperature. B: carbon isotope values and soil temperature, note the inverted carbon isotope value axis.

4.4.3 Cave carbon dynamics

4.4.3.1 Bedrock carbon isotope values

Rock samples were taken from inside and outside the cave entrance and from a collapsed roof section within the cave. These rock samples were dolomitic with calcite intergrown (section 3.1). The carbon isotope values from the rock samples exhibit a range of 4.69‰ between -2.44‰ and +2.25‰ (table 4.5).

Table 4.5: Carbon isotope values from rock samples.

Rock sample type	Rock sample	δ13C (‰)
Rock from cave entrance	RCE1	1.96
	RCE2	0.73
Rock from outside cave	ROC1	2.25
	ROC2	1.61
Rock from cave roof	RCR1	-2.44
	RCR2	1.57

4.4.3.2 Cave atmosphere CO_2 concentration

Carbon dioxide was monitored hourly within Cueva de las Perlas between Feb-15 and Dec-17 (figure 4.12A). The gaps within the dataset relate to battery malfunctions within the logger.

Average annual cave CO_2 concentrations were 421ppm, 425ppm and 456ppm in 2015 (number of days in average (n) = 119), 2016 (n= 190) and 2017 (n= 207) respectively. In 2015 and 2016 CO_2 values had a range of 505ppm and 590ppm. However, in 2017 the CO_2 range was almost five times greater than previous years, at 2490ppm (table 4.6).

CO_2 concentrations are shown to fluctuate daily (figure 4.12B) with an average variability of 182ppm (n=507). The daily CO_2 variability exhibits a range between 30-2430ppm.

Table 4.6: Annual and seasonal CO_2 concentrations.

Year	Annual average (ppm)	Annual range (ppm)	Summer average (ppm)	Winter average (ppm)
2015	421	505	422	418
2016	425	590	424	426
2017	456	2490	486	434

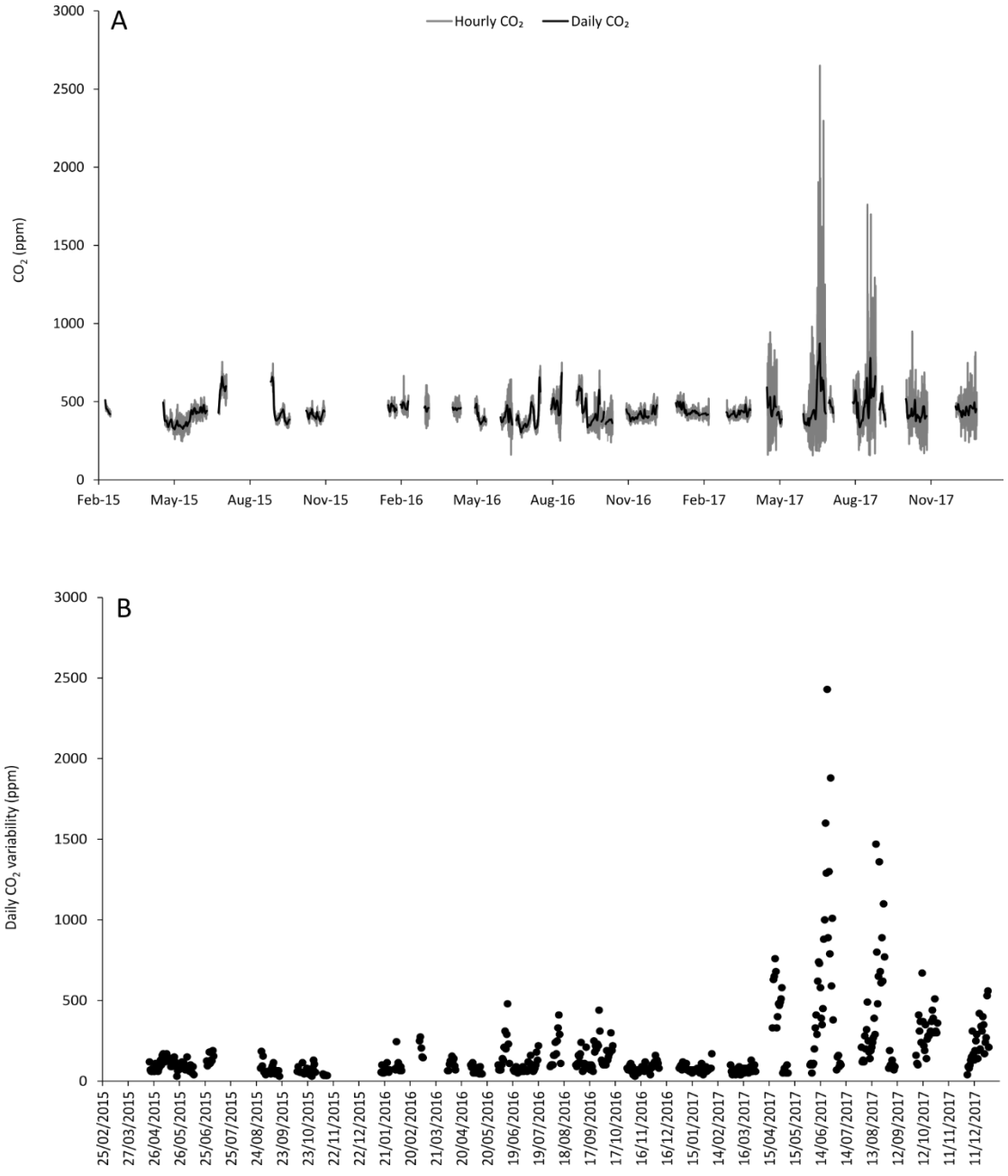

Figure 4.12: Hourly and daily cave CO_2 concentration (A) and daily variability (B).

Figure 4.12 demonstrates the variability within the CO_2 record which is apparent throughout the year. Seasonality is minimal as CO_2 concentrations fluctuate on a diurnal basis. Additionally, summer and winter CO_2 averages (except for summer 2017) both lie close to annual CO_2 averages (table 4.6).

4.4.3.3 Cave air carbon isotopes

Cave air was sampled between Feb-15 and Jan-18 and results are presented in figure 4.13. Annual averages for 2015 (n= 15) and 2016 (n= 22) were both -12.81‰ and -

12.59‰ in 2017 (n= 8). Carbon isotope values demonstrated intra-annual variability of 5.17‰, 4.35‰ and 3.06‰ in 2015, 2016 and 2017 respectively. Variability in carbon isotope values occurs throughout the year with no distinctive seasonal variation.

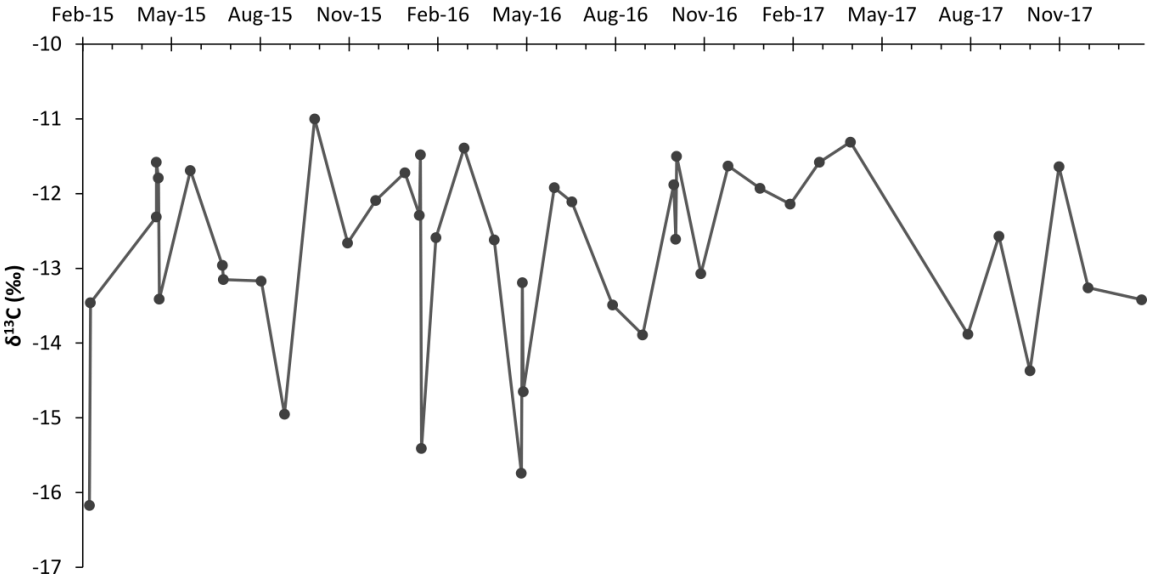

Figure 4.13: Carbon isotope composition of cave air.

4.4.3.4 Cave carbon dynamics interpretation

Carbon dioxide

Cave carbon dioxide concentrations are variable on an hourly scale throughout the year and do not show distinct seasonal variations. CO_2 concentrations are compared to internal and external hourly temperature in figure 4.14. Daily variability in CO_2 corresponds to external temperatures crossing the internal cave temperature threshold which occurs throughout the year. When external hourly temperature falls below internal hourly temperature a density-driven ventilation causes a rapid influx of CO_2-poor air into the cave. As external temperatures exhibit a large diurnal range and appear to cross internal temperatures nearly every day, this switch in ventilation causes significant daily variability in CO_2 values.

Typically, this dynamic ventilation leads to low CO_2 concentrations in the cave throughout the year. However, in Jun-17 there is a distinctive increase in CO_2 concentration within the cave. Figure 4.15 demonstrates that when external temperatures remain higher than internal temperatures for an extended period, CO_2 concentrations rise within the cave as a result of reduced ventilation. This is the primary reason for the high CO_2 values in Jun-17. However, a secondary influence of pressure will also be assessed in section 4.4.3.5.

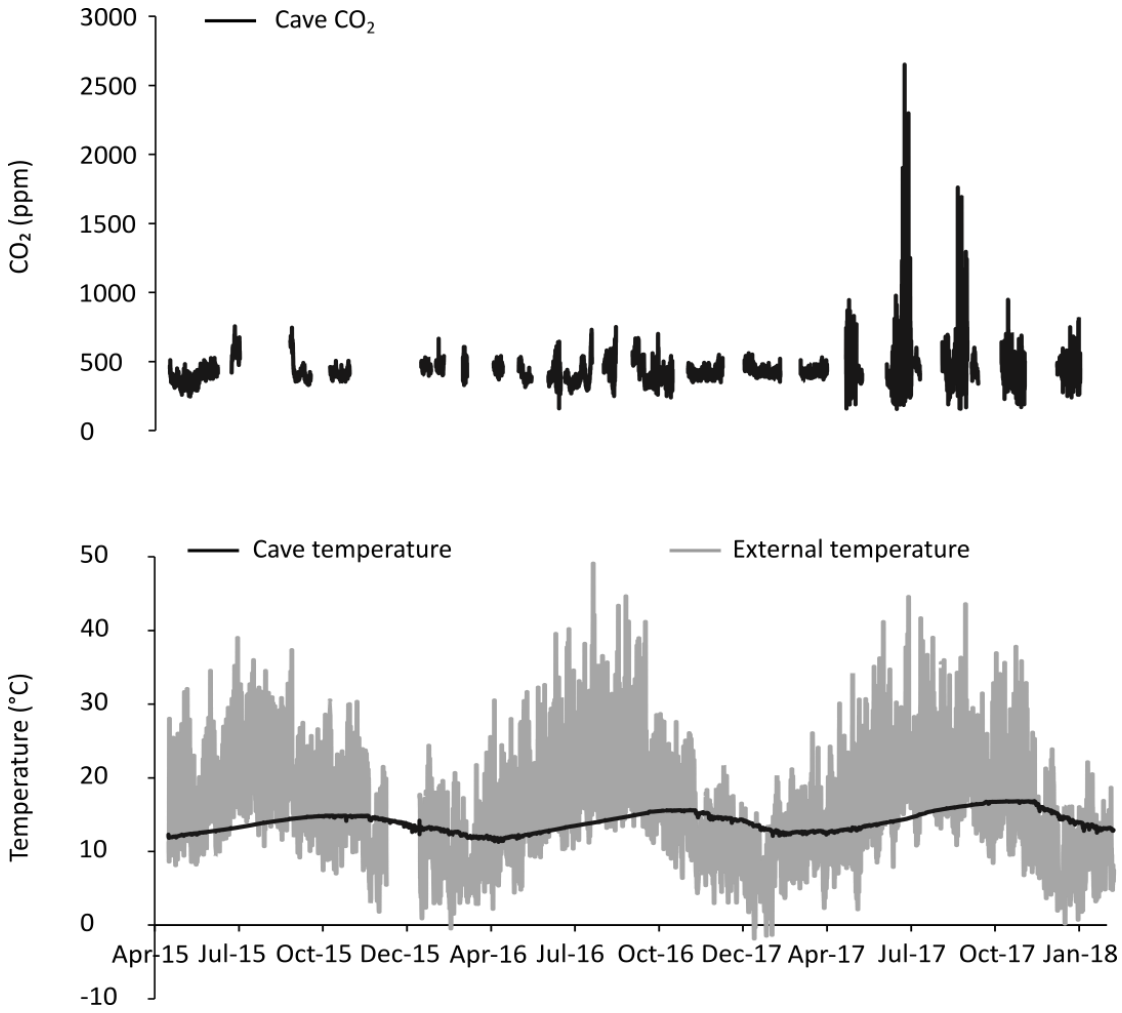

Figure 4.14: Hourly cave CO_2 concentrations and external and internal hourly air temperature.

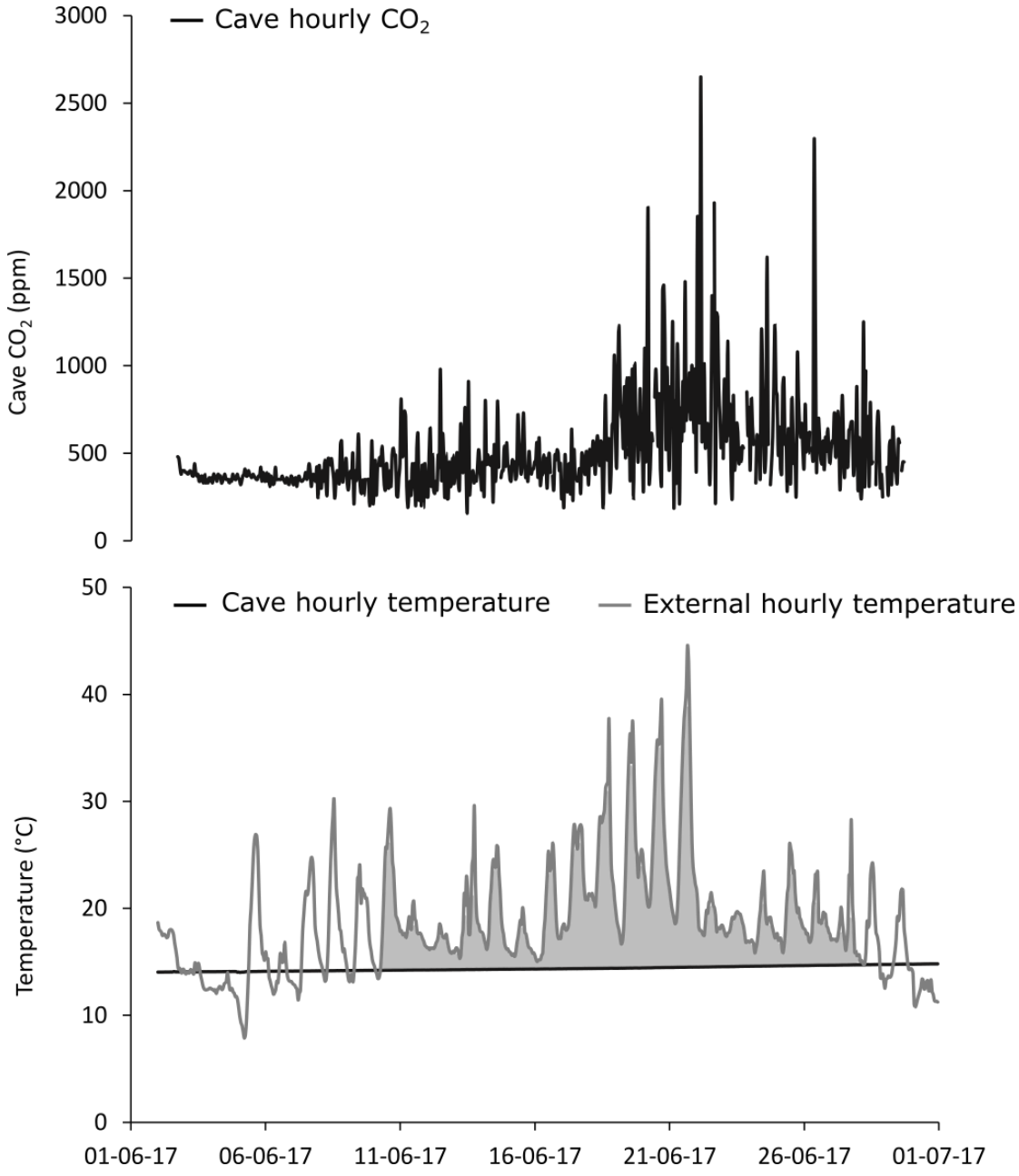

Figure 4.15: Cave hourly CO_2 and internal and external temperatures Jun-17. Shading represents a prolonged period of external temperatures exceeding internal cave temperatures.

Cyclicity in cave CO_2 concentration

Spectral analysis was undertaken on months where over 14 days of CO_2 data was collected to determine whether oscillations in CO_2 concentration are diurnal. The majority of months demonstrate a peak suggesting seven cycles per week which would suggest daily oscillations in CO_2. Interestingly, no cyclicity is evident in Jun-17 which supports section 4.4.3.4 (figure 4.15) as no cyclicity would be expected as external temperatures are consistently higher than internal cave temperatures and subsequently CO_2 rises within the cave.

A case study from Nov-16 is used herein to assess the validity of the spectral analysis. Figure 4.17A demonstrated a pronounced peak at seven cycles per week. However, when the individual data are presented alongside cave and external temperatures it is clear that the cyclicity is not persistent throughout the record (figure 4.17B). CO_2 is clearly variable on a diurnal basis and most likely a response to external temperatures crossing the internal cave temperature threshold. The degree to which this pattern is cyclical requires further analysis.

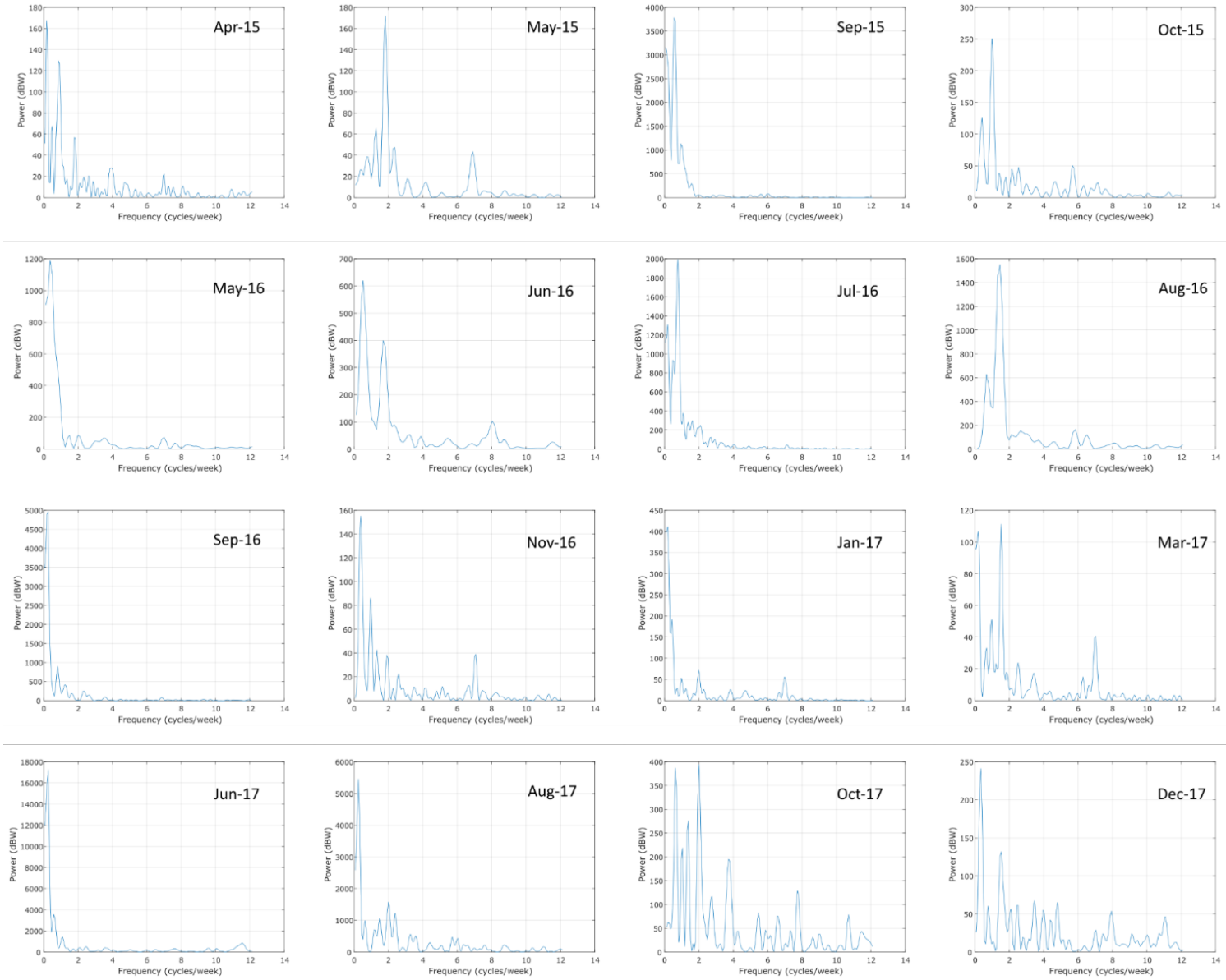

Figure 4.16: Spectral plots for monthly CO_2 data.

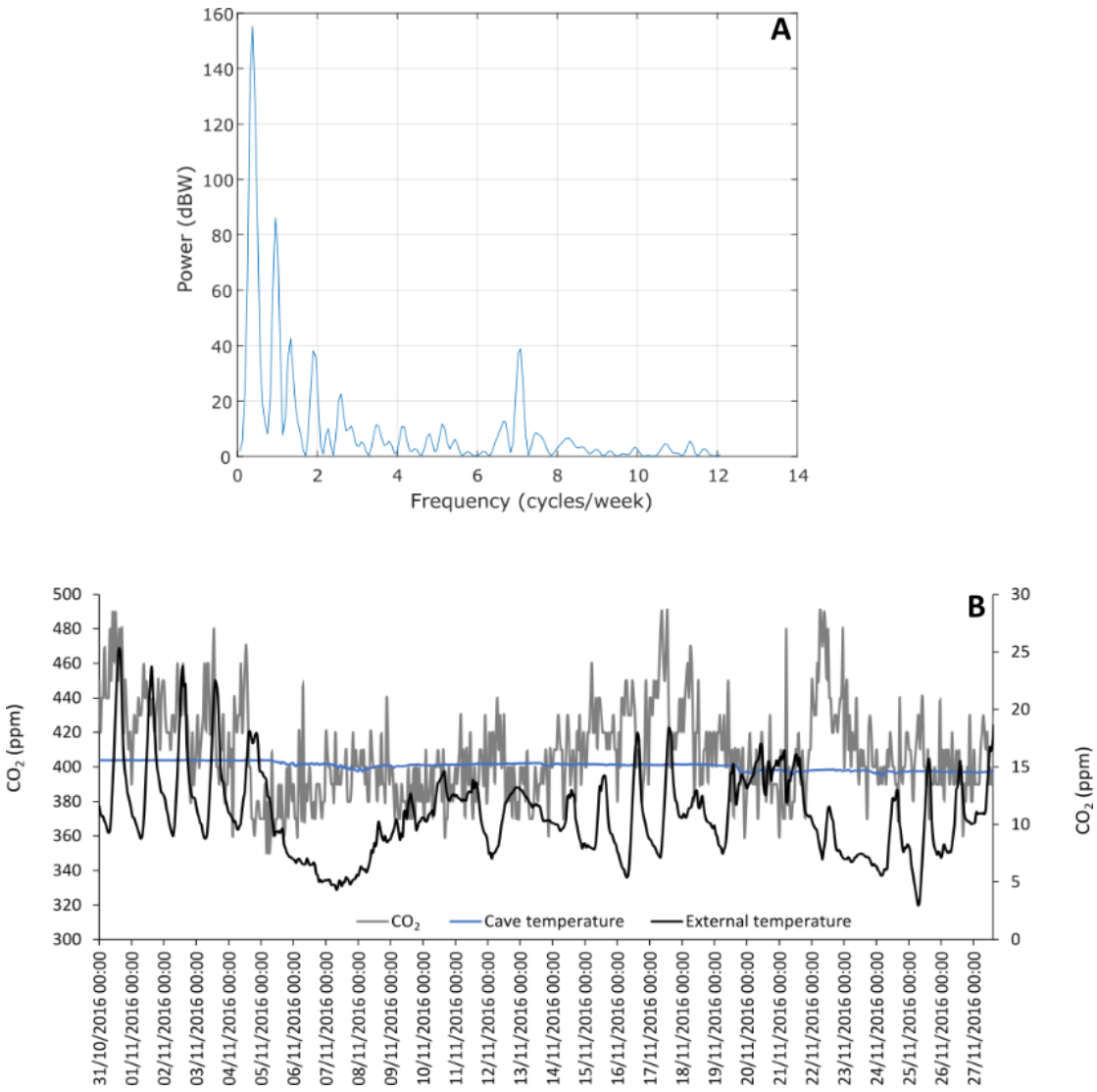

Figure 4.17: Spectral analysis case study from Nov-16. A: Spectral plot from Nov-16. B: CO_2 concentration, internal and external hourly temperature for Nov-16.

Carbon isotopes

The carbon isotope composition of cave air lies upon a mixing line between the soil air and external air carbon isotope compositions (figure 4.18). Cave air carbon isotope composition lies closer to the external air isotope composition shown through lower CO_2 concentrations and relative enrichment in ^{13}C compared to soil air.

The close relationship between internal cave air and external air supports the model proposed above that the cave is being continuously ventilated with atmospheric CO_2-

poor air throughout the year. The trend was constructed using average EA, CA and SA data and predicts a soil $\delta^{13}C$ end member of -23.5‰.

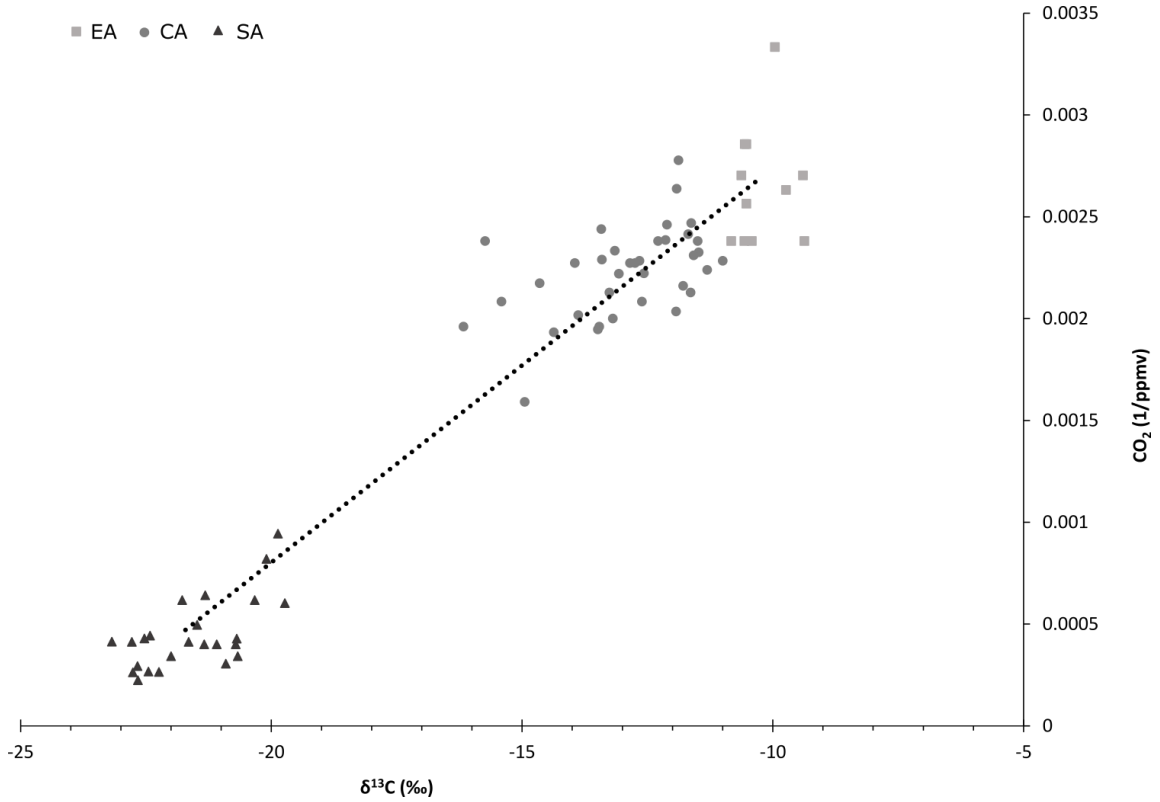

Figure 4.18: Carbon isotope values for cave air (CA), external air (EA) and soil air (SA) plotted against individual CO_2 measurements.

4.4.3.5 Pressure-induced ventilation

CO_2 values have been shown to oscillate on a daily basis due to external hourly temperature fluctuating around cave temperature (section 4.4.3.4). Variations in pressure have also been proposed as a mechanism driving CO_2 concentrations within the cave void on an hourly basis (Denis *et al.,* 2005; James *et al.,* 2015, Smith *et al.,* 2015). The potential for this hourly influence of pressure on cave carbon dynamics is explored in figure 4.19 through assessing the relationship between CO_2 concentrations, external/internal temperature and pressure variability. Jun-17 shows an increase in cave CO_2 during a period of consistently higher external temperatures relative to cave temperature as well as a reduction in pressure. This is highlighted on figure 4.19 by the grey shading. Periods of high CO_2 concentrations coincide with

external temperatures being consistently higher than cave temperatures which would reduce density-driven advection of air into the cave. However, periods of high CO_2 concentrations also correspond to decreases in cave pressure. A reduction in external pressure causes a pressure gradient between the cave and external air. To ensure pressure equalisation between the internal and external environments, air will flow out of Cueva de las Perlas. Consequently, the CO_2 of the cave will increase due to a larger proportion of CO_2-rich air being drawn down from the karst and therefore increasing CO_2 concentration within the cave void (Denis *et al.,* 2005; James *et al.,* 2015; Smith *et al.,* 2015).

Therefore, a model of ventilation is proposed for cave carbon dynamics where the external versus internal temperature dynamics drive ventilation on an hourly-scale and pressure acts as a secondary forcing mechanism. This model will be further discussed in section 4.5.

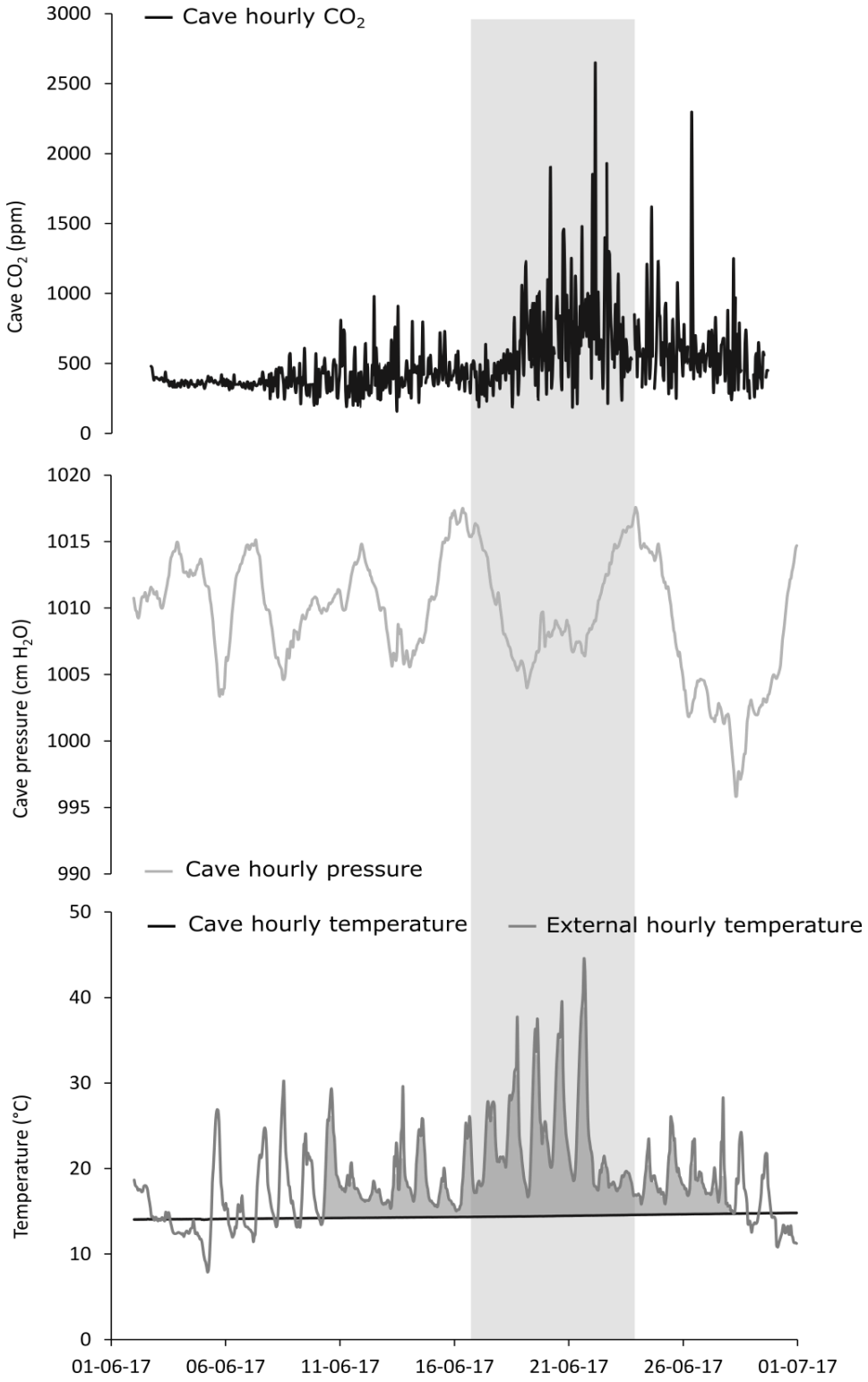

Figure 4.19: Cave CO_2 concentration, cave pressure and external and internal temperature for Jun-17. Shading represents heightened influence of pressure on cave air CO_2 concentrations.

4.5 Conceptual model of cave ventilation within Cueva de las Perlas

Ventilation within Cueva de las Perlas can be summarised using the model presented in figure 4.20. Changes in cave temperature are being controlled by density-driven ventilation. The result is a seasonal cycle in temperature as also evidenced in previous studies from a variety of cave sites across the globe (Spötl *et al.,* 2005; Šebela and Turk, 2011; Ravbar and Kosutnik, 2013; Smith *et al.,* 2016a; Vieten *et al.,* 2016). Internal temperatures are cooler in the winter as a result of strong ventilation and warmer in the summer during weak ventilation. Additionally, latent bedrock heating potentially acts as a mechanism to temporally offset peak external and internal temperatures.

Variability within the cave carbon dynamics appears to occur on much shorter timescales than changes in temperature. External hourly temperatures cross the cave internal temperature on a diurnal basis inducing ventilation switches between weak and strong states. As a result, CO_2 concentrations within the cave remain relatively low throughout the year and the carbon isotope composition of the cave air is similar to that in the external atmosphere. A key component of speleothem growth is the CO_2 concentration within the cave. An increase in CO_2 will limit calcite precipitation whereas a decrease will encourage calcite precipitation (James *et al.,* 2015). Studies from Cueva Larga, Puerto Rica (Vieten *et al.,* 2016) and Obir Caves, Austria (Spötl *et al.,* 2005) have demonstrated significant seasonal variations in pCO_2 as a consequence of seasonal ventilation driven by external temperature variability. As a result, strong ventilation in winter leads to an influx of CO_2-poor cold air which in turn promotes degassing of CO_2 and supersaturation of dripwaters within the cave. In contrast, weak ventilation in summer leads to a build-up of CO_2 within the cave which acts to limit calcite precipitation (Spötl *et al.,* 2005). In Cueva de las Perlas, there is minimal evidence for seasonal cyclicity in CO_2 values (except in summer 2017) and degassing of dripwaters is promoted due to the low CO_2 concentration throughout the year. Therefore, calcite precipitation in Cueva de las Perlas is not biased to winter. It is important to note the low concentrations of CO_2 within the cave and subsequent high

soil-cave CO_2 gradient may result in rapid outgassing of CO2 from drip waters and potentially lead to kinetically-induced isotopic fractionation effects.

Changes in external pressure appear to act as a secondary forcing mechanism on carbon dynamics within the cave. Smith *et al.* (2015) identified pressure as a regulator of CO_2 concentration with low pressure driven by storm events causing a subsequent increase in CO_2 being drawn down from the karst. Pressure changes occur on diurnal scales and therefore responses expressed through CO_2 concentrations are rapid.

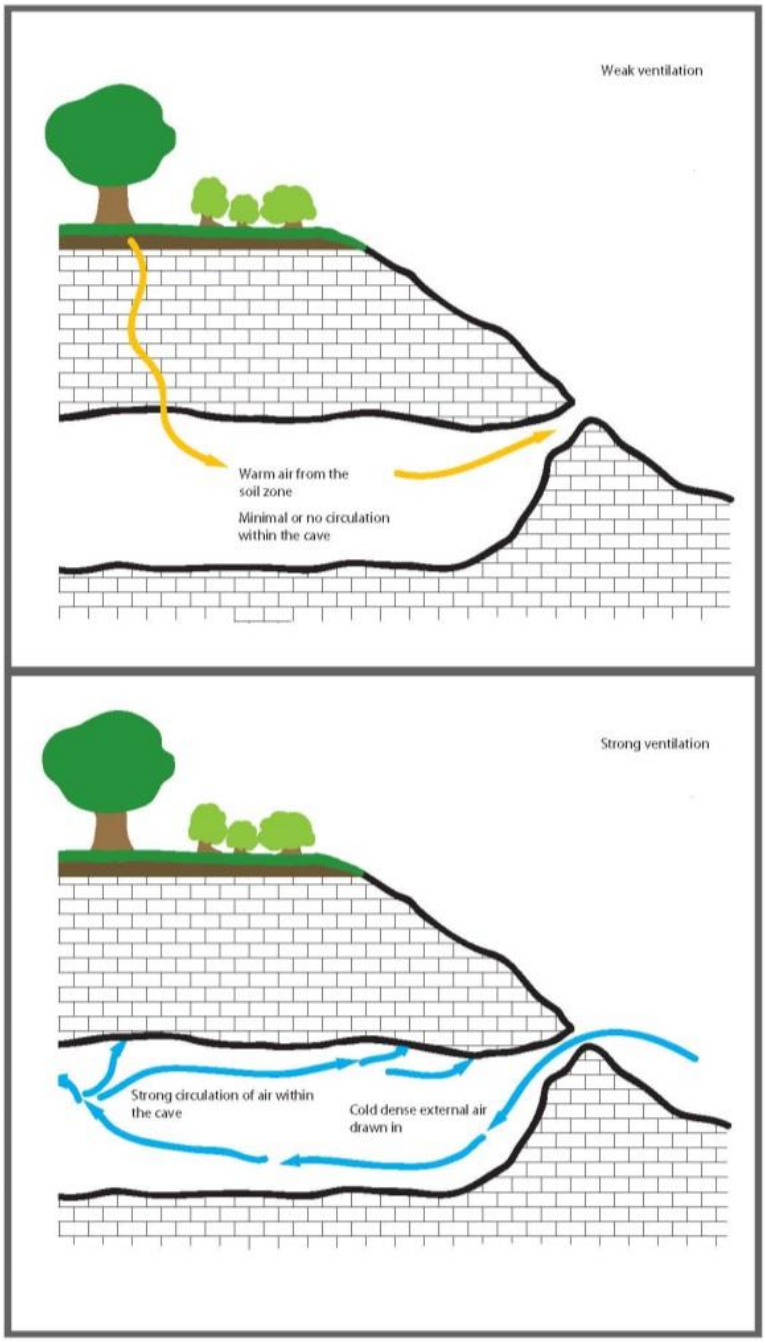

Figure 4.20: Schematic diagram of cave ventilation within Cueva de las Perlas; illustrating summer/weak ventilation and winter/strong ventilation.

4.6 Cave air characteristics of Cueva de las Perlas

Cave temperatures are controlled by variations in daily external temperatures fluctuating around daily internal cave temperatures. In contrast, carbon dynamics are controlled by hourly external temperature oscillations crossing the internal cave

temperature threshold. Both cave temperature and carbon dynamics are driven by density differences inducing ventilation. However, temperatures are only seasonally driven in response to density-differences and lag peak external temperatures as a result of latent bedrock heating. Carbon dynamics within the cave are driven on diurnal timescales and this is evidenced by hourly oscillations in cave CO_2 concentrations and the near atmospheric carbon isotope composition of cave air. Additionally, pressure acts as a secondary forcing mechanism driving the carbon dynamics within the cave with low external pressures driving air flow out of the cave and drawing down CO_2-rich air from the karst. These responses in temperature and carbon dynamics to ventilation are likely a result of the shallow nature of the cave with the monitoring chamber situated only 15m from the cave entrance and beneath an overburden of 4m karst.

5. Cave monitoring: Assessment of modern hydrology and influence on water chemistry

5.1 Introduction

Understanding cave hydrology is key to interpreting speleothem palaeoclimate records. The hydrological system delivers water to the cave, controls the chemical composition of dripwaters and influences speleothem growth rates (Smith, 2014). Climate signals contained within precipitation and subsequent cave dripwaters are modified by hydrological routing, karst-water interaction processes such as prior calcite precipitation (PCP) and incongruent calcite dissolution (ICD) and cave ventilation (section 2.4.2). Therefore, it is important to monitor cave hydrology in order to understand the influence of such processes on dripwater chemistry and ultimately accurately interpret speleothem proxies of palaeoclimate and palaeoenvironmental processes.

This section aims to evaluate the karst hydrology overlying Cueva de las Perlas and determine the processes controlling the chemical composition of dripwaters. Assessment of karst hydrology and classification of processes influencing drip water chemistry will provide a contemporary insight into cave hydrological dynamics which will aid interpretation of speleothem palaeoclimate records.

5.2 External precipitation

5.2.1 Precipitation amount

Precipitation amount has been recorded in Matienzo since Feb-11 (figure 5.1), with data prior to Apr-15 collected by Smith *et al.* (2015; 2016a). Precipitation has been measured through a combination of manual collection and Pluvimate measurements from the Matienzo valley (43°19’00.1”N, 003°35’23.4”W). Collection of precipitation

measurements ceased between Apr-13 to Mar-15 representing the gap between the two monitoring studies (Smith, 2014 and this project).

The Matienzo depression is characterized by a wet and mild climate due to its proximity to the North Atlantic Ocean and mountainous landscape. The average precipitation for Matienzo is 1393mm/yr which is higher than the average precipitation recorded in Santander between 2000-2006 of 1000mm/yr (IAEA, 2018).

Typically, the wettest months lie between November to April with the highest monthly precipitation recorded in Feb-11 (203.40mm), Apr-12 (273.2mm), Nov-15 (257.93mm), Feb-16 (531.14mm) and Dec-17 (263.20mm). In contrast, the driest months lie between May to October with the lowest annual precipitation recorded in Aug-11 (35.52mm), Aug-12 (27.19mm), Sep-15 (29.71mm), Oct-16 (40.24mm) and Oct-17 (22.11mm).

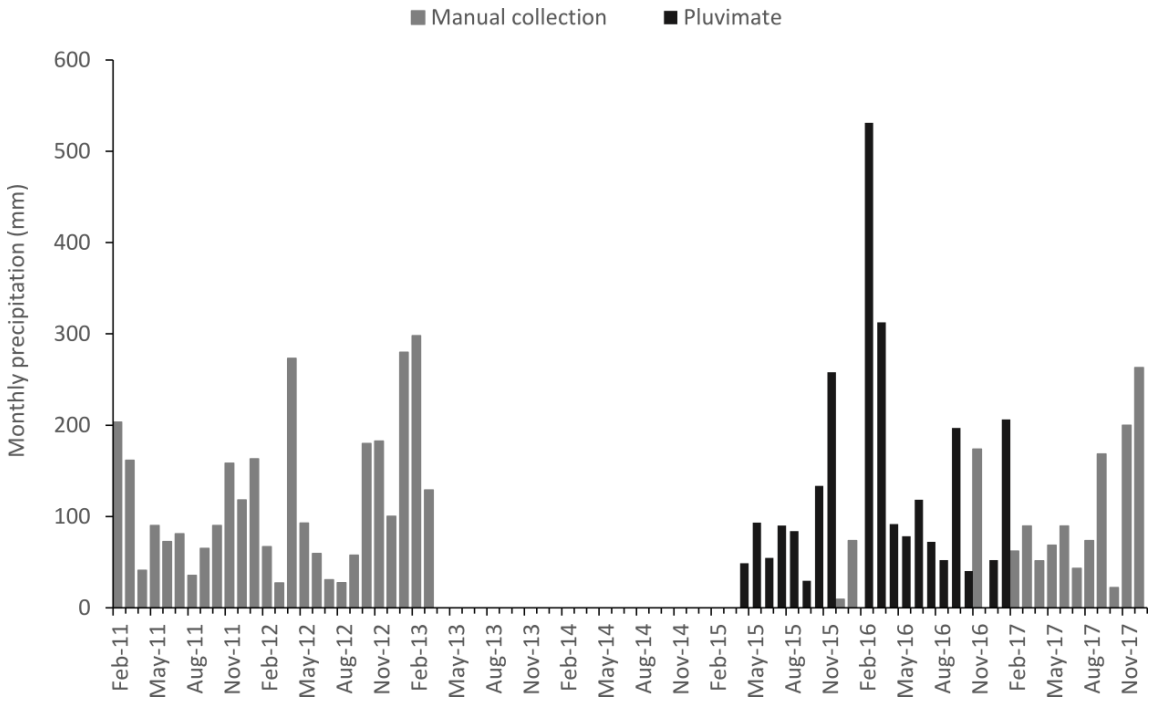

Figure 5.1: Matienzo precipitation between Feb-11 to Dec-17.

5.2.2 Water excess

Calculation of monthly water excess can indicate how much of the external precipitation infiltrates into the karst system and is a direct function of rainfall amount and temperature. Monthly water excess has been derived through first calculating the potential evapotranspiration (PET) by applying the Thornthwaite equation (eq. 5.1) (Thornthwaite, 1948).

$$PET = 16 \left(\frac{L}{12}\right) \left(\frac{N}{30}\right) \left(\frac{10T_a}{I}\right)^{\alpha} \quad \text{Eq. 5.1}$$

Where:

T_a is average daily temperature (°C), N is the number of days in the month, L is the average day length, I is the heat index calculated through eq. 5.2 and α is calculated using eq. 5.3.

$$I = \sum_{i=1}^{12} \left(\frac{T_{ai}}{5}\right)^{1.51} \quad \text{Eq. 5.2}$$

where T_{ai} = 12 monthly mean temperatures.

$$\alpha = (6.75\ x\ 10^{-7})I^3 - (7.71\ x\ 10^{-5})I^2 + (1.792\ x\ 10^{-2})I + 0.49239 \quad \text{Eq 5.3}$$

To calculate water excess, PET is then subtracted from monthly precipitation. The water excess values for Matienzo are presented in figure 5.2 alongside temperature and precipitation.

The water excess data indicate seasonal variation with the summer months (Apr-Sep) characterized by a negative water excess (water deficit) and the winter months (Oct-Mar) by a positive water excess. Calculations of water excess therefore demonstrate a winter recharge of the karst system. However, this seasonal relationship may be disrupted by seasonal abnormalities in rainfall and/or temperature.

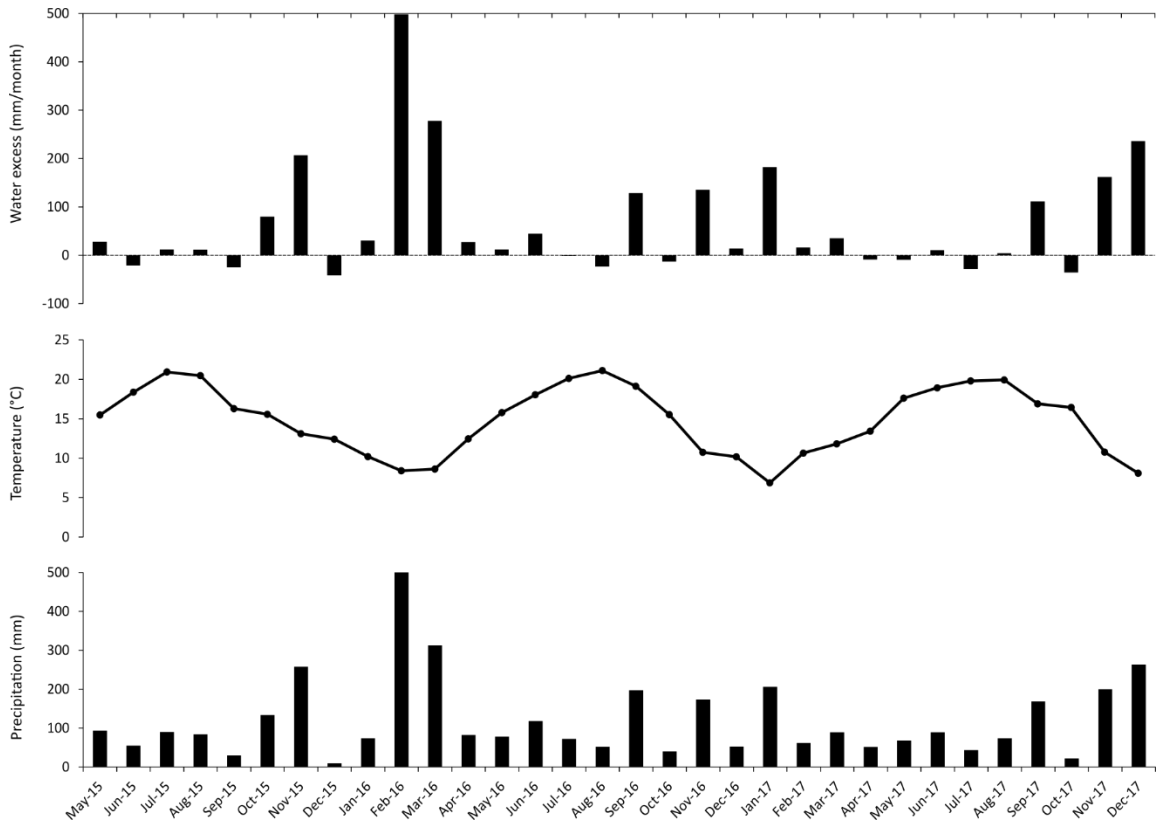

Figure 5.2: Water excess, temperature and precipitation amount from Matienzo. Water excess values for Matienzo calculated using the Thornthwaite equation (Thornthwaite, 1948).

5.2.3 Determination of moisture trajectories and source regions for Matienzo precipitation

5.2.3.1 Initiation point

Backwards air mass trajectories have been calculated using the NOAA Air Resources Laboratory Hybrid Single-Particle Lagrangian Integrated Trajectory (HYSPLIT) model (Stein *et al.,* 2015) which was run using the Real-time Environmental Applications and Display sYstem (READY) online system (Rolph *et al.,* 2017). This model was provided online by the NOAA Air Resources Laboratory (NOAA ARL, 2017). Each backward trajectory corresponds to a precipitation event in the Matienzo valley (43.31°N, 3.58°W) and is backward modelled over 120hrs at 1,500m a.s.l. The output of the model is a latitude and longitude for every hour along the backward trajectory as well as additional parameters such as ambient temperature, atmospheric pressure and relative humidity. A backward trajectory was calculated for each day precipitation was recorded in Matienzo between 1/5/15 – 30/4/16 excluding December 2015 as no precipitation was recorded due to a logger malfunction. Trajectories were plotted onto the maps shown in figure 5.3. In order to quantify the relative directions of the trajectories, the angle between the Matienzo valley and the trajectory initiation point was calculated on Google Earth (v.7.1.2.2041, 2013). The angles were placed in bins corresponding to direction and used to produce a rose diagram of trajectory initiation point. It must be noted that this method does not capture the variability across a 120hr transect but does give an overall direction between initiation point and the Matienzo valley end-point.

The backward trajectories for Apr-15 to Mar-16 are presented in figure 5.3. The HYSPLIT modelled trajectories indicate that the majority of trajectories initiated in the North Atlantic Ocean. This relationship is quantified in figure 5.4 where ~73% of trajectories lie between an angle of 270°-11.5° demonstrating a NW air mass trajectory.

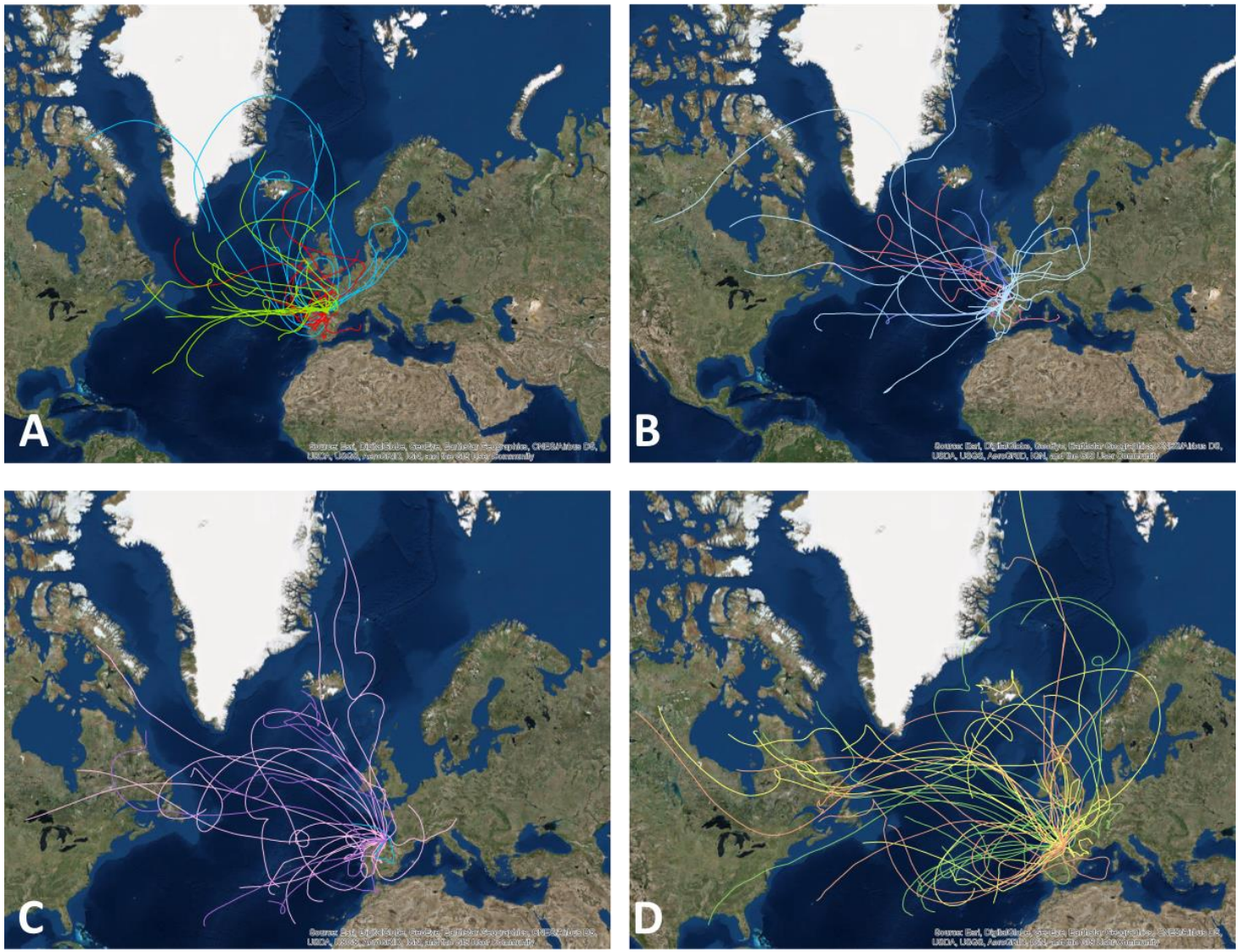

Figure 5.3: Backward modelled trajectories for each precipitation day recorded between 1/5/15 – 30/4/16 calculated through HYSPLIT (NOAA ARL, 2017). A = May-15, Jun-15 and Jul-15; B = Aug-15, Sep-15 and Oct-15; C = Nov-15, Dec-15 and Jan-16; D = Feb-16, Mar-16 and Apr-16. ArcGIS software by Esri was used to create the maps. Copyright © Esri. Basemap source: Esri, DigitalGlobe, GeoEye, Earthstar Geographics, CNES/Airbus DS, USDA, USGS, AeroGRID, IGN and the GIS User Community.

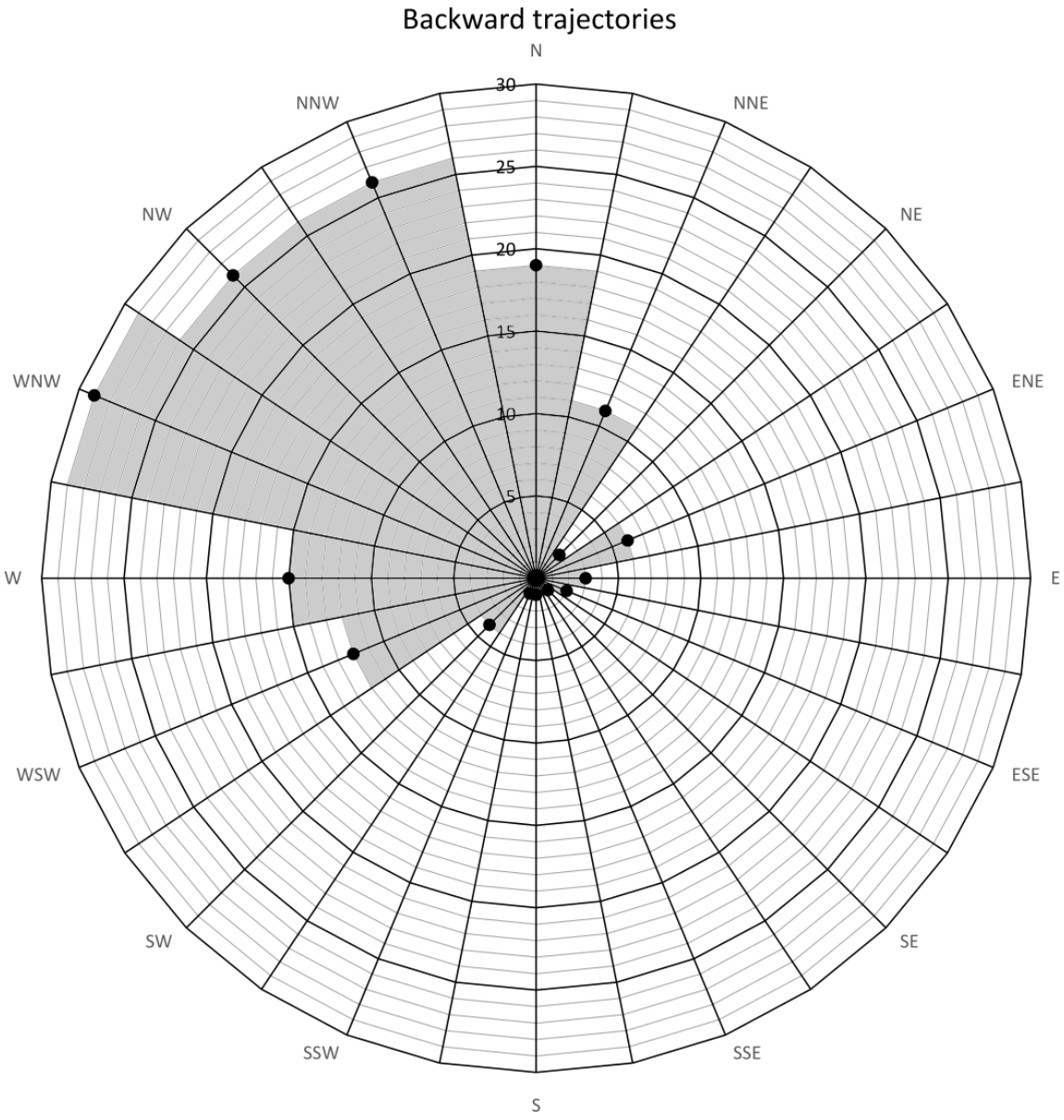

Figure 5.4: Rose diagram of trajectory initiation direction.

5.2.3.2 Moisture uptake regions

Moisture uptake regions were identified by using the method of Baldini *et al.* (2010) who optimized the method of Sodemann *et al.* (2008). Regions where there was a specific humidity increase of >0.5g/kg over 6hrs were indicative of moisture uptake. Specific humidity was calculated from the HYSPLIT meteorological data using the R humidity package (Cai, 2018). After moisture uptake regions were identified, the angles between the Matienzo valley and the uptake regions over the 120hr trajectory were calculated and an average angle was taken.

Precipitation events from the wettest month (Feb-16) and the driest month (Sep-15) of the study period were selected. Across the two months, 23 precipitation events were recorded. A trajectory summary rose diagram is presented in figure 5.5A alongside the source summary rose diagram (figure 5.5B). Of these, 16 are from a N-W direction (figure 5.5B). Therefore, of the precipitation events studied, 70% of moisture is sourced from the North Atlantic region with no difference between the two selected months.

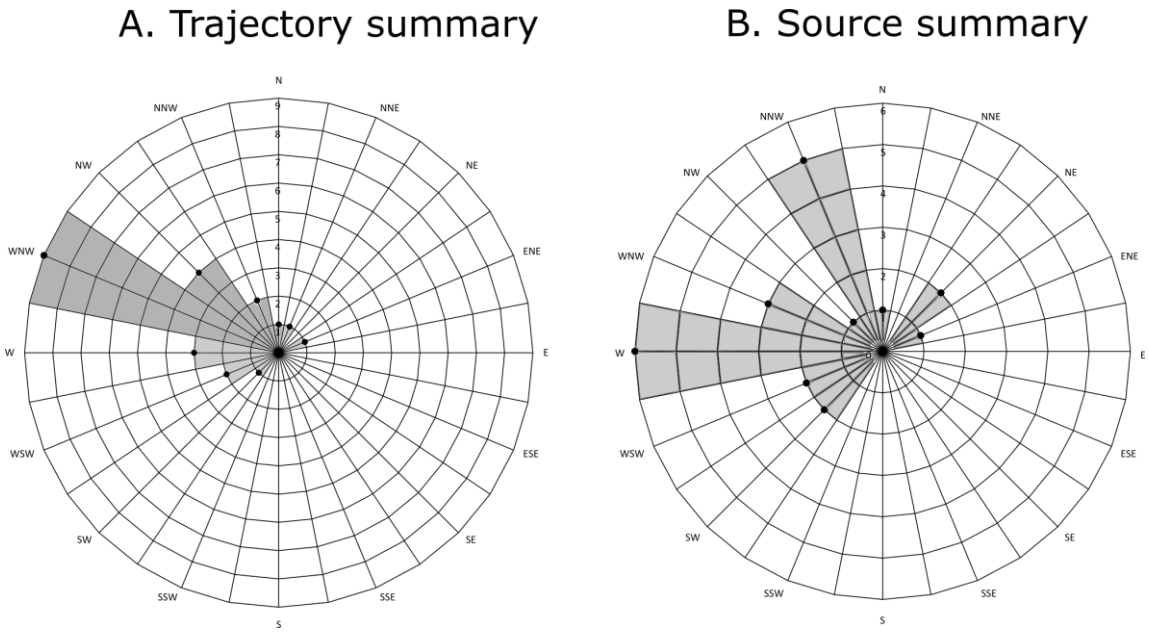

Figure 5.5: Rose diagrams illustrating the relative direction of the trajectory analysis *(A)* moisture source regions *(B)* for precipitation events from Sep-15 and Feb-16.

5.3 Cueva de las Perlas drip rates

Drip rates have been logged at three sites within Cueva de las Perlas. This section will present the drip records and interpret variability in relation to karst hydrology. All three drip records are presented in figure 5.6.

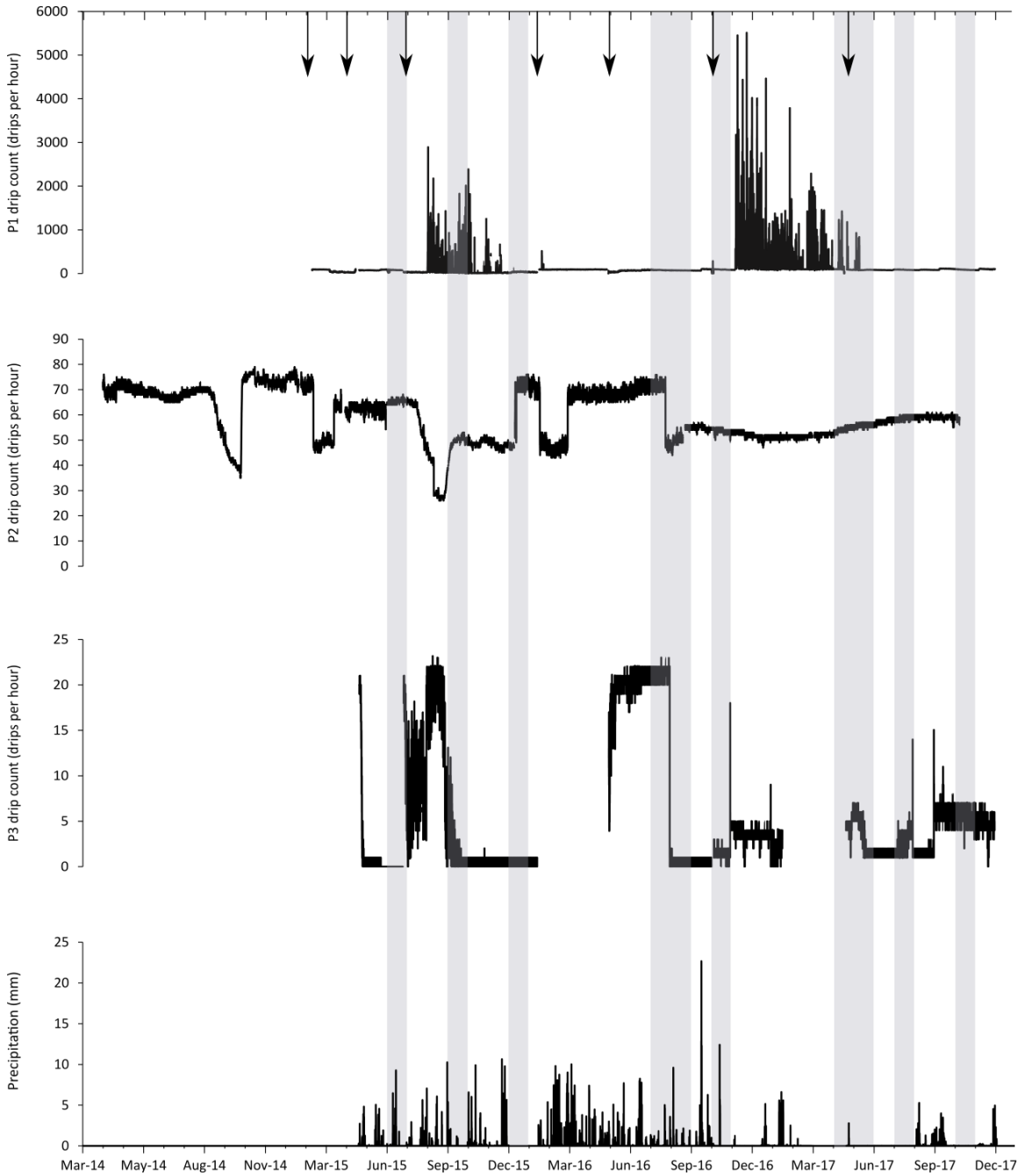

Figure 5.6: P1, P2 and P3 hourly drips and external precipitation. The grey shaded areas represent periods of negative water excess (water deficit). Arrows indicate field visits by the PI where logger positions were adjusted.

5.3.1 P1

Logger P1 recorded drip rates between Feb-15 and Dec-17. The overall average is 141 drips per hour. However, annual variation is evident with averages of 76, 164 and 145 for 2015 (number of days in average (n)= 318), 2016 (n=361) and 2017 (n=333). P1 hourly drip rates are variable with a range of 5435 over the record. The P1 drip record shows an irregular drip pattern with some periods of very high drips whilst others exhibit low drip counts.

5.3.2 P2

The P2 drip logger recorded drip rates between Mar-14 and Dec-17. The long-term hourly average is 59 drips per hour with a range of 98 across the dataset. The different years exhibit a slight fluctuation in hourly average drip rate (table 5.1).

Table 5.1: Average annual hourly drip rate for P2.

Year	Average hourly drip rate	No. days in average
2014	66	274
2015	57	354
2016	61	359
2017	55	333

5.3.3 P3

P3 has recorded drip rates between Apr-15 to Dec-17 with two gaps in the data between Jan-16 to Apr-16 and Jan-17 to May-17 due to logging malfunctions. The overall range of drips at the P3 site is 23 per hour with an average of 6 drips per hour. The annual drip rate is variable with the averages of 4, 8 and 3 drips per hour for 2015 (n= 254), 2016 (n=255) and 2017 (n= 240) respectively.

5.3.4 Interpretation of drip sites

Drip rates from the three loggers within Cueva de las Perlas demonstrate a complex drip pattern which is variable within individual records and inconsistent between records despite their close proximity. The next section will focus on forcing

mechanisms driving this variability, including: logging issues, water excess and precipitation amount.

5.3.4.1 Logging issues

Some of the rapid transitions in drip rate correspond to changes to the logger set-up through temporary removal of logging equipment and problems with repositioning, battery replacement and logger replacement (represented by arrows on figure 5.6). An example of this is P1 Apr-16 where the logger was temporarily removed and replaced at a slightly different angle which led to a reduction in the number of drips recorded. The drip records within Cueva de las Perlas are highly sensitive to logger positioning and field evidence suggests multiple straws may feed the same stalagmite. Where any record suffers from this, the data can only be used to interpret relative changes in drip rate. The shifts in P2 in Feb-16, Apr-16 and Sep-16 are most likely related to shifts in the logger positioning potentially in relation to heavy rainfall. It must be noted that these shifts are not coincident with site visits by the PI or field team.

5.3.4.2 Water excess

Periods of negative water excess (water deficit) correspond to decreases in drip rate at various points throughout each of the drip records. For example, P3 demonstrates a decrease in drip rate associated with a period of water deficit in Sep-15. Under periods of reduced precipitation, flow into the karst is reduced and the reservoirs within the karst become depleted. As the karst reservoirs are depleted and not replenished by precipitation, drip rates decrease within the cave.

5.3.4.3 Precipitation

Drip rates have been documented to respond rapidly to changes in precipitation such as the P1 record in Sep-17 and Nov-17 (figure 5.7). Precipitation increases on 9/9/17 and 7/11/17 following periods of significantly reduced rainfall. Following the increase in precipitation on these dates, P1 drip rates subsequently increase. The increase in precipitation may lead to changes in the flow pathways through the karst, potentially

inducing a fracture flow or piston-flow within the reservoir. This will be explored further in the following section (5.3.4.4).

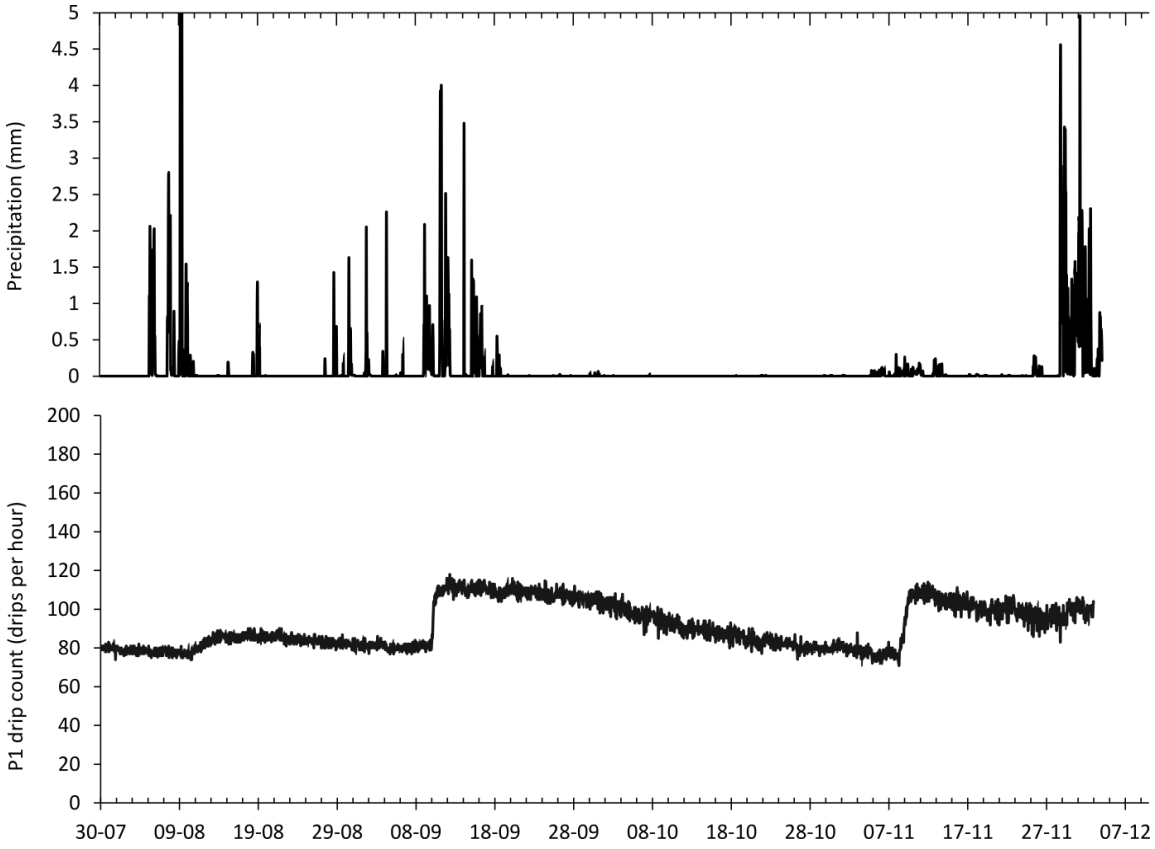

Figure 5.7: External precipitation and P1 drip count between 30/07/17 and 07/12/17.

5.3.4.4 Constructing hydrological regimes using drip rates

The drip sites analysed herein appear to reflect a combination of diffuse matrix flow and a smaller proportion of fracture flow induced during high precipitation events. Matrix flow is evident in all records through the persistent nature of all drip sites. The reservoir feeding the matrix flow must be a function of infiltrating water and is primarily recharged during periods of water excess. The reservoir becomes depleted during periods of water deficit and this is reflected by the reduction in speleothem drip rates.

The increase in drip rates during periods of enhanced precipitation suggests a secondary forcing mechanism is responsible for hydrological routing such as piston flow or conduit overflow. Piston flow is the result of an increase in infiltrating waters causing a build-up of pressure in the aquifer. Under piston flow conditions the older,

well-mixed water is forced out of the aquifer and into the cave. On the other hand, a conduit overflow would occur when the karst aquifer reached capacity inducing overflow routes through the karst. Overflow routes may inhibit mixing of water within the karst and therefore infiltrating waters would preserve a specific precipitation event signature. Due to the large number of stalactites overlying the studied drip sites, it is proposed heavy precipitation events reactivate fractures within the karst and subsequently induce fracture-flow along the flow pathways overlying the abundant and previously inactive stalactites.

Therefore, the drips sites studied herein appear to correspond to the class II drip sites classified in Crag Cave SW Ireland (Baldini *et al.,* 2006) (section 2.4.3.1, table 2.2). Even though the drip sites in Cueva de las Perlas exhibit slow drips coincident with class III drip sites, the variability within the annual signal demonstrated in the drip rates appears to reflect external conditions and responds to variations in water excess. Further insights into the chemical signature recorded in the cave dripwaters will be presented in the following section (5.4.2).

5.3.5 Summary

The variations in drip rate demonstrate the complex karst hydrology overlying the drip sites. Drip rates are controlled by a complex interplay between precipitation and water excess influencing the reservoir size and flow of water within the karst. Flow of water through the karst is most likely through diffuse matrix flow and a smaller proportion of fracture flow related to increases in precipitation. Additionally, logger positioning is known to significantly influence drip rates at each of the monitoring sites. Between each of the drip sites, drip patterns vary. An example of this is in February 2016 where P1 drip rate increases whilst P2 declines. These sites are less than 1m apart and demonstrate the spatial and temporal variability of drip rates within Cueva de las Perlas.

5.4 Water isotope chemistry

5.4.1 Precipitation isotope chemistry

In order to reconstruct past climate using oxygen isotopes in speleothems, it is critical to understand the factors which control the oxygen isotope composition of precipitation. Temperature, precipitation amount and the oxygen isotope composition of precipitation were recorded in Matienzo between Feb-11 and Dec-17. Data between 2011-2013 were collected by Smith (2014) and subsequent data has been recorded as part of the current project. No precipitation samples were collected between Apr-13 and Apr-15 due to a gap between the two monitoring projects.

Oxygen and deuterium isotope composition in precipitation is shown to vary seasonally (figure 5.8). The range across the whole dataset is 7.39‰ and 51.74‰ for $\delta^{18}O$ and δD values respectively. The highest $\delta^{18}O$ and δD values were recorded in Aug-11 (-1.37‰ and -3.65‰ respectively) and the lowest values recorded in Mar-13 (-8.76‰ and -55.38‰ respectively). Typically, oxygen and deuterium isotope values are higher in summer months with the highest $\delta^{18}O$ and δD values recorded in August and July. In contrast, the oxygen and deuterium isotope values are increasingly negative in winter months.

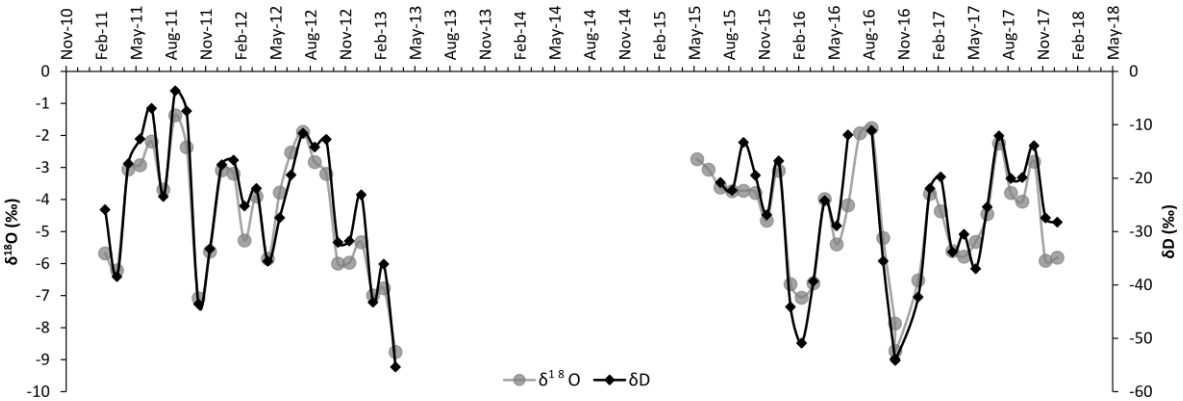

Figure 5.8: Oxygen and deuterium isotope composition of precipitation between Feb-11 and Dec-17.

Oxygen and deuterium isotope values from Matienzo precipitation have been used to construct a LMWL shown in figure 5.9. The LMWL is defined by eq. 5.4.

$$\delta D = 6.7199\, x\, \delta^{18}O + 5.0772 \qquad \text{Eq. 5.4.}$$

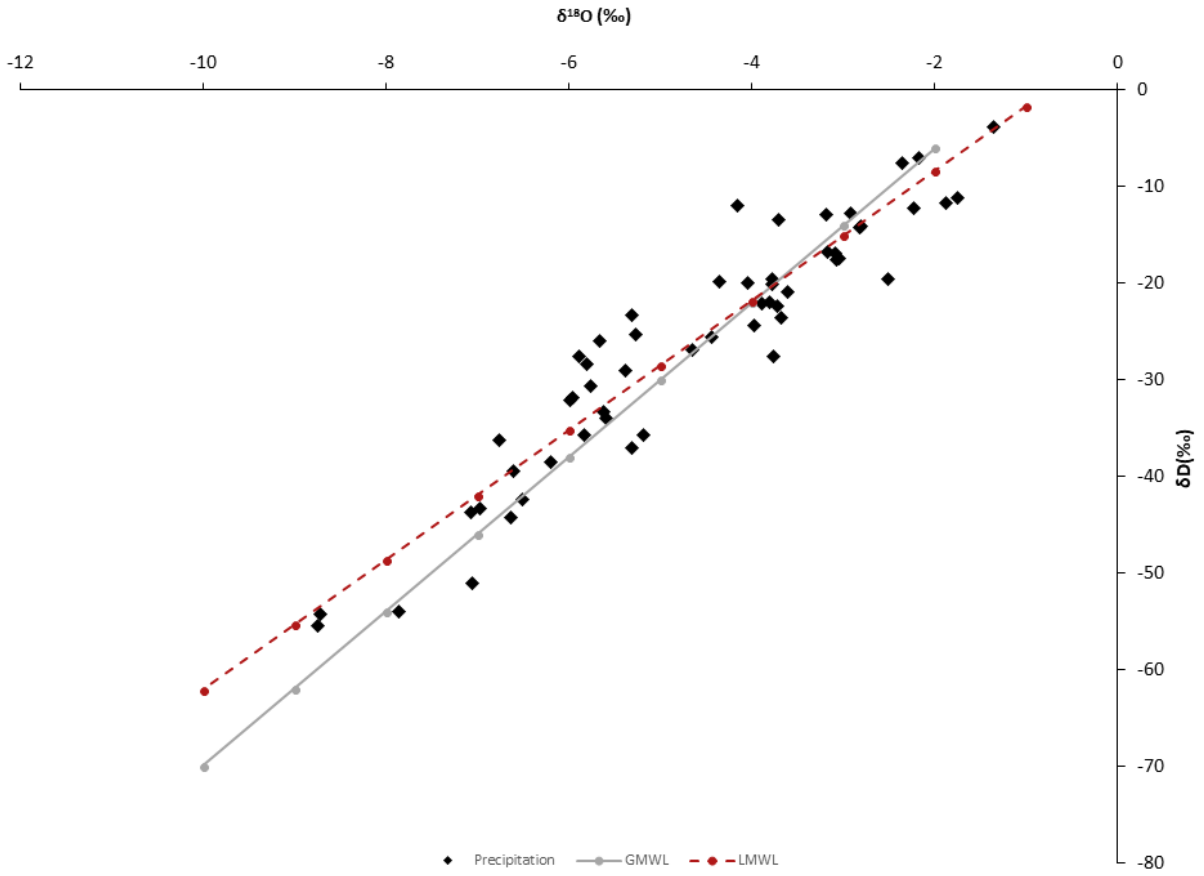

Figure 5.9: Precipitation $\delta^{18}O$ and δD values alongside the GMWL and LMWL. The GMWL was defined using the equation derived by Craig (1961a) (Eq 2.9) and the LMWL was defined from the precipitation data collected in Matienzo as part of this project (Eq. 5.4).

The oxygen isotope composition of precipitation ($\delta^{18}O_p$) has been compared to monthly precipitation amount and temperature to determine the dominant forcing mechanism (figure 5.10 and 5.11). Precipitation isotope data and Matienzo meteorological data since 2011 have been incorporated in this analysis. A negative relationship is shown between precipitation amount and $\delta^{18}O_p$ in figure 5.10 and by an R value of -0.62. Therefore, high $\delta^{18}O_p$ is correlated to low precipitation amount. Temperature is found to have a weaker positive relationship with $\delta^{18}O_p$ values shown through an r^2 of 0.43 (figure 5.11). The relationship implies higher temperatures lead to higher δ^{18}Op values.

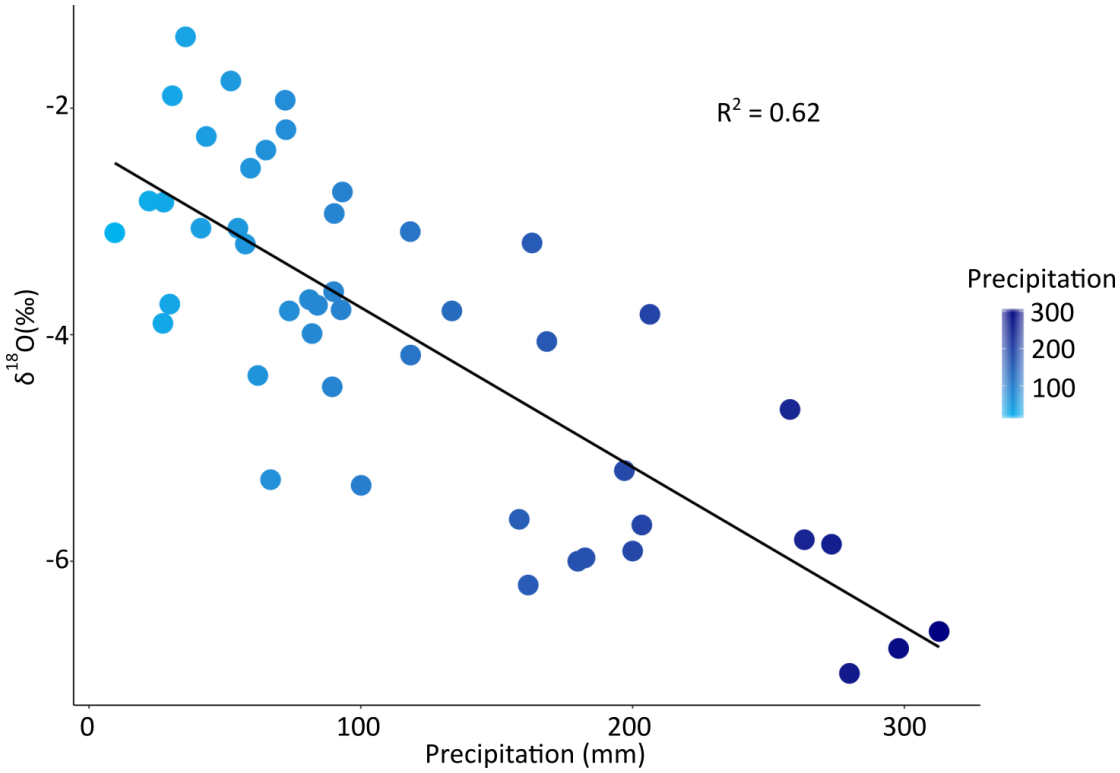

Figure 5.10: Precipitation amount and $\delta^{18}O_p$.

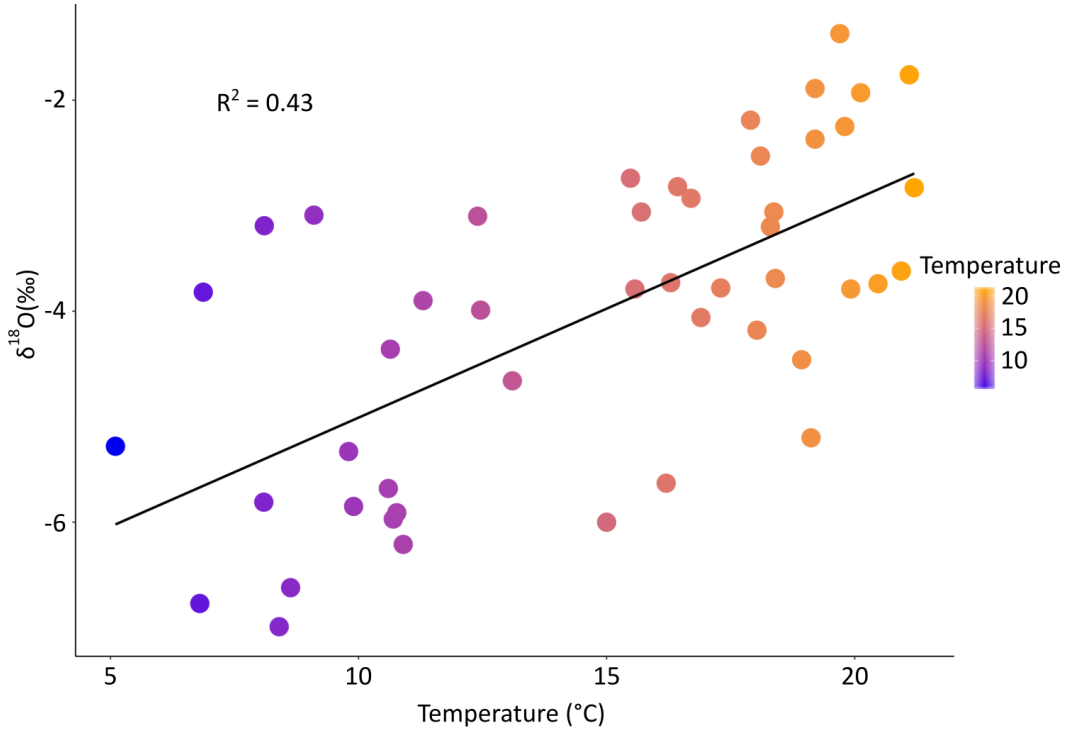

Figure 5.11: Temperature and $\delta^{18}O_p$.

Overall the stronger relationship between $\delta^{18}O_p$ and precipitation implies a predominant control of precipitation amount on $\delta^{18}O_p$ values with a potential weaker influence of temperature imprinted. As a consequence, $\delta^{18}O_p$ values will be interpreted to represent changes in precipitation amount and subsequently speleothem oxygen isotope profiles may be interpreted as palaeoprecipitation indicators. Analysis of possible secondary alteration of this signal (e.g. through kinetic processes) will be explored in sections 5.5 and 5.6.

5.4.2 Cave water isotope chemistry

Waters were collected from drip sites representing different water types and duration within the cave. A map of the different water collection sites can be found in section 3.4 (figure 3.3). The four types were:

- Waters collected from the three main monitoring speleothems (P1, P2 and P3) over less than a 24-hour period (instantaneous)
- Waters collected monthly from the three main monitoring speleothems (bulk waters)
- Waters collected from fast drip sites (ephemeral)
- Waters collected from pools (pool).

Section 5.4.1 demonstrated the broad range in isotopic values in precipitation. Drip waters support a more tightly clustered range in isotopic signature (Figure 5.12). Such a drip water clustering in both $\delta^{18}O$ and δD values is typical of aquifer mixing in the karst above the cave.

Averages and standard deviations for each of the different drip water types are shown in table 5.2. The average values again demonstrate a clustering of cave drip water $\delta^{18}O$ and δD values along the LMWL as shown in figure 5.12.

Table 5.2: Average isotopic values for different dripwater types.

Sample type	$\delta^{18}O$ (‰)		δD (‰)		Number of samples
	Average	Stdev	Average	Stdev	
Bulk	-5.68	0.5194	-33.02	3.03	88
Instantaneous	-5.70	0.5354	-33.54	3.03	79
Ephemeral	-6.11	1.0429	-35.12	5.35	14
Pool	-5.92	1.0851	-34.52	5.62	23

Dripwaters being fed from a well-mixed aquifer would be expected to show a more homogenous isotopic signature, present on figure 5.12 as a tight cluster in isotopic values. Therefore, there is evidence from $\delta^{18}O$ and δD drip water values for a similar range in isotopic value between all drip sites demonstrating a similar degree of aquifer mixing across all water types.

The homogenized nature of the drip waters suggests a significant reservoir in the karst as water is stored and allowed to mix prior to dripping into the cave. The ephemeral sites are only activated during periods of high precipitation. However, the isotopic signature of the ephemeral drip waters suggests waters have homogenized within the aquifer and therefore do not represent signatures of individual precipitation events. As a consequence, flow through these sites must be through activation of channels either through piston-flow or fracture flow as a result of reservoir overflow. Piston-flow results due to increases in pressure related to an influx of water which forces homogenized water out of the reservoir. Alternatively, increased water flow into the reservoir may result in filling of the reservoir and overflow of well-mixed reservoir water into fractures within the karst.

The pool sites are highly transient in Cueva de las Perlas which suggests they are fed by ephemeral drip sites. Isotopic composition of the pool waters is similar to the other water types which suggests the water is sourced from a well-mixed karst aquifer and flows along ephemeral drip pathways reactivated during periods of high water excess.

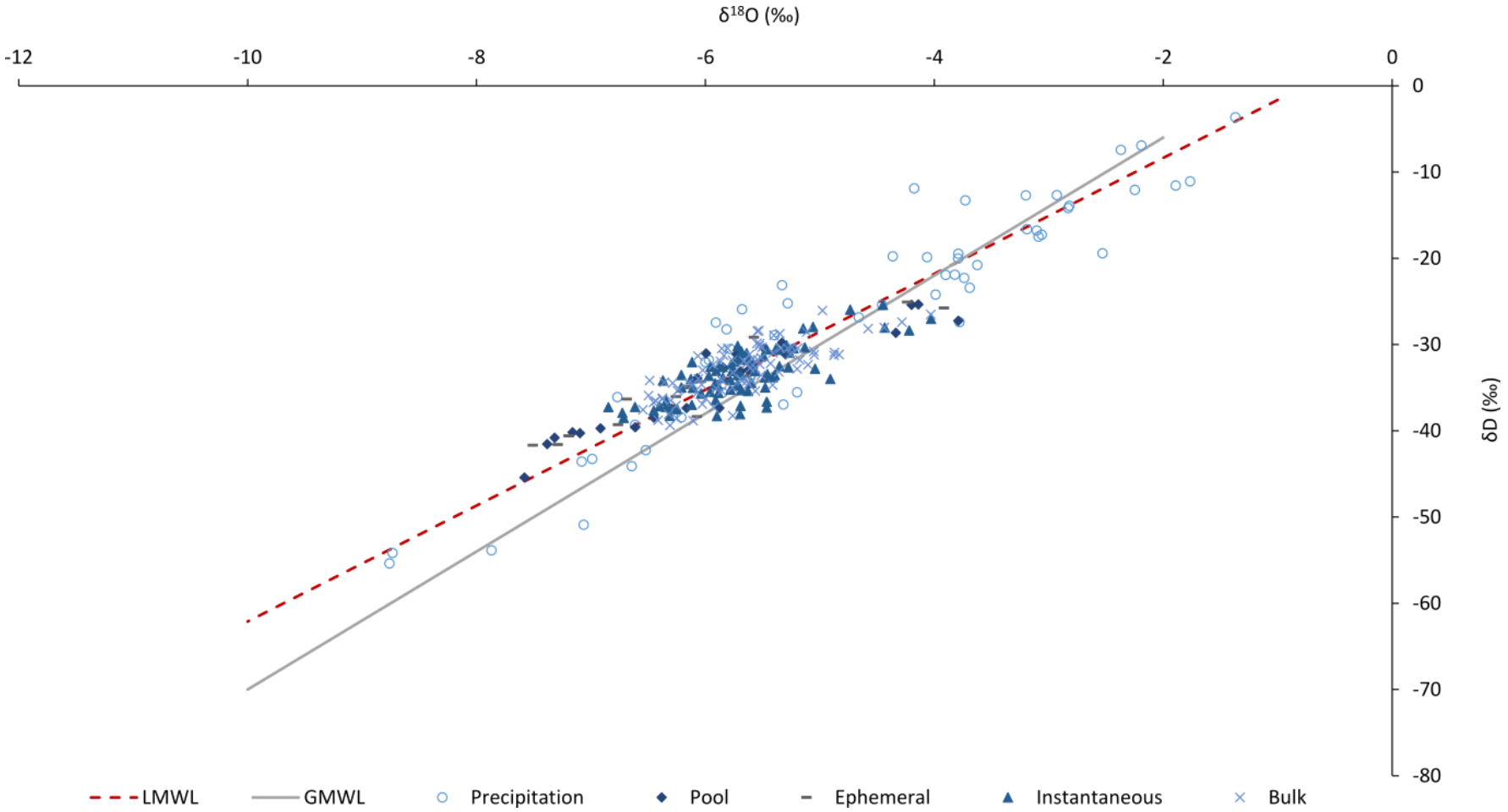

Figure 5.12: $\delta^{18}O$ and δD values for the different cave water types.

Cave waters appear to lie closer to the winter end of the LMWL line (figure 5.13). The winter end of the precipitation line typically has lower $\delta^{18}O$ and δD values. The average $\delta^{18}O$ and δD cave drip water values listed in table 5.2 also lie close to the winter precipitation averages of -5.63‰ and -32.32‰ for $\delta^{18}O$ and δD values respectively. Thereby suggesting cave water recharge occurs predominantly during the winter months and further supported by figure 5.2.

5.4.3 Summary

This section has examined the isotope chemistry of precipitation and cave dripwaters. The isotopic composition of precipitation demonstrates seasonal oscillations which are a function of precipitation amount. $\delta^{18}O$ and δD values in cave waters cluster to the winter end of the LMWL which points towards a well-mixed reservoir in the karst primarily recharged in winter. The primary mechanism feeding the drip sites is matrix flow. However, during periods of high water excess re-activation of ephemeral drip sites and pools must be either through piston flow or fracture overflow in order to allow for the isotopic similarity between all measured water collection points. The karst hydrology is summarized in figure 5.14.

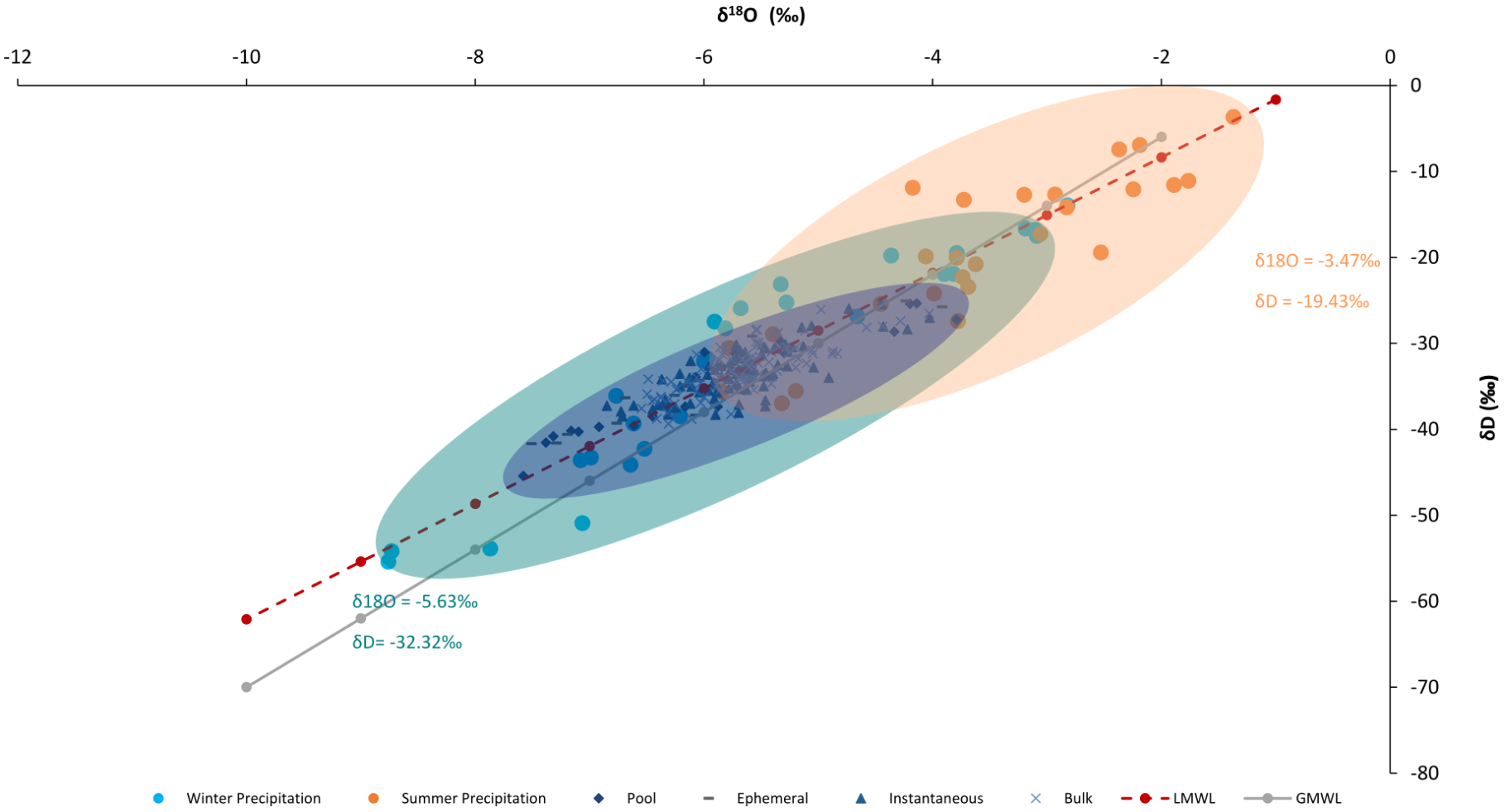

Figure 5.13: $\delta^{18}O$ and δD values from cave drip waters and seasonal precipitation.

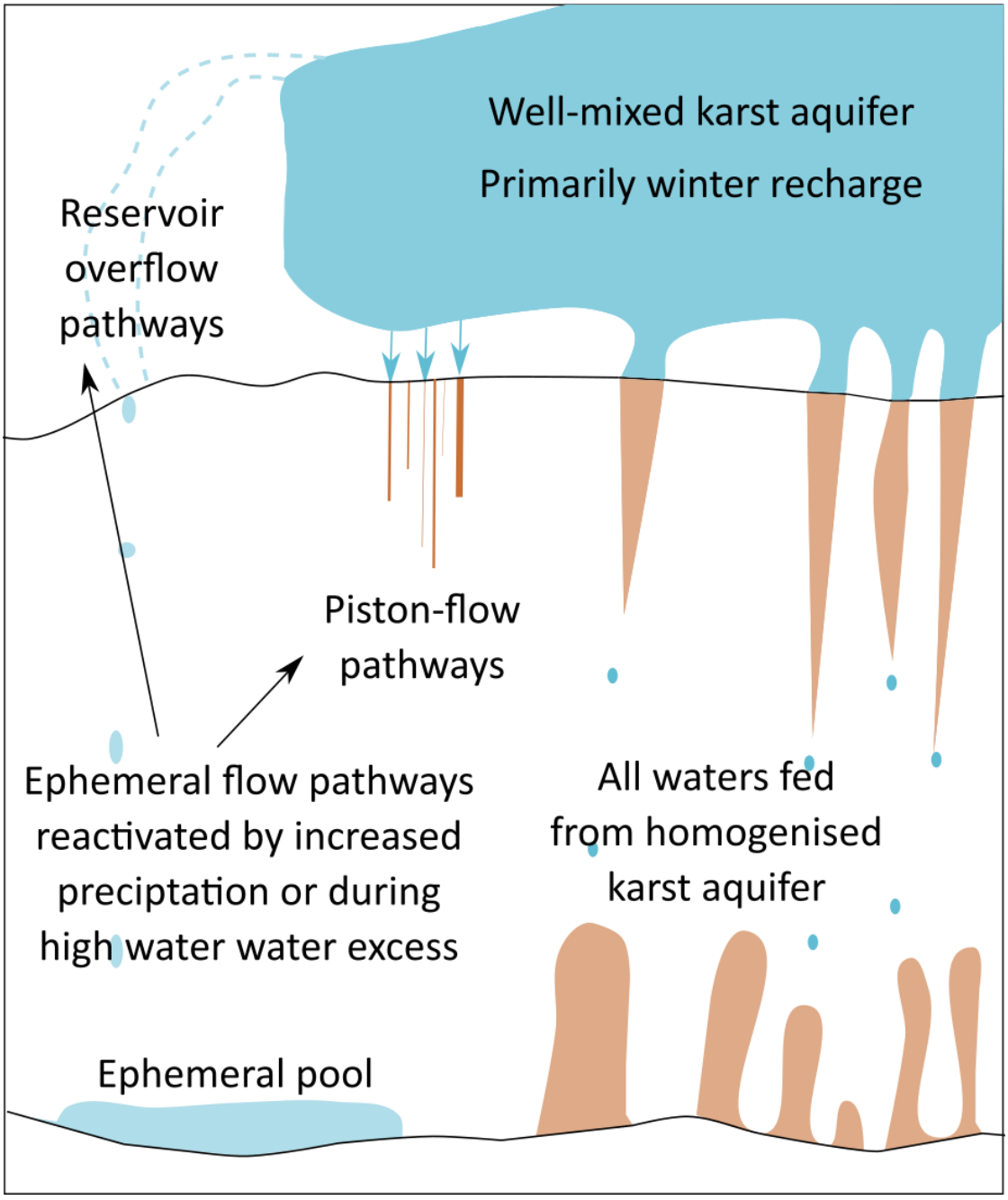

Figure 5.14: Schematic of karst and cave hydrology from Cueva de las Perlas.

5.5 Using calcite plates to determine isotopic equilibrium

Using artificial growth surfaces to collect deposited calcite has been extensively studied within the literature (Tremaine *et al.,* 2011; Day and Henderson, 2011; Tremaine and Froelich, 2013; Wang *et al.* 2018). Calcite grown within the cave environment can be used to determine the nature of isotopic fractionation between modern deposition and contemporary drip waters. Within Cueva de las Perlas, calcite plates were grown discontinuously between 2010 to 2017 to investigate whether the calcite deposited is forming in isotopic equilibrium with the drip waters.

Ten calcite plates were placed within Cueva de las Perlas under four different drip sites since 2010. Each of the locations is marked on a schematic map (figure 5.15) and field photos are shown in figure 5.16 to demonstrate the locations of some of the plates and the set-up. Plate locations, durations, associated drip sites and water sources are provided in table 5.3.

Table 5.3: Calcite plates collected from Cueva de las Perlas and associated drip sites and water sources. ** denotes when no direct $\delta^{18}O_{dw}$ data is available and therefore an average of all available data has been used.*

Plate	**Growth period**	**Collection**	**Associated drip site**	**Drip water source**
CP11	1 year	2011	P3	P3 I*
CP13	~1.5 - 2 years	2013	P3	P3 I*
CP1-15	~1.5 - 2 years	2015	P1	P1 I*
CP1-16	1 year	2016	P1	P1 I Apr-15 to Apr-16
CP3-16	1 year	2016	P1	P1 I Apr-15 to Apr-16
CP1 S-16	6 months	2016	P1	P1 I Apr-16 to Sep-16
CP1 W-17	6 months	2017	P1	P1 I Oct-16 to Mar-17
CP2-17	1 year	2017	P1	P1 I Apr-16 to Mar-17
CP3 S-16	6 months	2016	P1	P1 I Apr-16 to Sep-16
CP3 W-16	6 months	2017	P1	P1 I Oct-16 to Mar-17

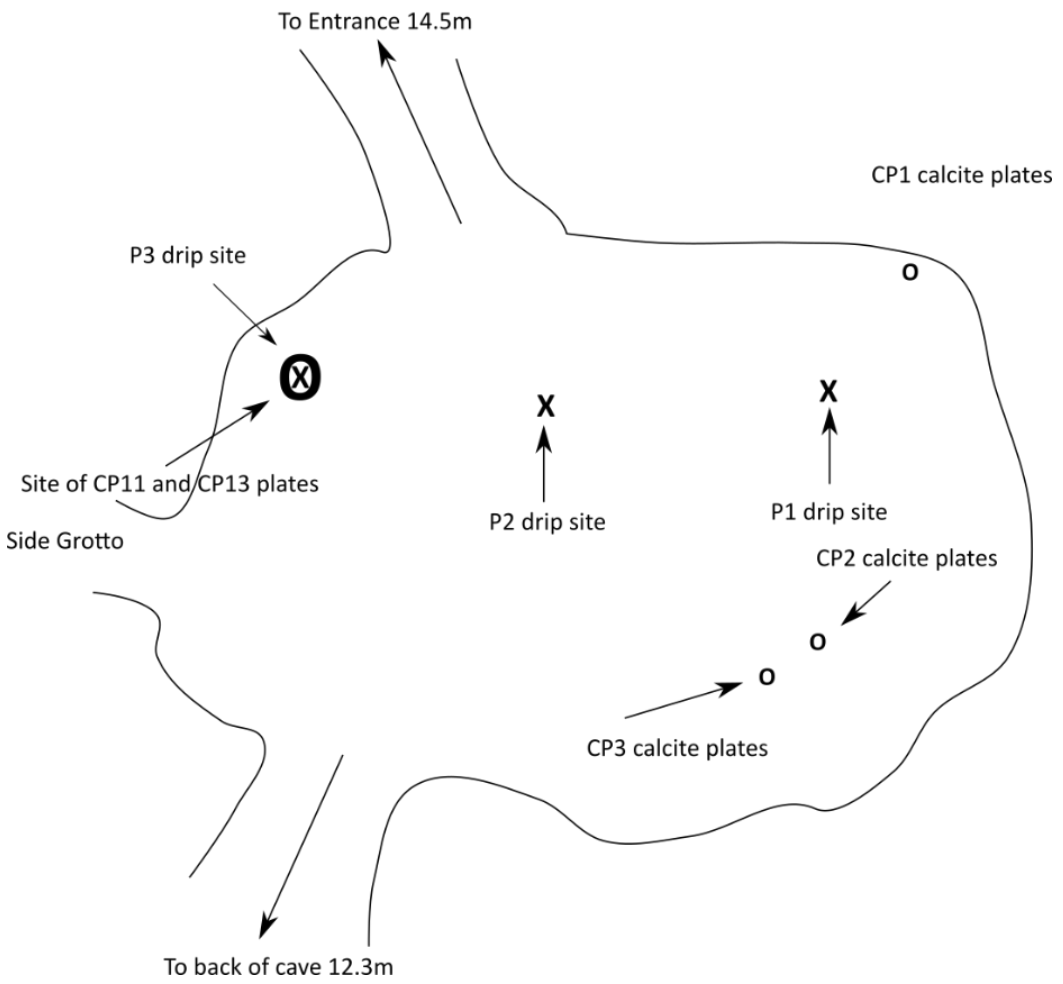

Figure 5.15: Calcite plate locations.

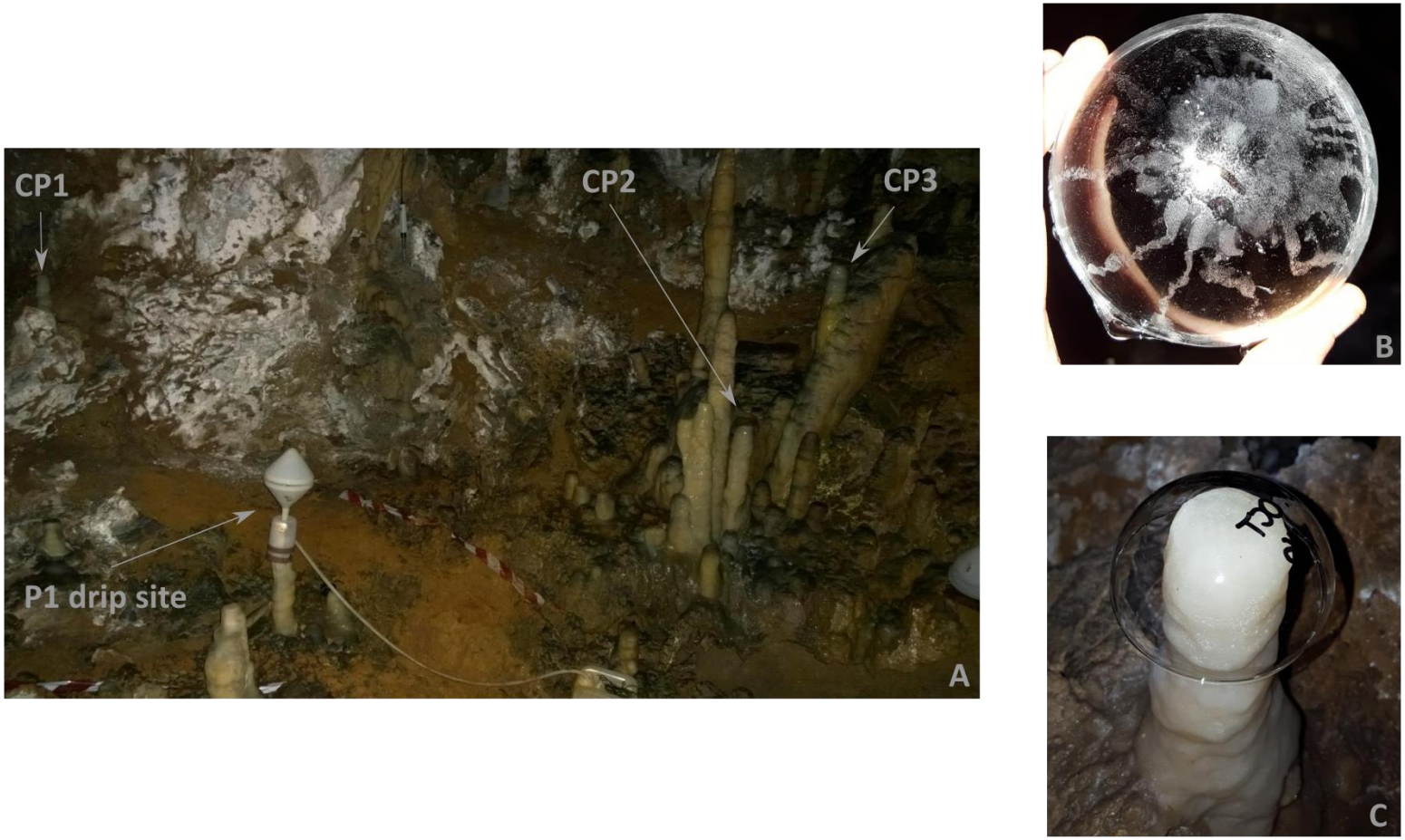

Figure 5.16: Field photos of calcite plates. A illustrates the placement of calcite plates CP1, CP2 and CP3 in relation to the P1 drip site. B is of P1 S-16 growth after collection in Oct-16. C demonstrates the calcite plate set-up of P1 W-16 after placement in Oct-16 prior to calcite deposition.

The plates were removed from the cave and calcite was carefully extracted using a scalpel. Samples were taken from two transects at approximately 1cm intervals across the plate. Sampling strategy for the plates is demonstrated in figure 5.17. After collection, samples were analysed for oxygen and carbon isotopes and the results are summarized in table 5.4.

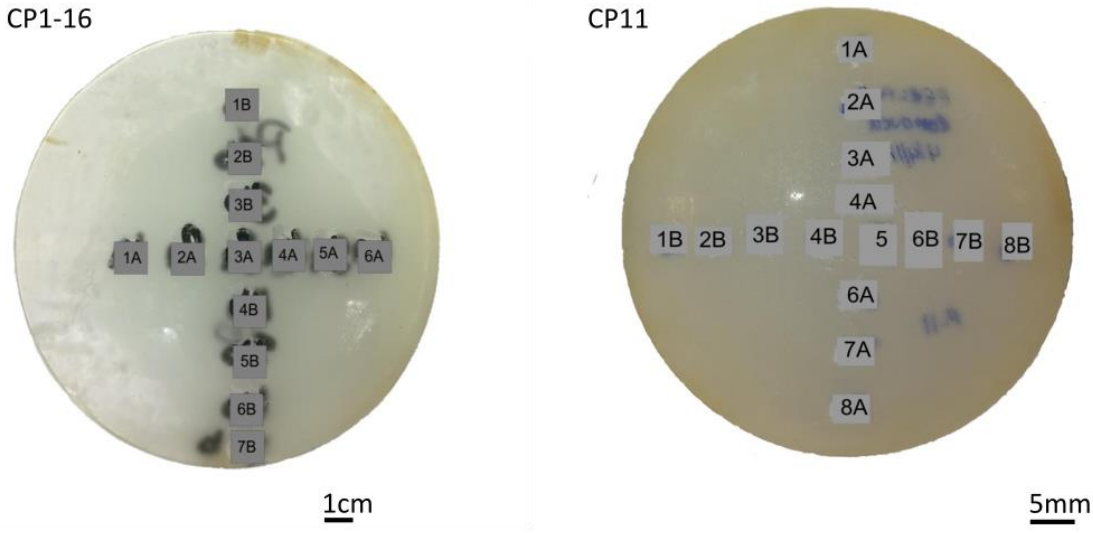

Figure 5.17: Isotope sampling strategy for calcite plates CP1-16 and CP11.

Table 5.4: Oxygen and carbon isotope composition of calcite plates.

Sample name	**Plate type**	**Number of samples**	**Average $\delta^{18}O$ (‰)**	**Range $\delta^{18}O$ (‰)**	**Centre value $\delta^{18}O$ (‰)**	**Average $\delta^{13}C$ (‰)**	**Range $\delta^{13}C$ (‰)**	**Centre value $\delta^{13}C$ (‰)**
CP11	Annual	15	-5.78	0.94	-5.76	-11.21	1.06	-10.94
CP13	Multi-annual	15	-4.01	2.75	-2.55	-9.74	2.79	-9.44
CP1-15	Multi-annual	8	-4.79	0.19	-4.88	-10.10	0.94	-10.64
CP1-16	Annual	10	-5.04	0.28		-10.40	1.07	-10.59
CP3-16	Annual	12	-5.18	0.80	-5.25	-9.13	0.54	-9.17
CP1 S-16	Seasonal (summer)	1	-5.29			-10.32		
CP1 W-16	Seasonal (winter)	4	-5.60	0.09	-5.62	-10.88	0.24	-10.74
CP2-16	Annual	2	-4.23	0.13		-7.12	0.14	
CP3 S-16	Seasonal (summer)	5	-4.66	0.71	-4.26	-8.32	0.88	-7.86
CP3 W-16	Seasonal (winter)	5	-4.87	0.26	-5.01	-9.17	0.71	-9.44

5.5.1 Determining isotopic equilibrium using within-plate isotopic analyses

5.5.1.1 Multi-annual calcite plates

Multi-annual plates CP1-15 and CP13 show within plate variability along transects (figure 5.18 and table 5.5). This variability in $\delta^{18}O$ values combined with a correlation between $\delta^{18}O$ and $\delta^{13}C$ values across individual transects is indicative of kinetic fractionation influencing the chemical composition of these calcite plates.

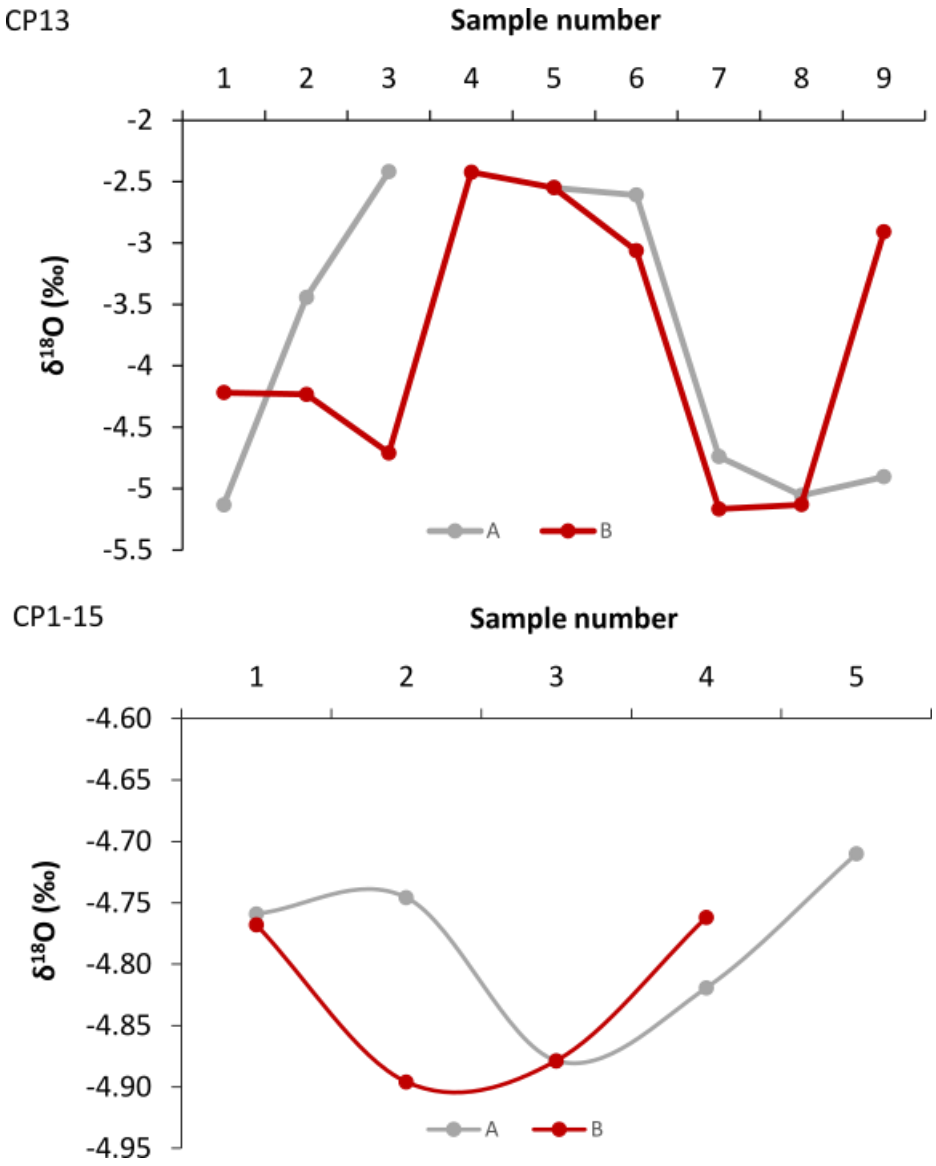

Figure 5.18: Variability in $\delta^{18}O$ values across transects for CP13 and CP1-15 calcite plates.

Table 5.5: Summary of transect indicators of equilibrium deposition ($\delta^{18}O$ average, standard deviation, R_2 between $\delta^{18}O$ and $\delta^{13}C$ values and within transect range) for CP13 and CP1-15 calcite plates.

Plate	Transect	Average $\delta^{18}O$ (‰)	Stdev	R^2 between $\delta^{18}O$ and $\delta^{13}C$	Transect range (‰)
CP1-15	A	-4.78	0.07	0.86	0.17
	B	-4.83	0.07	0.50	0.13
CP13	A	-3.86	1.22	0.63	2.72
	B	-3.82	1.10	0.34	2.74

5.5.1.2 Annual calcite plates

Similar to the multi-annual plates, the annual plates (CP11, CP1-16 and CP3-16) exhibit significant variability in $\delta^{18}O$ values along individual transects (figure 5.19 and table 5.6). Plates CP11 and CP3-16 show a correlation between $\delta^{18}O$ and $\delta^{13}C$ values which may imply kinetic deposition. In contrast, CP1-16 does not show a correlation and exhibits a low standard deviation for $\delta^{18}O$ values which would suggest equilibrium deposition. The different indicators used herein to determine equilibrium or kinetic deposition appear contradictory depending on which is chosen. For example, if only variability in $\delta^{18}O$ values is used, CP1-16 identifies kinetic deposition. However, if R^2 between $\delta^{18}O$ and $\delta^{13}C$ values is used, CP1-16 indicates equilibrium deposition.

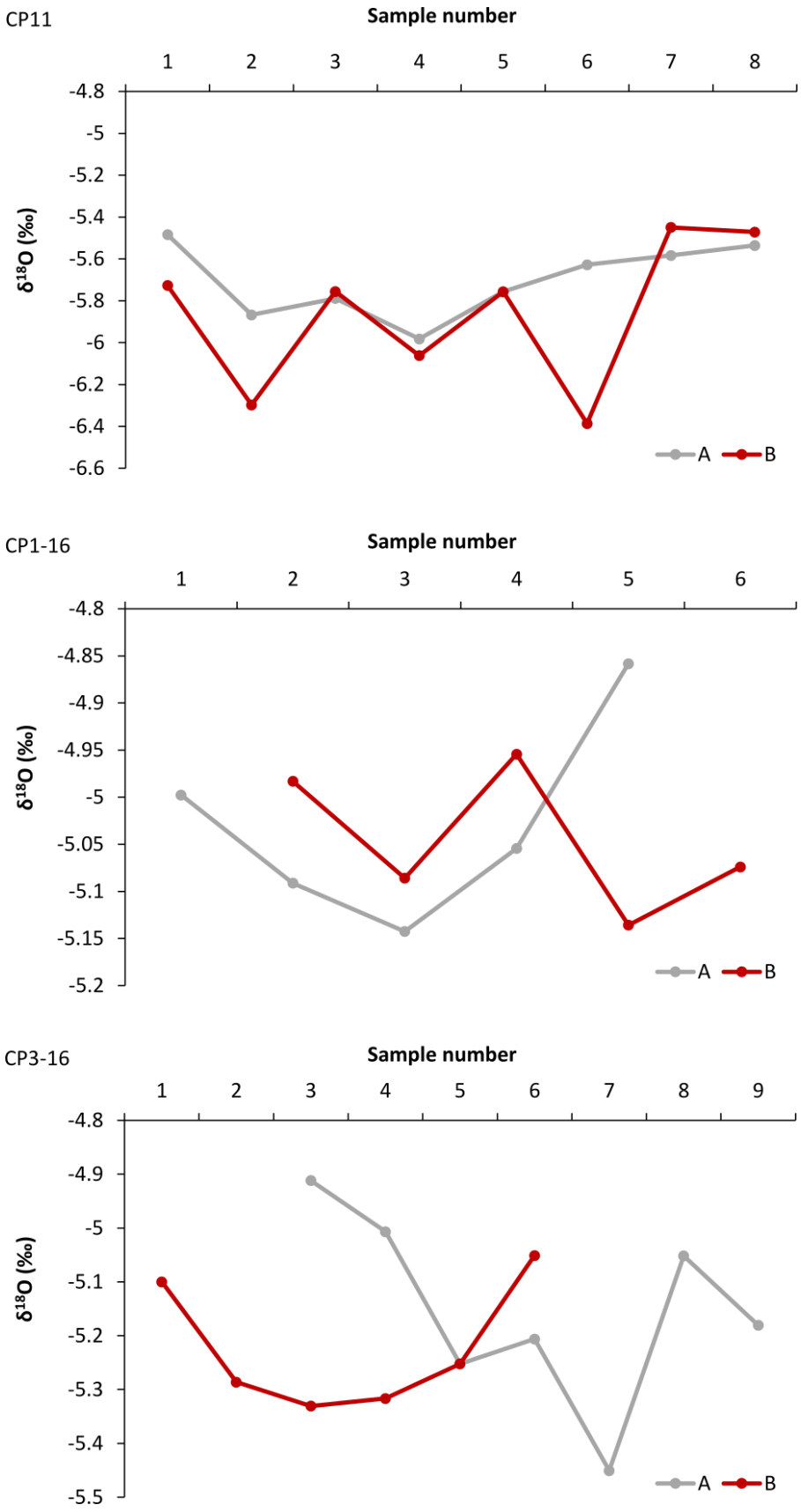

Figure 5.19: Variability in $\delta^{18}O$ values across transects for CP11, CP1-16 and CP3-16 calcite plates.

Table 5.6: Summary of transect indicators of equilibrium deposition ($\delta^{18}O$ average, standard deviation, R_2 between $\delta^{18}O$ and $\delta^{13}C$ values and within transect range) for CP11, CP1-16 and CP3-16 calcite plates.

Plates	Transect	Average $\delta^{18}O$ (‰)	Stdev	R^2 between $\delta^{18}O$ and $\delta^{13}C$	Transect range (‰)
CP11	A	-5.70	0.17	0.58	0.50
	B	-5.86	0.35	0.29	0.94
CP1-16	A	-5.03	0.11	0.04	0.28
	B	-5.05	0.08	0.08	0.18
CP3-16	A	-5.15	0.18	0.52	0.54
	B	-5.22	0.12	0.96	0.28

5.5.1.3 Seasonal calcite plates

Due to insufficient material precipitated on CP1 W-16, CP3 S-16 and CP3 W-16, isotopic variability along individual transects could not be determined. However, seasonal plates demonstrate within plate variability (table 5.7). P3 S-16 and P3 W-16 exhibit significant ranges in $\delta^{18}O$ values and correlation between $\delta^{18}O$ and $\delta^{13}C$ values which implies kinetic fractionation during calcite precipitation. In contrast, P1 W-16 suggests equilibrium deposition due to a minimal range in $\delta^{18}O$ values and lack of correlation between oxygen and carbon isotope values.

Table 5.7: Summary of indicators of equilibrium deposition ($\delta^{18}O$ average, standard deviation, R_2 between $\delta^{18}O$ and $\delta^{13}C$ values and within transect range) for CP1 W-16, CP3 S-16 and CP3 W-16 calcite plates.

Plate	Average $\delta^{18}O$ (‰)	Stdev	R^2 between $\delta^{18}O$ and $\delta^{13}C$	Transect range (‰)
P3 S-16	-4.66	0.30	0.78	0.71
P3 W-16	-4.87	0.09	0.77	0.25
P1 W-16	-5.60	0.04	0.02	0.09

A Hendy test (Hendy, 1971) will involve examining isotope values along a single growth layer in a speleothem to determine isotopic equilibrium. Modern calcite growth from Cueva de las Perlas has shown isotope values can vary across transects and therefore equilibrium deposition may not be assumed along a single growth lamina.

Additionally, the relationship between $\delta^{18}O$ and $\delta^{13}C$ values can vary between transects in a single plate. Therefore, the R^2 between $\delta^{18}O$ and $\delta^{13}C$ values should not be used as an indicator of equilibrium deposition. Equilibrium deposition may also be modelled through $\delta^{18}O$ dripwater ($\delta^{18}O_{dw}$) values and this is investigated below.

5.5.2 Determining isotopic equilibrium through dripwater modelling

In order to determine whether or not calcite has been deposited in equilibrium, a theoretical $\delta^{18}O_c$ was calculated from $\delta^{18}O_{dw}$ values. To model the temperature-dependent oxygen isotope fractionation factor two equations were used (eq. 5.5 and eq. 5.6).

$1000\ln\alpha = 18.03\ (10^3T^{-1}) - 32.42$ (Kim and O'Neil, 1997) Eq. 5.5

$1000\ln\alpha = 16.1 \pm 0.65\ (10^3T^{-1}) - 24.6 \pm 2.2$ (Tremaine *et al.,* 2011) Eq. 5.6

Where α is the fractionation factor and T is the temperature in Kelvin.

After the theoretical fractionation factor was calculated using one of the above equations, eq. 5.7 was used to determine the calcite oxygen isotope composition on the PDB scale (Fuller *et al.,* 2008).

$\delta^{18}O_c = 0.97002 * (\alpha * (1000 + \delta^{18}O_{dw}) - 1000) - 29.98$ (Fuller *et al.,* 2008) Eq. 5.7

The modelled $\delta^{18}O_c$ values are presented and compared to $\delta^{18}O_c$ values from the calcite plate (table 5.8). Each $\delta^{18}O_c$ value modelled through equations 5.5 and 5.6 is presented as a range, taking into account the minimum and maximum $\delta^{18}O_{dw}$ input values. Figure 5.20 is a visual representation of these results.

When modelled through the Kim and O'Neil (1997) equation, four of the ten calcite plates (CP11, P1-16, P3-16 and P1-17) lie within predicted equilibrium (table 5.8, figure 5.20). The remaining six plates could therefore be interpreted to lie outside theoretical equilibrium and oxygen isotope values of precipitated calcite may reflect kinetic isotope effects. Conversely, when the Tremaine *et al.* (2011) equation is applied, seven of the ten plates lie within the typical cave specific water-calcite isotope fractionation range. The primary difference between the two equations is that the Kim and O'Neil (1997) represents laboratory grown calcite, whilst the Tremaine *et al.* (2011) equation

represents natural cave systems and is calculated using different cave sites from different latitudes and altitudes.

True equilibrium fractionation remains difficult to identify in both laboratory and cave environments due to the complex nature of the kinetic effects which may influence the oxygen isotope composition of calcite. Speleothems with $\delta^{18}O$ values lying outside the predicted range of equilibrium (calculated using the associated $\delta^{18}O$ values of associated dripwaters) can still be utilised within speleothem palaeoclimate studies particularly if the disequilibrium effects can be accounted for. McDermott *et al.* (2011) demonstrated that due to the close relationships between speleothem isotope values and longitude, speleothems from Europe can be used as recorders of rainfall and air temperature during the Holocene despite not precisely reflecting calculated equilibrium values.

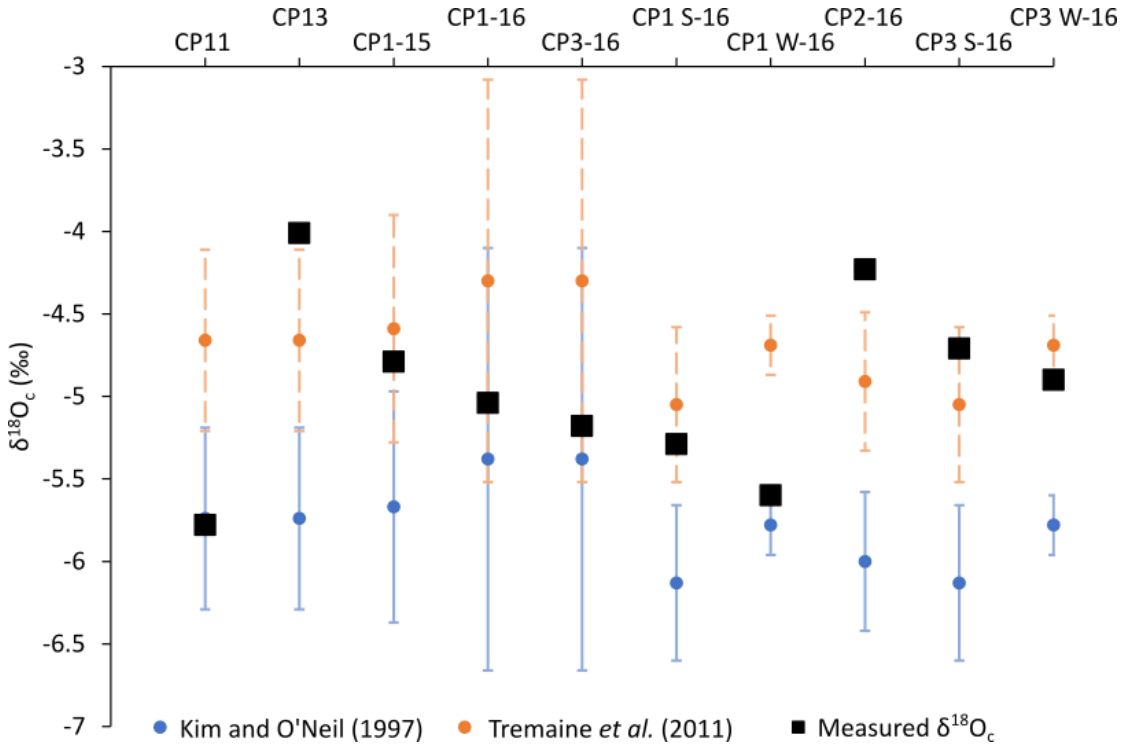

Figure 5.20: Comparison of modelled (Kim and O'Neil, 1997; Tremaine et al. 2011) and measured oxygen isotope values from calcite plates.

*Table 5.8: Determination of isotopic equilibrium using calcite plates. Actual $\delta^{18}O_c$ values from calcite plates and modelled $\delta^{18}O_c$ values calculated through Kim and O'Neil (1997) and Tremaine et al. (2011). Parameters used in the fractionation factor calculations have been included in the table. * denotes when no direct $\delta^{18}O_{dw}$ data is available and therefore an average of all available data has been used.*

Plate	Growth period	$\delta^{18}O_c$ value	$\delta^{18}O_c$ range	R^2 ($\delta^{18}O_c$ & $\delta^{13}C_c$)	Cave temperature (K)	$\delta^{18}O_{dw}$	$\delta^{18}O_{dw}$	$\delta^{18}O_{dw}$	Drip water source	Kim and O'Neil (1997)			Tremaine *et al.* (2010)		
						Max	Min	Average		Max	Min	Average	Max	Min	Average
CP11	1 year	-5.78	0.94	0.37	286.57	-5.24	-6.34	-5.79	P3 I*	-5.19	-6.29	-5.74	-4.11	-5.21	-4.66
CP13	~1.5 - 2 years	-4.01	2.75	0.4	286.57	-5.24	-6.34	-5.79	P3 I*	-5.19	-6.29	-5.74	-4.11	-5.21	-4.66
CP1-15	~1.5 - 2 years	-4.79	0.19	0.62	286.57	-5.28	-6.42	-5.72	P1 I*	-4.97	-6.36	-5.67	-3.89	-5.03	-4.59
P1-16	1 year	-5.04	0.28	0.01	286.57	-4.53	-6.36	-5.44	P1 I Apr-15 to Apr-16	-6.66	-4.16	-5.38	-3.39	-5.22	-4.30
P3-16	1 year	-5.18	0.80	0.65	286.57	-4.53	-6.36	-5.44	P1 I Apr-15 to Apr-16	-6.66	-4.16	-5.38	-3.39	-5.22	-4.30
P1 S-16	6 months	-5.29			286.69	-5.69	-6.63	-6.16	P1 I Apr-16 to Sep-16	-5.66	-6.60	-6.13	-4.58	-5.52	-5.05
P1 W-16	6 months	-5.60	0.09	0.02	287.04	-5.56	-5.92	-5.74	P1 I Oct-16 to Mar-17	-5.60	-5.96	-5.78	-4.51	-4.87	-4.69
P2-16	1 year	-4.23	0.13		286.86	-5.57	-6.41	-5.99	P1 I Apr-16 to Mar-17	-5.58	-6.42	-6.00	-4.49	-5.33	-4.91
P3 S-16	6 months	-4.71	0.71	0.61	286.69	-5.69	-6.63	-6.16	P1 I Apr-16 to Sep-16	-5.66	-6.60	-6.13	-4.58	-5.52	-5.05
P3 W-16	6 months	-4.90	0.26	0.77	287.04	-5.56	-5.92	-5.74	P1 I Oct-16 to Mar-17	-5.60	-5.96	-5.78	-4.51	-4.87	-4.69

5.5.3 Summary

Analysis of calcite plates has provided evidence for kinetic deposition of calcite through within-plate variability in oxygen isotope values and positive correlation of $\delta^{18}O$ and $\delta^{13}C$ values. However, modelling of calcite using drip water isotope composition has highlighted the complexities when predicting isotopic equilibrium with $\delta^{18}O_{dw}$ calculated through either the Tremaine *et al.* (2011) or the Kim and O'Neil (1999) equations. However, variability within plates (even those indicated to be in isotopic equilibrium) demonstrates the importance of sampling along the central growth axis and stresses the limitations of a Hendy test for testing isotopic equilibrium deposition in speleothem studies.

5.6 Karst hydrological modelling of the oxygen isotope composition of cave dripwaters and calcite

The oxygen isotope composition of speleothems is influenced by various processes including the isotopic composition of precipitation, mixing within the soil, vadose zone and cave and within cave oxygen isotope fractionation (Hartmann and Baker, 2017). Baker and Bradley (2010) demonstrated that variations in karst hydrology can lead to interannual variability of 0.5-1.2‰ in the $\delta^{18}O$ values of speleothem calcite. Therefore, karst hydrological variability may influence the oxygen isotope composition of speleothems which could modify interpretation of palaeoclimate records. Forward modelling approaches combine $\delta^{18}O$ values from precipitation, surface climate parameters and a relatively simple karst model to model the $\delta^{18}O$ values of cave drip water and speleothem calcite (Baker and Bradley, 2010; Bradley *et al.,* 2010; Hartmann and Baker, 2017). Hydrological modelling of the oxygen isotope systematics allows variability related to karst hydrological processes to be accounted for within interpretations of speleothem palaeoclimate records (Bradley *et al.,* 2010; Hartmann and Baker, 2017).

5.6.1 Modelling of drip water and the oxygen isotope composition of calcite

A simple spreadsheet-based forward model was used to quantify the uncertainty in speleothem oxygen isotope records related to processes within the overlying soil and

karst above Cueva de las Perlas (Baker and Bradley, 2010). The spreadsheet was acquired from A. Baker (pers. comm) and is the same linear hydrological model used in the Baker and Bradley (2010) study which is summarized in figure 5.21. Monthly precipitation amount, monthly average temperature and the oxygen isotope composition of precipitation ($\delta^{18}O_p$) were the inputs into the model. Precipitation and temperature were used to calculate water excess using the Thornthwaite (1948) equation (eq. 5.1). Annually weighted $\delta^{18}O_p$ was calculated and input into the model.

The model parameters were the total storage capacity (S), the amount of water stored in the reservoir at any given time (St), the initial reservoir capacity (St_i) and the outflow rate (v) (figure 5.21). Within the model, reservoir capacity, initial reservoir capacity and outlet size were altered to model different scenarios. The output is modelled $\delta^{18}O_{dw}$ which was then converted into modelled $\delta^{18}O_c$ assuming equilibrium fractionation between $\delta^{18}O_{dw}$ and $\delta^{18}O_c$ using the equation of Tremaine *et al.* (2011 – eq. 5.6) and the conversion to PDB of Fuller *et al.* (2008 – eq. 5.7).

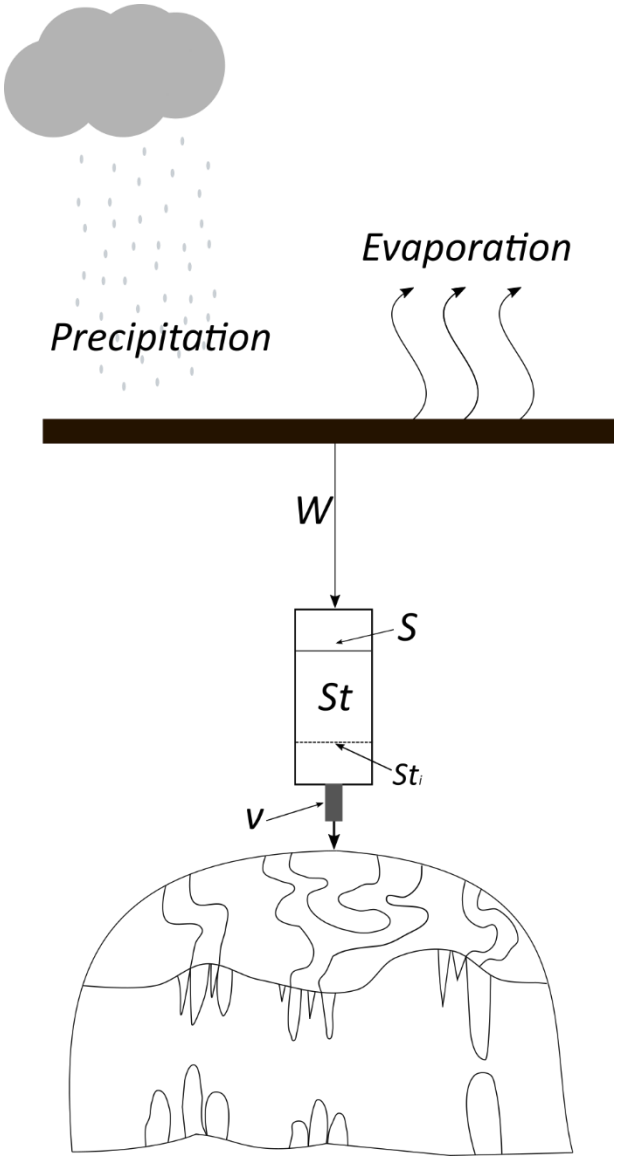

Figure 5.21: Schematic of the karst hydrological model of Baker and Bradley (2010). The diagram is redrawn based upon that presented in Baker and Bradley (2010). In the diagram W is mean annual water excess (or amount of infiltration into the karst), S is the total storage capacity within the reservoir, St_i is the initial reservoir capacity, St is the total storage capacity at a given point and v is the outlet size.

Three models were run with the altered parameters listed in table 5.9. The models used data from Matienzo rainfall, temperature and $\delta^{18}O_p$ from 2012-2017. Data from before Feb-2015 were collected by Smith (2014) and for months without data monthly averages were used. This model accurately portrays the system as it uses climatic data

collected from Matienzo and runs between September to August which captures the hydrological year.

Table 5.9: Parameters used within the hydrological models. W represents the mean annual water excess which for Matienzo was calculated to be 1023mm per year.

Model	***S***	***St$_i$***	***v***
Model 1	Six times *W*	66% of *S*	100% *W*
			80% *W*
			60% *W*
			40% *W*
			20% *W*
Model 2	2000 times *W*	10% of *S*	10% *W*
			100% *W*
			150% *W*
			200% *W*
Model 3	Six times *W*	66% of *S*	*100% W*
		50% of *S*	
		33% of *S*	

Model 1 (figures 5.21 1A and 1B) was produced by modelling changes in *v* at 20%, 40%, 60%, 80% and 100% of the mean annual water excess. In this model, *S* is six times mean annual water excess and *St$_i$* is 66% of total reservoir capacity. Figure 5.22 1A indicates there is a low inter-annual variability (<0.4‰) at all outlet sizes. At higher output sizes (*v*), the impact of variable annual water excess is evident. For example, it is evident that 2015, a year of low water excess, was followed by a year of high water excess in 2016 and this is demonstrated by a 0.36‰ decrease in $\delta^{18}O_{dw}$ (where v = 100% W). It must be noted that inter-annual variability in $\delta^{18}O_{dw}$ is muted at the majority of outlet sizes, with variability across the record typically <0.4‰. As a consequence, the $\delta^{18}O_c$ model (figure 5.22 1B) indicates minimal inter-annual variability (<0.4‰) in the oxygen isotope composition of calcite.

Model two has been produced by increasing *S* to 2000 times mean annual water excess and setting *St$_i$* to 10%. Variations in *v* have been modelled at 10%, 100%, 150% and 200% of mean annual water excess. Minimal variability is expressed in $\delta^{18}O_{dw}$ values in model 2 with variation of 0.01‰ (figure 5.22 2A) as a result of the large volume of water stored within the reservoir. This model limits inter-annual variability based upon the high volume of water within the reservoir and therefore mixing of

water reduces the impact of any annual variation in $\delta^{18}O_{dw}$ and $\delta^{18}O_c$ values (figure 5.22 2B).

In Model 3, *S* is set to six times mean annual water excess, *v* is equivalent to mean annual water excess and St_i is varied to 66%, 50% and 33% of *S* (figure 5.22 3A). Variations in the $\delta^{18}O$ composition of dripwater are exhibited in years of high water excess following a year of low water excess and vice versa. An example is shown by a modelled 0.65‰ decrease in $\delta^{18}O_{dw}$ values between 2015, a year of low water excess, and 2016, a year of high water excess (where St_i = 33% of S). This relationship is also demonstrated by a fall of 0.67‰ in $\delta^{18}O_c$ values (figure 5.22 3B). Therefore, smaller initial reservoir sizes demonstrate an increased sensitivity to variations in water excess which subsequently influence $\delta^{18}O_{dw}$ values.

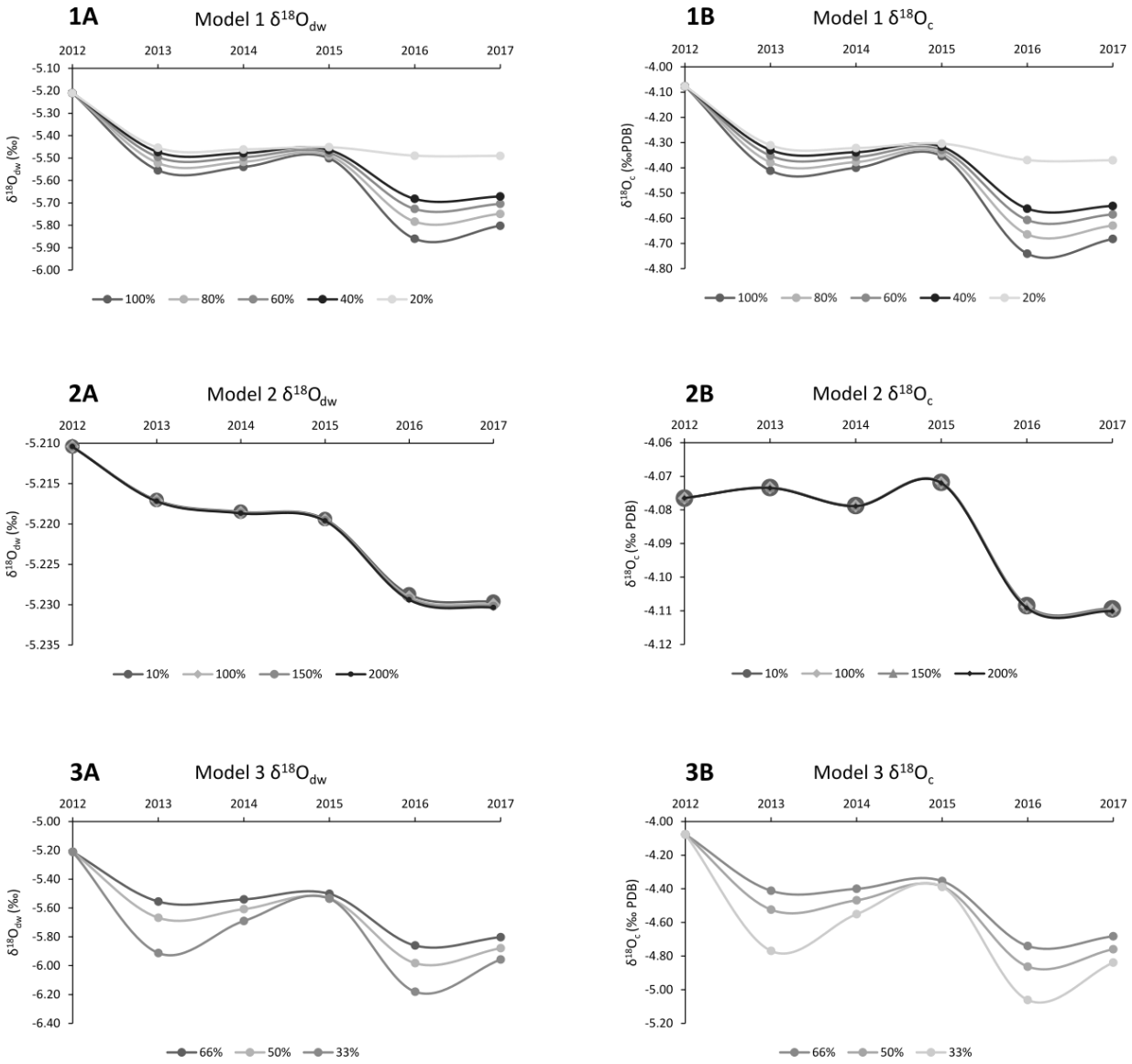

Figure 5.22: Modelled oxygen isotope values from three hydrological models. The models were produced using the Baker and Bradley (2010) model. Modelled results are $\delta^{18}O_{dw}$ (1A, 2A and 3A) and $\delta^{18}O_c$ (1B, 2B and 3B) for years between 2012-2017 inclusive.

5.6.2 Karst hydrological $\delta^{18}O$ modelling and calcite plate variability

Calcite plates CP1-15 and CP1-16 are used herein to assess the models of inter-annual variability in $\delta^{18}O$ values for modelled calcite. The calcite plate $\delta^{18}O$ values record a 0.25‰ reduction in 2016 relative to 2015. This variability may arise from the relatively low water excess (1070mm) compared to the higher water excess (1347mm) in 2016

which is predicted by the models as a reduction in $\delta^{18}O_{dw}$ and $\delta^{18}O_c$ values. Due to the low water excess in 2015, initial reservoir size in 2016 is reduced. Consequently, the lowered $\delta^{18}O_p$ value of -6.67‰ (compared to the higher $\delta^{18}O_p$ value of -5.39‰ from 2015) is reflected in the modelled $\delta^{18}O_{dw}$ values. Variability of -0.25‰ is predicted in modelled $\delta^{18}O_c$ values between 2015 and 2016 in model 1 when outlet size is modelled as 40% of water excess, with a reservoir capacity six times the mean annual water excess and an initial reservoir size of 66%.

5.6.3 Summary

The models in this section were produced using temperature, precipitation and $\delta^{18}O_p$ data collected from Matienzo between 2011-2016. The various models produced demonstrate the inter-annual variability in dripwaters and calcite is minimal (<0.4‰). Therefore, inter-annual variations in karst-hydrology have a negligible influence on the isotopic composition of dripwaters and subsequently speleothem calcite. The one exception to this is when changes to the size of the initial reservoir are applied. Shrinking the initial reservoir size (model 3) leads to inter-annual shifts of ~0.7‰ when water excess is variable. It must be noted these shifts are significant at inter-annual timescales, but the resolution of the current project will act to average out this variability.

5.7 Evaluating PCO_2 in dripwaters

5.7.1 Dripwater saturation state and CO_2 equilibrium with cave air

Dripwater saturation state and PCO_2 provide information about the extent of degassing. Drip water PCO_2 should be in chemical equilibrium with cave air PCO_2 and therefore drip water saturation state is a function of cave air PCO_2 (Tremaine *et al.,* 2011). Cave atmosphere has a lower PCO_2 than the cave drip waters, hence this drives the degassing and drip waters lose CO_2. This means there should be a fall in dripwater PCO_2 as pH increases and precipitation of $CaCO_3$ occurs increasing the saturation state. Drip water PCO_2 has been calculated through WEB_PHREEQ (Saini-Eidukat and Yahin,

1999; Saini-Eidukat, 2018) and the results have been compared to monthly cave air CO_2 (figure 5.23). WEB-PHREEQ is an online version of the PHREEQC aqueous geochemical modelling program of Parkhurst (1995) and is accessible online (Saini-Eidukat and Yahin, 1999; Saini-Eidukat, 2018). Inputs into the model were pH, temperature, bicarbonate (calculated through Ca + Mg ueq/l), cations (Ca, Na, K and Mg) and anions (Cl and SO_4). The drip water PCO_2 lies distinctly above the equilibrium line predicted by Tremaine *et al.* (2011) suggesting that the drip waters within Cueva de las Perlas were not completely degassed prior to collection and therefore do not lie in equilibrium with PCO_2 of the cave air. It is unexpected that none of the waters lie upon the equilibrium line as the majority of the waters have been collecting in the for cave one month or more (bulk and pool waters).

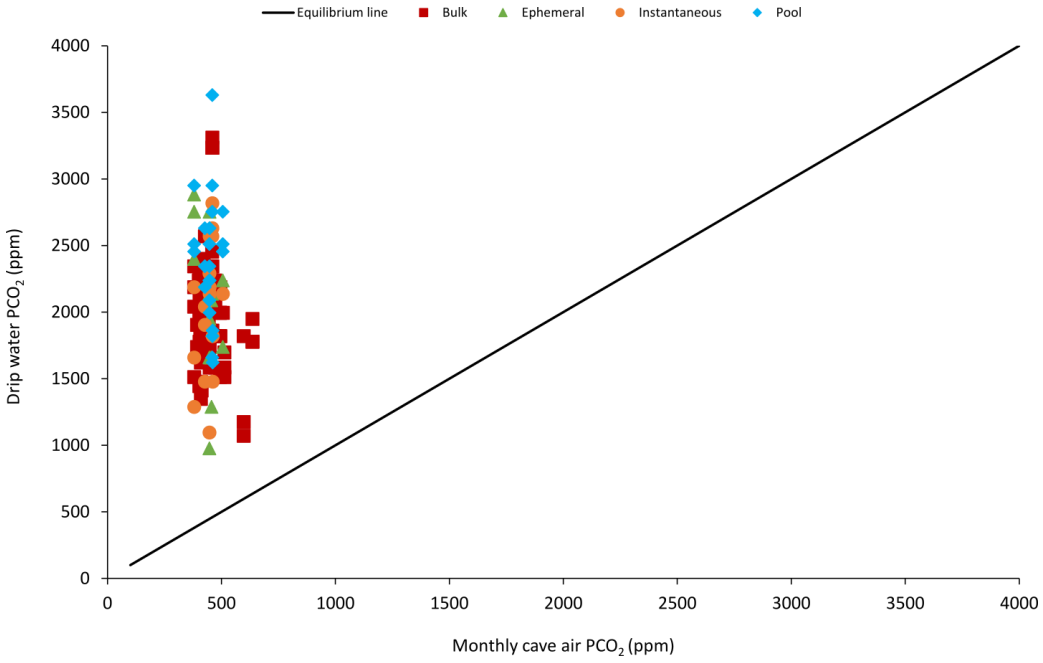

Figure 5.23: Monthly cave air CO_2 (ppm) and drip water PCO_2 (ppm).

Tremaine *et al.* (2011) identified a strong hyperbolic relationship between cave air PCO_2 and drip water saturation state. In the Cueva de las Perlas drip waters, the saturation state does not correlate to dripwater PCO_2 ($R^2 = 0.06$) (figure 5.24A) or cave air PCO_2 ($R^2 = 0.02$) (figure 5.24B). This relationship supports the findings in figure 5.23 suggesting incomplete degassing of dripwaters or potentially equilibration of waters with a higher PCO_2 atmosphere.

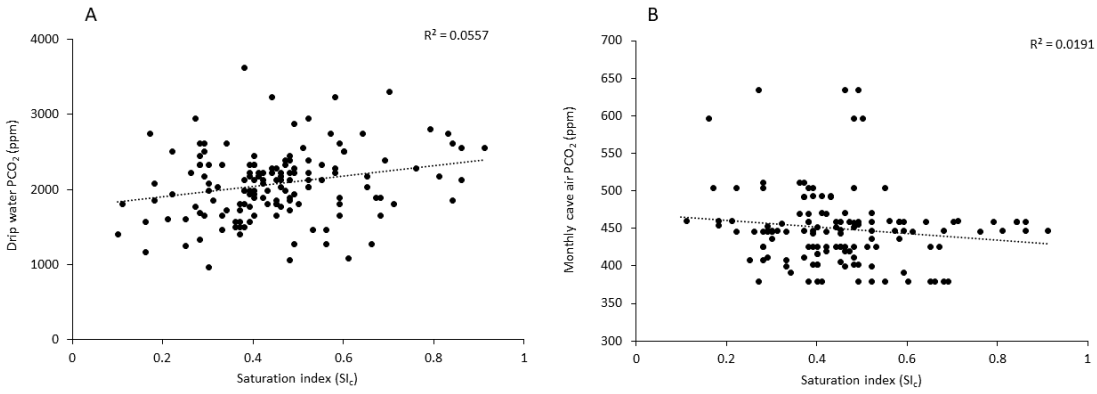

Figure 5.24: Relationships between calcite saturation index (SI_c) and dripwater PCO_2 (A) and SI_c and monthly cave air PCO_2 (B).

However, instantaneous samples demonstrate a correlation between saturation state and PCO_2 dripwater (figure 5.25A). A positive correlation between the variables in figure 5.25A suggests instant waters have degassed and precipitated $CaCO_3$ as a result of PCO_2 dripwater equilibration with PCO_2 cave air prior to collection (Tremaine *et al.,* 2011). Additionally, the correlation shown in figure 5.25B suggests that it is more useful to compare instantaneous waters and spot measurements taken on the same day. Therefore, future studies should aim to collect instantaneous waters over a period not exceeding 24hours and to take a corresponding CO_2 measurement.

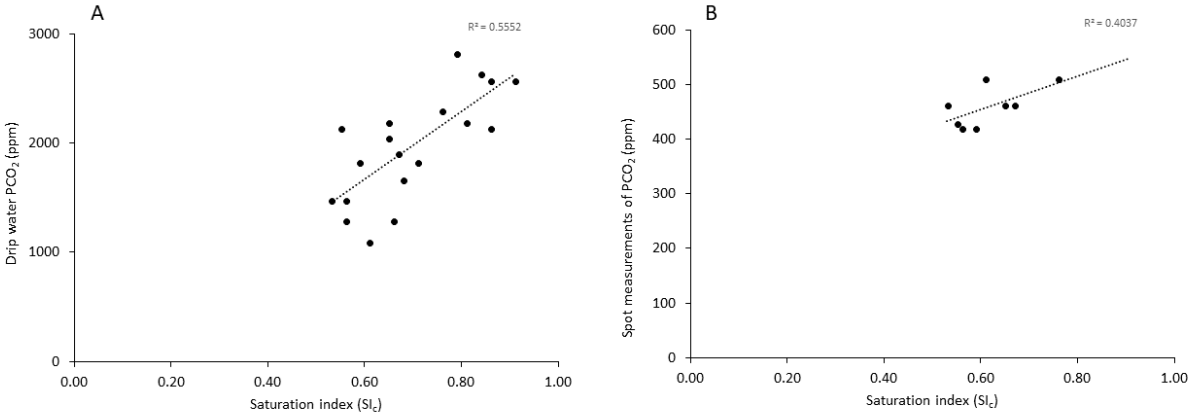

Figure 5.25: Relationships between instantaneous drip water saturation state, drip water PCO_2 and cave air PCO_2. Instantaneous drip water saturation state and drip water pCO_2 (A) and drip water saturation state and cave air PCO_2 (B). Cave air PCO_2 measurements represent spot measurements taken when drip water sampling was undertaken.

Section 4.4.3 demonstrated the variable CO_2 concentrations within Cueva de las Perlas are related to diurnal oscillations in temperature dynamics between external and internal temperatures. As CO_2 is variable on a short-term basis, the measurement of CO_2 taken on the collection date may not be the same as when the water degassed and therefore instantaneous measurements provide a better indication of the true nature of the relationship between saturation state and PCO_2 in the dripwaters and cave air. Additionally, as highlighted by Smith (2014), high PCO_2 dripwater may reflect limitations of bulk collection techniques. The bulk water collection method limits air flow and water may be equilibrating with an artificially high PCO_2 atmosphere as a result. However, the diurnal oscillations in PCO_2 of cave air may cause the cave waters to always lie out of equilibrium with cave atmospheric conditions.

5.7.2 Summary

The saturation state of waters from Cueva de las Perlas does not appear to be a function of cave air PCO_2 as predicted by Tremaine *et al*. (2011). However, this may be

due to a longer residence time in the cave prior to collection. Subsequently, future studies should aim to examine contemporaneous instant water samples and cave air PCO_2. Alternatively, this may be a function of rapidly changing cave air PCO_2 which results in disequilibrium between cave drip waters and prevailing cave atmospheric conditions.

5.8 Electrical conductivity in dripwaters

5.8.1 Spot measurements of electrical conductivity

Spot measurements for pools, instantaneous and ephemeral drips were carried out during field visits. Bulk water spot measurements of EC have been measured monthly. Electrical conductivity measurements for each of the drip water types are displayed in figure 5.26. Electrical conductivity varies seasonally and for the majority of water types electrical conductivity was highest in winter and lowest in summer.

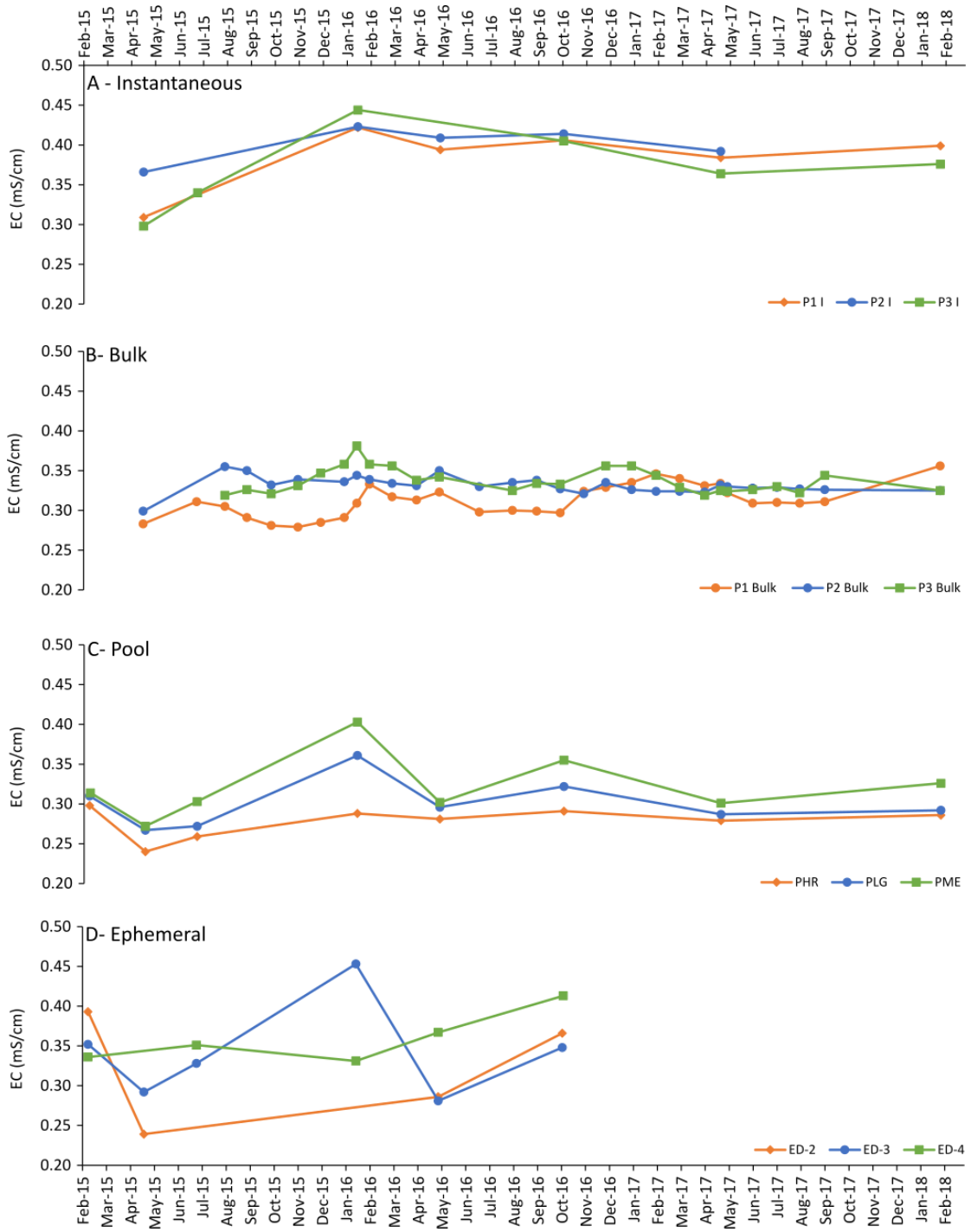

Figure 5.26: Electrical conductivity spot measurements from instantaneous drips (A), bulk waters (B), pools (C) and ephemeral drips (D).

5.8.2 Continuous P2 record of electrical conductivity

A continuous record of specific conductivity (at 25°C) (referred to herein as electrical conductivity) has been collected since Jun-15 from the P2 drip site (figure 5.27) using

the method described in section 3.5.4.2. The overall range of the dataset is 0.053mS/cm with a minimum value of 0.324mS/cm and a maximum value of 0.377mS/cm. The average value of the dataset was 0.337 mS/cm with annual average values of 0.344 mS/cm, 0.336 mS/cm and 0.337 mS/cm for 2015, 2016 and 2017 respectively.

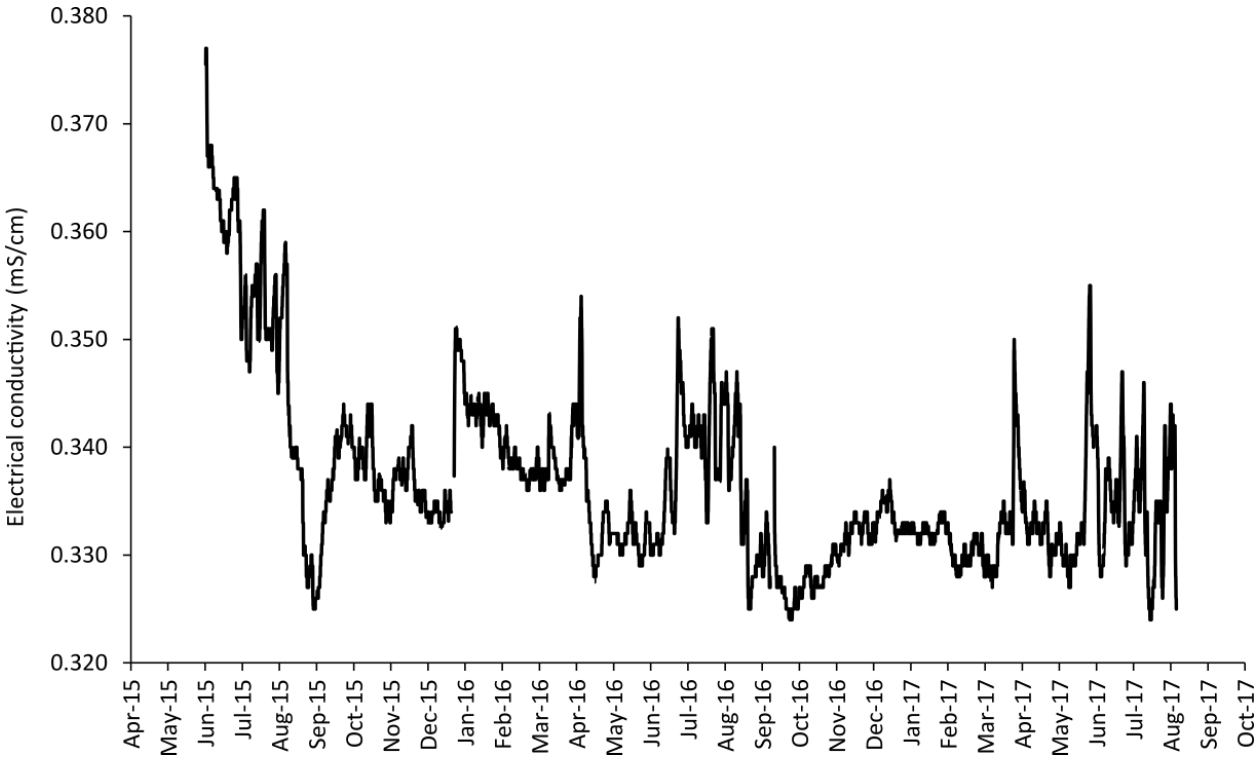

Figure 5.27: Hourly electrical conductivity at 25°C for P2 water.

5.8.3 Mechanisms driving electrical conductivity variability

5.8.3.1 Karst hydrology and drip rates

Previous studies have identified karst residence times as a forcing mechanism driving variations in electrical conductivity (Borsato, 1997; Miorandi *et al.,* 2010). In these studies, periods of water deficit increase residence times of water in the karst and lead to a subsequent rise in EC. However, rock water contact times do not appear to drive EC variations in Cueva de las Perlas (figure 5.28), with a distinct decline in EC during a period of water deficit in Sep-15.

A drip rate control has previously been identified in other studies such as Genty and Deflandre (1998) and Fernandez-Cortes *et al.* (2007) related to increased hydraulic pressure associated with periods of high water excess. An increase in EC and drip rate is observed as supersaturated waters are forced out of pores and microfissures in the karst. The decline in EC in Sep-15 is accompanied by a distinct decline in drip rate and occurs during a period of water deficit (figure 5.28). However, after Jan-16 the variability in EC appears to be independent of drip rate and therefore, drip rate cannot be the primary forcing mechanism driving electrical conductivity variations.

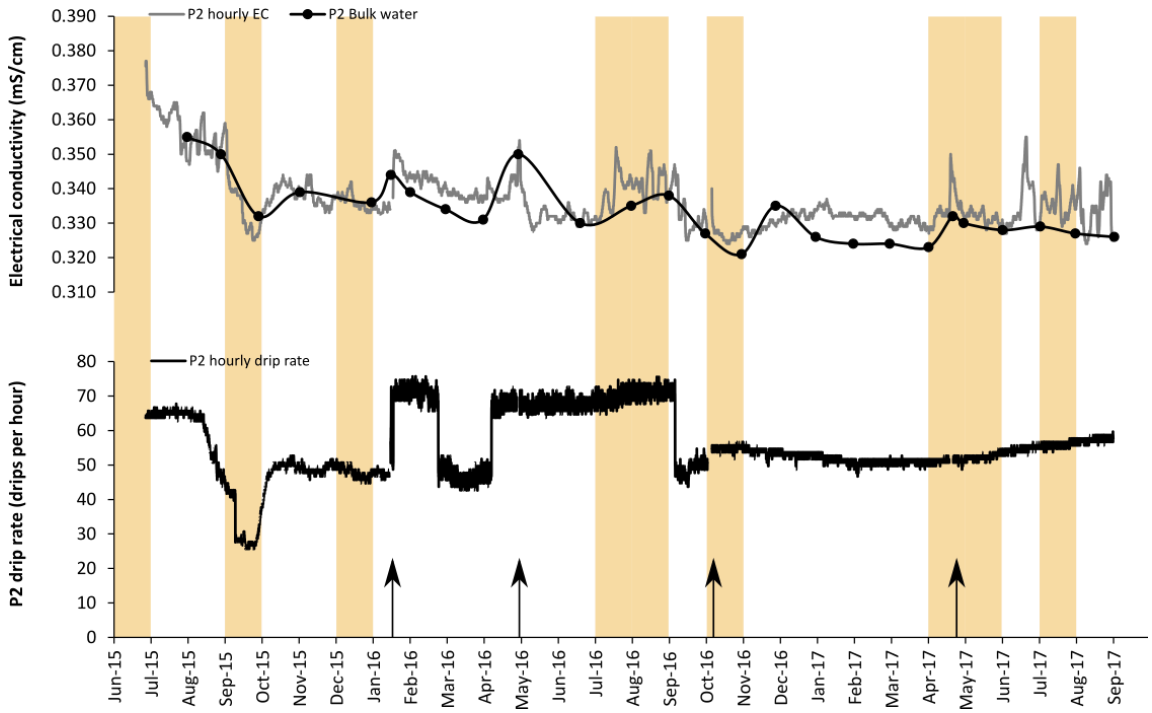

Figure 5.28: Electrical conductivity and drip rate. Both hourly electrical conductivity and monthly bulk measurements are shown alongside the P2 hourly drip rate record. Arrows mark manual logger repositioning by the PI. Yellow shading denotes periods of water deficit.

5.8.3.2 Carbon dioxide

A third control mechanism is proposed as electrical conductivity (EC) varies during relatively "stable" periods of drip rate and water excess conditions. This final mechanism is related to variations in CO_2 with periods of reduced CO_2 corresponding to decreases in EC.

The seasonal relationship demonstrated by the spot measurements breaks down when individual events are considered within the P2 continuous EC record. The P2 continuous EC record demonstrates rapid responses in EC corresponding to variability in CO_2 concentrations (figure 5.29). In addition, daily CO_2 and daily EC from P2 exhibit a positive correlation of 0.74, 0.51 and 0.62 for 2015, 2016 and 2017 respectively (figure 5.30). High CO_2 concentrations within the cave result in limited degassing potential of infiltrating drip water and therefore retain Ca^{2+} ions in the solution. In contrast, low CO_2 concentrations within the cave enhance degassing and remove Ca^{2+} ions from the solution due to $CaCO_3$ precipitation thereby decreasing EC values.

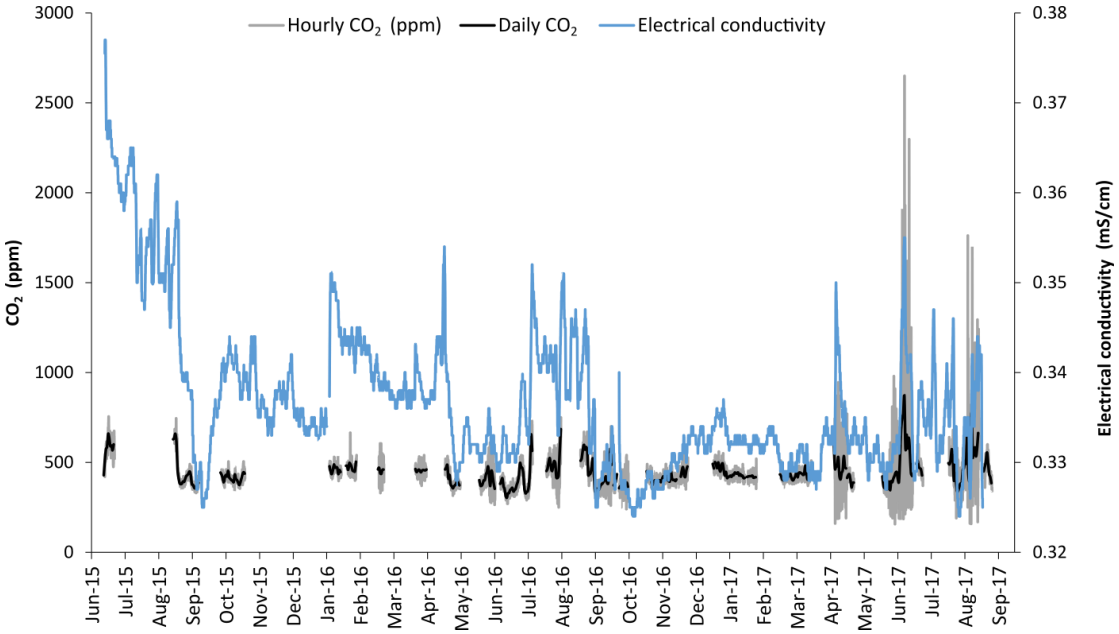

Figure 5.29: Hourly CO_2 and hourly electrical conductivity from the P2 drip site.

Section 4.4 demonstrated cave air CO_2 responds rapidly to ventilation changes when external temperatures fall below internal cave temperatures. The differences in temperature result in a density driven air flow between the external and internal environments and lead to a reduction in CO_2 within the cave due to the inflow of external CO_2-poor air. This ventilation occurs throughout the year and even in summer external temperatures exhibit a large diurnal range and ventilation within the cave occurs. When ventilation is strong EC decreases as a result of reduced CO_2 in the cave which enhances the degassing of drip waters resulting in calcite precipitation and loss of Ca^{2+} ions from the solution. Conversely when ventilation is weak, high CO_2 levels

act to limit degassing of drip waters and EC remains relatively high. This pattern has previously been identified in nearby Asiul Cave by Smith *et al.* (2015).

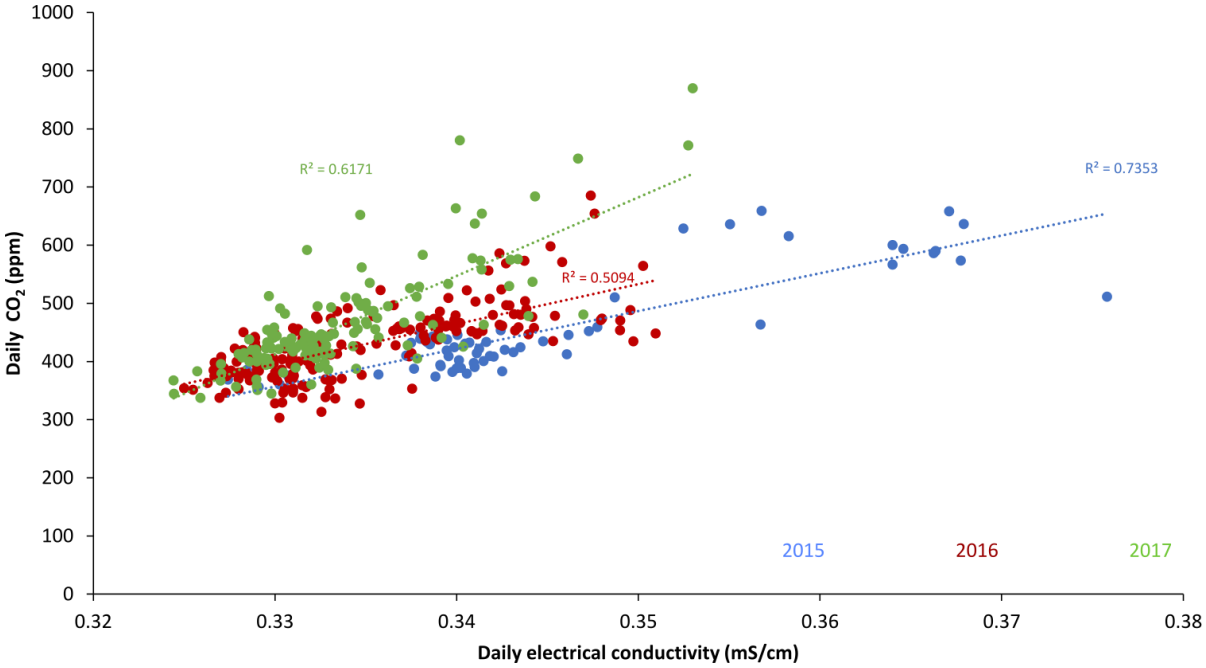

Figure 5.30: Scatter plot of daily electrical conductivity and daily cave air CO_2 organized by year.

5.8.3.3 Short-term oscillations in EC

Logging was undertaken at hourly and sub-hourly intervals for EC, CO_2, cave pressure, internal temperature and external temperature; providing a unique insight into the chemical responses of dripwaters to variations in cave ventilation dynamics either through density-driven ventilation or through pressure-influenced ventilation. This section will use a case study from June 2017 to examine the EC response to variations in ventilation dynamics.

June 2017 EC case study

The addition of EC data builds upon the pressure-model discussed in section 4.4.3.5. Between 10/6/17 and 28/6/17 external temperatures were consistently higher than cave temperatures (figure 5.31). As a result, density-driven ventilation was weakened and there was a subsequent build-up of CO_2 within the cave which lead to a gradual rise in EC. However, the sharp rise in EC on 17/6/17 is coincident with the onset of

declining external pressure. A reduction in pressure would lead to a pressure gradient between external and internal air and result in the movement of air out of Cueva de las Perlas. A fall in cave pressure would act to draw down CO_2-rich air from the karst, increasing cave air CO_2 which would limit degassing and concentrate Ca^{2+} ions in solution. Therefore, the parameters in June 2017 identify a period of weakened density-driven cave ventilation causing CO_2 concentration to rise within the cave. This regime is heightened by a period of low pressure leading to the addition of karstic CO_2-rich air into the cave void.

5.8.4 Summary

Electrical conductivity in Cueva de las Perlas dripwaters has varied throughout the monitoring period. Prior to Jan-16, variations appear to coincide with low drip rates during periods of water deficit (section 5.8.3.1). However, this relationship is not consistent and variations in density-driven and pressure-induced ventilation have been determined as the primary forcing mechanisms driving EC variability.

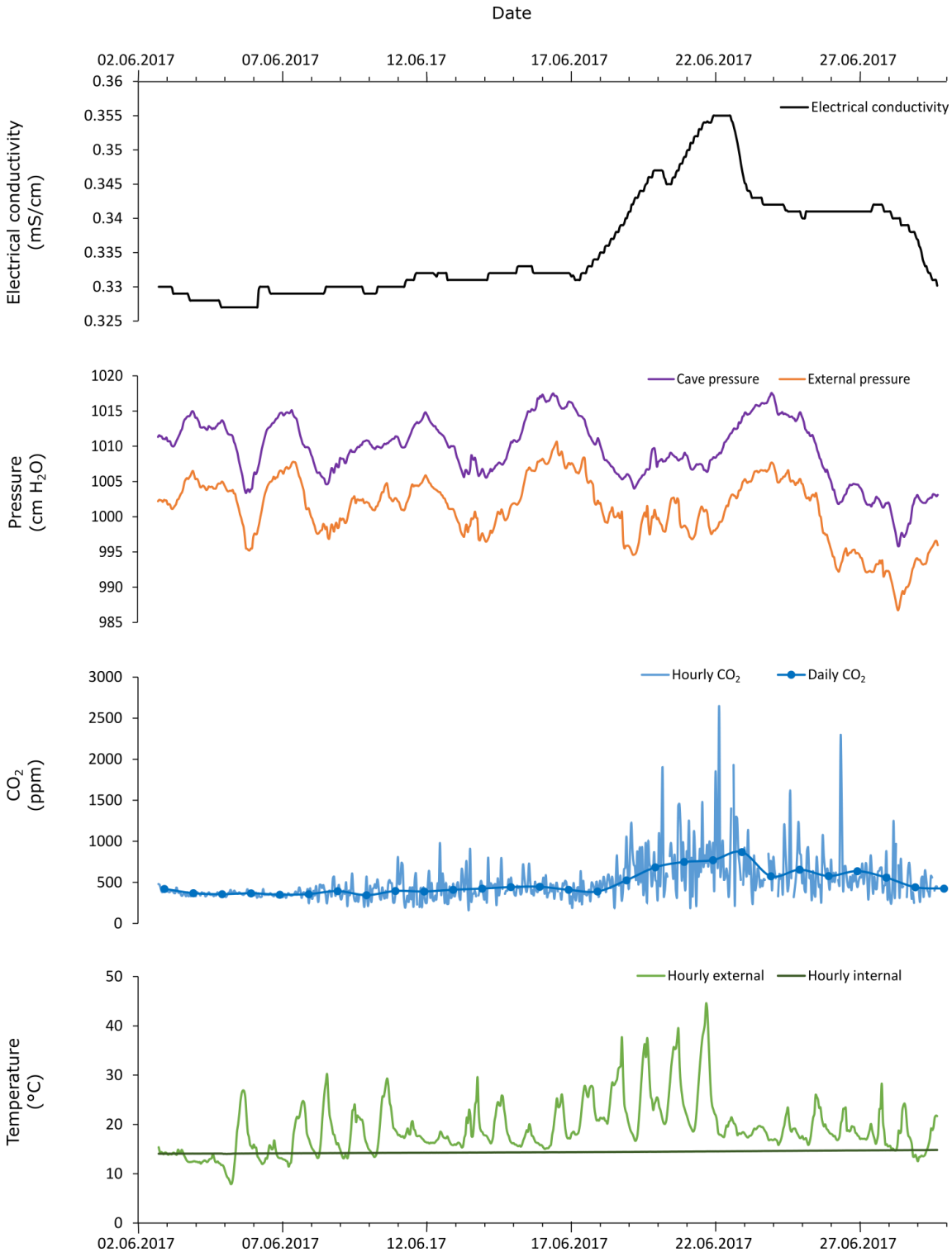

Figure 5.31: Dripwater electrical conductivity and monitored cave parameters (pressure, CO_2 and temperature) between 2/6/17 and 30/6/17.

5.9 Dissolved inorganic carbon in dripwaters

5.9.1 Seasonality in dissolved inorganic carbon

5.9.1.1 Seasonal trends in $\delta^{13}C$ values

Carbon isotopes within dissolved inorganic carbon were measured in the Cueva de las Perlas dripwaters between Aug-15 to Jul-16 and Apr-17 to Dec-17. Primarily bulk water was sampled monthly but instantaneous samples were taken by the PI during fieldwork. The bulk water data is presented in figure 5.32. P1 bulk waters demonstrate the largest range of 4.83‰ whilst those of P2 and P3 are smaller at 3.89‰ and 3.68‰ respectively. Although a full year was not sampled, the highest $\delta^{13}C$ values occur in late summer (Sep-15) and the lowest in winter and early spring (Jan-16 and Mar-17).

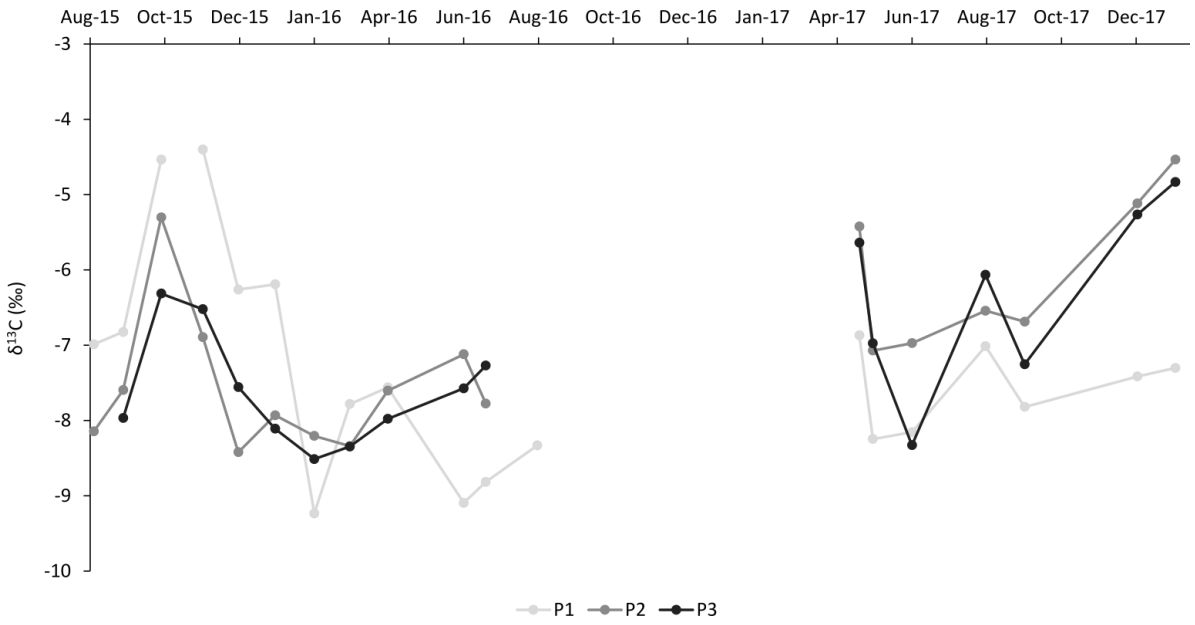

Figure 5.32: Carbon isotope composition of bulk cave dripwaters.

5.9.1.2 Soil and vegetation processes as drivers of seasonal $\delta^{13}C$ change

Seasonal productivity as a function of temperature and moisture availability may influence the carbon isotope composition of cave dripwaters. Figure 5.33 presents soil CO_2 and $\delta^{13}C$ values from the three bulk water collections (P1, P2 and P3) as well as monthly soil temperature. In 2015, maximum $\delta^{13}C$ values lag maximum summer temperatures by ~3 months. However, the 2016 and 2017 data do not appear to conform to this trend. This may relate to missing data within the soil temperature record and DIC samples. It must be noted that not all of the variability within the DIC record can be explained by variations in soil temperature and soil CO_2 and therefore the influence of a secondary mechanism is investigated below.

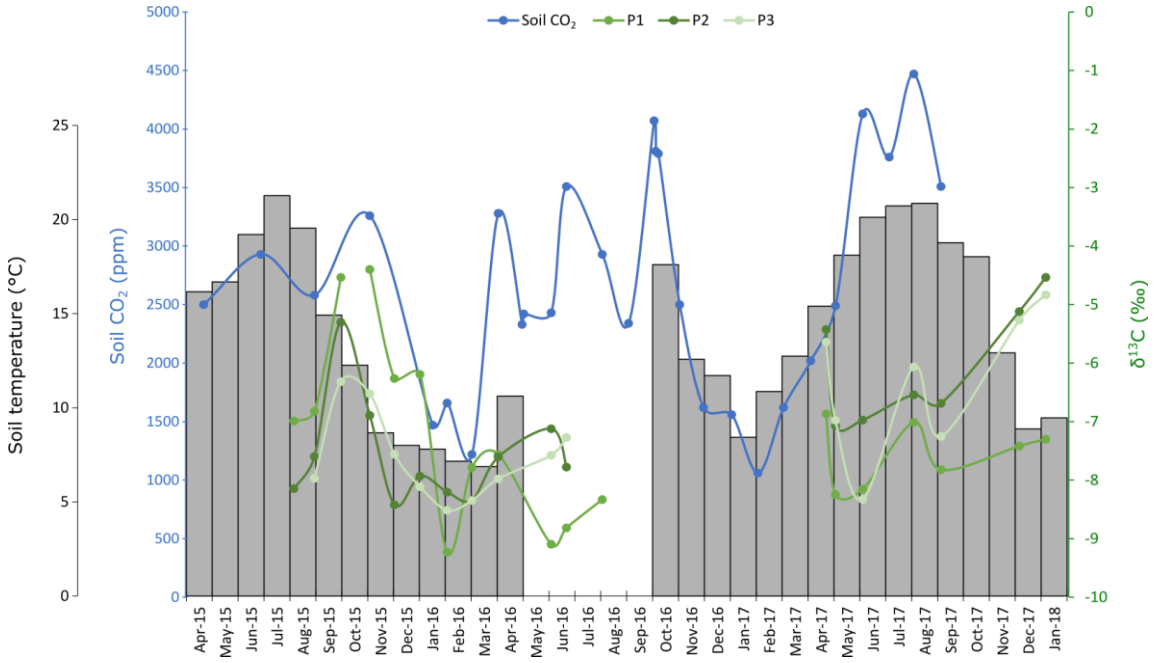

Figure 5:33: Soil temperature, soil CO2 and δ13C values from bulk waters. Bars indicate soil temperature.

5.9.1.3 Karst hydrological processes as drivers of seasonal $\delta^{13}C$ change

Variations within carbon isotopes appear to correspond to changes in water excess/deficit and therefore are partly a function of the amount of water infiltrating into the karst system (figure 5.34). Periods of water deficit correlate to increases in carbon isotope values. Two processes may be responsible for increased $\delta^{13}C$ values within the dripwater during periods of water deficit, bedrock dissolution and/or prior

calcite precipitation. Both processes would lead to an increase in carbon isotope values in the drip waters. However, not all increases in carbon isotope values correspond to periods of water deficit. The erratic nature of the bulk water carbon isotope composition may be an artefact of the bulk water collection method. Bulk waters have collected over a period of one month and the effect of within-cave degassing cannot be determined. Therefore, instantaneous values have also been considered below.

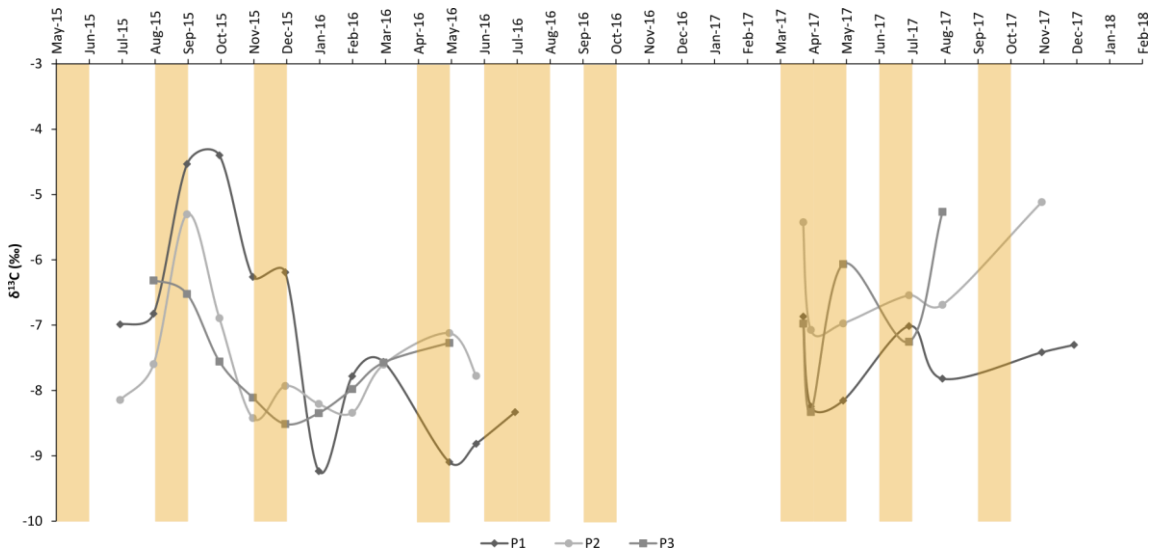

Figure 5.34: Carbon isotope values from bulk water collections. Periods of water deficit are represented by the orange shading.

5.9.2 Dissolved inorganic carbon in instantaneous dripwaters

The carbon isotopes in the instantaneous drip waters are significantly lower than those collected from the bulk collections (table 5.10, figure 5.35). This pattern would be expected as bulk waters have time to degas and under Rayleigh-fractionation processes lighter ^{12}C is lost to the cave void. Clark and Fritz (1997) have established equilibrium fractionations for $\delta^{13}C$ from soil gas to drip water CO_3^{2-} as an enrichment of 8.6‰ in ^{13}C between phases at 15°C. Smith (2014) previously calculated an equilibrium dissolved carbon $\delta^{13}C$ value of ~-10.1‰ based upon average soil carbon isotope values of -18.7‰. However, data collected between 2015-2017 indicate a lowered soil gas $\delta^{13}C$ value with an average of -22.02‰. Therefore, in this study, the equilibrium dissolved carbonate value is calculated to be -13.42‰.

Table 5.10: Average instantaneous and bulk carbon isotope values for the different drip sites.

Sample	Instantaneous	Bulk
P1	-11.46	-7.31
P2	-11.39	-7.09
P3	-9.81	-7.09

The solid arrow on figure 5.34 demonstrates the theoretical equilibrium between average soil air and cave waters. The dashed arrow represents the additional fractionation undergone by the P1 instantaneous waters. The instantaneous and bulk waters presented in figure 5.34 are less negative than the theoretical dissolved carbon $\delta^{13}C$ value (-13.42‰) representing additional fractionation.

Prior calcite precipitation and bedrock dissolution are the proposed mechanisms driving the increase in $\delta^{13}C$ values within instantaneous drip waters. Prior calcite precipitation within the karst leads to a preferential incorporation in ^{12}C within carbonate and leaves the solution enriched in ^{13}C. Bedrock dissolution within a closed system will also act to increase $\delta^{13}C$ values within drip waters (Smith, 2014). The influence of within cave processes such as degassing is interpreted herein as minimal due to the collection time of less than 24hours.

5.9.3 Summary

Dripwaters within Cueva de las Perlas demonstrate an isotopic enrichment in ^{13}C relative to the soil air. Karst processes such as bedrock dissolution and PCP have increased $\delta^{13}C$ values within the cave dripwaters. Further investigation of the influence of these processes on trace elements is shown in section 5.10. Finally, degassing has led to higher carbon isotope values within the bulk and pool waters compared to the instantaneous waters.

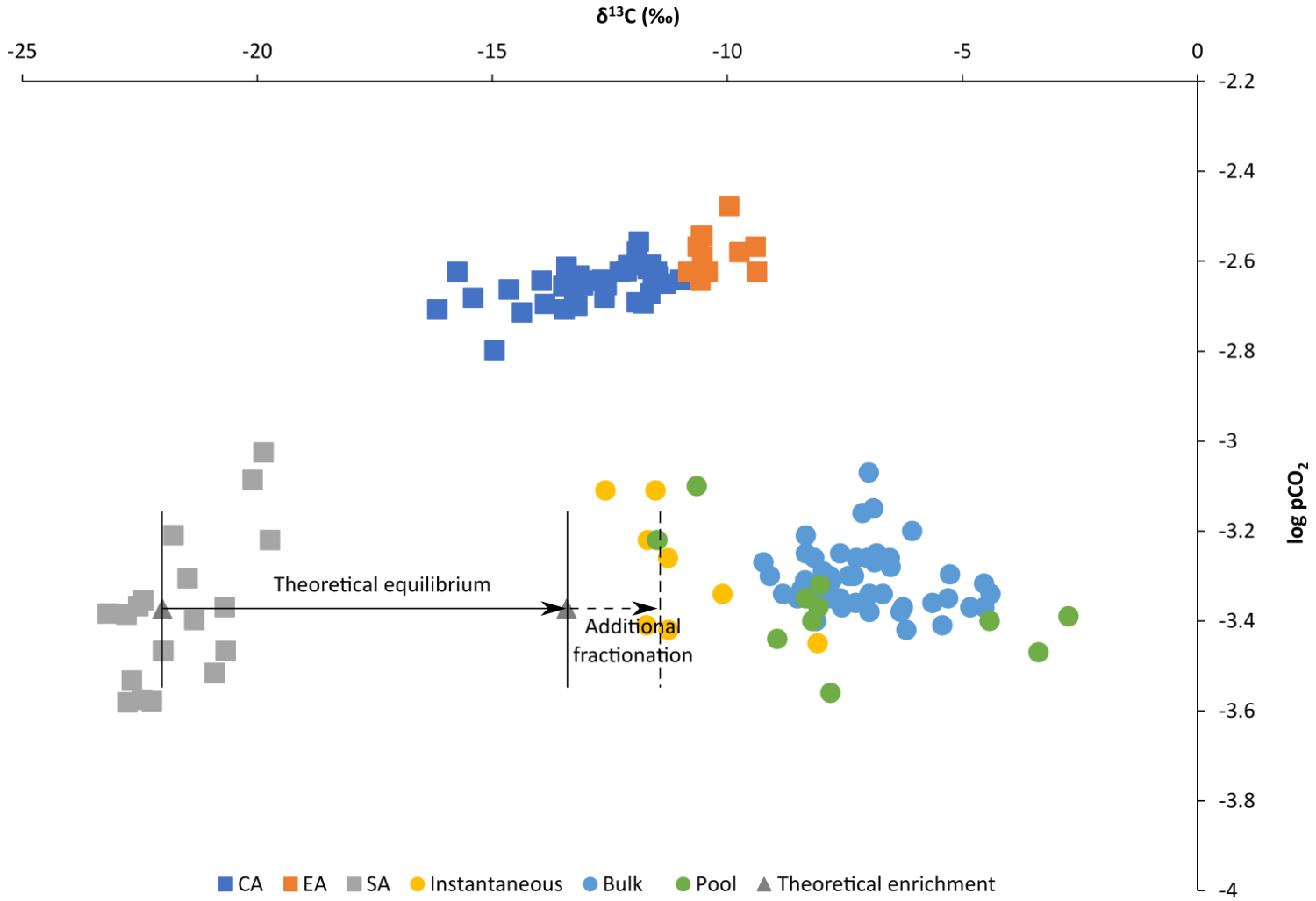

Figure 5.35: Carbon isotope values for cave, external and soil air and instantaneous, bulk and pool water plotted against log pCO_2. Carbon isotope values of air samples and CO_2 values are taken from section 4.4. Cave water isotope values are presented as $\delta^{13}C_{DIC}$ (this section) and PCO_2 was calculated in section 5.7.

5.10 Trace element concentration of dripwaters

5.10.1 Rainfall element chemistry

Water sampled at monthly intervals was analysed for an array of trace elements (Ca, K, Mg, Na, Si, Sr, Cl, SO_4 and NO_3) and the averages are presented in table 5.11. The samples used within the averages were collected between May-15 and Sep-16. Trace element concentrations of Ca, Mg, Si, SO_4 and NO_3 within rainfall remain relatively low compared to cave water. The low concentrations of these elements in rainwater compared to cave water advocates that these elements are sourced from within the soil and karst. The exception to this is SO_4 where there is minimal difference between the rainwater and cave water. The SO_4 within the rainwater may be derived from marine sources or from atmospheric pollution but these cannot be confirmed due to the absence of $\delta^{34}S$ isotope analysis.

Table 5.11: Average rainwater and cave water trace element concentrations.

	Ca (ppm)	K (ppm)	Mg (ppm)	Na (ppm)	Si (ppb)	Sr (ppb)	Cl (ppm)	Sulphate (ppm)	Nitrate (ppm)
Average rainwater	1.75	0.49	0.52	2.7	38.78	4.21	5.40	2.823	0.767
Average cave water	35.11	0.88	23.89	4.77	199.94	7.33	8.41	3.316	2.468
LOD	0.44	0.10	0.04	0.21	15.73	1.56	0.03	0.287	0.004
Blank stdev	0.15	0.04	0.01	0.07	5.24	0.52	0.01	0.096	0.001

5.10.2 Rock trace element chemistry

Bedrock samples were taken and analysed according to the methodology described in section 3.6.4.4. Rocks were sampled from the cave entrance (RCE), cave roof (RCR) and area outside overlying the cave (ROC). Trace element concentrations (Ca, K, Mg, Na and Sr) from the different rock sample types are displayed in table 5.12. Measured Ca concentrations were converted to a stochastic distribution of 400,000ppm (mg/kg) in calcite and all other element concentrations have been calculated to the stoichiometric Ca concentration (Jochum *et al.,* 2011). The high concentrations of magnesium in the overlying rocks suggests a Mg-rich host rock such as dolomite ($CaMg(CO_3)_2$). This agrees with the work of Dewit *et al.* (2014) who proposed evidence

for the occurrence of a large stratabound hydrothermal dolomite in Matienzo, particularly on the El Naso hillside in which Cueva de las Perlas is situated. Calcite has been identified to be interbedded within the dolomite and this may explain the variability of Mg values between different rock types.

Table 5.12: Trace element concentrations for bedrock samples. Data are presented in ppm.

Sample	Ca	K	Mg	Na	Sr
RCE 1	400,000	788	179,694	1,639	76
RCE 2	400,000	273	49,884	642	21
RCR	400,000	1024	93,679	1,147	16
ROC 1	400,000	586	206,421	1,096	46
ROC 2	400,000	526	199,288	859	47
ROC 3	400,000	631	223,122	2,787	47

5.10.3 Drip water element chemistry

5.10.3.1 Overview

The majority of trace elements within dripwaters (and subsequently speleothems) are derived from the soil, vegetation and karst and this is demonstrated in table 5.11 by the concentrations of Ca, Mg, Si and NO_3 in dripwater being consistently higher than those in rainfall.

Incorporation of elements into infiltrating waters occurs through the following processes:

- Colloidal and particulate flushing (e.g. Fairchild and Hartland, 2010; Hartland *et al.,* 2012) characterized by key trace element indicators, including Zn, Pb, Y and also P.
- Bedrock dissolution (e.g. Fairchild *et al.,* 2000; McDermott, 2004) characterized by high concentrations of Ca, Mg, Sr and Si within drip waters
- Soil biogeochemical processes (e.g.Treble *et al.,* 2003; Borsato *et al.,* 2007) characterized by changes to sulphate, nitrate and phosphate biogeochemical cycling.

Residence time within the soil and karst is the primary process controlling the uptake of elements. When residence times are longer, chemical weathering releases ions from the less soluble sections of karst. In contrast, shorter residence times only allow for the mobilisation of pre-existing solutes and elements attached to colloids and particles (Fairchild and Treble, 2009).

5.10.3.2 Assessment of karst evaporation

Evaporative processes within the karst can be demonstrated through analysis of the SO_4/Cl ratios and the SO_4 and Cl concentrations within rainfall and cave drip water. Under evaporative conditions, concentrations of SO_4 and Cl will increase however the SO_4/Cl ratio will remain constant. Cl is assumed to be conservative and therefore any enhancement in concentration must be due to evaporation. Increases in the concentration of other elements due to evaporation can therefore be calculated. If the ratio to chloride changes, other drivers of concentration must also be present within the system.

In the Cueva de las Perlas dripwaters, there is an enrichment in SO_4 (0.28ppm) and Cl (2.62ppm) relative to rainfall. The SO_4/Cl ratio is not consistent between rainfall and cave drip waters. Therefore, it is proposed evaporative processes are not responsible for the enrichment of SO_4 and Cl in cave dripwaters.

The larger increase in Cl values relative to SO_4 in cave dripwaters compared to precipitation may be a result of SO_4 loss or Cl enrichment. Sulphate could be lost via SO_4 reduction or uptake of SO_4 by vegetation through assimilation. Additional Cl may be added to the solution by redissolution of salts. However, the influence of these processes remains difficult to distinguish unless isotopic analyses of sulphur are undertaken (Wynn *et al.,* 2013).

5.10.3.3 Seasonality in drip water

The trace element data for the three bulk drip water collections (P1, P2 and P3) are presented in figure 5.36 and represent monthly collection between Apr-15 to Sep-17. Ca and Na values demonstrate peaks in winter. Mg values appear to peak in late summer or early autumn. Sr values demonstrate a peak in winter or early spring. K concentrations are variable throughout the year and do not appear to show seasonal

cycles. The anions presented in figure 5.36 (Cl, SO_4 and NO_3) only record a year and a half and therefore true assessment of seasonal cycles is inhibited. However, within the data, Cl demonstrates a clear peak at all sites during Apr-16. SO_4 and NO_3 concentrations appear to vary throughout the year and no seasonal cycles have been identified.

The karst hydrology overlying each of these drips has been shown to be complex (section 5.3) and because of this complex hydrology, varying patterns of trace element concentrations have been identified. For example, P2 demonstrates a complicated trace element signal with minimal seasonal variability demonstrated within the different elements. In contrast, P1 demonstrates evidence for seasonal cycles in Mg, Ca, Na, Sr and Cl. Concentrations for other elements including Zn, Fe and Mn were analysed but were outside detection limits and therefore data are not presented herein.

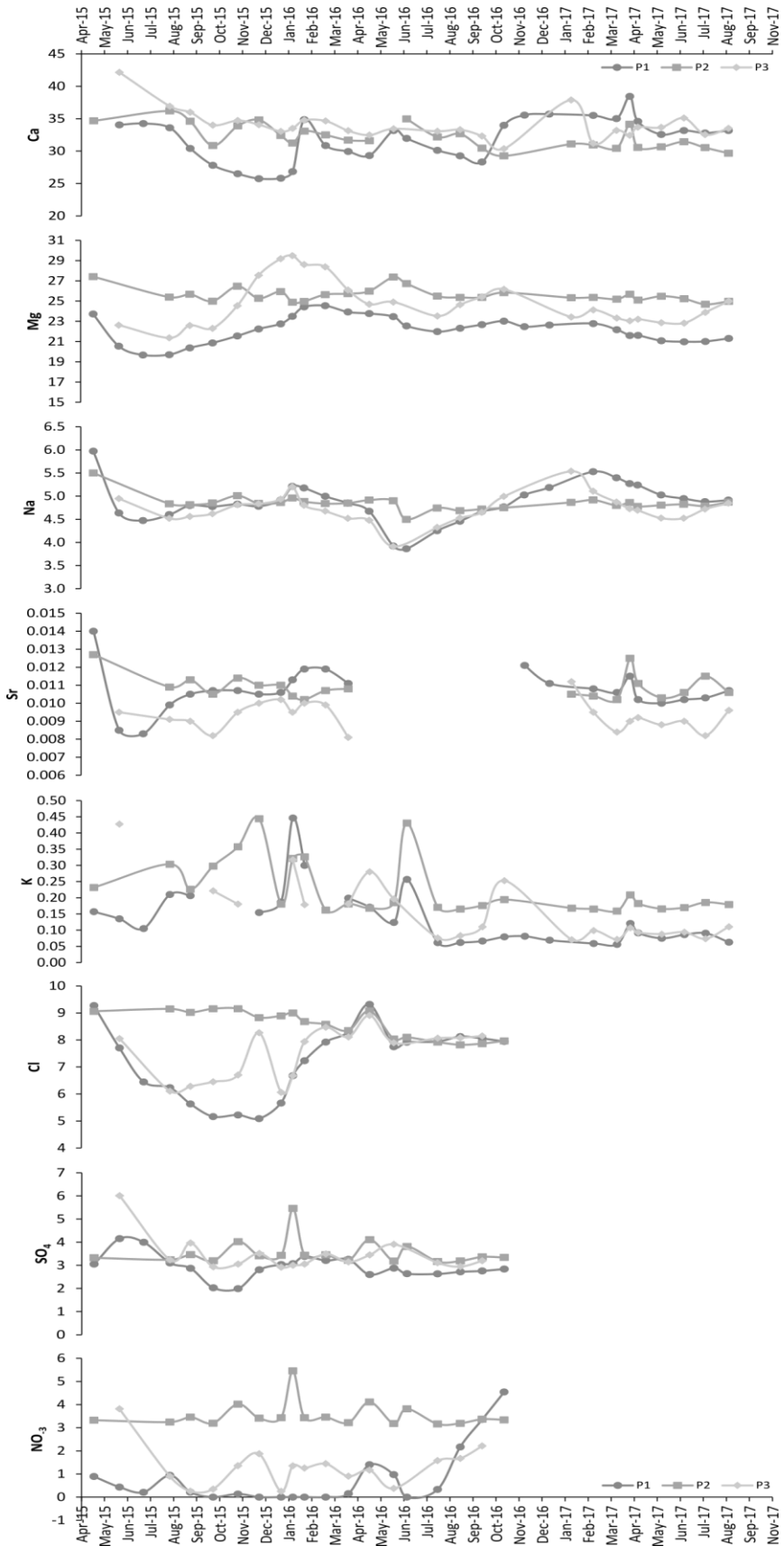

Figure 5.36: Trace element concentrations in bulk waters (P1, P2 and P3). Concentrations are given in ppm.

5.10.3.4 Influence of karst hydrology on trace element concentrations in dripwaters

The relationship between different trace elements and between trace elements and karst components such as drip rates or water excess can enhance understanding of karst processes. Assessment of these relationships using modern karst and dripwater monitoring (water excess, drip rates and trace element chemistry) can identify karst-water interaction processes such as PCP and ICD, rock-water contact times, karst hydrology and within-cave degassing dynamics.

Section 5.8.3.2 demonstrated rapid diurnal oscillations in CO_2 concentration led to changing EC values as a result of degassing. This pattern cannot be assessed using the monthly resolution of the trace element data. However, this section will assess the influence of drip rates, water excess and karst-water interaction processes on trace element chemistry.

Drip rate influence on Ca concentrations

The simplest of these relationships is between Ca and drip rate and section 5.8.3.1 assessed the influence of drip rate on EC concentrations which are predominantly composed of Ca and CO_3 in cave drip waters. During periods of reduced drip rate, the Ca concentration of the bulk drip water decreases due to degassing of CO_2 within the cave which results in loss of Ca^{2+} ions from the remaining solution. Conversely, when drip rate increases, the greater volume of dripwater being delivered will release CO_2 into the cave atmosphere, thereby raising cave air CO_2 concentrations. Consequently, degassing will be restricted and $CaCO_3$ precipitation will be reduced, retaining Ca in solution and minimizing a fall in EC.

Ca concentrations from the three bulk water collection sites are plotted in figure 5.37 alongside drip rates from associated drip sites. P2 bulk waters appear to track drip rate trends particularly in the period prior to Dec-16. However, in each of the records the relationship between drip rate and Ca is not clear as shown by an R^2 of 0.03 between monthly drip rate and monthly Ca concentration (figure 5.38). Therefore, other forcing mechanisms must be explored to determine the processes driving Ca. This relationship supports the findings in section 5.8.3.1 that EC is not primarily driven by changes in drip rate and other driving processes must be forcing changes in Ca and EC.

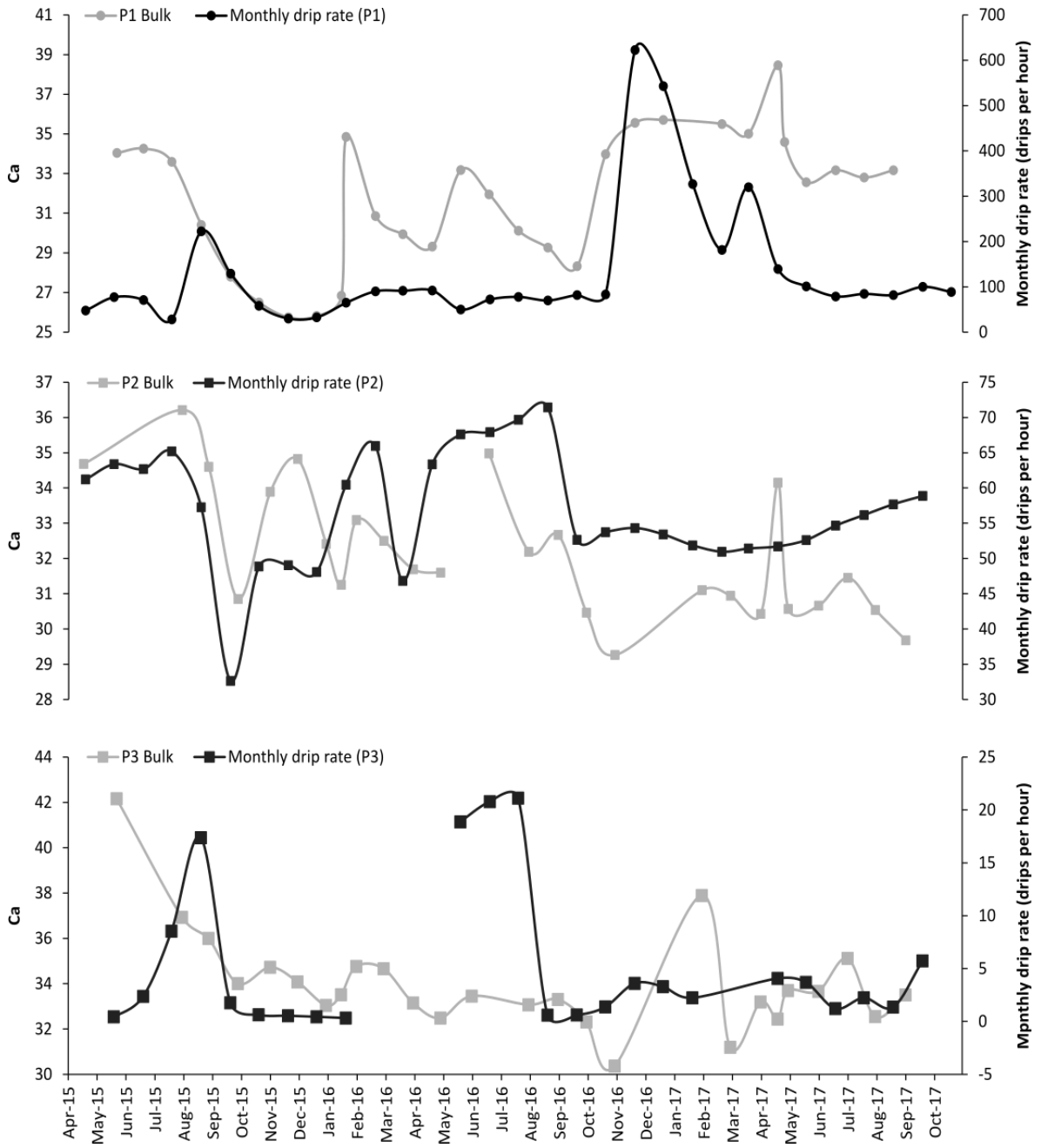

Figure 5.37: Ca concentration and drip rate for each sample site.

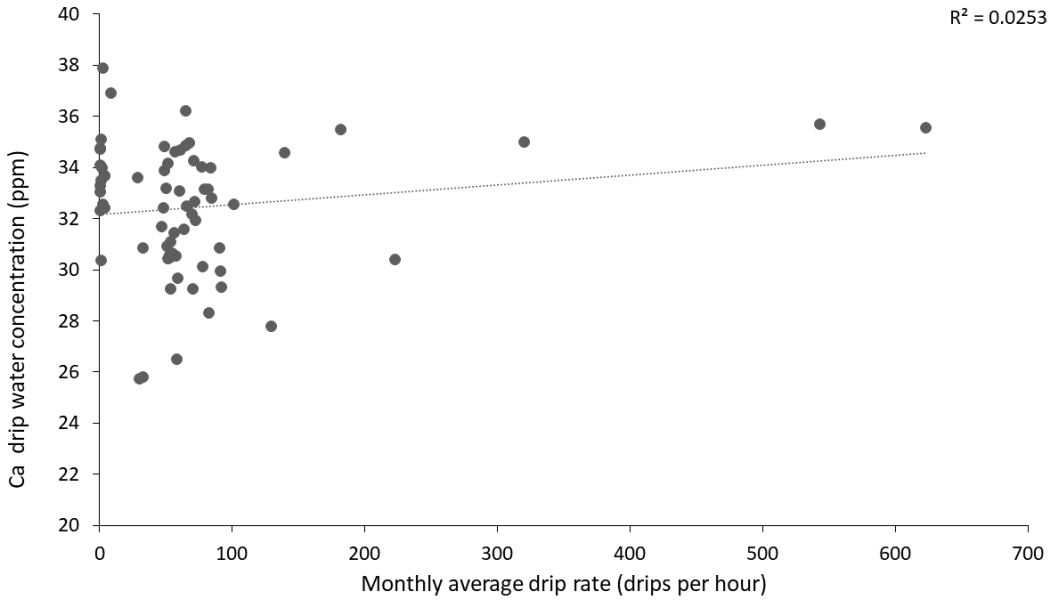

Figure 5.38: Monthly average drip rate (P1, P2 and P3) plotted against monthly bulk water Ca for the three different drip sites. Bulk water Ca concentrations have been plotted against associated drip rate.

Prior calcite precipitation and incongruent calcite dissolution evidenced through trace element chemistry

Karst hydrological components such as drip rate and water deficit/excess influence other elements including Mg and Sr. The two processes of incongruent calcite dissolution (ICD) and prior calcite precipitation (PCP) influence the concentrations of Mg and Sr in cave drip waters within the karst. Incongruent calcite dissolution influences Mg and Sr by either:

- Preferential leaching of Mg and Sr during fresh bedrock dissolution
- Or through re-dissolution of previously deposited $CaCO_3$ within the karst (Sinclair, 2011).

Through either of the processes above, ICD results in an enrichment of Sr and Mg relative to Ca in solution.

Prior calcite precipitation occurs when infiltrating waters degas along the flow pathway preferentially incorporating Ca into the $CaCO_3$ precipitate. Consequently, there is a significant reduction in Ca and an increase in the trace element to Ca ratio.

PCP occurs when infiltrating waters have time to degas and has been associated with drier conditions (Fairchild *et al.,* 2000; Fairchild and Treble, 2009).

The relationships between Mg/Ca, Sr/Ca, drip rate and water excess/deficit for the three bulk collection sites are shown in figure 5.39. Peaks in Mg/Ca and Sr/Ca correspond to periods of reduced drip rate and negative water excess at all three drip sites. This relationship is indicative of karst-water interactions such as PCP or ICD. Differential partitioning of elements within the crystal lattice during these processes gives rise to distinctive elemental ratios within the drip waters. Therefore, these ratios can be used to identify calcite/bedrock dissolution and $CaCO_3$ deposition within the karst (Sinclair, 2011; Sinclair *et al.,* 2012).

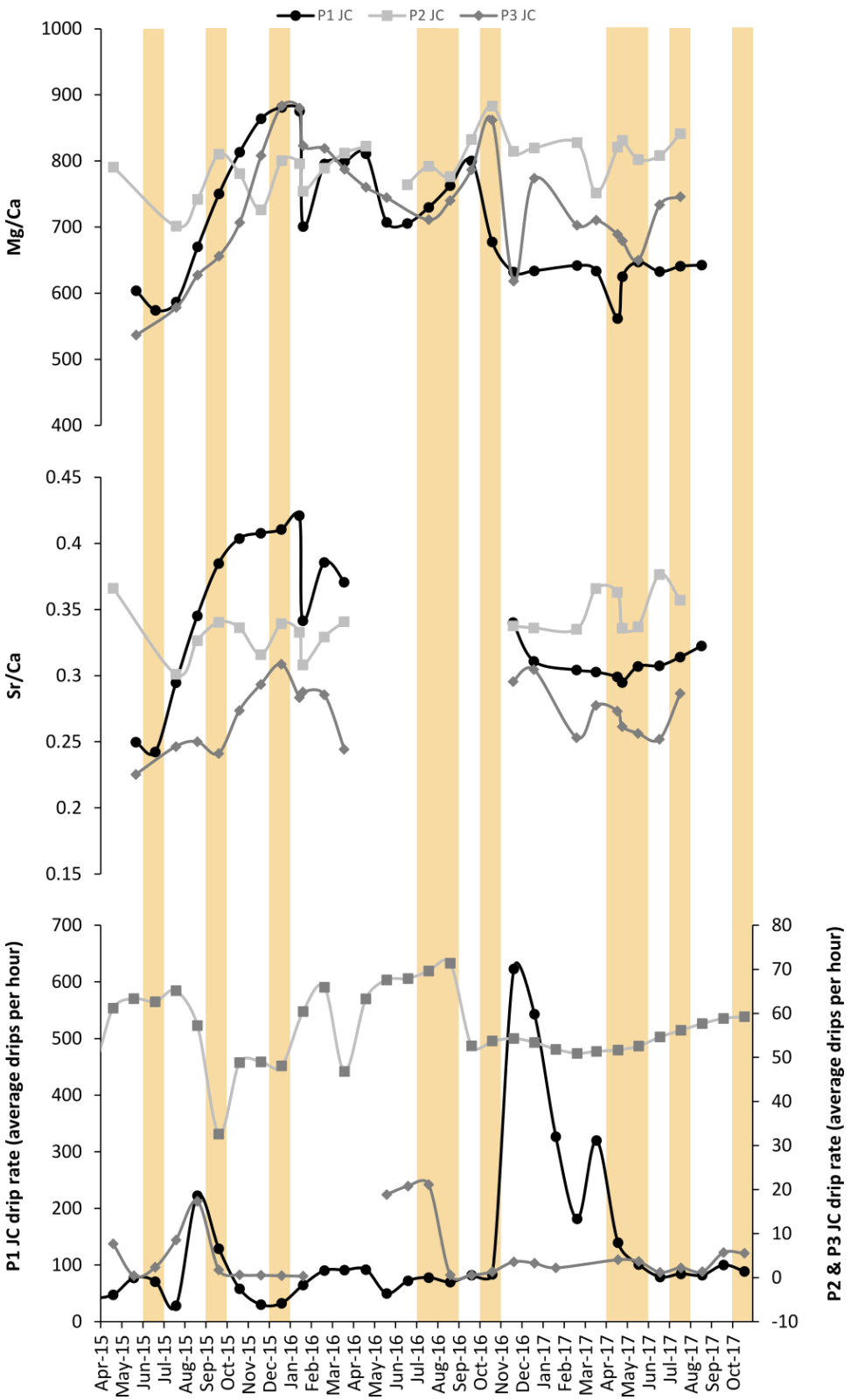

Figure 5.39: Mg/Ca, Sr/Ca and drip rates for P1, P2 and P3 bulk collection sites. Orange bars indicate periods of water deficit. Sr data was not collected between Apr-16 and Nov-16 due to technical difficulties with the ICP-OES method.

Karst-water interactions can be backward modelled using the partition coefficient for Mg and Sr combined with MIX-4 modelling. Karst-water interaction processes are associated with a partition coefficient (K) calculated through eq. 5.8.

$$(Tr/Ca)_{CaCO3} = K \times (Tr/Ca)_{solution} \quad \text{Eq. 5.8.}$$

Where Tr represents a trace element (commonly Mg or Sr) (Fairchild *et al.,* 2006b). The value of K is typically <<1 (Morse and Bender, 1990; Huang and Fairchild, 2001) and therefore minimal amounts of the trace element are removed during PCP, consequently leading to a rise in the ratios of Mg/Ca and Sr/Ca in the residual solution (Fairchild *et al.,* 2006b). The theoretical enrichment lines on figures 5.40 A and B were taken from Fairchild and Baker (2012: figures 5.23C and D) and used data from Fairchild *et al.* 2006b. The lines were calculated using the MIX4 reaction option. In the reaction, solution Ca concentrations corresponding to particular PCO_2 values at equilibrium were calculated using CO_3 as -1 equilibrating with $CaCO_3$. Partition coefficients of 0.04 and 0.1 were used to calculate changes in Mg and Sr respectively. Trajectories were modelled using a higher Mg source rock (5 times that used by Fairchild and Baker, 2012) and a much lower Sr source (2.5% of that used by Fairchild and Baker, 2012) to reflect the dolomitic bedrock composition overlying the Cueva de las Perlas cave system (section 5.10.2).

Waters from all sources within Cueva de las Perlas lie along the theoretical PCP trajectory for both Mg/Ca and Sr/Ca (figures 5.40 A and B). This pattern would indicate that karst-water interactions (such as PCP and ICD) are occurring year-round in Cueva de las Perlas. It is apparent that instant waters from the three drip sites are less evolved than corresponding bulk waters e.g. figure 5.41 shows the Ca and Mg/Ca values for P1 instant waters and associated P1 bulk waters throughout the monitoring period. The discrepancy may relate to the bulk sampling technique although this is unlikely due to the spread-out nature of the bulk water values along the PCP line. A second reason may relate to the low-resolution sampling of the instantaneous waters which may not capture the full variability within the dataset. The final reason may relate to enhanced degassing of bulk waters due to a longer residence time within the cave.

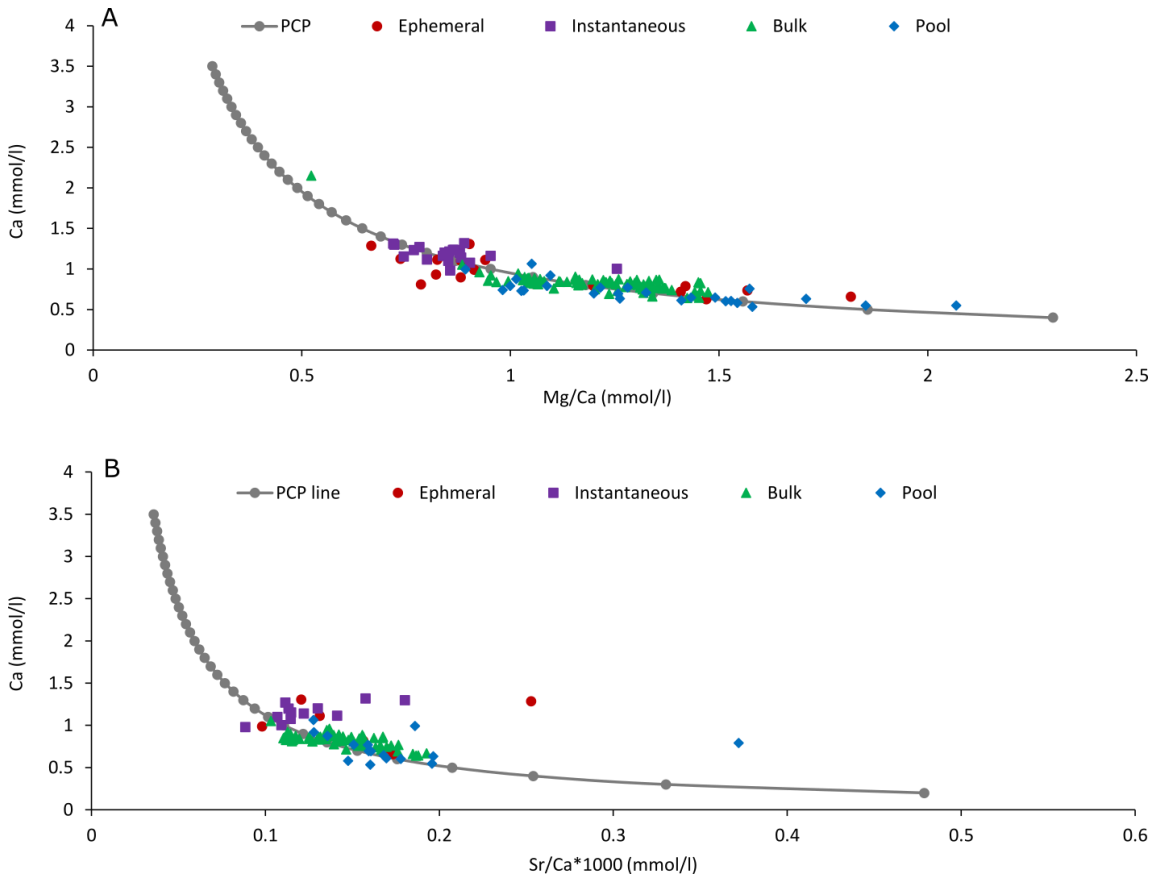

Figure 5.40: PCP lines for ephemeral, instantaneous, bulk and pool water data. A shows the spread of the Cueva de las Perlas data around the Mg/Ca PCP line whilst B demonstrates Sr/Ca. PCP lines were calculated using Fairchild and Baker (2012).

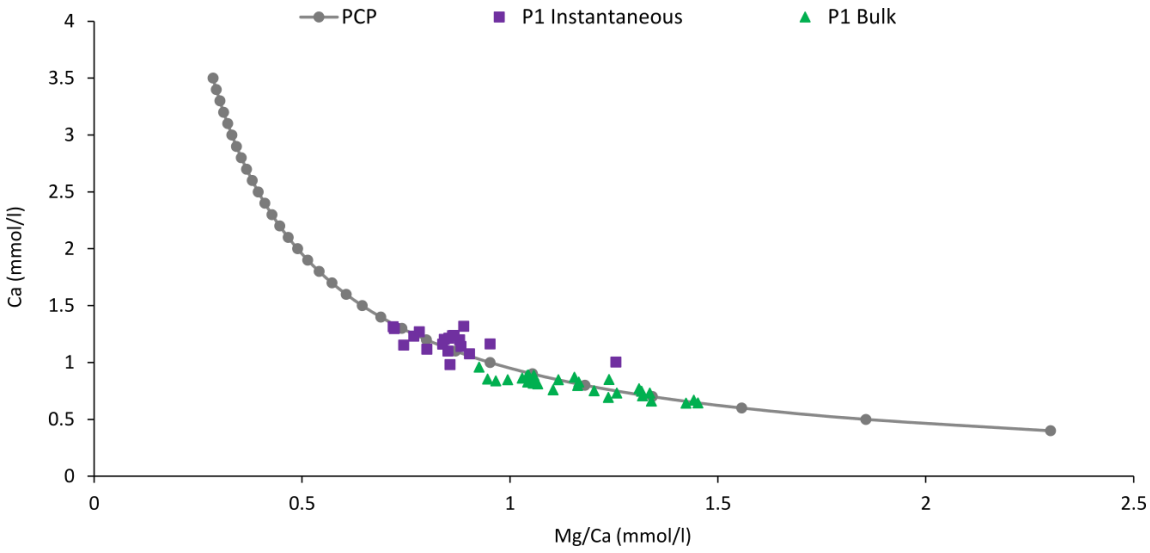

Figure 5.41: PCP line for Mg/Ca showing P1 instant waters and P1 bulk waters. PCP lines were calculated using Fairchild and Baker (2012).

Ephemeral waters demonstrate a wide spread of Mg/Ca and Ca values along the PCP line (figure 5.40) and represent some of the more evolved waters in the system. This pattern suggests that these waters have undergone karst-water interactions due to a relatively significant residence time within the karst. Ephemeral waters may therefore be related to piston flow or reservoir overflow during periods of increased precipitation and do not reflect the chemistry of individual precipitation events. Thereby supporting the karst hydrological model presented in figure 5.14.

A linear correlation between ln(Sr/Ca) and ln(Mg/Ca) with a theoretical slope of 0.88±0.13 is a tracer for karst-water interactions and the minimum and maximum range of the slope can lie between 0.709 and 1.003 (Sinclair *et al.,* 2012). This linear relationship is an indicator of waters which have interacted with calcite within the karst through either PCP or ICD processes (Sinclair, 2011). Drip waters from Cueva de las Perlas are compared to this slope (figure 5.42A) to identify potential calcite-water interactions in the karst overlying the cave.

Waters from Cueva de las Perlas lie within the lower boundary of the "Max and Min" theory of Sinclair *et al.* (2012) with a slope of 0.73. Therefore, calcite-water interactions such as PCP and ICD may be occurring in the karst overlying the cave due to the slope value lying within the range predicted by Sinclair *et al.* (2012). Additionally, figure 5.42 demonstrates the influence of karst-water processes on dripwater chemistry is stronger in summer (figure 5.42B) than in winter (figure 5.42C). This relationship would be expected as during the summer months precipitation is reduced and temperatures increase resulting in a water deficit (section 5.2.2). As a consequence of the drier conditions, infiltrating waters are influenced by stronger PCP and/or ICD within the karst.

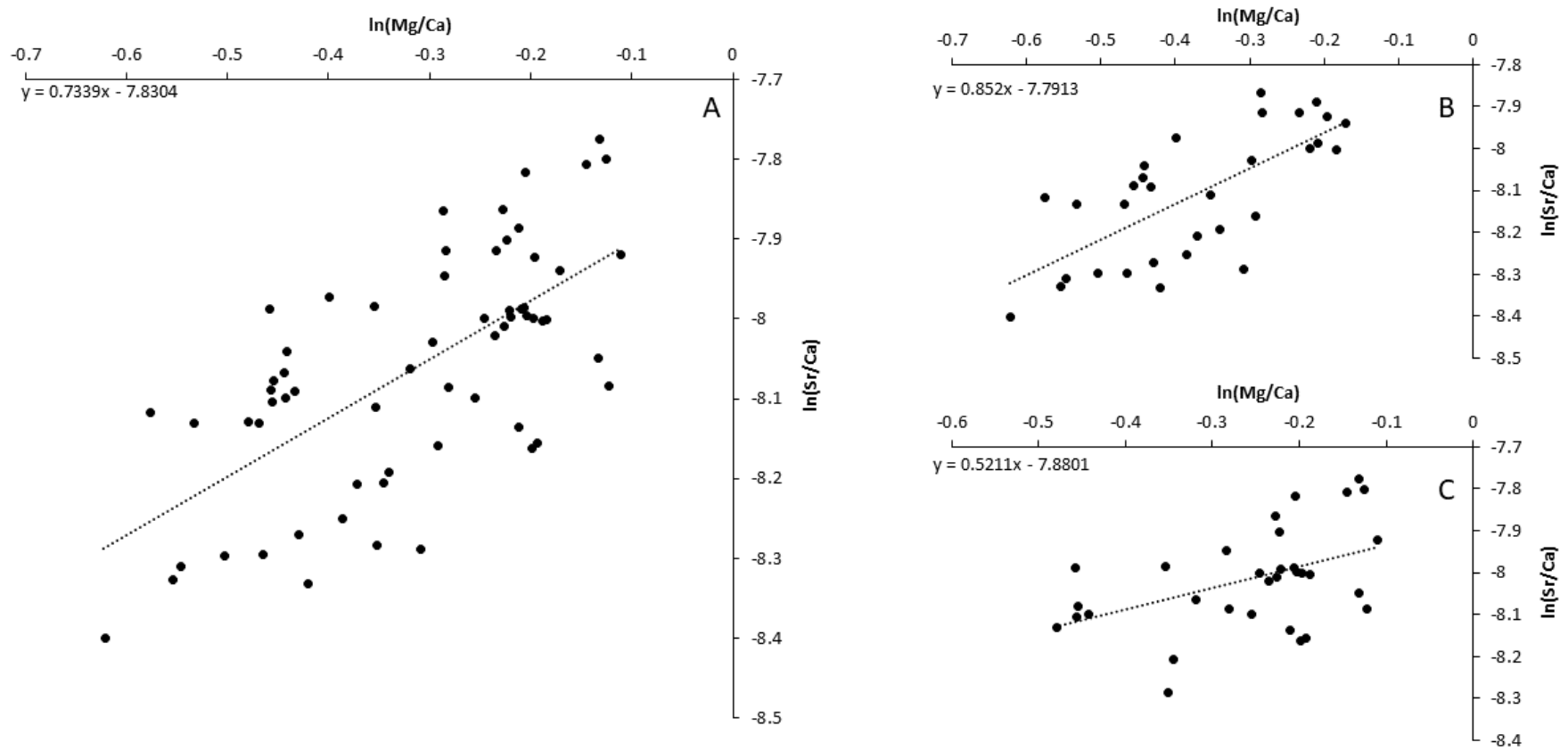

Figure 5.42: Assessment of the relationships between ln(Mg/Ca) and ln(Sr/Ca) in cave dripwaters. Ln(Mg/Ca) and Ln(Sr/Ca) plots for all bulk water (A), summer bulk water (B) and winter bulk water (C).

5.10.4 Summary

The majority of trace elements in cave dripwaters are derived from the vegetation, soil and karst overlying the cave as shown by the relatively low concentrations in precipitation. Trace element analysis of rocks indicates Cueva de las Perlas is situated in a dolomitic Mg-rich bedrock. The influence of karst-water processes such as PCP and/or ICD is apparent in the cave dripwaters, especially during the summer months under dry conditions. Smith (2014) highlighted that the processes of PCP and ICD may be masked by bulk water collection techniques. Subsequently, more instantaneous samples should be analysed.

5.11 Karst and cave hydrology and their influence on speleothem records

Karst and cave hydrology has been assessed in this chapter in order to accurately interpret palaeoclimate and palaeoenvironmental records from speleothems. Backward trajectory modelling has revealed ~73% of trajectories initiate from between a westerly-northerly source and moisture is also derived from a predominantly North Atlantic source region. Variability in the stable oxygen and deuterium isotope compositions of precipitation reflects changes in precipitation amount. Water excess ultimately controls water infiltration into the karst and recharge of the karst aquifer occurs primarily during winter periods of high water excess. Stable isotope compositions of cave waters indicate a well-mixed aquifer and record a predominantly winter precipitation signature. Calcite growth plates have established within-plate stable isotope ($\delta^{18}O$ and $\delta^{13}C$) variability dependent on distance and direction from the central growth axis. This has called into question the validity of the traditional Hendy test. However, equilibrium deposition of calcite from Cueva de las Perlas has been demonstrated through analysis of modern calcium carbonate and modelling through equilibrium equations.

Infiltrating waters are transmitted through the karst primarily by diffuse matrix flow and the homogenised nature of the cave dripwater $\delta^{18}O$ and δD signal suggests a well-mixed reservoir within the karst. There is evidence for periods of high dripwater flow

associated with increases in precipitation and chemical data from these waters indicates a significant karst residence time. Subsequently waters are allowed to mix within the aquifer. The flow of these waters may be through piston flow or reservoir overflow as a consequence of increased influx of precipitation. Variations in karst hydrology have been modelled and have demonstrated minimal inter-annual variability in $\delta^{18}O$ values related to karst hydrological dynamics. Therefore, it is proposed that speleothem stable oxygen isotope values will not preserve a signature of inter-annual variations in karst hydrology.

Vegetation and soil productivity have been demonstrated to influence carbon isotope values. However, the influence of these processes on trace elements has been difficult to determine due to the limits of analytical precision associated with the ICP-OES methodology. Within the overlying karst, carbon isotope values are fractionated by karst-water interaction processes such as PCP and/or ICD. Further evidence for the influence of these processes on infiltrating waters is also demonstrated through the analysis of Ca, Mg and Sr in cave dripwaters. Therefore, these geochemical indicators ($\delta^{13}C$, Mg and Sr) may be interpreted in speleothem records as proxies for aridity. Within the cave chamber, drip waters become further evolved due to interactions with PCO_2. Variations in cave air PCO_2 determine the degree to which drip water can degas, thereby forcing variability in electrical conductivity and Ca ion concentrations.

6. Speleothem records of past climate and environmental change from Cueva de las Perlas

6.1 Introduction

Three speleothems were collected for palaeoclimate and palaeoenvironmental reconstruction (PER0, PER10.4 and PER10.3) and these are described in sections 3.3.2 and 3.4. This section will present the U-series ages and use these to construct age models. Raw geochemical data will be presented and used in conjunction with the age models to produce a speleothem palaeoclimate and palaeoenvironmental record for each of the three speleothems. The records will then be interpreted in the context of local past climatic and environmental change on orbital and sub-orbital timescales.

6.2 Constructing a chronology for each speleothem

6.2.1 Overview

Speleothem chronologies have been constructed for each sample using U-Th dating. This method uses the decay of ^{238}U to ^{230}Th and has been widely applied to speleothem deposits dating up to 500,000 years (sections 2.6.1 and 3.6.4.1). This section will present the raw dates for each speleothem and discuss rejection of outliers, evaluate different age models and then present age models for each speleothem record.

6.2.2 U-Th dates

When the Cueva de las Perlas samples were selected within the cave their age was unknown and therefore initial dates were taken from the top and base of each speleothem. Further dates were then taken at equal intervals across each speleothem sample. At points across the speleothems where changes in texture or colour occurred, U-Th samples were taken either side as they were thought to represent changes in growth rate such as hiatuses. Dates for all samples taken from PER0, PER10.3 and PER10.4 are displayed in table 6.1.

Prior to age modelling, outliers were identified as different models will handle outliers differently. Outliers which were influenced by problems during processing or that were stratigraphically inconsistent were rejected prior to age modelling. During Dec-16, a set of samples had a low Th recovery rate which affected seven of the 20 samples in the batch and was most likely related to the loss of Th during chemical preparation. As a consequence, these seven samples were rejected from the analysis based on a low ^{230}Th signal intensities. Additionally, one sample was rejected based upon a small sample size relative to other samples in the batch.

Uranium series dating relies upon the assumption of a closed system. Dates which were rejected based upon stratigraphic age inversions likely represent a shift to open system behaviour or result from detrital contamination. The addition or loss of radionuclides from calcite after deposition is most likely to occur in the outer layer of the sample when it is exposed to moisture for an extended duration (Richards and Dorale, 2003) such as during a hiatus.

Table 6.1: U-Th sample data for PER0, PER10.3 and PER10.4. The final three columns relate to the outlier analysis prior to age modelling. For samples where there are two dates, an average of the age and error has been taken. The exception to this is when the two dates did not overlap within error and the younger date has been taken due to the likelihood of the older sample being contaminated as the result of problems with the autosampler. Dates were rejected on the basis of low ^{230}Th counts related to loss of ^{230}Th during sample prep (Dec-16 run)**, stratigraphic age inversion (outside of associated error)*** or sample size****.*

Name	Analysed	Distance from top (mm)	Weight (mg)	U (ppm)	232Th (ppm)	230/232 Activity Ratio	Age (ka BP)	±2abs	Accepted or Rejected	Date used in model (ka BP)	Error used in model
PER0											
2606 PER0-1	Dec-17	5	101.30	0.02374	0.00018	248.7	75.78	0.65	Rejected***		
PER0 TOP	Aug-15	19	112.90	0.03503	0.00154	40.2	65.31	0.86	Accepted	65.31	0.86
2606 PER0-2	Dec-17	47	109.60	0.03838	0.00014	532.9	76.68	0.47	Accepted	76.68	0.47
2606 PER0-3	Dec-17	63	125.40	0.09047	0.00010	1729.9	78.40	0.37	Accepted	78.40	0.37
PER0 – 1	Dec-16/ Mar-17	107	113.50	0.05927	0.00047	254.5	79.26	0.48	Accepted	79.64	0.49
				0.05933	0.00047	256.5	80.030	0.499			
PER0 - 2	Dec-16/ Mar-17	157	104.80	0.07117	0.00012	1190.4	83.688	0.632	Rejected*		
				0.07110	0.00012	1189.9	81.421	0.534	Accepted	81.421	0.534
PER0 – 3	Dec-16/ Mar-17	216	109.50	0.07366	0.00024	605.0	82.688	0.538	Accepted	82.227	0.535
				0.07367	0.00024	602.9	81.765	0.532			
PER0 – 4	Dec-16/ Mar-17	282	108.70	0.07928	0.00037	418.6	82.967	0.520	Accepted	82.967	0.520
2606 PER0-4	Dec-17	325	112.40	0.08860	0.00025	702.4	82.846	0.410	Accepted	82.846	0.410

PER0 BASE	Aug-15	374	80.80	0.07208	0.00032	455.7	85.369	0.533	Accepted	85.362	0.533
Name	**Analysed**	**Distance from top (mm)**	**Weight (mg)**	**U (ppm)**	**232Th (ppm)**	**230/232 Activity Ratio**	**Age (ka BP)**	**±2abs**	**Accepted or Rejected**	**Date used in model (ka BP)**	**Error used in model**
PER10.3											
3006 PER10.3-1	Dec-17	6	105.7	0.04601	0.00027	186.6	32.400	0.192	Rejected***		
PER10.3 – 1	Dec-16	8	110.4	0.03787	0.00801	29.0	-26928434.452	0.000	Rejected**		
PER10.3 TOP	Jul-16	14	115.52	0.04170	0.00621	6.9	27.941	2.398	Accepted	27.941	2.398
3006 PER10.3-2	Dec-17	20	106	0.03175	0.00034	107.4	34.874	0.279	Accepted	34.874	0.279
PER10.3 – 2	Dec-16 / Mar-17	26	109.5	0.05514	0.00429	36.5	111.154	1.291	Rejected***		
				0.05522	0.00429	36.3	109.854	1.283			
3006 PER10.3-3	Dec-17	35	105.8	0.05257	0.00016	528.6	51.806	0.267	Rejected***		
PER10.3 below hiatus	Jul-16	39	101.23	0.06738	0.00698	18.4	64.901	1.659	Rejected***		
3006 PER10.3-4	Dec-17	44	112.5	0.05095	0.00013	602.3	49.884	0.312	Accepted	49.884	0.312
PER10.3 – 3	Dec-16	51	105.7	0.06720	0.01813	754.5	41956.917	47.207	Rejected**		
3006 PER10.3-5	Dec-17	56	107.7	0.05509	0.00012	1072.2	82.534	0.518	Rejected***		
PER10.3- 4	Dec-16/ Mar-17	62	107.8	0.05253	0.00056	148.1	51.417	0.317	Accepted	51.611	0.320
				0.05252	0.00056	147.8	51.805	0.323			
PER10.3 – 5	Dec-16	72	117.2	0.05296	0.00110	77.2	53.822	0.775	Rejected**		
PER10.3 – 6	Dec-16/ Mar-17	85	110.3	0.04574	0.00034	220.9	55.149	0.391	Rejected*		
				0.04557	0.00033	214.7	52.449	0.363	Rejected***		
PER10.3- 7	Dec-16/ Mar-17	95	135.6	0.05754	0.00231	39.0	51.962	0.906	Accepted	51.636	0.921
				0.05748	0.00235	37.9	51.310	0.935			
PER10.3 – 8		105	122	0.05497	0.00190	45.9	52.993	0.521	Accepted	52.503	0.567

	Dec-16/ Mar-17			0.05487	0.00191	45.1	52.013	0.614			
3006 PER10.3-6	Dec-17	124	104.5	0.05396	0.00023	368.0	51.536	0.464	Accepted	51.536	0.464
PER10.3- 10	Dec-16/ Mar-17	127	111.5	0.04970	0.00032	241.9	51.679	0.365	Accepted	51.968	0.408
				0.04964	0.00032	242.7	52.257	0.451			
PER10.3 – 11	Dec-16/ Mar-17	136	112.3	0.05258	0.00060	142.6	54.680	0.344	Rejected***		
				0.05254	0.00060	141.9	54.343	0.348	Rejected***		
PER10.3 – 12	Dec-16/ Mar-17	145	143.4	0.04514	0.00023	317.8	53.971	0.330	Rejected***		
				0.04517	0.00023	316.7	53.537	0.360	Rejected***		
PER10.3 BASE	Jul-16	156	99.06	0.05427	0.00082	102.6	51.232	0.391	Accepted	51.232	0.391
PER10.3- 13	Dec-16/ Mar-17	163	106	0.05148	0.00068	119.6	52.013	0.332	Accepted	52.013	0.332
PER10.3- 14	Dec-16/ Mar-17	182	117.7	0.04655	0.00066	112.9	52.962	0.386	Accepted	52.962	0.386
				0.04654	0.00068	113.7	55.336	0.509	Rejected*		
PER10.3- 15	Dec-16/ Mar-17	190	105.6	0.04725	0.00078	98.5	54.019	0.387	Accepted	54.263	0.396
				0.04718	0.00078	98.9	54.507	0.405			
Name	**Analysed**	**Distance from top (mm)**	**Weight (mg)**	**U (ppm)**	**232Th (ppm)**	**230/232 Activity Ratio**	**Age (ka BP)**	**±2abs**	**Accepted or Rejected**	**Date used in model (ka BP)**	**Error used in model**
PER10.4											
2906 PER10.4-1	Dec-17	6	113.20	0.03	0.001	47.8	27.868	0.529	Accepted	27.868	0.529
PER10.4 TOP	Jul-16	12	105.16	0.05	0.007	8.3	36.977	2.433	Accepted	36.977	2.433
2906 PER10.4-2	Dec-17	17	112.50	0.03	0.000	401.6	49.632	0.419	Rejected***		
PER10.4 – 1	Dec-16/ Mar-17	21	109.50	0.03	0.001	45.0	46.358	0.580	Accepted	45.828	0.578
				0.03	0.001	44.2	45.299	0.577			

2906 PER10.4-3	Dec-17	27	108.10	0.04	0.000	466.9	49.224	0.297	Rejected***		
PER10.4 – 2	Dec-16	34	120.30	0.06	0.007	11.5	42.286	2.060	Rejected **		
PER10.4 – 3	Dec-16/ Mar-17	45	132.60	0.05	0.000	216.2	49.477	0.513	Rejected***		
				0.05	0.000	201.0	50.191	0.607	Rejected***		
2906 PER10.4-4	Dec-17	50	105.20	0.05	0.000	506.4	50.823	0.290	Rejected***		
PER10.4 – 4	Dec-16/ Mar-17	55	124.90	0.08	0.001	98.4	47.612	0.302	Accepted	47.563	0.337
				0.08	0.001	98.4	47.513	0.372			
PER10.4 – 5	Dec-16/ Mar-17	68	103.30	0.06	0.008	12.5	46.723	1.931	Accepted	46.432	1.933
				0.06	0.008	12.3	46.142	1.935			
PER10.4 – 6	Dec-16/ Mar-17	79	108.60	0.06	0.001	161.1	49.867	0.295	Accepted	49.867	0.295
PER10.4 – 7	Dec-16	93	129.90	0.06	0.002	59.0	45.983	0.809	Rejected **		
PER10.4 – 8	Dec-16/ Mar-17	106	125.50	0.05	0.001	110.9	50.884	0.334	Accepted	50.758	0.373
				0.05	0.001	110.5	50.632	0.411			
PER10.4 – 9	Dec-16/ Mar-17	122	109.50	0.05	0.001	86.0	52.725	0.677	Rejected***		
PER10.4 – 10	Dec-16/ Mar-17	136	100.70	0.06	0.000	215.6	51.482	0.290	Rejected***		
				0.06	0.000	215.9	51.528	0.367			
PER10.4 – 11	Dec-16	148	109.10	0.06	-0.009	7657.1	-634.928	389.43	Rejected **		
PER10.4 – 12	Dec-16/ Mar-17	158	101.10	0.06	0.000	298.8	51.703	0.309	Rejected***		
				0.06	0.000	297.2	51.681	0.357			
PER10.4 – 13	Dec-16/ Mar-17	168	113.90	0.06	0.002	43.6	51.295	0.673	Accepted	51.078	0.685
				0.06	0.002	44.0	50.861	0.698			
3006 PER10.4-5	Dec-17	174	106.20	0.06	0.000	1004.3	51.844	0.284	Rejected***		
PER10.4 BASE-2	Jul-16	183.5	89.70	0.07	0.002	62.3	45.115	0.429	Rejected****		
PER10.4 – 14	Dec-16/ Mar-17	190	104.90	0.06	0.000	175.2	50.307	0.329	Accepted	50.416	0.348
			104.90	0.06	0.000	174.0	50.525	0.368			

PER10.4 - 15	Dec-16/ Mar-17	204	105.40	0.05	0.001	60.9	53.021	0.589	Rejected***		
				0.05	0.001	60.4	52.936	0.610	Rejected***		
PER10.4 BASE	Jul-16	216	108.60	0.05	0.003	27.3	52.444	0.981	Accepted	52.444	0.981
3006 PER10.4-6	Dec-17	222	102.60	0.06	0.000	549.6	51.833	0.333	Accepted	51.833	0.333

6.2.3 Evaluating different age models

6.2.3.1 Introduction

The high precision U-series dates generated from speleothems have a vast potential to provide high resolution palaeoclimate records. However, modelling these ages to create an optimised age-depth model remains a challenge with numerous different models available (Scholz *et al.,* 2012). Two age models are compared in this section to demonstrate the significance of model selection and identify the most suitable for this study.

The two models discussed below are OxCal (Bronk Ramsey, 2008) and COPRA (Breitenbach *et al.,* 2012). Bayesian methods are used in the OxCal model to produce a P-sequence deposition model. In the P-sequence, deposition is not assumed to be uniform and therefore fluctuations can be accounted for (Bronk Ramsey, 2008). COPRA models are generated through a monte-carlo simulation of age-depth data and then interpolation between dates through either linear, cubic or spline functions (Breitenbach *et al.,* 2012).

6.2.3.2 Age model envelopes

Two different age models were constructed for PER10.4 using the accepted dates listed in table 6.1. The first model was created using COPRA (Breitenbach *et al.,* 2012) and the second through OxCal (Bronk Ramsey, 2008). In order to construct the COPRA age model, four additional dates (55mm, 106mm, 168mm and 216mm) had to be removed. Although these dates overlapped within ±2σ error, COPRA was unable to run and consequently they were removed from the model.

Both age models are shown in figure 6.1. The errors of each model are shown by the shaded areas and these have been termed the age model 'envelopes'. It is apparent that the model envelopes overlap within uncertainty. However distinct differences in errors and mean ages are apparent and these will be explored further in the sections below.

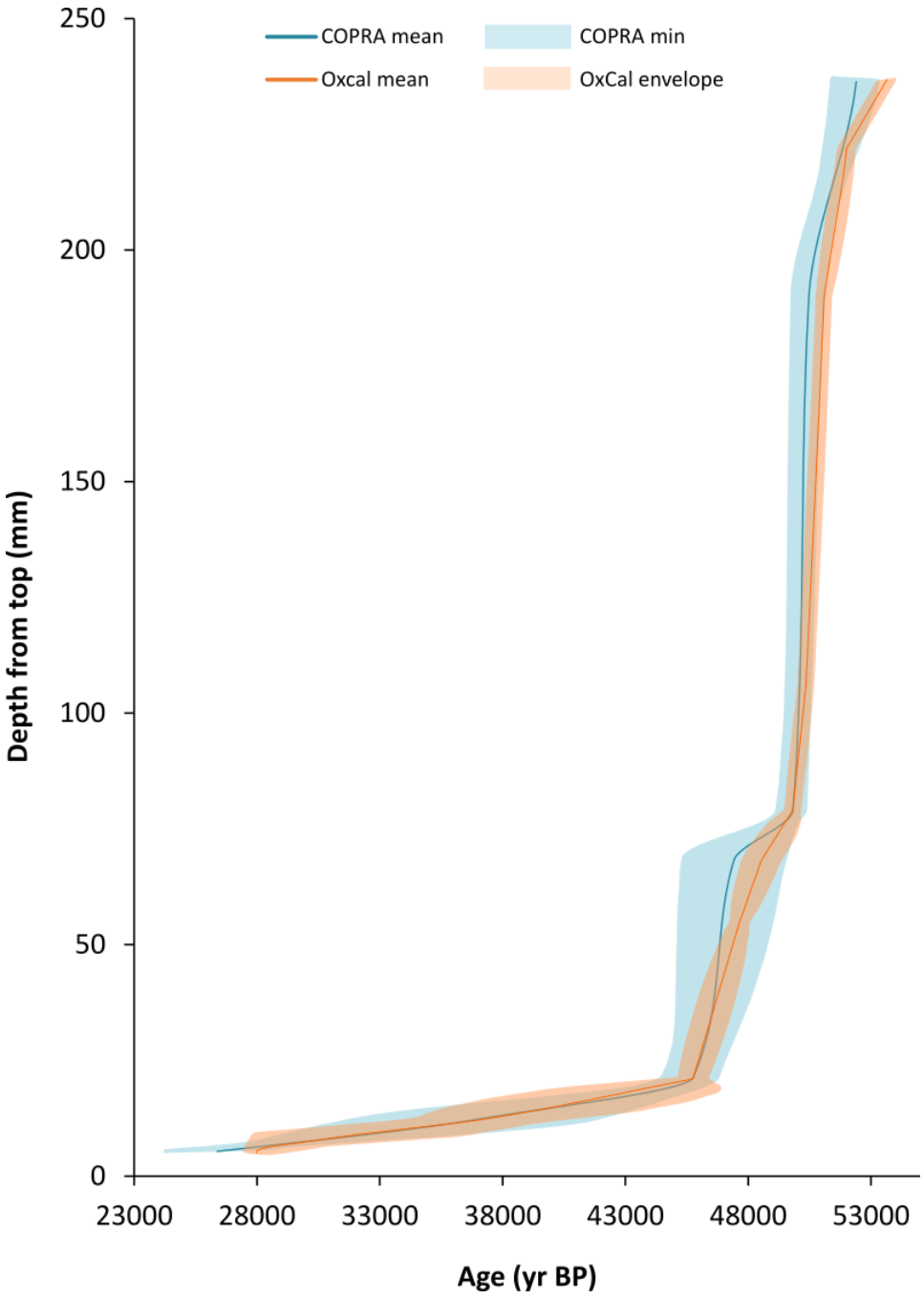

Figure 6.1: Age model 'envelopes' for the PER10.4 dates produced through COPRA and OxCal.

6.2.3.3 Age model errors

The uncertainty on the OxCal model is smaller than that on the COPRA model as illustrated by figure 6.2. The OxCal and COPRA models have maximum uncertainties of 8393yr and 9412yr and minimum uncertainties of 505yr and 876yr respectively.

Additionally, the average uncertainty associated with the OxCal model is 1099yr whilst for the COPRA model the average uncertainty is 1850yr.

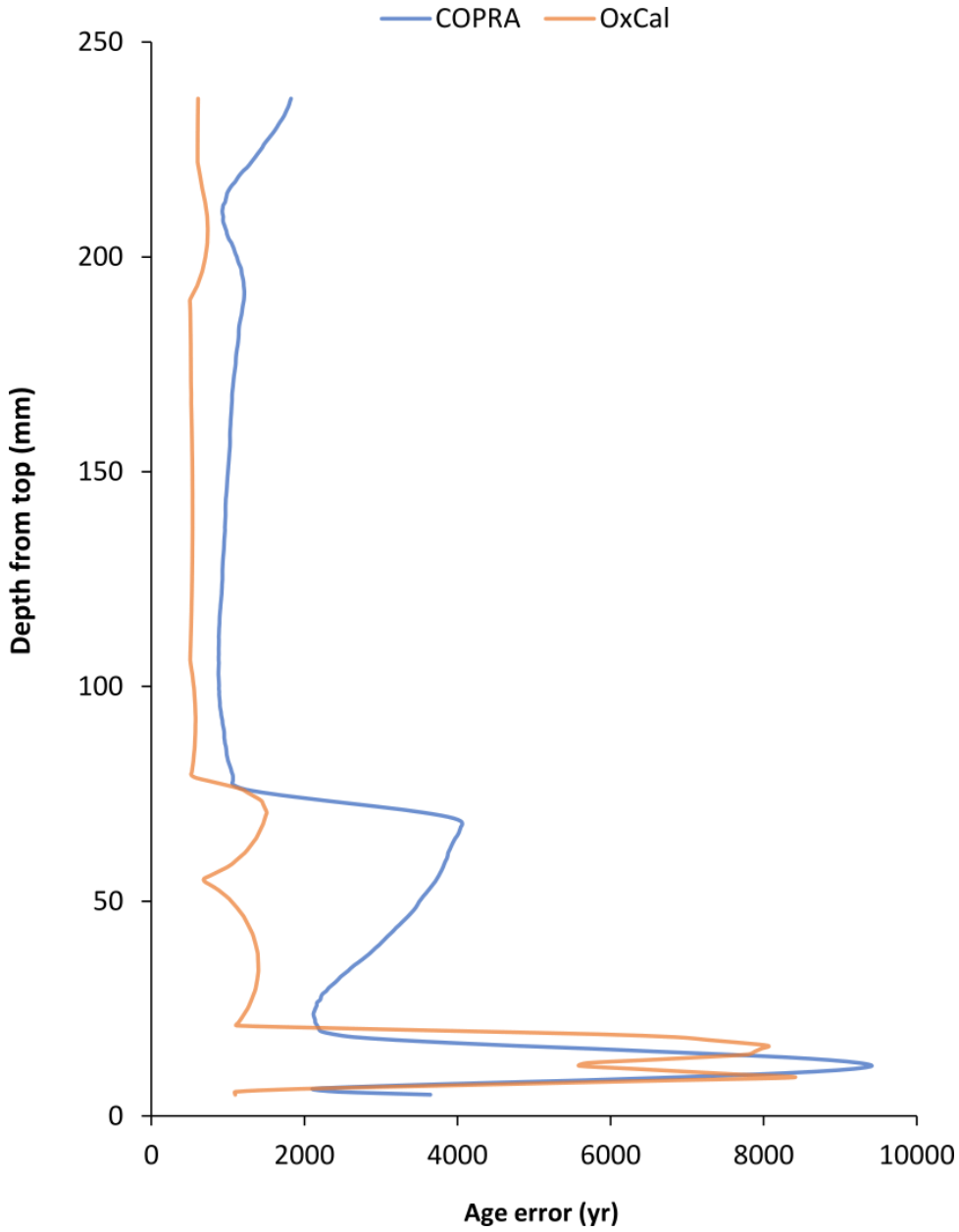

Figure 6.2: Age errors on PER10.4 COPRA and OxCal models.

6.2.3.4 The significance of age model selection shown through proxy data

The differences in the proxy-age models generated from the two different modelling programmes are highlighted in figure 6.3 (see section 6.3.3 and 6.4.3 for data interpretation). The dates of key transitions can be offset between the models such as the positive excursion in oxygen isotope values at 19.07mm from top which is offset between the two models by 1108yrs. Additionally, the start and end dates are offset in

each of the models by 1146yrs and 1743yrs respectively. However, these offsets are not significant when the age errors associated with each model are considered (figure 6.1).

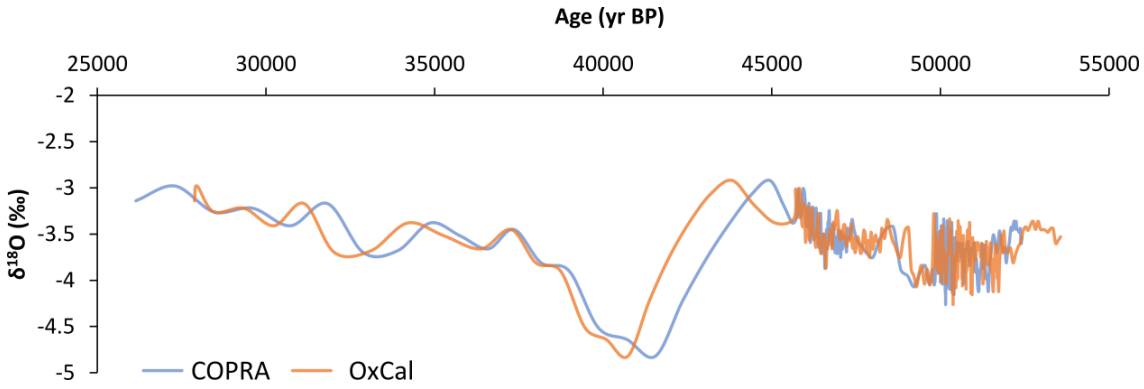

Figure 6.3: Proxy comparison of the PER10.4 age models run through COPRA and OxCal.

Even though the two models overlap within uncertainty, the analysis herein demonstrates the significance of running multiple models using different programmes and selecting the one most suitable for purpose. Based upon this analysis, the OxCal model was selected as the underlying chronology for PER10.4 as it was able to incorporate a larger number of dates (n= 11) compared to COPRA (n= 7), model age inversions within error and had an overall reduced uncertainty.

6.2.4 Construction of speleothem age models

6.2.4.1 Overview

Following the evaluation of different program model outputs (section 6.2.3), the final chronologies for PER0, PER10.3 and PER10.4 were run through OxCal v4.3.2 (Bronk Ramsey, 2008; Bronk Ramsey, 2017). A Poisson-process deposition model (P-sequence) was used as it does not assume uniform deposition and accounts for variations in deposition rates by introducing undated events at set intervals throughout the sequence (Bronk Ramsey, 2008). The model parameters in the P-sequence were:

P Sequence (*name*, k_0, *p* and *D*)

Where *name* is the label for the sequence, k_0 represents the number of events per unit length, *p* is the interpolation rate and *D* is some prior distribution which is equivalent to *v* where $v = \log_{10}(k/k_0)$. The *v* value represents the prior of a variable *k* value to allow

variability of *k* within a set range (Bronk Ramsey and Lee, 2013; Bronk Ramsey, 2018). All parameters used for each sample are shown in table 6.2 and an example for PER0 is shown below.

P_Sequence (PER0, 0.1, 0.3, U(-2,2)

Where k_0 = 0.1mm^{-1}, p = 0.3mm^{-1} and variability in *k* was allowed between a factor of 10^{-2} and 10^{2}. Therefore, the model output was given every 3.3mm and the model averaged over values of *k* between 0.01 and 100mm^{-1}. The use of a variable *k* value allows for a robust deposition model to be constructed (Bronk Ramsey and Lee, 2013).

Table 6.2: Parameters used in OxCal age models for PER0, PER10.3 and PER10.4.

Name	k_0	p	***D* (~*v*)**	**units**
PER0	0.1	0.3	-2,2	mm
PER10.3	0.1	0.5	-2,2	mm
PER10.4	0.1	0.5	-2,2	mm

6.2.4.2 PER0

The OxCal modelled age-depth plot for PER0 is shown in figure 6.4. The raw dates from PER0 indicated a change in deposition rate between dates sampled at 63mm and 47mm from top. Between 107-63mm growth rate was estimated to be 35.38µm/yr whereas between 63-47mm growth rate fell to 9.31µm/yr. Therefore, a change in deposition was input into the age model and this boundary change is represented on figure 6.4 by a change in colour. The model agreement index (A_{model}) for PER0 was 78.3.

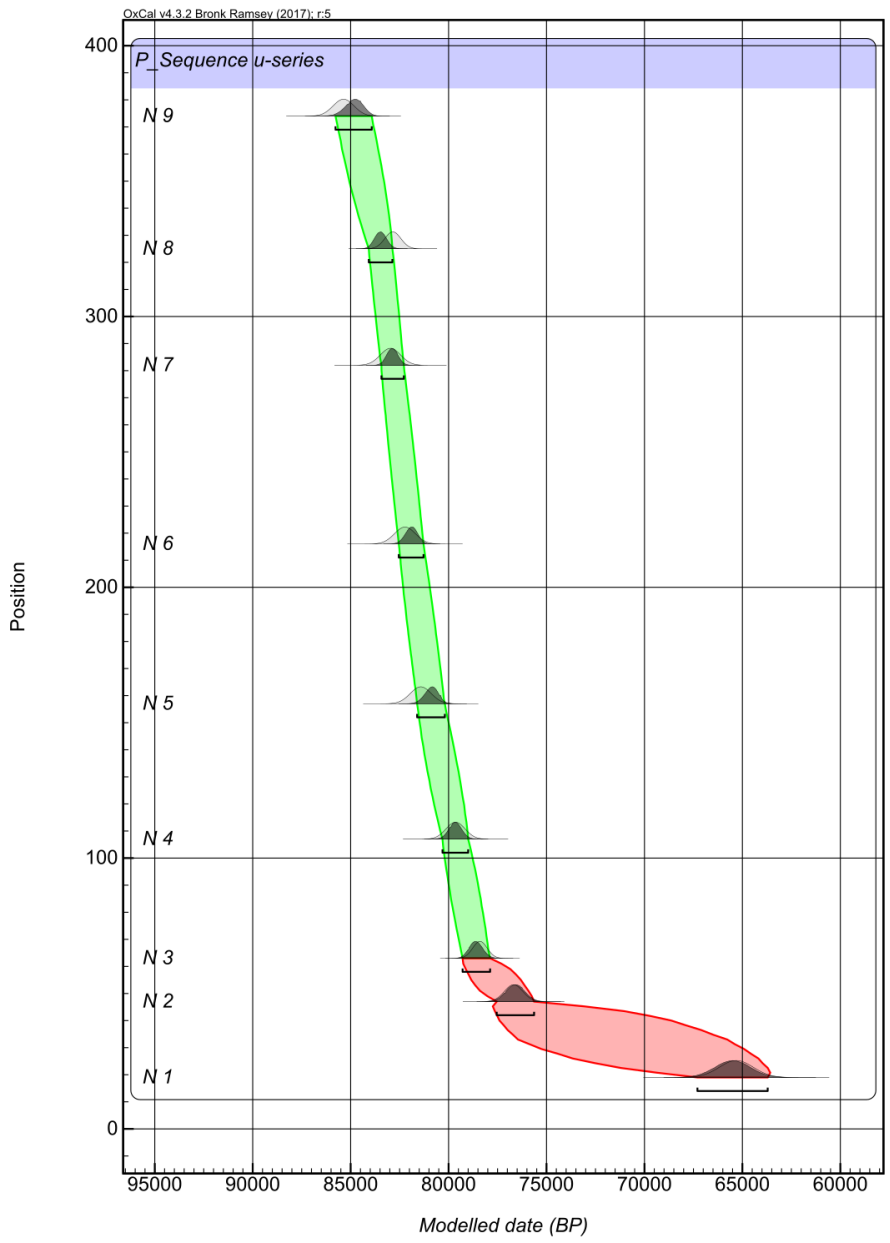

Figure 6.4: OxCal modelled age-depth plot for PER0.

6.2.4.3 PER10.3 and PER10.4

The OxCal modelled age-depth plots for PER10.3 and PER10.4 are shown in figure 6.5. The top sections of both speleothems have proven challenging to date with evidence from the initial dating suggesting a reduced growth rate and/or a hiatus occurring within the top 50mm of each sample. To incorporate this information into the model a change in deposition was added between dates 44-20mm from top in PER10.3 and between

dates 21-12mm from top within PER10.4. Model agreement indices were 54.5 and 35.3 for PER10.3 and PER10.4 respectively.

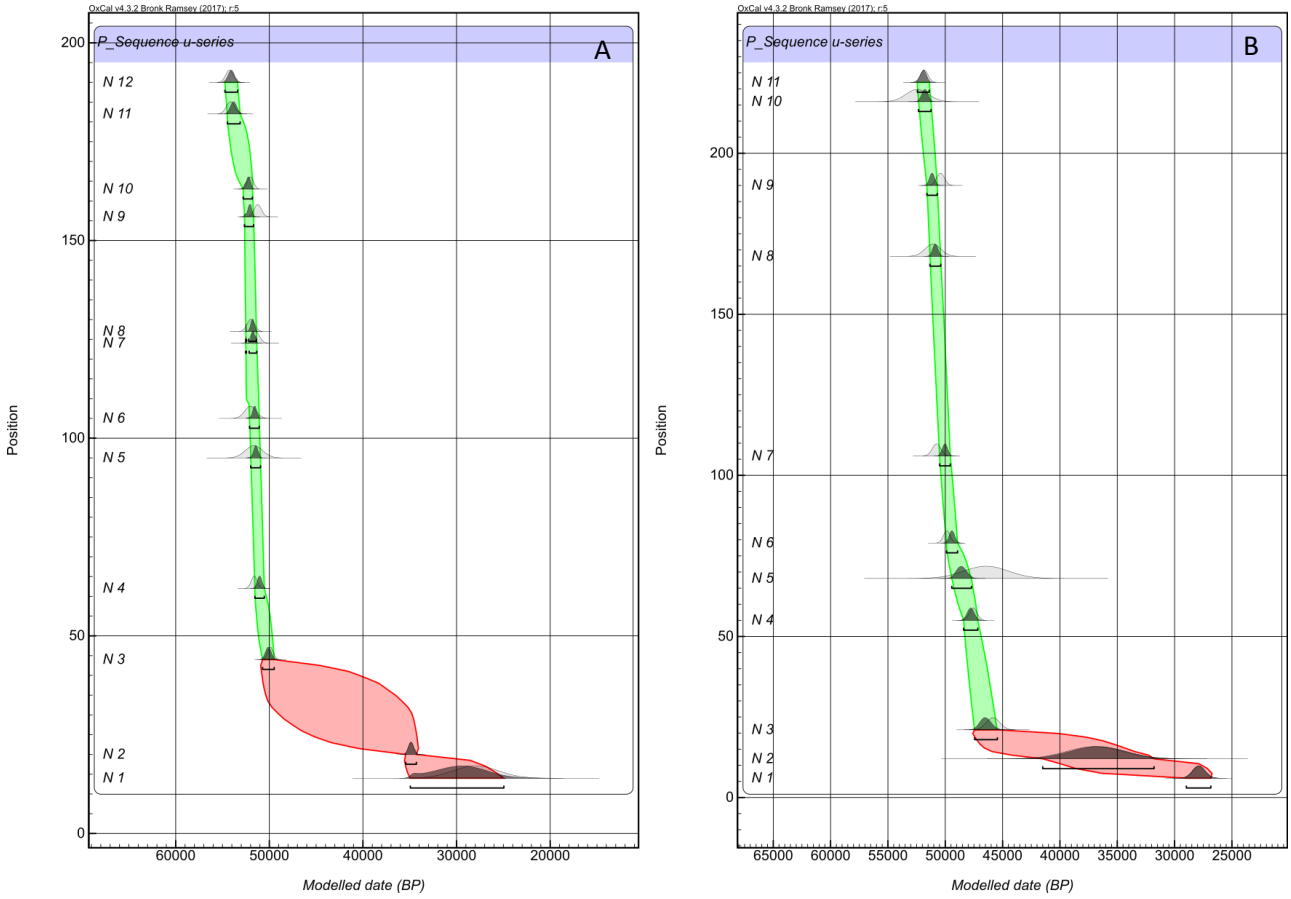

Figure 6.5: OxCal modelled age-depth plots for PER10.3 (A) and PER10.4 (B).

6.3 Raw geochemical data

6.3.1 PER0

6.3.1.1 Isotopes

Samples for oxygen and carbon isotope analysis were taken at ~2mm intervals between 2mm and 390mm from PER0. Overall, 195 samples were analysed, and the results are plotted against depth in figure 6.6. The oxygen isotope values had a range of 1.63‰ and an average of -4.63‰ while the carbon isotope values had a range of 5.7‰ and an average of -9.07‰. Co-variation of oxygen and carbon isotope values is applied as a method to test for kinetic fractionation which has been discussed previously in section 2.6.2.2 and assessed using modern calcite growth in section 5.5. In PER0, oxygen and carbon isotope values were found not to co-vary with an R^2 of 0.16.

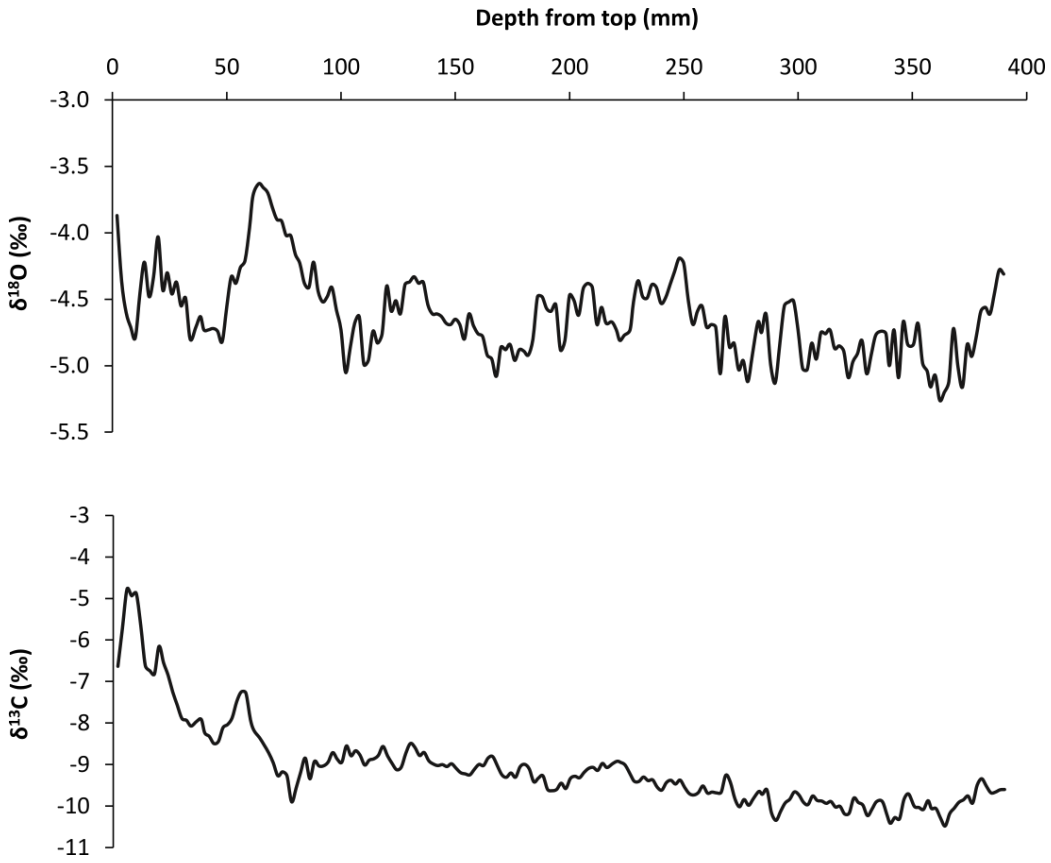

Figure 6.6: Oxygen and carbon isotope profiles for PER0 plotted against depth.

6.3.1.2 Growth rate

Growth rates were calculated using age modelling data generated through OxCal and proxy sample depths. The differences between depths and between modelled ages were used to calculate growth between two proxy data points. Growth rates for PER0 are presented in figure 6.7. Prior to 78.6ka, growth rate is variable with a peak at 83.3ka. Growth rates exhibit a significant decline at 78.6ka and remain low until 65.9ka. Towards the end of the record, growth rates show a slight increase.

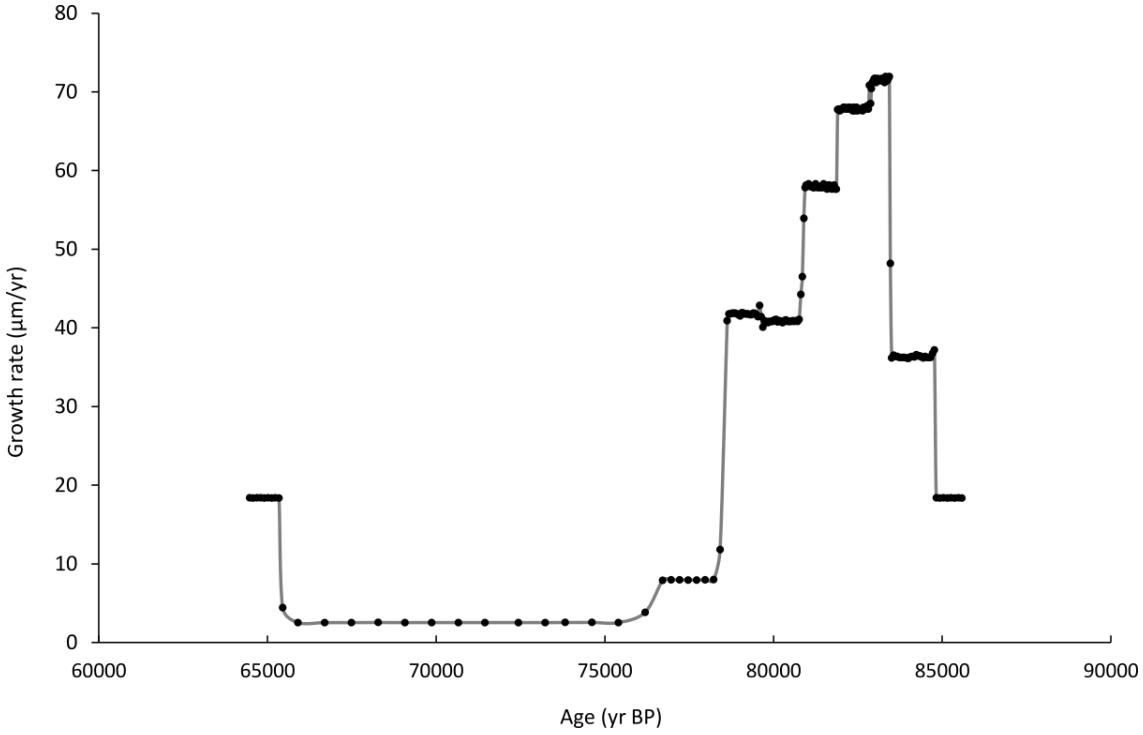

Figure 6.7: Growth rate for PER0.

6.3.2 PER10.3

6.3.2.1 Isotopes

An initial low-resolution isotope track was run on PER10.3 and this was sampled at 3mm intervals (figure 6.8). High-resolution oxygen and carbon isotope samples were micromilled from PER10.3 at 340µm intervals between 1.98mm and 203.1mm from the top of the speleothem. The oxygen and carbon isotope profiles are shown in figure 6.8. The oxygen isotope values from the high-resolution track exhibit a range of 1.65‰ and an average value of -3.81‰ while the carbon isotope values exhibit a range of 4.74‰ and an average value of -7.09‰. An R^2 value of 0.3 was found between oxygen and

carbon isotope values which suggests kinetic fractionation has not influenced the isotopic composition of the speleothem carbonate.

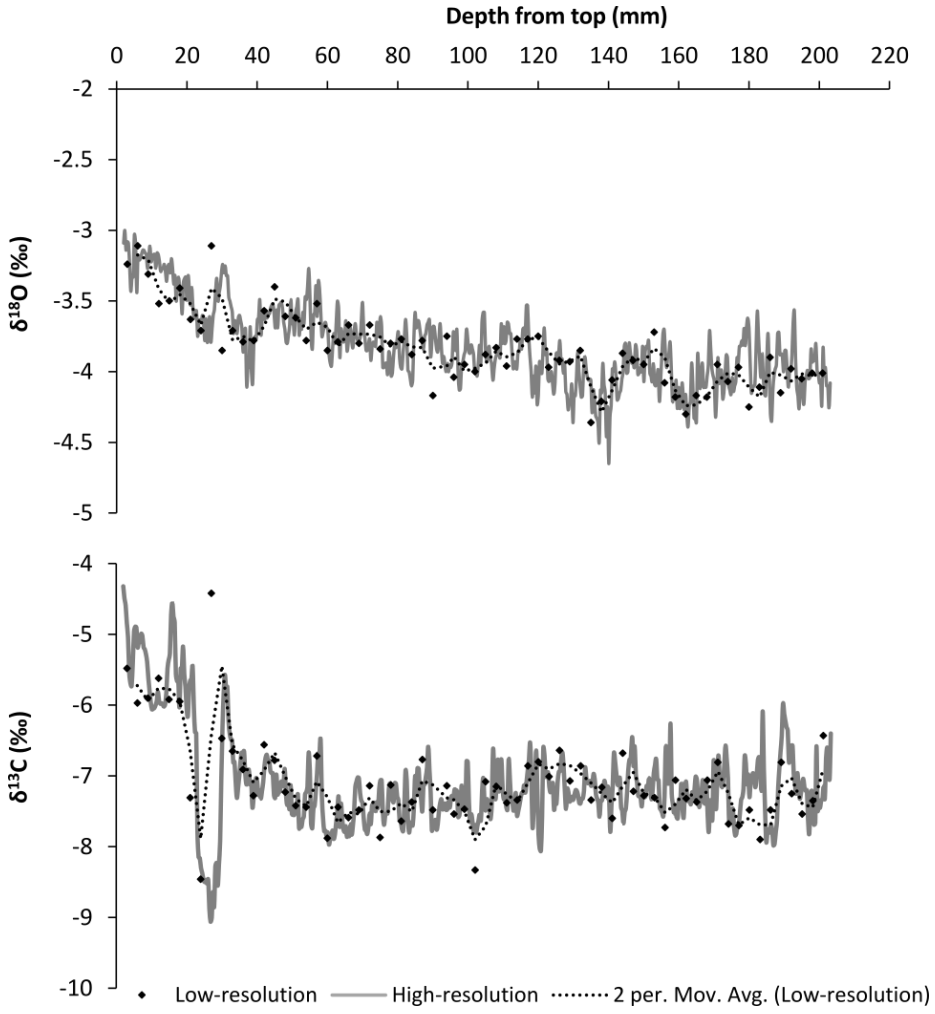

Figure 6.8: Oxygen and carbon isotope profiles for PER10.3 plotted against depth.

6.3.2.2 Trace elements

PER10.3 was cut into six segments for LA-ICP-MS and summarised data (averages, standard deviations and ranges) are presented for each segment in table 6.3 alongside the depth of each section. Data are presented as concentrations in parts per million (ppm) and were processed using MACS-3 and NIST612 standards. Full datasets will be used in section 6.4.2 alongside age models and isotope data to assess past climatic variability.

Table 6.3: Summarised trace element data for PER10.3.

Line name	Depth (mm from top)		Calibration standard	Mg			Ca			Sr			Ba		
	from	to		Average	Std Dev	Range	Average	Std Dev	Range	Average	Std Dev	Range	Average	Std Dev	Range
PER10.3 - 6	30.90	1.73	MACS 3	533	155	1423	540	85	740	15.53	17.80	261.51	1.84	2.08	32.78
PER10.3 - 5	67.71	28.74	MACS 3	586	122	1099	543	79	790	10.91	2.42	22.13	1.93	3.46	159.29
PER10.3 - 4	105.00	72.55	NIST612	653	159	1697	540	94	1078	11.31	3.62	27.61	4.97	8.00	148.63
PER10.3 - 3	146.00	106.39	NIST612	637	153	1238	540	65	671	10.75	4.13	35.10	2.16	6.42	21.96
PER10.3 - 2	176.00	147.23	MACS 3	588	90	993	540	70	712	11.33	2.23	22.32	1.94	1.80	55.44
PER10.3 - 1	203.00	180.77	MACS 3	540	74	686	540	46	407	11.65	2.18	34.56	1.71	1.84	102.74

6.3.2.3 Growth rate

Growth rates for PER10.3 are displayed in figure 6.9. Prior to 50.2ka, growth rate is variable with a peak at 51.4ka. A period of low growth rate (<2µm/yr) is evident between 29.8-50.1ka. Towards the end of the record there is a slight rise in growth rate.

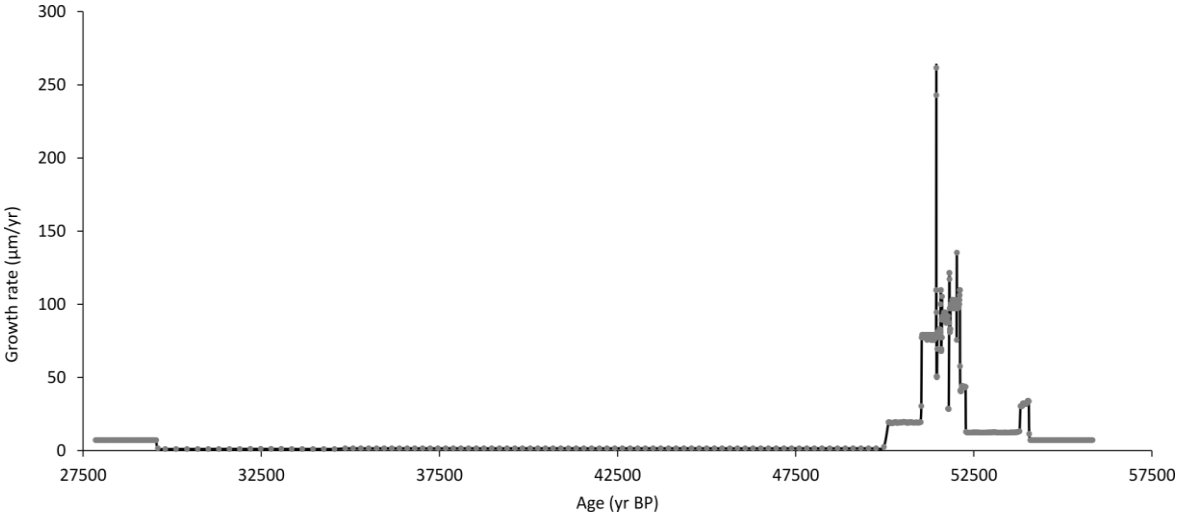

Figure 6.9: PER10.3 growth rate.

6.3.3 PER10.4

6.3.3.1 Isotopes

Samples for a low-resolution isotope analysis were hand-drilled from PER10.4 at 5mm intervals and high-resolution samples were micromilled at 670µm intervals between 5mm and 236.82mm and results are presented in figure 6.10. The oxygen isotope values from the high-resolution samples exhibited a range of 1.9‰ and an average value of -3.66‰ whilst the carbon isotope values exhibited a range of 6.16‰ and an average value of -6.71‰. Oxygen and carbon isotope values were found not to co-vary with an R^2 of 0.12.

6.3.3.2 Trace elements

PER10.4 was cut into six segments for LA-ICP-MS and summarised data (averages, standard deviations and ranges) are presented for each segment in table 6.4. Data are presented as concentrations in ppm and were processed using the NIST612 standard. The full dataset will be used in section 6.4.3 alongside isotope and age model data to assess past climatic variability.

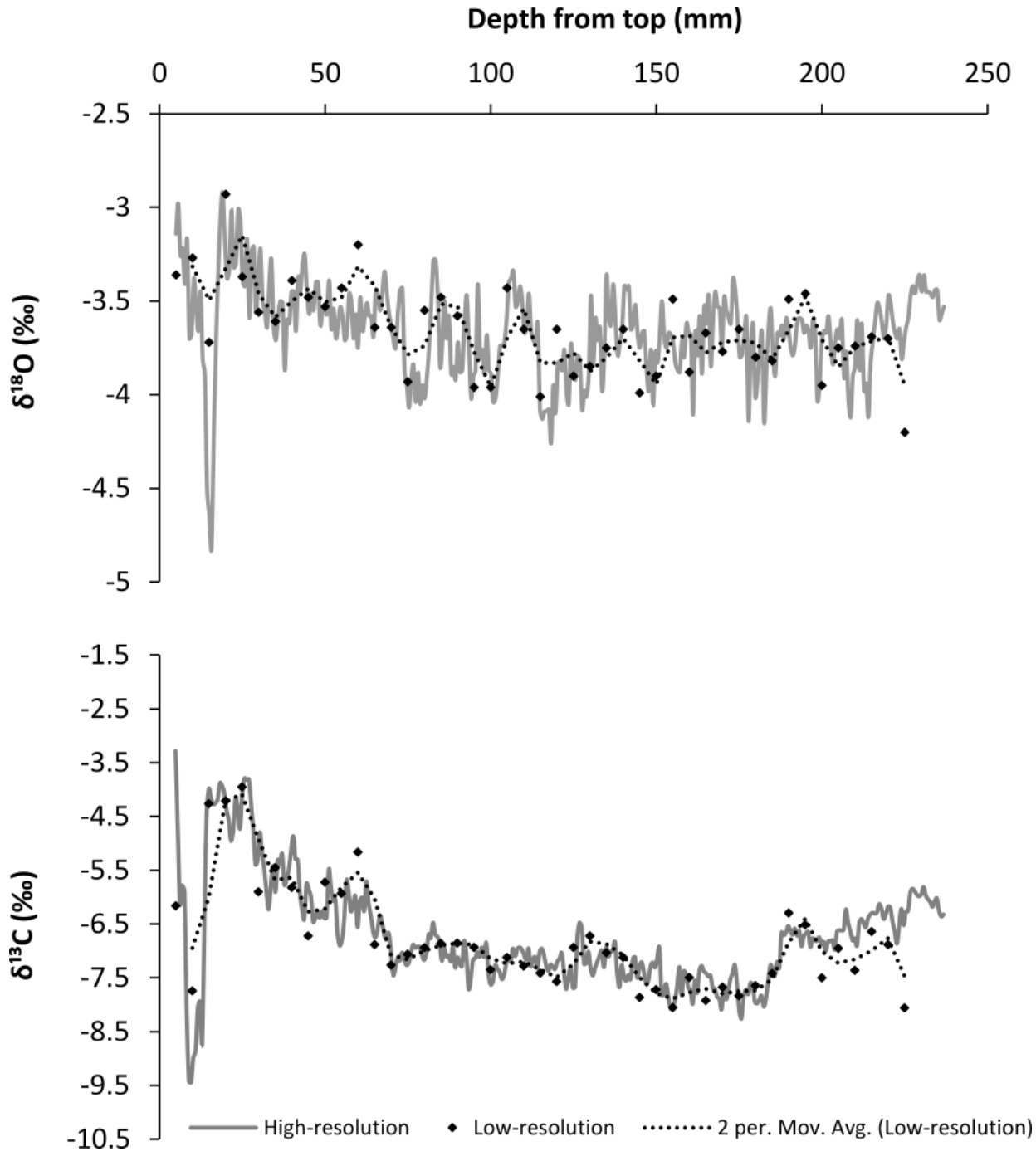

Figure 6.10: Oxygen and carbon isotope profiles for PER10.4 plotted against depth.

Table 6.4: Summarised trace element data for PER10.4. The column "R" represents the range of trace element concentrations.

Line name	**Depth (mm from top)**		**Standard**	**Mg**			**Ca**			**Sr**			**Ba**		
	from	***to***		***Aver***	***Std Dev***	***R***	***Average***	***Std Dev***	***R***	***Average***	***Std Dev***	***R***	***Average***	***Std Dev***	***R***
PER10.4 - 1.1	236.13	224.70	NIST612	829	165	1074	541	58	527	12.19	1.96	19.07	2.15	1.58	19.95
PER10.4 - 1.2	224.70	204.64	NIST612	742	146	1506	542	69	680	11.55	2.38	18.30	1.82	2.21	29.74
PER10.4 - 2	199.97	160.57	NIST612	652	152	1282	545	71	781	12.21	2.83	23.31	2.07	2.99	84.65
PER10.4 - 3	157.68	123.81	NIST612	566	110	1494	544	79	736	11.58	3.42	47.11	2.32	3.02	50.67
PER10.4 - 4	121.00	85.63	NIST612	626	147	1475	540	114	1026	11.62	3.42	26.07	13.23	49.23	727.64
PER10.4 - 5	78.98	44.60	NIST612	622	105	1087	540	67	860	13.09	2.43	24.68	1.58	0.59	14.33
PER10.4 - 6	40.60	0.34	NIST612	726	121	1496	542	40	889	14.11	11.97	211.86	2.42	5.55	134.53

6.3.3.3 Growth rate

Changes in growth rate occur throughout the PER10.4 record and are shown in figure 6.11. Prior to 46.5ka growth rate is variable, reaching a peak at 51ka. After 46.5ka, growth rate decreases, and values remain low (<1µm/yr) until the end of the record. The final two samples indicate a slight increase in growth rate prior to termination of growth.

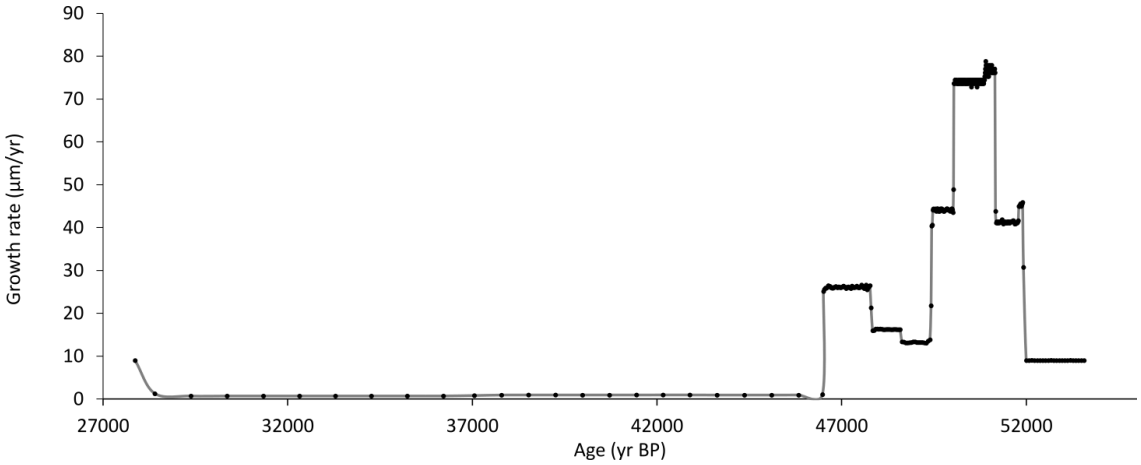

Figure 6.11: PER10.4 growth rate.

6.3.4 Determination of the signal preserved in speleothem proxies in relation to climate, environmental and cave processes.

Chapters 4 and 5 identified mechanisms which could influence proxies in speleothem calcite from modern monitoring data. This section explores these relationships and will investigate if such processes can be identified in the speleothem calcite geochemical records from Cueva de las Perlas over longer timescales.

6.3.4.1 Speleothem oxygen isotope records

Analysis of the oxygen and deuterium isotope composition of precipitation from the Matienzo region has revealed $\delta^{18}O_p$ responds primarily to variations in precipitation amount (section 5.4). Modern speleothem calcite has been identified to form in quasi-equilibrium with the cave environments (section 5.5). Consequently, speleothem oxygen isotope values are herein interpreted as a function of external precipitation amount.

6.3.4.2 Identifying karst-water interactions using speleothem proxies

Modern monitoring revealed the influence of karst-water interactions such as PCP and/or ICD on cave drip waters as evidenced by changes in $\delta^{13}C$ values and trace element (Mg and Sr) concentrations (sections 5.9.1.3 and 5.10.3.4). This section will use similar techniques used in chapter 5 to determine whether such karst-water interactions influence carbon isotope values and Mg and Sr concentrations in speleothems over long timescales.

Carbon isotopes

Sections 5.9.1.3 and 5.10.3.4 identified $\delta^{13}C$ values and Mg concentrations (subsequently Mg/Ca) in modern cave drip waters as a function of karst-water interactions such as PCP/ICD. However, the signal may be complicated by trying to assign a single forcing mechanism to account for variability on long timescales. Additionally, section 5.9.1.2 identified the role of vegetation and soil productivity in influencing carbon isotope values of percolating waters. Therefore, a continuous correlation between $\delta^{13}C$ values and Mg would not be expected.

Patterns of $\delta^{13}C$ values and Mg appear to be related in the speleothem calcite with high $\delta^{13}C$ values corresponding to high Mg values (figure 6.12). However, this relationship appears to be offset particularly <50ka BP. This offset may be a function of speleothem cutting for LA-ICP-MS and the positioning of the trace element sampling tracks in relation to isotope sampling. Additionally, the offset may be related to the low-resolution isotope sampling <50ka in PER10.3 and <46.5ka in PER10.4. Therefore, it remains challenging to draw any conclusion using the C isotope data independently due to the time series distortion.

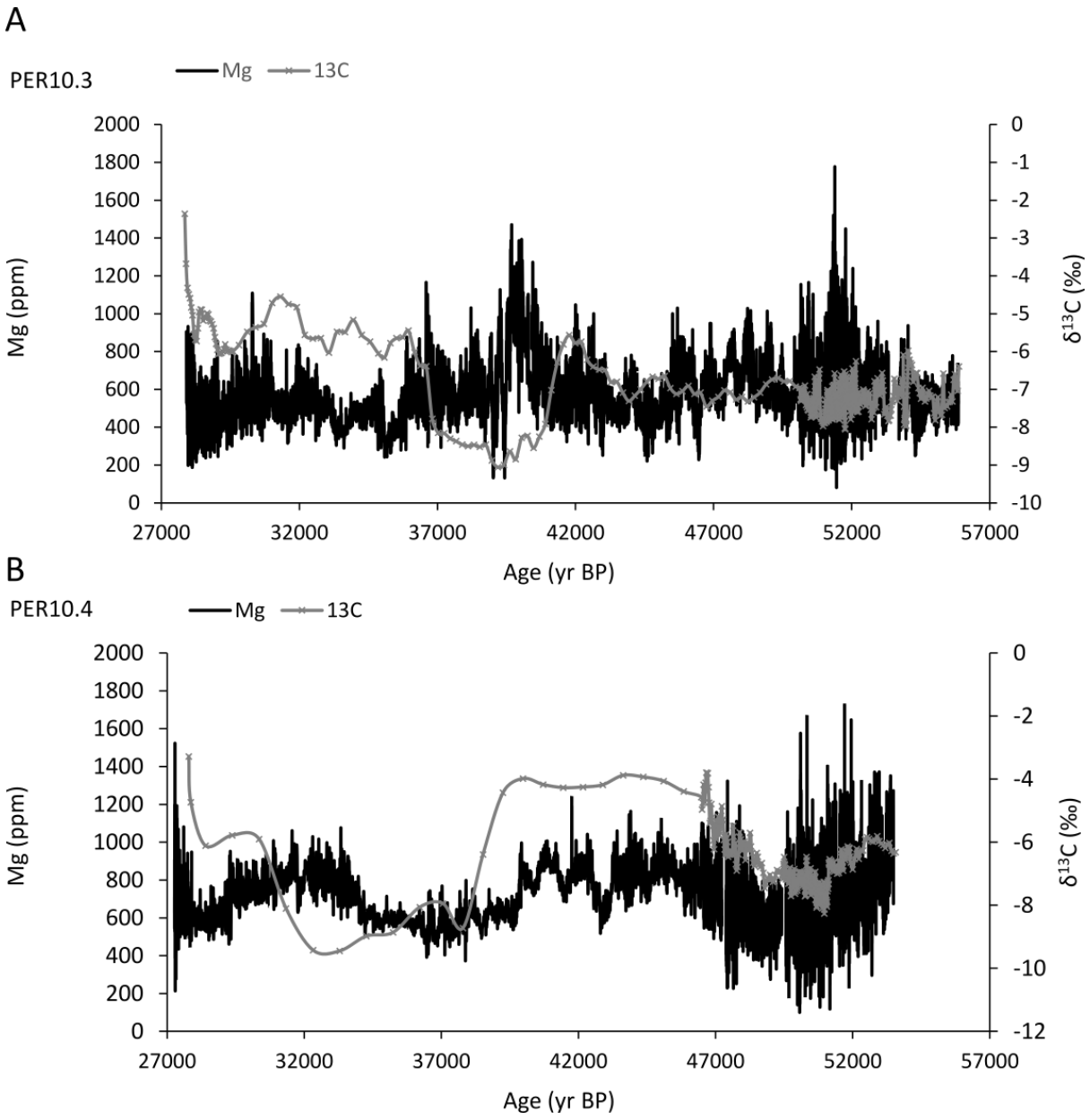

Figure 6.12: $\delta^{13}C$ values and Mg concentrations for PER10.3 (A) and PER10.4 (B).

Co-variation of Mg and Sr

The direct correlation between Mg and Sr is weak as demonstrated by an R^2 of 0.2 and 0.15 for PER10.3 and PER10.4 respectively (figure 6.13A and 6.13B). However, a CORREL statistical analysis was used to distinguish if the relationship between Mg and Sr was variable across the record (figure 6.13C and 6.13D). A CORREL function provides a Pearson Product-Moment Correlation Coefficient between Mg and Sr across a set range. Consequently, the CORREL function was used herein to provide a running correlation between Mg and Sr over set intervals of 20 data points. In figures 6.13C and 6.13D values

lying above the confidence intervals suggest a statistically significant correlation with those lying above 0 indicative of a positive correlation whilst those below 0 indicate a negative correlation. The CORREL analysis identified 76% of the PER10.3 record and 68% of the PER10.4 record exhibited a statistically significant correlation between Mg and Sr and therefore the relationship is indicative of PCP/ICD throughout the record with evidence for other processes driving variability at points where Mg and Sr are not correlated.

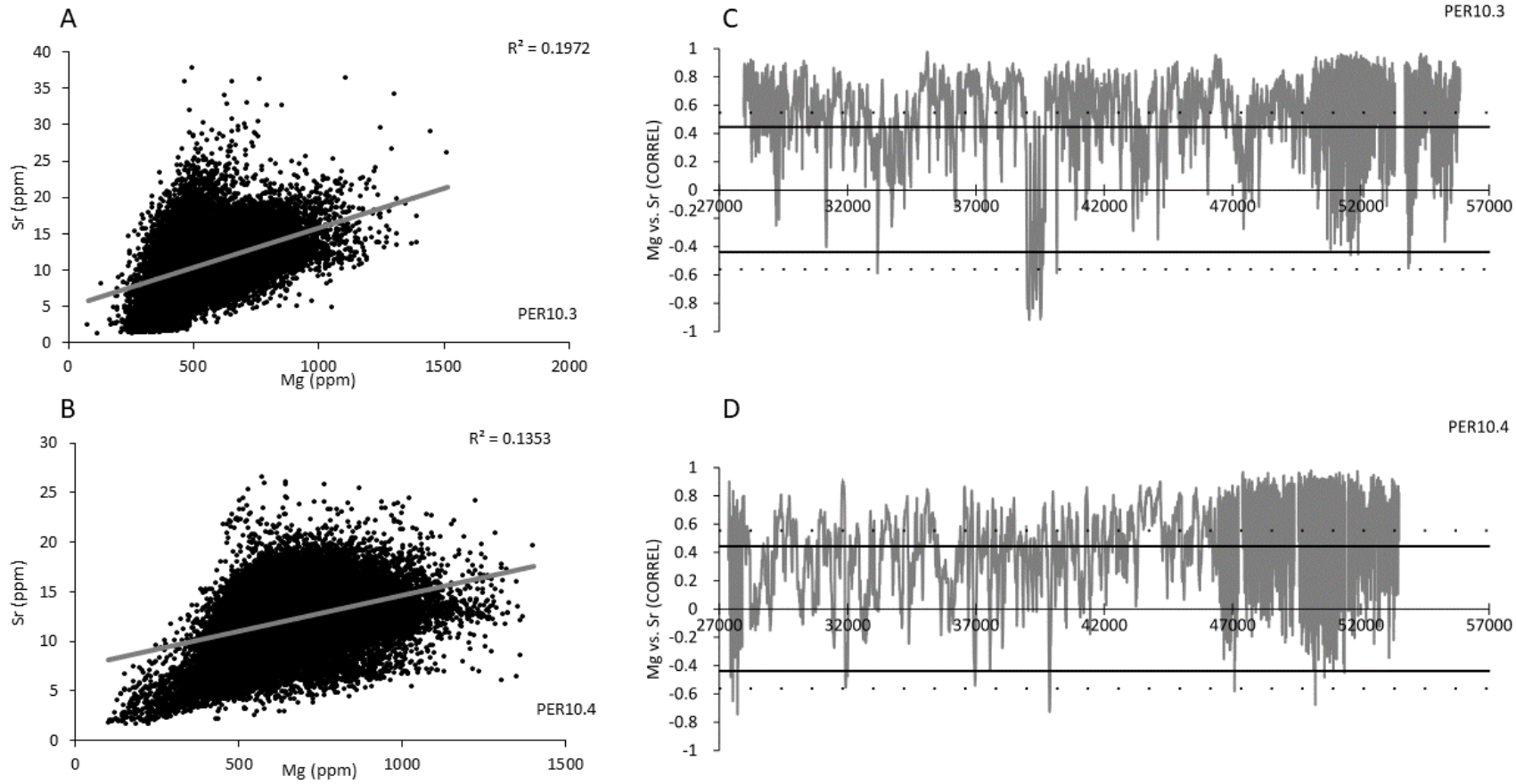

Figure 6.13: Relationships between Mg and Sr for PER10.3 and PER10.4. Mg and Sr plots for PER10.3 (A) and PER10.4 (B) and CORREL plots for Mg vs. Sr for PER10.3 (C) and PER10.4 (D). The solid black lines on figures C and D represent 95% confidence intervals of 0.444 and the dashed lines represent 99% confidence intervals of 0.561 where n-2=18.

Assessment of karst-water interaction through Sr/Ca and Mg/Ca

Modern dripwaters within Cueva de las Perlas have identified the influence of PCP/ICD processes within the overlying karst using ln(Sr/Ca) and ln(Mg/Ca) (section 5.10.3.5) according to the methodology of Sinclair *et al.* (2012). The same principal was used to compare the trace elements (Mg and Sr) from speleothem calcite (figures 6.14A and 6.14B). The slope of ln(Sr/Ca) and ln(Mg/Ca) was 0.68 for PER10.3 which lies on the boundary of the range predicted by Sinclair *et al.* (2012) of 0.703-1.03 to one decimal place. In contrast, PER10.4 does not lie within the predicted range of Sinclair *et al.* (2012) for ln(Sr/Ca) and ln(Mg/Ca) with a slope of 0.29.

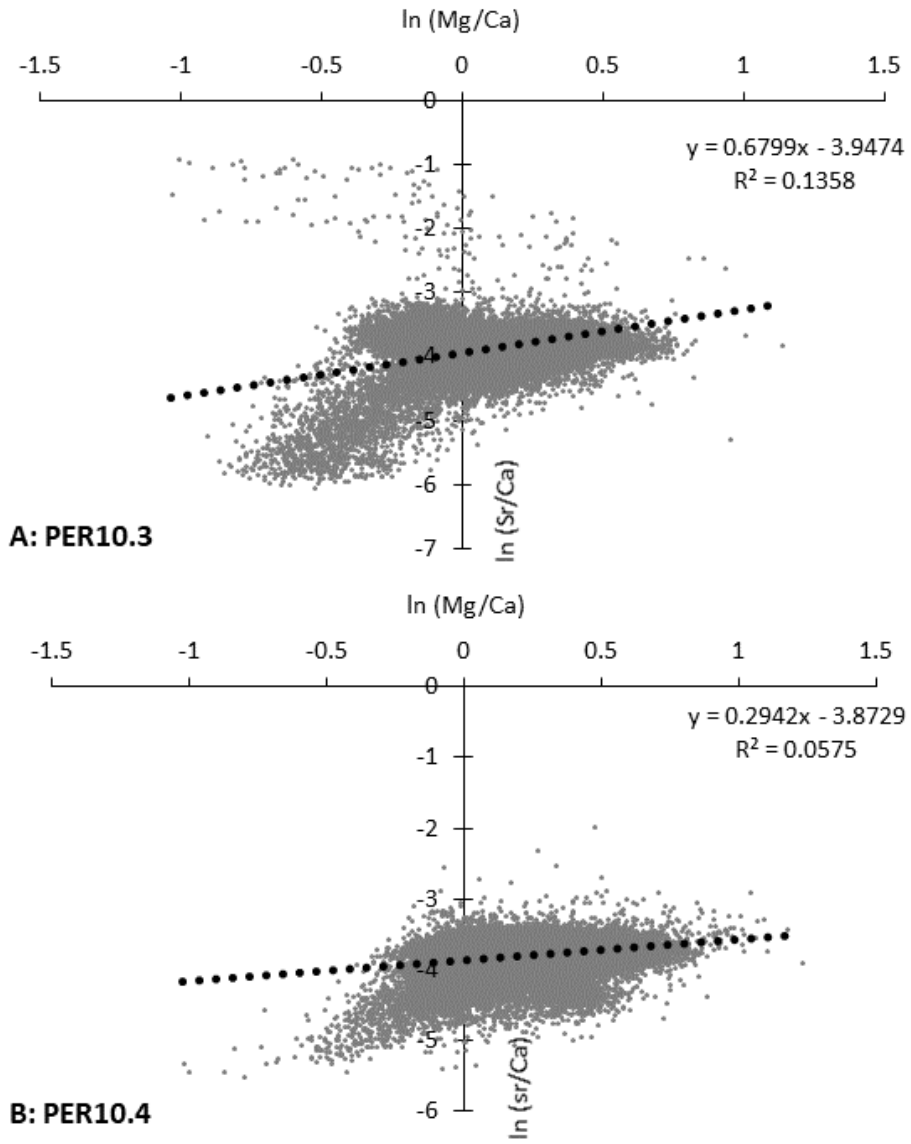

Figure 6.14: ln(Sr/Ca) and ln(Mg/Ca) plots for Mg vs. Sr for PER10.3 (A) and PER10.4 (B).

As deposition of these speleothems occurred over a period exceeding 25ka, a consistent relationship between Mg and Sr across the whole record would not be expected. Previously the CORREL analysis identified 76% and 68% of the PER10.3 and PER10.4 records exhibited a positive correlation indicating karst-water interaction processes such as PCP or ICD as the predominant controlling mechanism. However, each record contains a proportion where Mg and Sr are not correlated, 24% for PER10.3 and 32% for PER10.4. Thereby, invoking alternative independent forcing mechanisms which influence the different trace element concentrations at different periods of time. During these periods, ln(Sr/Ca) and ln(Mg/Ca) would not be expected to plot along the Sinclair *et al.* (2012) line and this is illustrated by the degree of scatter in figures 6.14 A and 6.14B.

Investigating variability of karst-water interaction processes within speleothem records

As suggested above, consistency in the relationships between ln(Sr/Ca) and ln(Mg/Ca) should not be expected over long speleothem records due to the changing driving mechanisms over time which may or may not be a function of climate and/or environmental variability. This section will analyse evidence for this variability across each record using the methodology of Sinclair *et al.* (2012) across time-slices of 500yrs. The results of this analysis are presented in figures 6.15A and 6.15B. These figures demonstrate that only a small proportion of values actually lie within the predicted Sinclair *et al.* (2012) range indicative of PCP/ICD processes and highlight the variability across the record. This analysis calls into question the applicability of the Sinclair *et al.* (2012) PCP/ICD determination method using ln(Sr/Ca) and ln(Mg/Ca) to long high-resolution speleothem palaeoclimate datasets.

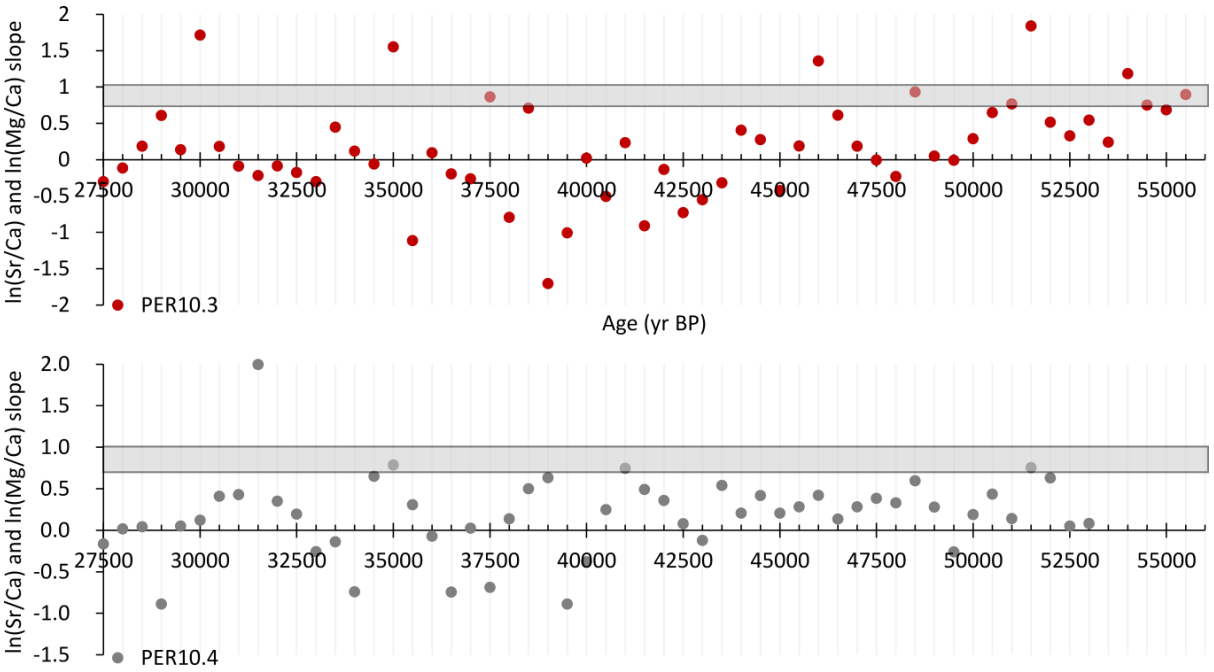

Figure 6.15: Slope values for 500yr time-slices from PER10.3 and PER10.4. Slope values define the relationship between ln(Sr/Ca) and ln(Mg/Ca). Grey shaded boxes represent the theoretical slope for PCP/ICD calculated by Sinclair et al. (2012).

Investigating the influence of alternate processes: A case study from PER10.3

A cluster of values in the PER10.3 record exhibit an inverse trend to the rest of the dataset and these are highlighted in figure 6.16A. These values span the period between 39.1-40ka and record a negative relationship between ln(Sr/Ca) and ln(Mg/Ca) values with an R^2 value of -0.76 (figure 6.16B). The negative correlation between these values indicates mechanisms other than PCP or ICD controlling trace element uptake into percolating waters and subsequent incorporation into speleothem calcite.

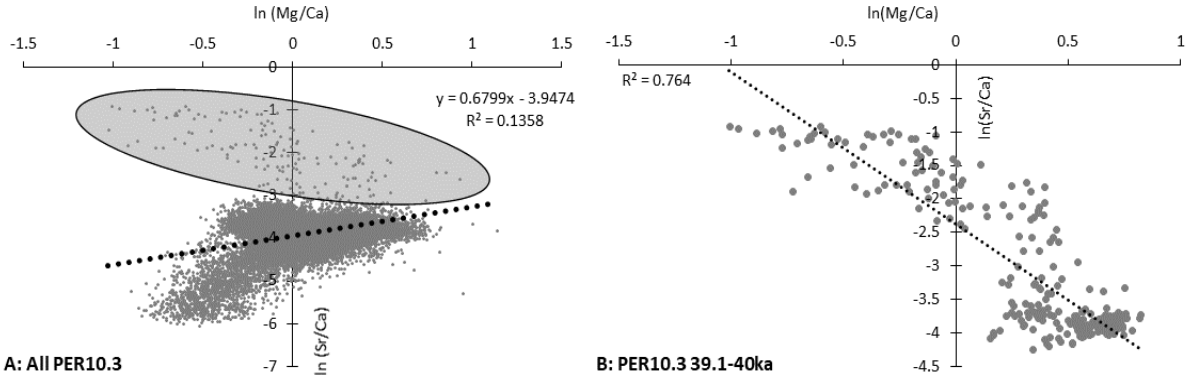

Figure 6.16: ln(Mg/Ca) and ln(Sr/Ca) values for all of PER10.3 (A) and between 39.1-40ka (B). Grey shading on A highlights the values shown in B relative to the remaining dataset.

Increases in Mg relative to Sr indicate an independent control driving trace element concentrations. Dolomite dissolution has been suggested to drive Mg values independently of Sr values due to the chemical composition of the host rock (high Mg and low Sr) (Webb *et al.,* 2014). During prolonged water-contact times associated with periods of water deficit and aridity, slow dolomite dissolution will enhance Mg concentrations of infiltrating waters. Additionally, growth rate has been demonstrated to influence Sr partitioning into speleothem calcite (Huang and Fairchild, 2001; Treble *et al.,* 2003; Webb *et al.,* 2014) and is invoked herein as having a secondary influence on Sr concentrations. This influence is shown by the strong positive correlation between Ba and Sr of R^2= 0.88 (figure 6.17). In summary, Mg concentrations are influenced by PCP and/or ICD and enhanced by dolomite dissolution under dry conditions. Sr and Ba are influenced by PCP and/or ICD but are influenced by growth kinetics at key points throughout the record.

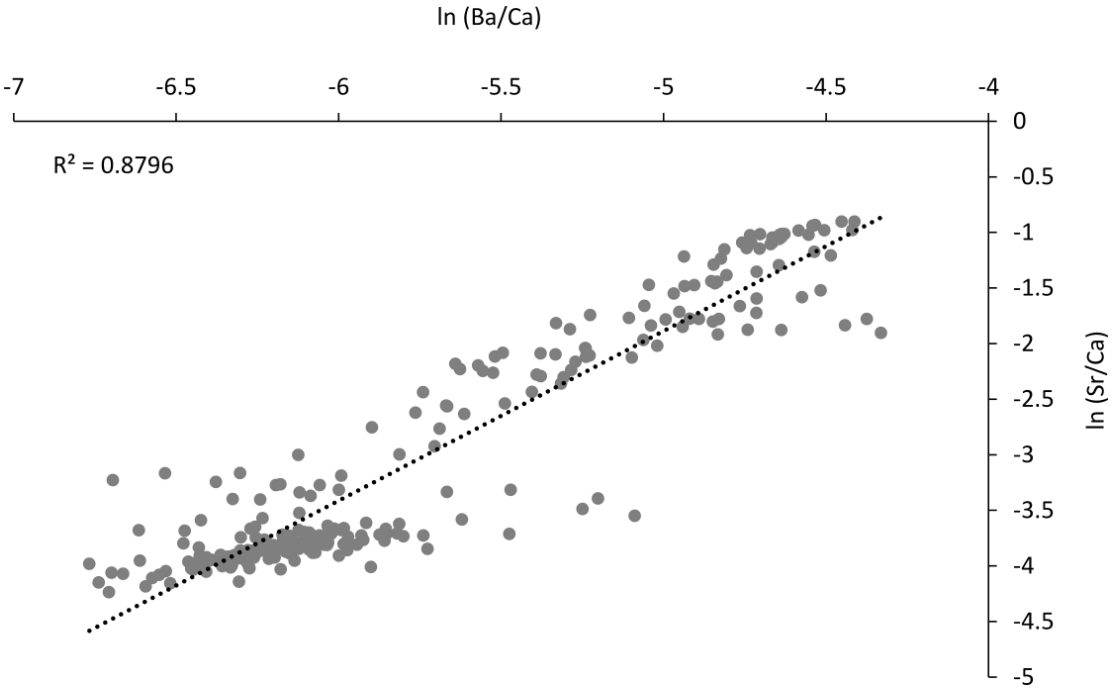

Figure 6.17: ln(Ba/Ca) and ln(Sr/Ca) for PER10.3 between 39.1-40ka.

6.3.4.3 Summary

Oxygen isotope values from speleothem calcite are interpreted to represent variations in precipitation amount. Carbon isotopes are interpreted to represent variations in soil productivity and karst processes such as PCP and ICD. Further analysis is needed to clarify the influence of soil productivity on $\delta^{13}C$ values in speleothem calcite. Under dry conditions these processes will lead to an increase in $\delta^{13}C$ values.

Evidence for karst-water interaction processes such as PCP and ICD throughout each of the datasets is shown through a running correlation between Mg and Sr values for each speleothem. However, these relationships are variable through time and therefore do not fit the predicted ln(Sr/Ca) and ln(Mg/Ca) slope of Sinclair *et al.* (2012). Numerous processes influence trace element concentrations (and $\delta^{13}C$ values) prior to preservation in speleothem calcite and it is proposed that the relative influence of these processes vary over timescales captured by the speleothems. The example given from PER10.3 (6.3.4.2) demonstrates the potential of growth kinetics influencing Sr and Ba values, furthering the evidence that a single forcing mechanism cannot be assigned to trace elements over the time period documented in the speleothem records (~25ka).

6.4 Identifying palaeoclimate and palaeoenvironmental patterns in the speleothem proxy records

Sections 6.2 and 6.3 created age models and presented the raw geochemical data for the three speleothems analysed. This section aims to link the previous sections together by presenting records of past climate and environmental variability for each speleothem. Each record is used to identify palaeoclimate and palaeoenvironmental patterns through analysing proxy shifts within the speleothem geochemical data.

6.4.1 PER0

The PER0 record (figure 6.18) spans the period between 85,964 ±461yr BP to 64,469 ±897 yr BP. The oxygen and carbon isotope records demonstrate an overall shift to increasingly positive values throughout the record with some oscillations and variability superimposed.

A positive oxygen isotope excursion occurs at 78.6ka and is represented by a 1.42‰ shift. This excursion can also be seen in the carbon isotope values at 77.5ka by a shift of 2.65‰. After this excursion, oxygen and carbon isotope values decline until 71ka. After 71ka, oxygen isotope values rise until 65.9ka. A significant isotopic excursion at 65ka is represented by a negative isotopic shift of 0.76‰ and 0.67‰ in the oxygen and carbon isotope values respectively. Towards the end of the record both carbon and oxygen isotope values rise until cessation of growth at 64.5ka.

For the majority of the PER0 record, 86%, the growth rate is relatively high at >18µm/yr (figure 6.18). Between 80.9ka and 83.4ka the growth rate is particularly high at >50µm/yr and sampling resolution during this period was therefore also high with 42% of samples for isotope analysis taken from this section. Between 65.4ka and 78.2ka growth rate falls to <10µm/yr and sampling resolution is low during this period. After this decline, growth rates increase to 18µm/yr at 65.3ka to the end of the record at 64.5ka.

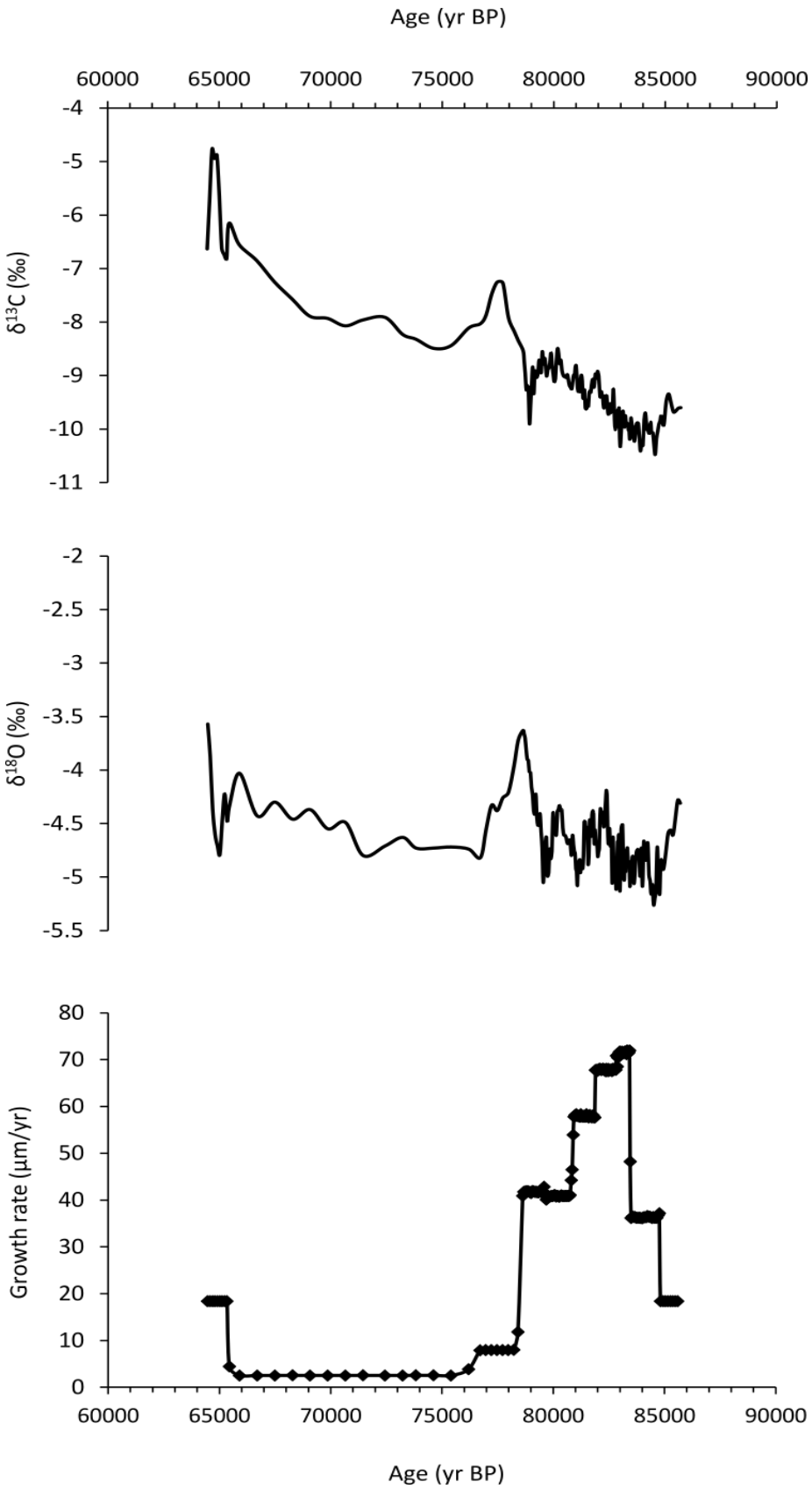

Figure 6.18: PER0 oxygen and carbon isotope values and growth rate. The black diamonds on the growth rate plot illustrate isotope sampling resolution.

6.4.2 PER10.3

PER10.3 grew between 55,880±395yr BP and 27,850±2,668yr BP. Oxygen and carbon isotope values, growth rate, Mg and Sr are presented against age in figure 6.19 and are summarised in table 6.5.

Prior to 51.1ka, the stalagmite growth rate is relatively fast with 91% of values greater than 10µm/yr and 76% greater than 30µm/yr. The high sampling resolution during this period allows high-magnitude variability within each of the different proxies to be identified.

Growth rate declines at 50.1ka which coincides with an upwards shift towards positive oxygen and carbon isotope values. Both carbon and oxygen isotope values demonstrate a peak at 41.3ka and 41.8ka respectively. The higher-resolution Mg and Sr values exhibit distinct positive excursions at 39.7ka and 39.4ka. Although these peaks are offset from the stable isotope excursions, the onset of the rise in Mg starts at 41.7ka.

Following the positive isotope and trace element excursion, values decline between ~40-35ka. At 35ka there is a slight decline in growth rate (0.42µm/yr). This decline is accompanied by an increase in Mg and Sr values with a peak at 35ka and the onset of increasing $\delta^{13}C$ values with a later peak at 34ka.

Between 30-35ka carbon isotope values demonstrate a distinct series of peaks which correspond to oscillations in Mg and Sr. For example, the peak in $\delta^{13}C$ values at 31.1ka corresponds to peaks in Mg and Sr at 30.8ka and 30.7ka respectively. After <30ka, both oxygen and carbon isotope values and trace elements increase which coincides with the termination of the record at 27,850yr BP.

Table 6.5: Summary of proxy shifts in the PER10.3 record.

Age	**Proxy shifts**
Prior to 51.05ka	Growth rate is high
50.1ka	Growth rate decline, upwards shift in $\delta^{13}C$ and $\delta^{18}O$ values
39.5-42ka	Positive isotope and trace element excursion
30-32ka	Increase in Mg and Sr values
27.9ka	Cessation of growth increase in $\delta^{13}C$, $\delta^{18}O$, Mg and Sr values.

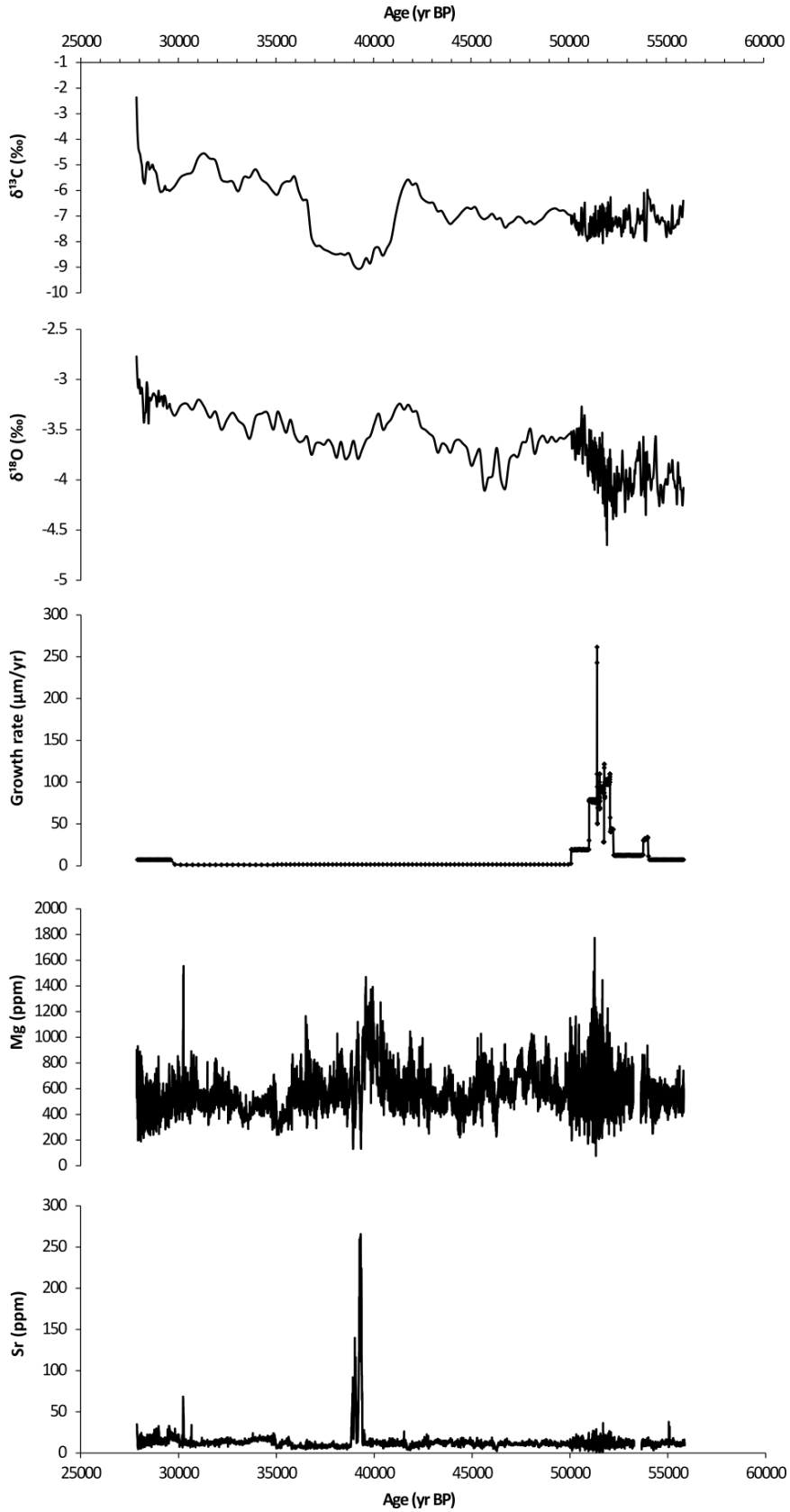

Figure 6.19: PER10.3 speleothem proxies (carbon isotope values, oxygen isotope values, growth rate, Mg and Sr). Growth rate was calculated using the isotope data and the markers indicate sampling resolution.

6.4.3 PER10.4

The PER10.4 record spans 25,772yrs between 53,564±272 yr BP and 27,792±545 yr BP. Oxygen and carbon isotope values, growth rate, Mg and Sr are presented against age in figure 6.20 and key shifts are summarised in table 6.6.

The earliest part of the record between 46.5ka and 53.6ka has a high sampling resolution, a high growth rate (9-78µm/yr) and a low age error (<400yrs). During this period oxygen and carbon isotope values and Mg and Sr values are variable. At 50-51.2ka, growth increases to >70µm/yr and $\delta^{13}C$ values decrease by 1.55‰. Additionally, during this period Mg and Sr values exhibit an increased degree of variability related to an increased sampling resolution. A positive excursion in oxygen and carbon isotope values is evident between 44.4-47.1ka. During this period carbon isotope values increase by 2.41‰ and oxygen isotope values increase by 0.95‰.

After 46.5ka, the sample resolution for the isotope values decreases, growth rates become very slow at <1µm/yr and age errors become larger at ±2.5-3.5ka. A negative oxygen isotope excursion is represented by a decrease of 1.9‰ in oxygen isotope values at 40.7ka and a decrease of 4.72‰ in carbon isotope values at 37.8ka.

Following this, $\delta^{13}C$ and $\delta^{18}O$ values increase to a peak at 37.1ka which is also expressed by a peak in Sr and Mg values at 36.8ka and 36.7ka respectively. Carbon isotope values decline significantly after this event by 1.51‰ until 32.3ka. Oxygen and carbon isotope values increase between 32.3-29.4ka by 0.53‰ and 3.67‰ respectively. Sr and Mg display a peak at 31.7ka. The end of the record (<30ka) indicates a shift toward higher carbon and oxygen isotope values accompanied by an increase in Mg and Sr concentrations.

Table 6.6: Summary of proxy shifts in the PER10.4 record.

Age	**Proxy shifts**
Prior to 46.5ka	High growth rate increase in $\delta^{13}C$ and $\delta^{18}O$
46.5ka	Growth rate declines
40.7-37.8ka	Negative isotope excursion in both oxygen and carbon isotope values.
32.3-29.4ka	Positive excursion in $\delta^{13}C$ and $\delta^{18}O$ values and Mg and Sr concentrations
27.8ka	$\delta^{13}C$ and $\delta^{18}O$ values and Mg and Sr concentrations all increase until termination of growth.

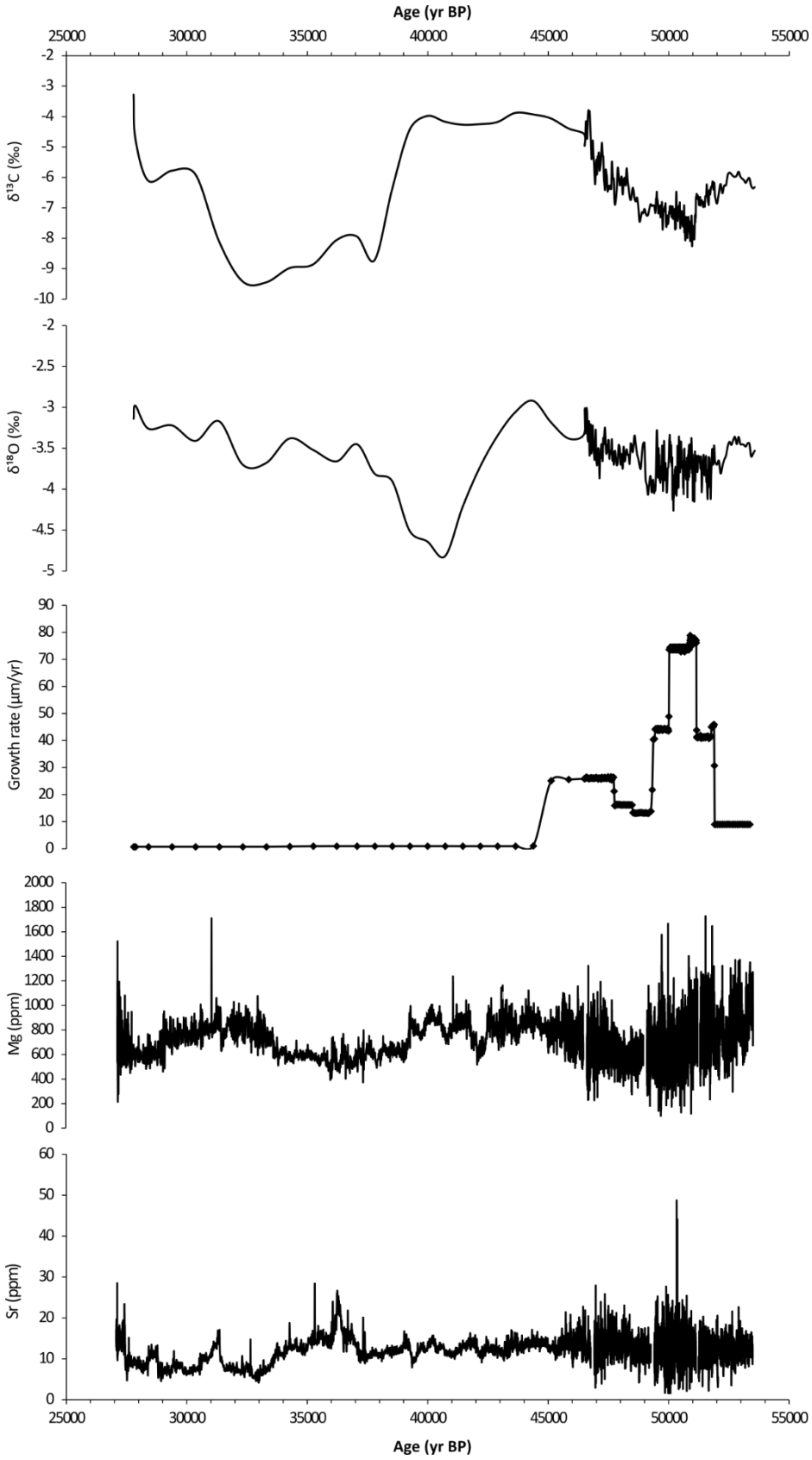

Figure 6.20: PER10.4 speleothem proxies (carbon isotope values, oxygen isotope values, growth rate, Mg and Sr). Growth rate was calculated using the isotope data and the markers indicate sampling resolution.

6.4.4 Comparison of PER10.3 and PER10.4 isotope records

Both PER10.3 and PER10.4 records have been presented separately in sections 6.4.2 and 6.4.3 respectively. The aim of this section is to compare the isotope records for each of these sections. Trace element series are not compared here due to the higher sampling resolution. Due to the 'twinned' depositional nature of these samples (section 3.3.2) a similar isotopic signature would be expected within both the speleothem records. The oxygen and carbon isotope profiles for PER10.3 and PER10.4 are directly compared in figures 6.21A and 6.21B through the inclusion of age error bars.

The earliest sections of both speleothem isotope records are characterized by relatively low age errors (typically less than ±500yr) and high sampling resolutions because of higher growth rates. Isotope sampling resolution decreases in PER10.3 at 50ka whereas PER10.4 remains relatively high until 46.5ka.

Throughout both the records, similar patterns emerge from the $\delta^{18}O$ and $\delta^{13}C$ isotope values. Table 6.7 shows that there are distinct differences in the timing of the isotopic shifts. However, with the exception of the first peak in $\delta^{13}C$ values, the other isotopic shifts from PER10.3 and PER10.4 overlap within age error.

Table 6.7: Timings of isotopic shifts in PER10.3 and PER10.4.

Event	**PER10.3**		**PER10.4**	
	Age (yr BP)	**Error (±)**	**Age (yr BP)**	**Error (±)**
$\delta^{18}O$ values increase	41772	4254	44365	2638
$\delta^{13}C$ values increase	41772	4254	46713	480
$\delta^{18}O$ values decrease	39185	3837	40711	3419
$\delta^{13}C$ values decrease	39185	3838	37789	2907

The leads and lags between the isotopic peaks and troughs demonstrated in the PER10.3 and PER10.4 records may be a function of their individual age models. Benson *et al.* (2018) have demonstrated the importance of an individual robust chronology for each speleothem even when they lie within close proximity to each other. Each of the age models were constructed using a different number of dates and therefore models may be offset. The differences between the two records may also be a function of the isotope sampling resolution. The isotope sampling resolution in PER10.4 becomes significantly

reduced after 46.5ka with an average of one sample per 800yr and only 24 samples cover the 16mm section representing 18,689 years of growth. Therefore, it is argued that the isotope record from PER10.4 post-46.5ka does not provide an accurate representation of the palaeoclimate due to a low isotope sampling resolution. Sampling resolution of PER10.3 falls to one sample per 200-300yrs after 50ka which although not ideal, will provide a more accurate indication of climatic and environmental variability compared to the sparse resolution of PER10.4.

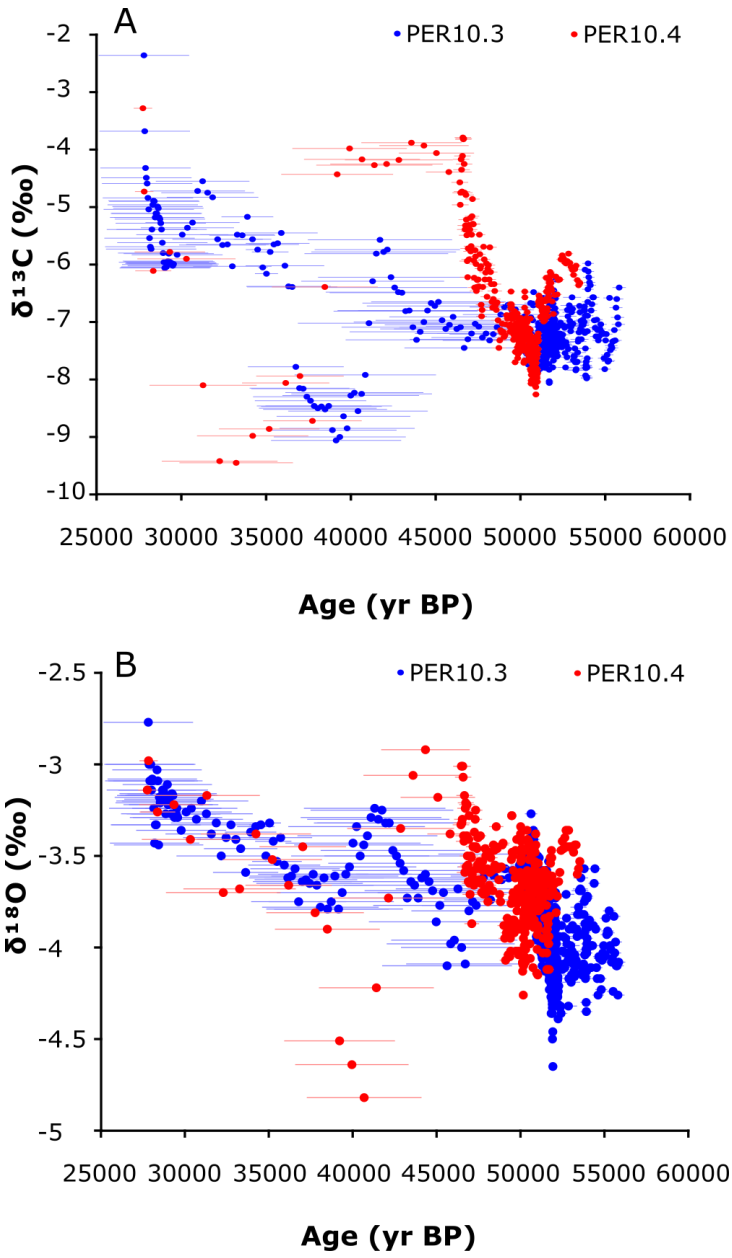

Figure 6.21: Comparison of carbon and oxygen isotope profiles from PER10.3 and PER10.4.

6.5 Assessment of climatic and environmental variability in the Matienzo valley on orbital and sub-orbital timescales

6.5.1 The response of speleothem records to environmental change on orbital timescales

Orbital forcing has been long identified as a forcing mechanism driving glacial-interglacial variability propagated by changing insolation intensity and distribution (section 2.2.2). In order to assess the long-term trends in the speleothem proxies from Cueva de las Perlas in relation to orbital forcing, the speleothem oxygen and carbon isotope records and growth rates have been compared to NH summer insolation at 65°N. Proxies from the Cueva de las Perlas speleothems correspond to Northern Hemisphere insolation on orbital timescales (figure 6.22). The earliest section of the PER0 record represents late MIS5 with the MIS5a peak at 82ka. During this period oxygen isotopes are at their lowest value indicating predominantly wet conditions. Additionally, carbon isotopes which indicate high levels of productivity are relatively low and growth rates are significantly higher. This period coincides with a maximum in insolation. As insolation begins to decline at ~78ka, growth rate slows, and isotope values begin to increase towards the MIS4 boundary until cessation of growth at 64.5ka. The MIS4 boundary at 71ka marks the onset of glacial conditions across the northern hemisphere and an insolation minimum which is expressed in the Cueva de las Perlas palaeoclimate record as a shift to drier conditions.

Initiation of growth of PER10.3 at 55.9ka and PER10.4 at 53.6ka coincides with a return to higher insolation values during MIS3. Growth rates from the early part of both of these records are high and oxygen isotopes indicate relatively high levels of precipitation. Additionally, carbon isotope values are relatively low, supporting a wetter climate with high vegetation and enhanced soil productivity. The decline in growth rates in PER10.3 at 50.1ka and PER10.4 at 46.5ka correspond to declining insolation, and isotope proxies indicate a shift towards drier conditions. The increase in oxygen and carbon isotope values and continued low growth rate in both speleothems towards termination of growth corresponds to declining insolation and the onset of glacial conditions associated with MIS2.

Therefore, figure 6.22 demonstrates that oxygen and carbon isotope values and speleothem growth rates are reflecting variations in NH summer insolation on orbital timescales. During periods of NH summer insolation maxima (interglacial periods), northern Iberia was wetter as demonstrated by the high speleothem growth rates and relatively low oxygen and carbon isotope values. In contrast, during periods of NH summer insolation minima (glacial periods), northern Iberia was drier, and this is recorded in Cueva de las Perlas through low speleothem growth rates and relatively higher oxygen and carbon isotope values.

Although the speleothems presented in figure 6.22 correspond to variations in NH summer insolation on orbital timescales, it is apparent that there is sub-orbital variability demonstrated by significant isotopic shifts throughout the records. These will be examined in the section below in conjunction with trace element data.

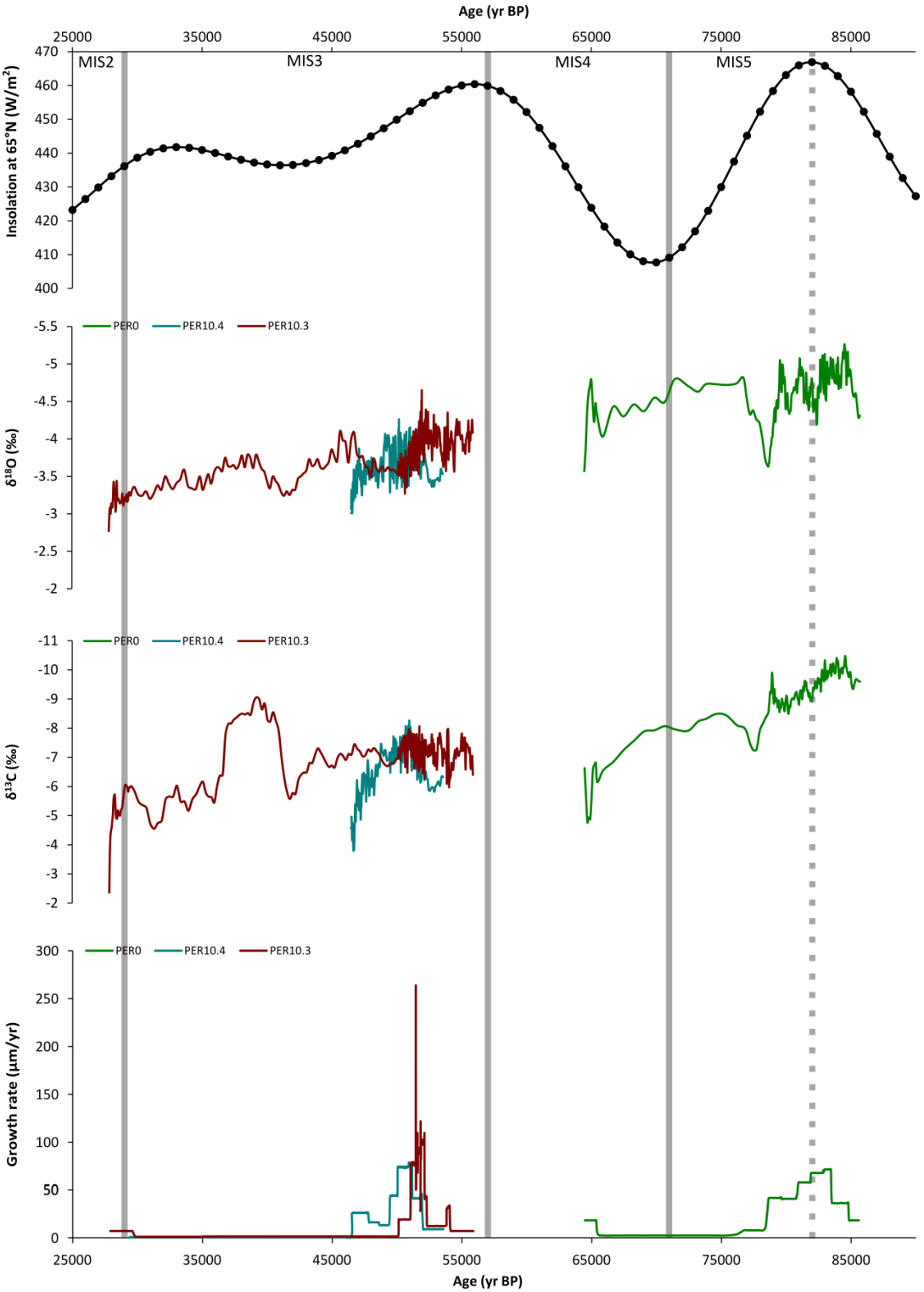

Figure 6.22: Speleothem palaeoclimate record from Cueva de las Perlas and NH Hemisphere summer insolation at 65°N (Berger and Loutre, 1991; data: Berger and Loutre, 1999). Grey bands represent MIS boundaries and the dashed line represents the MIS5a peak (Lisiecki and Raymo, 2005). PER10.4 isotopes <46.5ka have been removed following section 6.4.4.

6.5.2 The timing, onset and characterisation of millennial scale events in the Cueva de las Perlas speleothem records

6.5.2.1 Overview

Millennial-scale events, referred to as Heinrich events, have been documented in marine and terrestrial archives from across the Northern Hemisphere. Evidence for millennial-scale events from the Cueva de las Perlas sequence was identified in sections 6.4.2 and 6.4.3 and also superimposed onto the orbital cyclicity evidenced in section 6.5.1. Three 'Perlas Events' have been identified from the speleothem records at 28-33ka, 38-43ka and 46.5-51ka based upon variations in each of the different proxies. This section will assess the evidence for each of these 'Perlas Events' individually using $\delta^{18}O$ and $\delta^{13}C$ values, changes in growth rate and trace elements (primarily Mg, Sr and Ba).

6.5.2.2 Perlas Event 1

Proxies from both PER10.3 and PER10.4 have identified Perlas Event 1 (28-33ka) as a period of climatic variability with a signature similar to millennial-scale events (figure 6.23). The PER10.3 record identifies a shift in Mg relative to the baseline at 31ka and a peak in $\delta^{13}C$ values at 31.3ka. Additionally, a running mean (n=60) indicates a period of heightened correlation between Mg, Sr and Ba (R^2 = >0.8) between 30.3-30.6ka. This increased correlation suggests a primary forcing mechanism is controlling these elements, as well as $\delta^{13}C$ values during this period. As previously indicated in section 6.3.4, correlation between these elements and $\delta^{13}C$ values would suggest PCP/ICD as the primary forcing mechanism. Peaks in these elements indicate a shift towards drier conditions as a result of enhanced PCP/ICD.

Perlas Event 1 is less clearly shown within the PER10.4 record. A peak at 31.7ka is evident in both Mg and Sr (figure 6.23). The most significant correl peak between Mg vs. Sr is demonstrated at 31.9-32.2ka which is replicated in the Sr vs. Ba and Ba vs. Mg records. However, a secondary significant peak in Mg vs. Sr is evident between 30.8-31.4ka which is replicated in only the Sr vs. Ba record.

Using the PER10.3 record, Perlas Event 1 can be defined to occur between 30.3-31.3ka. During event 1 peaks in Mg and $\delta^{13}C$ values and a strengthened correlation between

Mg, Sr and Ba indicate heightened PCP/ICD within the karst as a result of drier conditions.

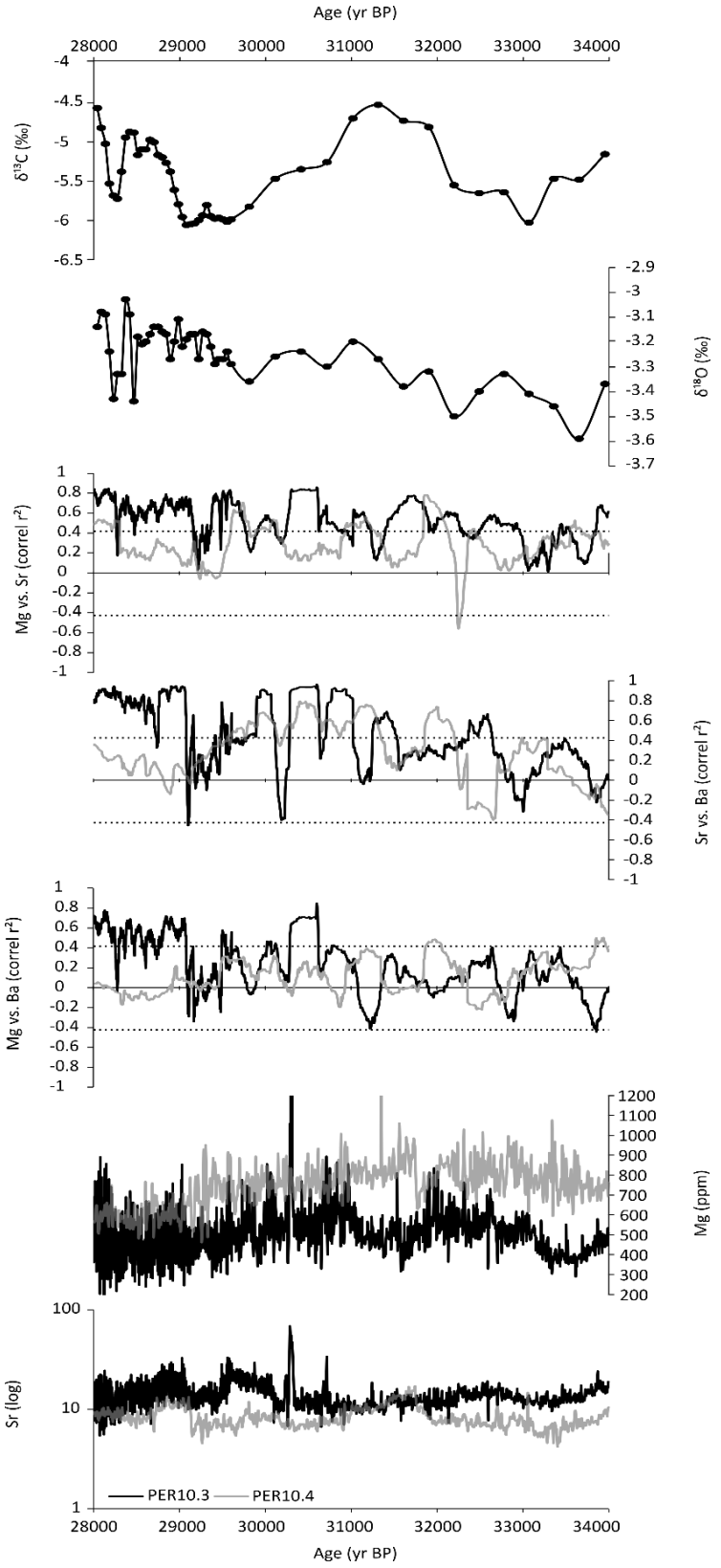

Figure 6.23: Paleoclimate and palaeoenvironmental proxies for PER10.3 and PER10.4 across Perlas event 1. Dashed lines on the correl plots indicate 99.9% confidence levels of 0.408 (n-2=60).

6.5.2.3. Perlas Event 2

Perlas Event 2 has been documented in the Cueva de las Perlas speleothem records as a positive excursion in isotope ($\delta^{18}O$ and $\delta^{13}C$) and trace element (Mg and Sr) proxies (figure 6.24). The event is characterised in PER10.3 by peaks in $\delta^{13}C$ and $\delta^{18}O$ values at 41.8ka and 41.3ka respectively. The trace element record from PER10.3 identifies the event through peaks in Mg and Sr later than the isotope record, at 39.7-40.3ka and 39.4-39.5ka. The delay in the expression of Perlas Event 2 in the isotope and trace element data may potentially relate to the low sampling resolution of the isotope record. Low resolution sampling may not capture the full extent of climate variability. Although, the offset may also result from the location of trace element sampling transects relative to isotope sampling.

A running correlation (where n-2= 60) between Mg vs. Sr, Sr vs. Ba and Ba vs. Mg shows a distinctive signature of the event in both PER10.3 and PER10.4. Figure 6.24 demonstrates a strong negative correlation between Mg vs. Sr and Ba vs. Mg in PER10.3 between 39.1-39.7ka and in PER10.4 between 39.5-40.2ka. Interestingly, during the corresponding period on each of the records, correlations between Sr vs. Ba become stronger with R^2 exceeding 0.8. This pattern of correlation indicates that during event 2 Sr and Ba have a different forcing mechanism to Mg.

Section 6.3.4.2 discussed previous studies which have identified that Sr and Ba can be influenced by growth kinetics (Huang *et al.,* 2001; Treble *et al.,* 2003; 2005b; Webb *et al.,* 2014). Therefore, Sr and Ba variability during this period is a function of variations in growth kinetics as opposed to Mg which remains a function of PCP/ICD. Additionally, the increase in Mg during this period independently of Sr and Ba, may indicate enhanced dolomite dissolution as a result of prolonged rock-water contact times (Webb *et al.* 2014).

The peak in Sr and Ba at 39.4ka coincides with a negative excursion in Mg (figure 6.24). The decrease in Mg is a result of increased precipitation resulting in reduced PCP/ICD. The peak in Sr and Ba is also a response to increased precipitation and subsequent increase in growth rate (Treble *et al.,* 2003).

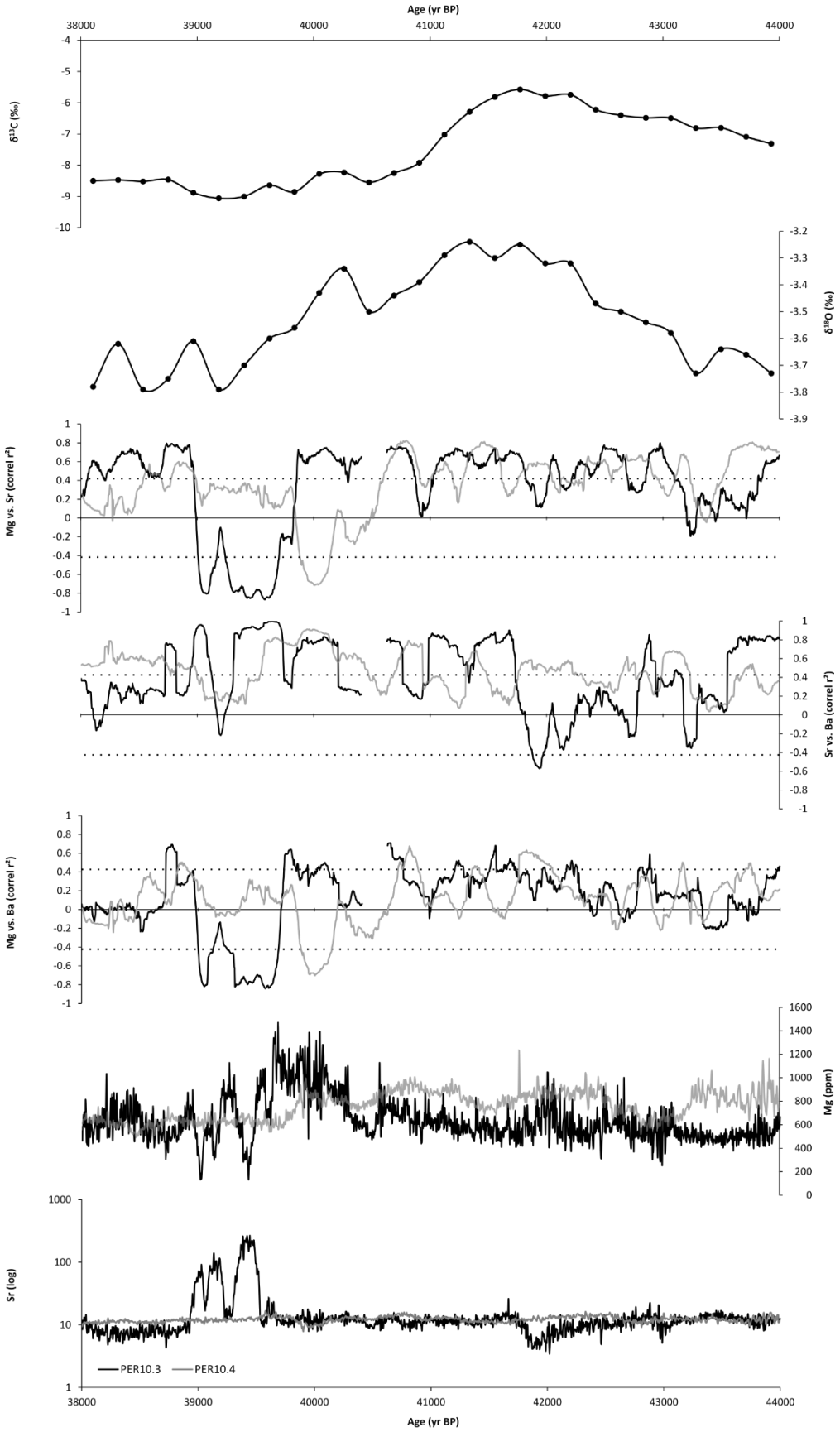

Figure 6.24: Paleoclimate and palaeoenvironmental proxies for PER10.3 and PER10.4 across Perlas event 2. Dashed lines on the correl plots indicate 99.9% confidence levels of 0.408 (n-2=60).

6.5.2.4 Perlas Event 3

The primary indicator of Perlas Event 3 in both speleothem records is a change in growth rate (figure 6.25). Each of the records presents a different story of the event with PER10.3 characterised by a decline in growth rate (at 50.1ka) whilst PER10.4 is defined by a more complicated growth rate pattern with a later overall reduction in growth rate at 45.6ka. Under dry conditions stalagmite growth slows and therefore there is increased potential for hiatuses to occur which can impact U-Th dating and subsequent age models. In summary, Perlas Event 3 marks a distinct shift towards drier conditions which has resulted in reduced stalagmite growth within Cueva de las Perlas. However, due to the dating complexities introduced by variations in growth rate and potential hiatuses, the exact timing of this event is difficult to determine. Additionally, there are no detected changes within the geochemical proxies from the baseline during this period which makes Perlas Event 3 difficult to distinguish.

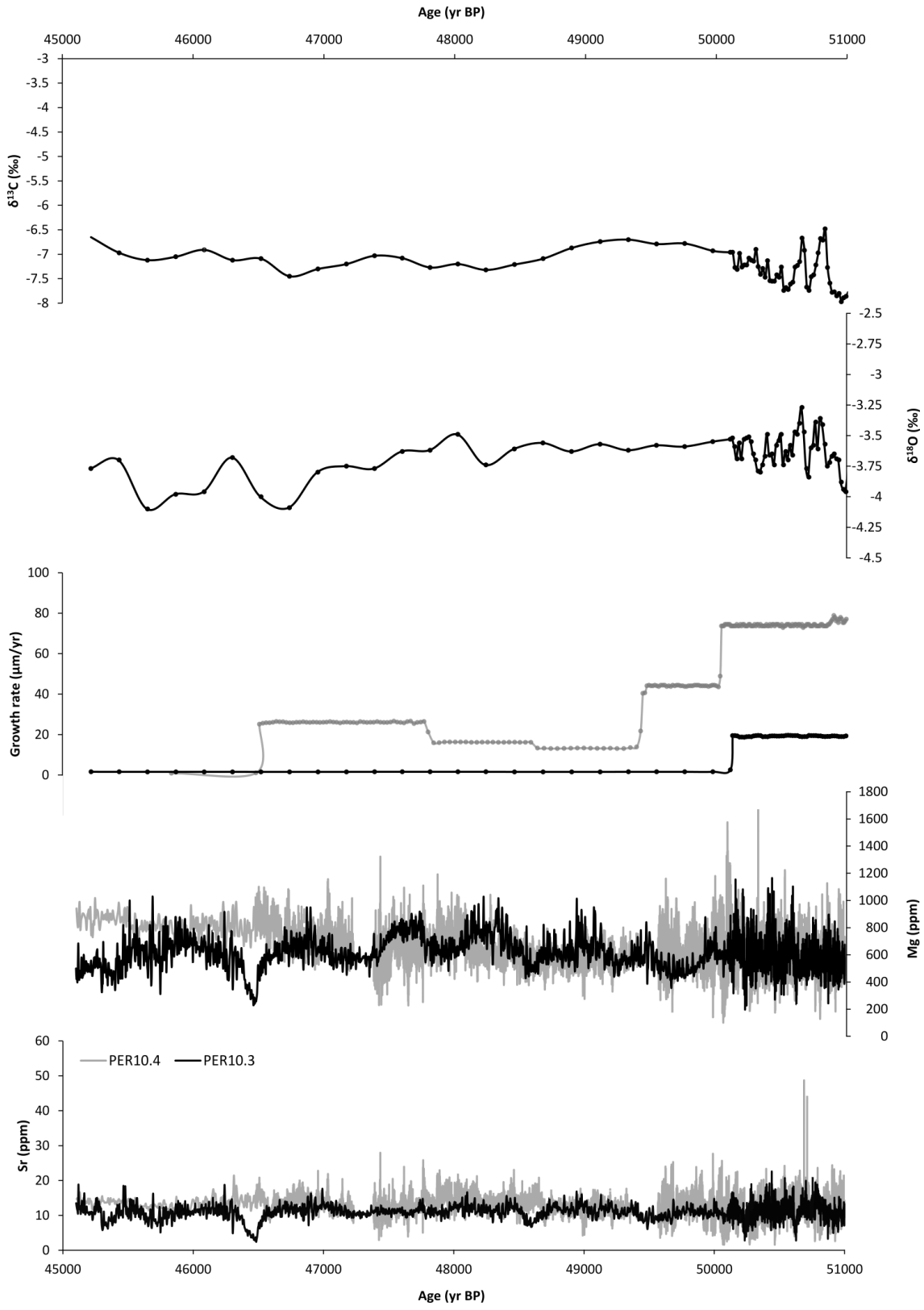

Figure 6.25: Paleoclimate and palaeoenvironmental proxies for PER10.3 and PER10.4 across event 3.

6.5.2.5 Summary

Three millennial-scale events have been identified in the Perlas speleothem records and summarised in figure 6.26. Each of these three 'Perlas events' indicates a distinctive shift to drier conditions on the northern Iberian Peninsula. Dry conditions during the Perlas events have a significant influence on speleothem growth and lead to slower or even cessation of growth. Therefore, dating across these events is challenging with large errors associated with the timing of each event. It must be noted that the presence of these events, particularly Perlas Events 1 and 3, remains speculative due to the nature of the chronology and low-resolution chemical data across this section. Evidence for Perlas Event 2 is the strongest of the three events and the presence of the event is justified by peaks in oxygen and carbon isotope values and Mg concentrations. Additionally, the relationships between Mg, Sr and Ba indicate the differing forcing factors controlling trace element concentrations across the event.

If these events are present in the Cueva de las Perlas speleothem records, they are coincident with North Atlantic Heinrich Events 3 (31ka), 4 (38ka) and 5 (45ka) (Hemming, 2004). Further discussion of these events in the context of North Atlantic climate change, specifically Heinrich events, can be found in chapter 7.

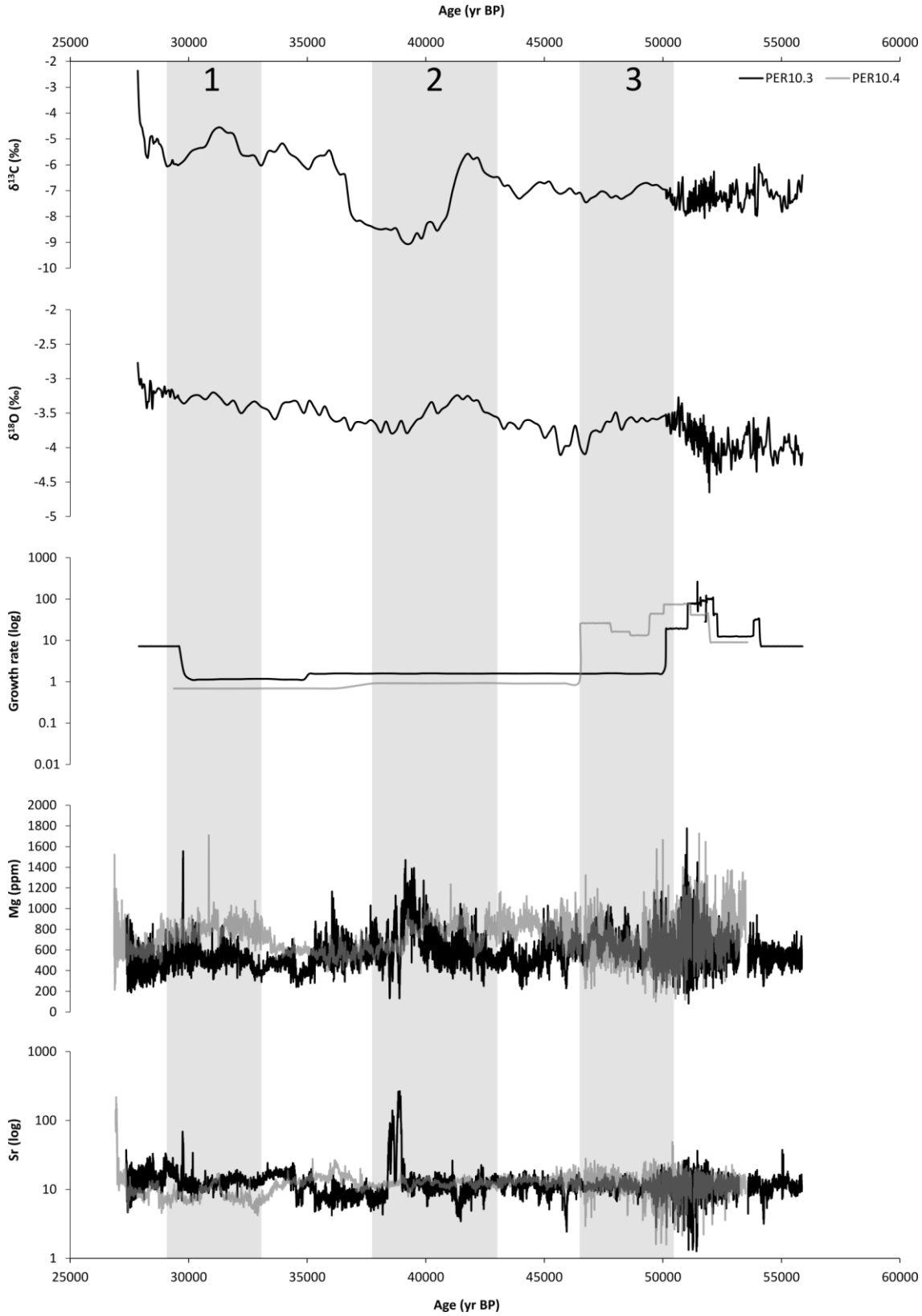

Figure 6.26: Identification of three climatic events within the PER10.3 and PER10.4 proxy records. Events are characterised based upon the speleothem records presented in section 6.5.2.

6.5.3 Sub-orbital variability within the Cueva de las Perlas speleothem records

The Mg/Ca records from PER10.3 and PER10.4 have been interpreted to respond to changes in karst-water interactions (section 6.3.4). Therefore, Mg/Ca ratios can be used to identify shifts between dry and wet conditions as a function of PCP/ICD processes. Under arid conditions, Mg/Ca ratios will increase as a result of PCP/ICD leading to Mg ions being concentrated in solution relative to Ca. Additionally, dolomite dissolution may be enhanced under prolonged periods of aridity and as a consequence, Mg concentrations will rise in percolating waters and associated calcite. In contrast, under wet conditions where PCP/ICD are reduced, Mg/Ca ratios in speleothem calcite will decrease. Speleothem Mg/Ca ratios are increasingly being utilised as a geochemical signal recording changes in epikarst processes and ultimately as a palaeoaridity proxy (Johnson *et al.,* 2006; Wu *et al.,* 2012; Hori *et al.,* 2013; Arienzo *et al.,* 2017).

Analysis of Mg/Ca ratios in both speleothems has identified abrupt millennial-scale variability (figures 6.27 and 6.28). The abrupt climatic shifts from dry to wet conditions appear to be remarkably similar to the Northern Hemisphere DO events (Roucoux *et al.,* 2005; Sánchez Goñi *et al.,* 2008; Naughton *et al.,* 2009; Genty *et al.,* 2010; Moseley *et al.,* 2014) or Greenland Interstadials recorded in the Greenland ice cores (Rasmussen *et al.,* 2014).

Although abrupt millennial-scale shifts from dry to wet conditions are present within the Mg/Ca records from PER10.3 and PER10.4, it remains difficult to distinguish the nature, magnitude and timing of each individual event due to the large age errors associated with the chronology and low-resolution isotope data. However, it is evident from the Mg/Ca signal, abrupt climatic variability was pronounced throughout MIS3.

Section 6.5.2.3 presented evidence for "Perlas Event 2". The distinctive signature of event was shown by high $\delta^{18}O$ and $\delta^{13}C$ values and a peak in Mg between ~39.7-40.3ka in PER10.3. "Perlas Event 2" is characterised by a shift to dry conditions and may be coincident with Heinrich Event 4 (H4). The abrupt decline in Mg/Ca at 39,515±3,918ka may be coincident with DO8 based upon the magnitude of the shift and broad timing. DO8 would therefore be characterised by a decline in PCP and/or ICD processes as a function of increased precipitation shown through declining Mg/Ca. Additionally, the

peak in Sr and Ba at 39.4ka (discussed in section 6.5.2.3) would imply an increased growth rate in response to wetter conditions associated with DO8.

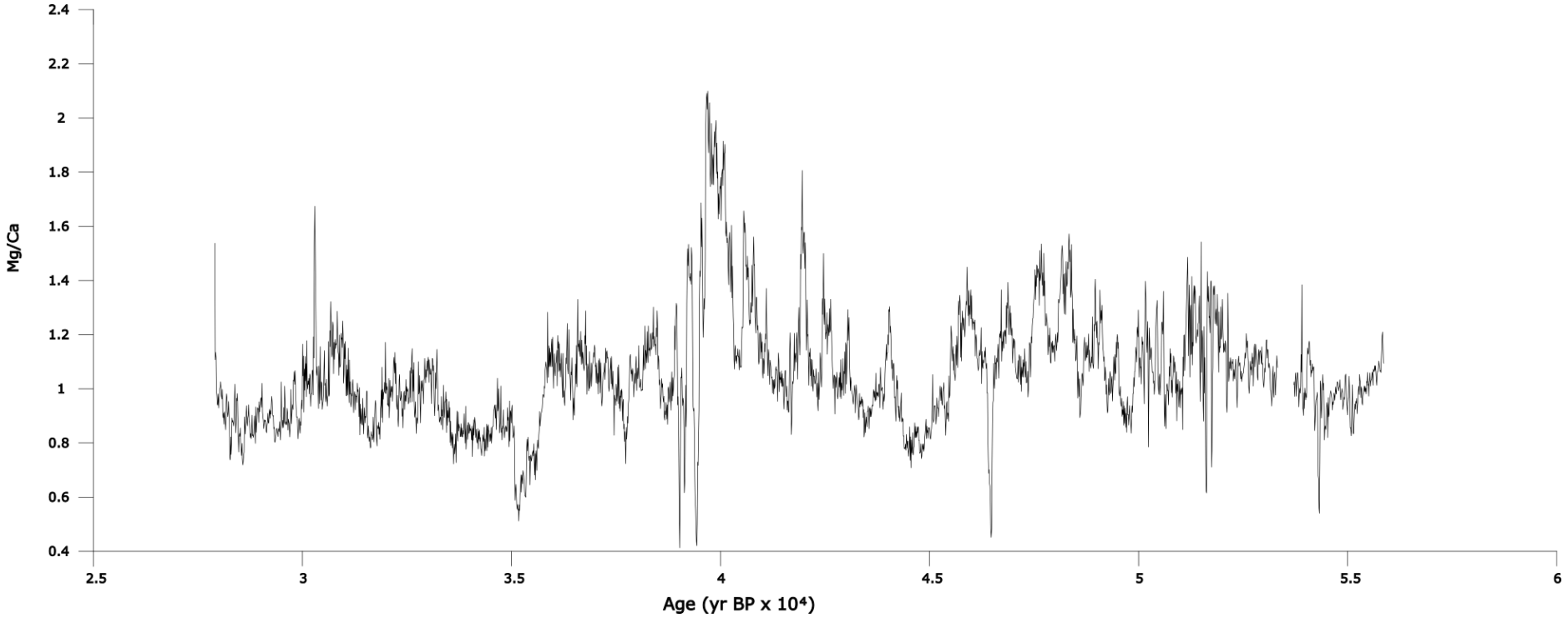

Figure 6.27: Averaged 10-yr Mg/Ca from PER10.3.

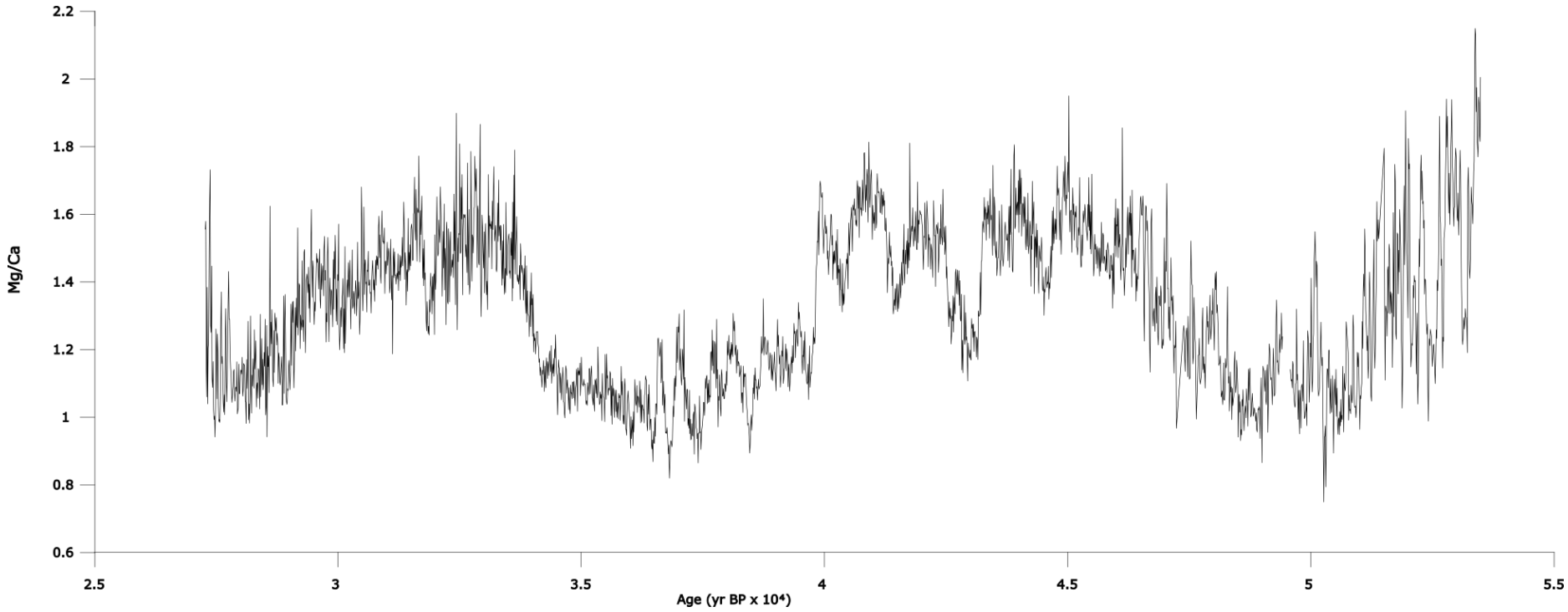

Figure 6.28: Averaged 10-yr Mg/Ca from PER10.4

6.5.4 Identification of sub-orbital cyclicity in the Cueva de las Perlas speleothem records demonstrated through timeseries analysis

Millennial-scale climate events in the Holocene have been identified with periodicities of ~1500yrs (Bond *et al.,* 2001; Mayewski *et al.,* 2004). Furthermore, recently Northern Iberian speleothems from Matienzo have identified similar millennial-scale events with a pacing of ~1500yrs throughout the Holocene (Smith *et al.,* 2016b). However, the extension of these cycles back into the Last Glacial Period remains debated (Wolff *et al.,* 2010). Abrupt, millennial-scale oscillations have punctuated the most recent glacial period, and these are known as Dansgaard-Oeschger events (Dansgaard *et al.,* 1982; Johnsen *et al.,* 1992; Rasmussen *et al.,* 2014) and represent shifts between fully glacial and relatively mild conditions. These millennial-scale events have been identified in the Cueva de las Perlas speleothem records as shifts towards wet conditions (section 6.5.3). Statistical analysis of palaeoclimate records has identified a periodicity of ~1500yr across some of the MIS3 records (Schulz, 2002). Ditlevsen *et al.* (2007) questioned the statistical significance of the DO periodicity but others have argued a periodic forcing mechanism cannot be discounted (Ditlevsen and Ditlevsen, 2009; Woillez *et al.,* 2012). This section will use Dynamic Harmonic Regression Analysis to determine whether there is any periodicity within the Cueva de las Perlas speleothem records.

Timeseries analysis of the PER10.3 and PER10.4 Mg/Ca trace element profiles was undertaken using code created by W. Tych and D. A. Mindham of Lancaster University. The method used ASDHR (arbitrary sampling dynamic harmonic regression) analysis with code derived from Mindham and Tych (2018) and using the Captain toolbox (Taylor *et al.,* 2007) in MatLab (v2016a). Regularisation of the dataset was undertaken with a prefiltering method set to sub-sample every 100yrs (figures 6.29 and 6.31). This allowed the density of samples to be accounted for but also permitted a resolution closer to the dating error. The regularised data can be interpolated at a lower resolution which remains appropriate for seeking millennial-scale cycles. The timeseries analysis from PER10.3 demonstrated two strong periodicities at 1900-yr and 2000-yr (figure 6.30). A model combining the 1900-yr and 2000-yr periodicities was created and accounts for 60% of variability within the dataset (figure 6.30). The timeseries analysis from PER10. 4 demonstrated two strong periodicities at 1600-yr and 2000-yr (figure 6.32). A model

combining the 1600-yr and 2000-yr periodicities was created and accounts for 83% of variability within the dataset (figure 6.32). Interestingly, the two speleothem Mg/Ca records both record a periodicity of ~2000-yr but only PER10.4 records a periodicity at ~1600-yr. The differences between the periodicities may be a function of their individual age models. Additionally, karst hydrology has shown to be dynamic above Cueva de las Perlas and this may play a role in influencing the environmental signals preserved within the speleothem calcite.

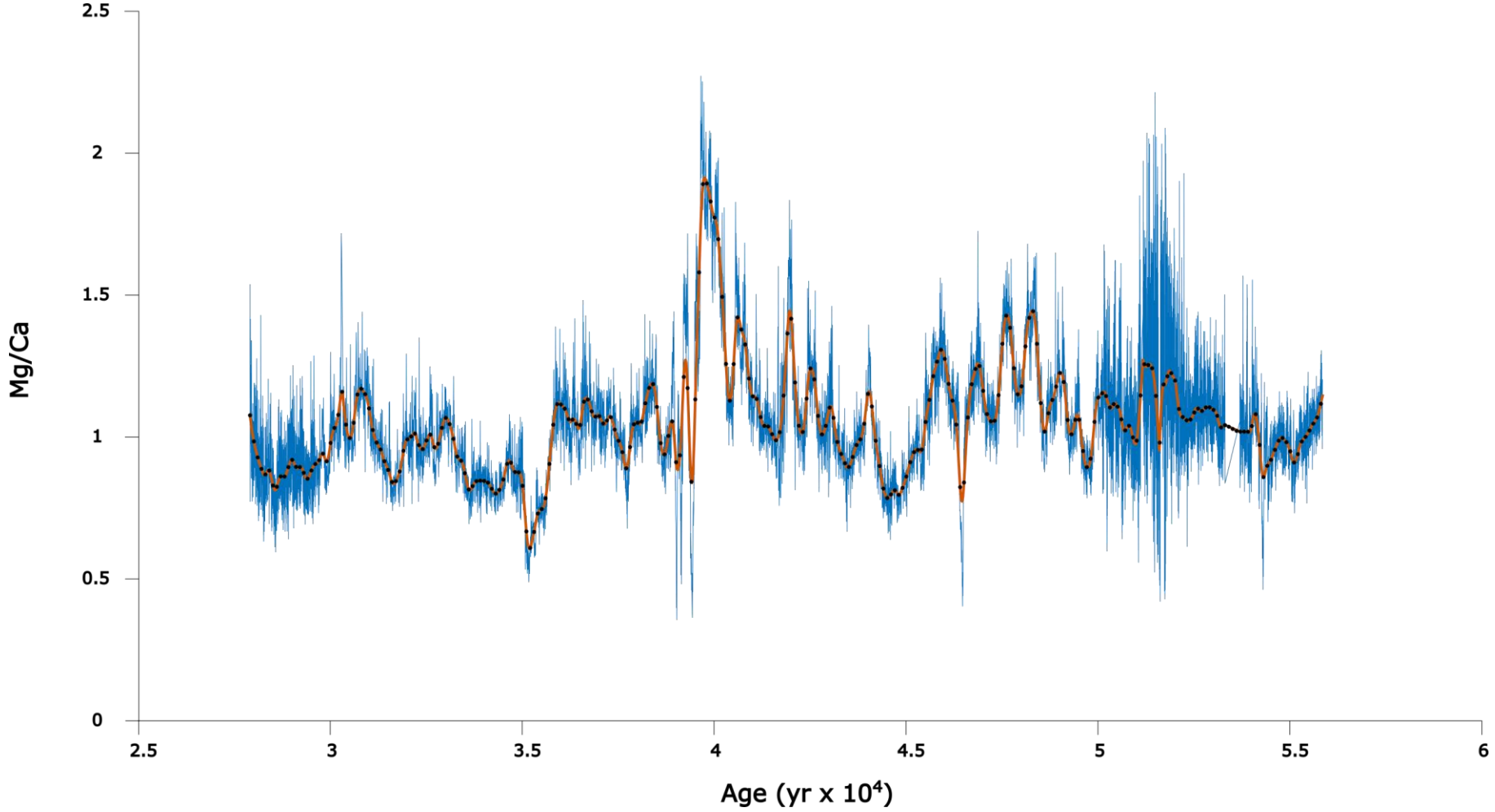

Figure 6.29: PER10.3 Mg/Ca data used within the timeseries analysis. The blue line represents the entire dataset, the black dots represent the 100-yr sub-samples and the orange line represents the trend of the sub-sample data.

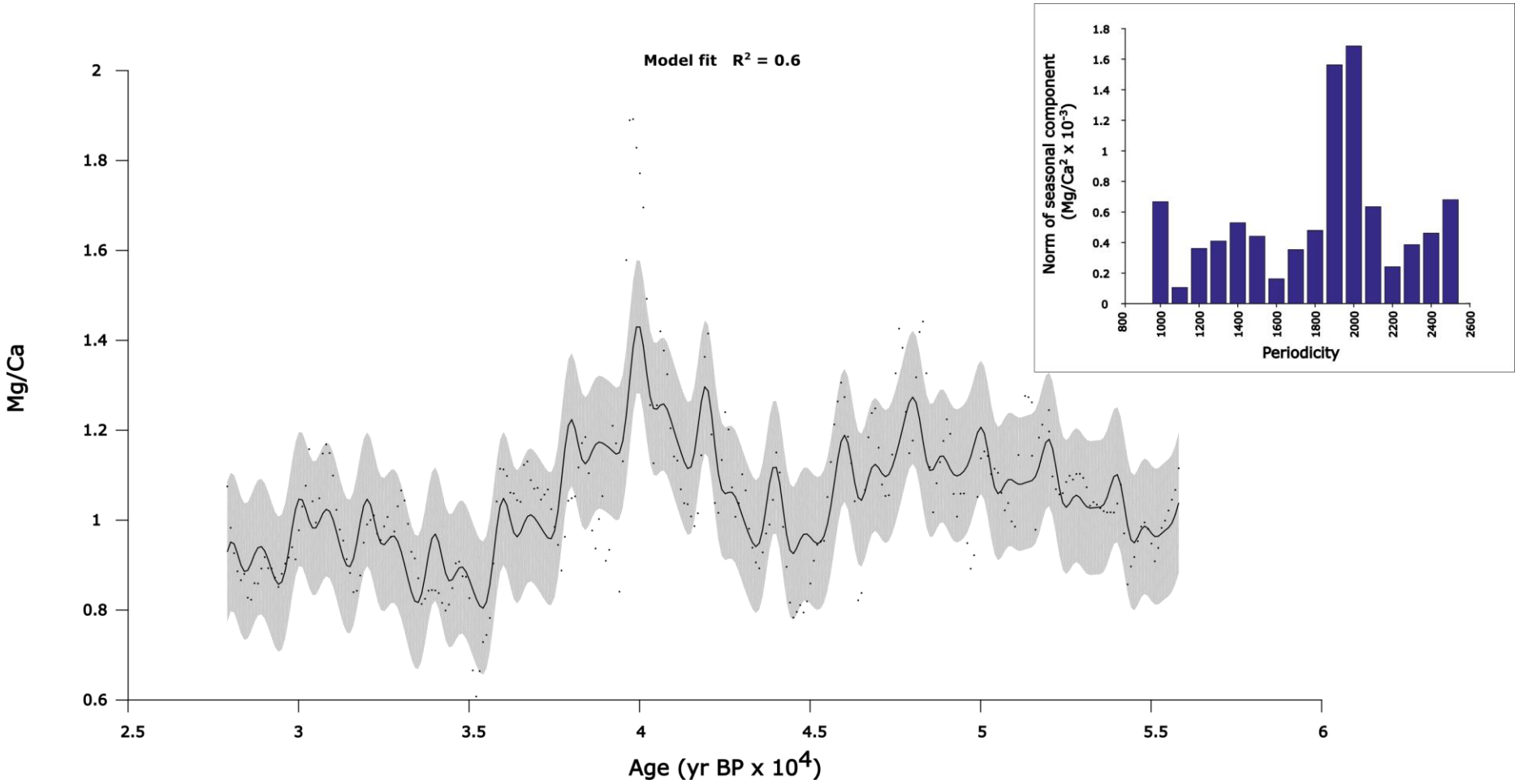

Figure 6.30: Model constructed for PER10.3 Mg/Ca using 1900-yr and 2000-yr periodicities with the periodicity analysis inset.

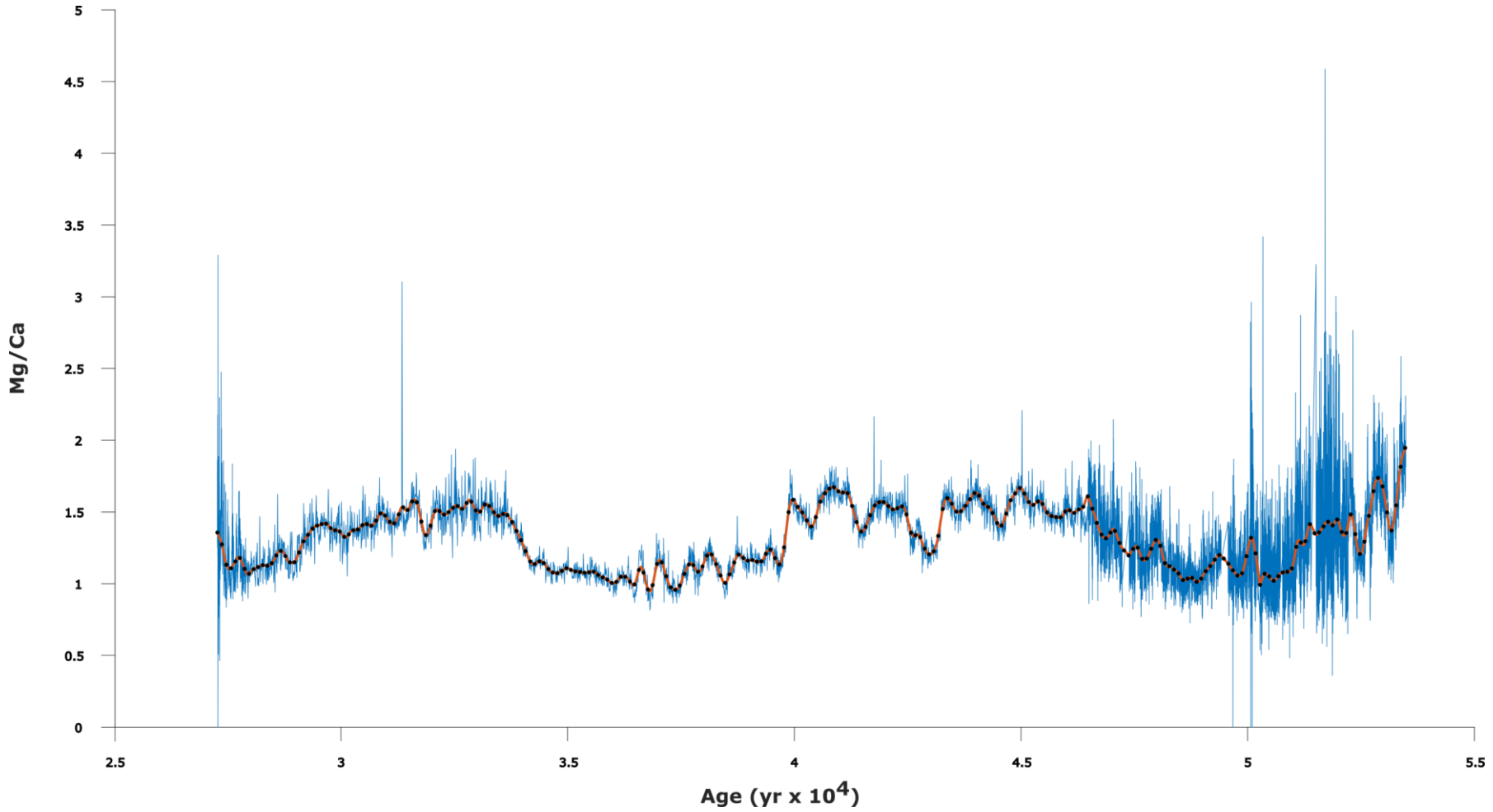

Figure 6.31: PER10.4 Mg/Ca data used within the timeseries analysis. The blue line represents the entire dataset, the orange represents the trend and the black dots represent the 100-yr sub-samples used within the analysis.

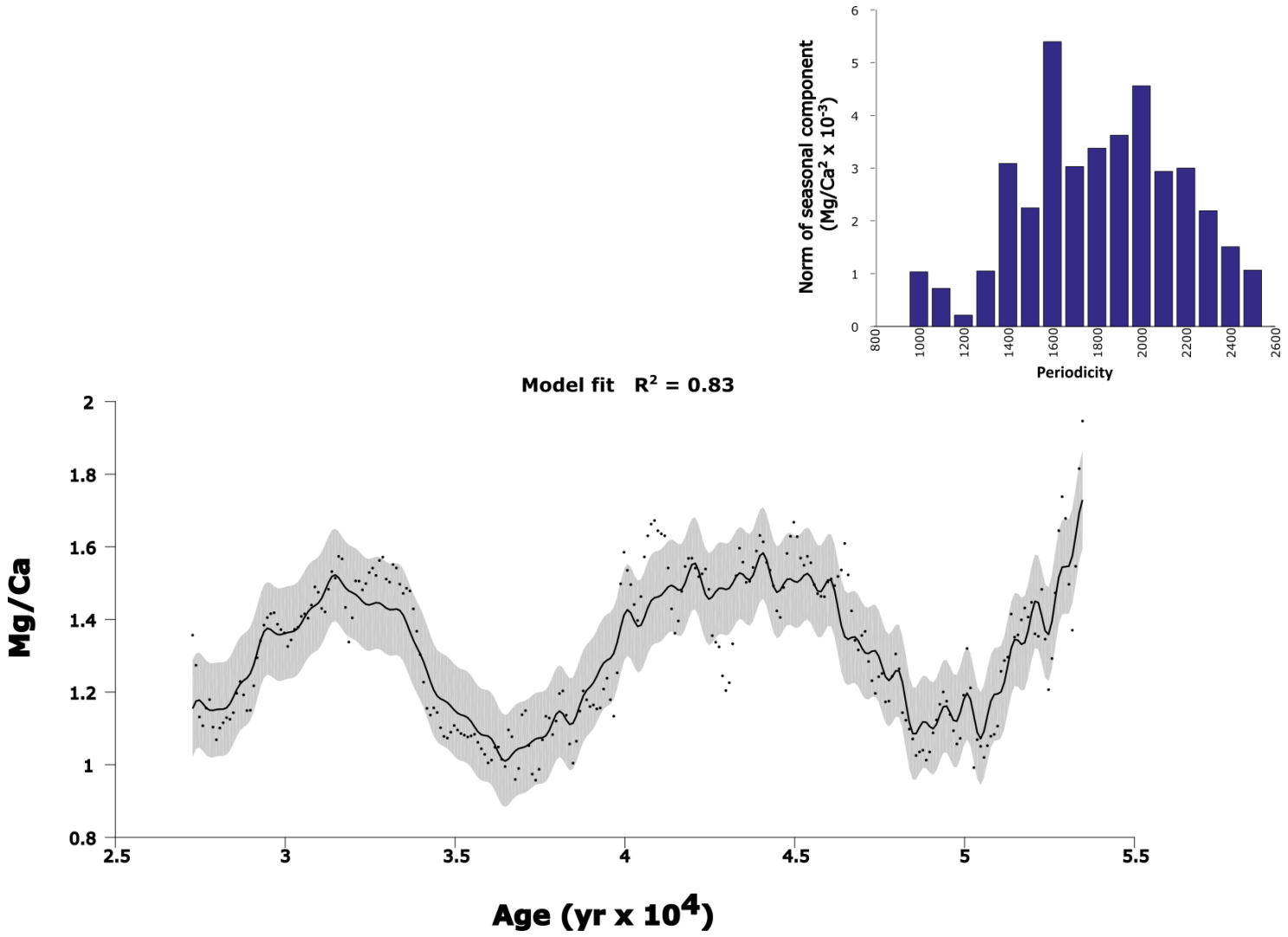

Figure 6.32: Model constructed for PER10.4 Mg/Ca using 1600-yr and 2000-yr periodicities with the periodicity analysis inset.

One caveat underlies the ASDHR analysis presented in figures 6.30 and 6.32 and this relates to the errors associated with the U-Th dating and how these are reflected in the model. The age-model input into the periodicity analysis contains an average error of ±890yrs with a minimum error of ±240yrs and a maximum error of ±4300yrs. Therefore, errors in the periodicity model may be underpinned by errors within the age-model. Prefiltering of the data aimed to reduce the influence of error but due to the variable size of the errors across the entire dataset, it remains difficult for the errors to be accounted for within the model. As a consequence, the age errors are greater than the periodicity defined at points within the record. Although the models distinguish periodicities of 1900-yr and 2000-yr (PER10.3) and 1600-yr and 2000-yr, the ~1500-yr periodicity frequently attributed to DO variability in the North Atlantic has not been identified. A discussion of the timeseries analysis in relation to the wider literature can be found in section 7.5.5.

6.6 Cueva de las Perlas speleothems as recorders of past climatic and environmental change over orbital and sub-orbital timescales

Isotope and trace element analyses have been undertaken on three speleothems from Cueva de las Perlas. In conjunction with U-Th dating, these have been used to construct records of past climate and environmental change from Northern Iberia between 86-27ka. Speleothem isotope values were demonstrated to respond to variations in NH summer insolation on orbital timescales. Sub-orbital variability was identified to be superimposed onto the orbital trends. Three millennial-scale events were recognised to occur at 30.3-31.3ka, 39.4-41.8ka and 46.5-51ka and these may correspond to the timing of North Atlantic Heinrich events. Sub-orbital variability has been demonstrated within the PER10.3 and PER10.4 Mg/Ca records and this is similar with North Atlantic DO variability. It remains challenging to define each event, but evidence indicates an abrupt shift to wet conditions at 39.5ka is consistent with the onset of DO8. A periodicity of ~2000-yr has been shown through ASDHR analysis of the PER10.3 and PER10.4 Mg/Ca records. The next chapter will discuss the Cueva de

las Perlas speleothems in the wider context of North Atlantic climate and environmental change between 86-27ka. Additionally, the following chapter aims to place the decline and eventual extinction of the Northern Iberian Neanderthal populations onto this climatic backdrop.

7. Placing the Cueva de las Perlas speleothem records in the context of regional North Atlantic climate and environmental dynamics between 86-27ka

7.1 Introduction

Speleothem records from Cueva de las Perlas have identified evidence for climatic and environmental variability over orbital timescales with sub-orbital oscillations superimposed onto this general trend. Chapter 6 identified and examined these changes within the speleothem records. The following chapter will analyse the climatic variability in light of other records from across the North Atlantic region on the different timescales previously discussed (orbital, sub-orbital events and sub-orbital variability) and aims to discuss potential forcing mechanisms. The final section will place the Neanderthal extinction onto the climatic and environmental platform derived from the speleothem and wider European records.

7.2 Responses of North Atlantic records to climate and environmental change on orbital timescales

Section 6.5.1 identified broad trends in the speleothem proxy records from Cueva de las Perlas which appear to be forced by Northern Hemisphere Summer Insolation (NHSI) at 65°N. During periods of NHSI maxima, speleothems exhibited lower $\delta^{18}O$ and $\delta^{13}C$ values, higher growth rates and lower Mg concentrations which are all indicative of wetter climates. In contrast, proxies suggested drier conditions were dominant on the northern Iberian Peninsula during insolation minima. This section will examine the evidence for orbital forcing on long-timescales throughout MIS5-2 on the Iberian Peninsula and the wider North Atlantic region.

7.2.1 Astronomical forcing theory

According to the astronomical forcing theory of Milankovitch (1941), changes in the amount of incoming solar radiation (insolation) are forced by changes in the Earth's orbital and rotational parameters of:

- Eccentricity: the shape of the Earth's orbit which occurs on a ~100,000yr cycle
- Obliquity: tilt of the Earth's axis with a periodicity of 41,000yrs
- Precession: the rotation of the Earth's axis with a periodicity of 23,000yrs

The Milankovitch hypothesis proposed a minimum in NHSI at high-latitudes induced the glacial cycles which are known to occur throughout the Pleistocene. The hypothesis is underpinned by the notion that cold summers as a result of NHSI minima are required in order to stop winter snow and ice from melting. Positive feedback mechanisms would then lead to further extension of ice cover and increased albedo (Berger and Loutre, 2007). Milankovitch identified that the NHSI intensity varied over 600,000yrs and four low points in NHSI corresponded to the 'ice ages'.

As summarised in Berger and Loutre (2007), the Milankovitch model identifies that ice volume and climate are variable on the same scale as variations in insolation. Hays *et al.* (1976) identified evidence for orbital forcing at 19-, 23- and 41-kyr in marine sediment cores. Additional later work by Imbrie *et al.* (1984) proposed a consistent relationship between insolation, sea surface temperature and ice volume. Modelling work by Imbrie *et al.* (2011) continues to identify the significance of orbital-forcing on Earth's climate, particularly the long-term 100kyr glacial cycles evident throughout the Pleistocene.

7.2.2 The influence of orbital forcing on northern Iberia

Numerous proxy records from a variety of palaeoclimate archives across the North Atlantic region have acknowledged the influence of NHSI on long-term patterns of climate change. Stoll *et al.* (2013) demonstrated growth rates in 21 speleothems from six different caves in NW Iberia corresponded to changes in NHSI at 65°N. Throughout MIS5 speleothems grew relatively continuously in NW Iberia related to relatively

higher NHSI (Muñoz-García *et al.,* 2007; Stoll *et al.,* 2013). Summer insolation maxima on the Iberian Peninsula is suggested to have enhanced humidity which would promote greater vegetation cover and productivity, increasing soil CO_2 and increasing dripwater saturation states (Stoll *et al.,* 2013). Conversely, speleothem growth ceased at or prior to the MIS4 boundary which coincided with a period of declining NHSI and a fall in sea surface temperatures from 18°C to below 14°C (Martrat *et al.,* 2007; Stoll *et al.,* 2013). Speleothems from NW Iberia reinitiated growth during summer insolation maxima between 50 to 60ka. Similarly, speleothems from Cueva de las Perlas exhibit the same pattern of growth during MIS5, MIS4 and MIS3 which is further supported by the stable isotope record (section 6.5.1).

Spatial differences in growth during MIS3 exist between different cave sites in northern Iberia. Speleothem growth during MIS3 is periodic at Cueva Rosa and La Vallina (Stoll *et al.,* 2013) and these sites lie ~125km and ~100km to the west of Cueva de las Perlas. A reason behind this disparity may be found in the modern-day precipitation records. The sites investigated by Stoll *et al.* (2013) each have a mean annual precipitation of 1260mm/yr and 1230mm/yr for Cueva Rosa and La Vallina respectively. The modern precipitation average of Matienzo is higher at ~1400mm/yr. It is apparent that precipitation is variable across north western Iberia as demonstrated by the difference between local Matienzo mean annual precipitation and that of the nearest weather station of Santander at ~1200mm/yr (IAEA, 2018). Therefore, it is likely that higher precipitation amounts found within the Matienzo depression allowed the continuous growth apparent in the speleothem records from this area.

Marine sediment cores taken from different latitudes across the North Atlantic have identified long-term climatic and environmental changes in response to variations in NHSI. Pollen from marine cores provides an oceanic-terrestrial record of past climate and environmental conditions over long-timescales. Marine pollen shows a reduction in tree populations and ericaceous heathland during MIS3 which has been interpreted as a long-term cooling and aridity trend (Roucoux *et al.,* 2005; Fletcher and Sánchez Goñi, 2008). Long-term sea surface cooling demonstrated through alkenones has also

been identified to correspond to long-term trends in NHSI (Cacho *et al.,* 1999). Benthic $\delta^{18}O$ data from marine cores MD95-2039 (Thomson *et al.,* 1999; Schönfeld *et al.,* 2003; Roucoux *et al.,* 2005) and MD95-2042 (Shackleton *et al.,* 2000) have shown the variability in NH ice sheets across MIS3 and MIS2. The benthic oxygen isotope records demonstrate ice sheet growth during MIS3, reaching a maximum in MIS2 with ice sheet growth coincident with declining insolation (Thomson *et al.,* 1999; Schönfeld *et al.,* 2003; Shackleton *et al*., 2000; Fletcher and Sánchez Goñi, 2008). However, maximum ice sheet extent has been shown to lag NHSI minima by ~6ka (Ruddiman, 2006).

The correspondence between the aridity proxies from the Cueva de las Perlas speleothems, contraction of tree populations and ericaceous heathlands, lowered sea surface temperatures and the expansion of ice sheets suggests that the long-term cooling and drying trend on the Iberian Peninsula during MIS3 was a function of declining insolation. At this time build-up of continental ice-sheets associated with a decline in insolation is known to have caused reduced sea surface temperatures and aridity on the Iberian Peninsula. These changes are propagated through weakening of the global hydrological cycle and increased albedo which lowered global temperatures and strengthened wind systems (Fletcher and Sánchez Goñi, 2008).

7.3 Investigation of the millennial-scale 'events' recorded in Cueva de las Perlas speleothem records in relation to wider North Atlantic Heinrich events

7.3.1 Overview

Section 6.5.2 identified millennial-scale events superimposed onto orbital trends. Millennial events occurred at 30.3-31.3ka, 39.4-41.8ka and 46.5-51ka and these are referred to herein as Perlas events. Although these events require stronger chronologies and higher-resolution isotope data to validate their existence, the current dataset suggests the timing of these events is broadly synonymous with the timing of Heinrich events within the NA region with H3, H4 and H5 occurring at ~31ka,

38ka and 45ka respectively (Hemming, 2004) (table 7.1). This section will compare the evidence for each of these events in the Cueva de las Perlas records with evidence from wider regional North Atlantic records.

Table 7.1: Timing of Cueva de las Perlas millennial-scale events and North Atlantic Heinrich events taken from Hemming (2004).

Perlas event number	**Timing of Perlas event**	**Synonymous Heinrich event**	**Heinrich event age**
1	30.3 – 31.3ka	3	31ka
2	39.4 – 41.8ka	4	38ka
3	46.5 – 51ka	5	45ka

7.3.2 Perlas Event 1

The timing of Perlas Event 1 coincides with the timing of H3 in the North Atlantic (table 7.1). The presence of H3 in and around the Iberian Peninsula has been previously documented in various archives. Marine cores along the Iberian Margin have identified H3 by a peak in IRD. The presence of this peak is relatively smaller than the preceding H4 event and the succeeding H2 event (Baas *et al.,* 1997; Thomson *et al.,* 1999; de Abreu *et al.,* 2003; Schönfeld *et al.,* 2003; Roucoux *et al.,* 2005). The event was identified in marine core MD95-2042 as a cold event at 31ka associated with a decline in productivity demonstrated by reduced SST and declines in the palaeoproductivity proxies (carbonates, organic carbon and C_{37} alkenones) (Pailler and Bard, 2002). Later analysis of 15 marine cores from the Iberian Margin by Salgueiro *et al.* (2014) demonstrated H3 as a cold event with SST between 5-11°C and a reduction in productivity. When compared to H2, H3 was shown to be significantly colder with reduced productivity.

Moving onto the terrestrial environment, Wolf *et al.* (2018) identified H3 as a period of strongest aeolian activity between 32.2±2.7kyr and 28.4±2.4kyr expressed through maximum loess deposition and high $\delta^{13}C$ values. Similarly, pollen from marine cores exhibits a change in terrestrial vegetation assemblages during H3 with a decline in

Pinus (Roucoux *et al.,* 2005) and *Juniperus* associated with the expansion of steppic taxa such as *Artemisia* (González-Sampériz *et al.,* 2006) which are interpreted to represent a shift to cold and arid conditions. Further north in France, increases in $\delta^{13}C$ values and subsequent termination of growth in speleothems from Villars Cave coincide with H3 at 30ka. At Villars Cave, $\delta^{13}C$ values are interpreted to reflect variations in vegetation density and microbial activity in the soil overlying the cave system (Wainer *et al.,* 2009).

In section 6.5.2.2 evidence from PER10.3 demonstrated peaks in Mg, Sr and $\delta^{13}C$ values as well as a strengthening of the correlation between Mg, Sr and Ba between 30.3-31.3ka (figure 6.23). These proxies suggested a shift towards dry conditions related to enhanced karst-water interaction processes such as PCP or ICD. Therefore, the presence of a dry event between 30.3-31.3ka in the Cueva de las Perlas speleothem record agrees with local and regional records which identify a cold and arid period during H3.

7.3.3 Perlas Event 2

7.3.3.1 Comparison of Perlas Event 2 to North Atlantic records

Perlas Event 2 is proposed to be synonymous with H4 (table 7.1). The expression of H4 within marine cores surrounding the Iberian Peninsula has been characterised by the occurrence of IRD indicating the presence of icebergs (Baas *et al.,* 1997; Thomson *et al.,* 1999; Schönfeld *et al.,* 2003; Roucoux *et al.,* 2005; Sánchez Goñi *et al.,* 2008) between 38.3-40.2ka (de Abreu *et al.,* 2003). Thomson *et al.* (1999) recognised the H4 event was significantly larger in comparison to the other Heinrich events identified within the marine cores based upon a significantly large sediment flux in both marine cores analysed. H4 is also identified by the high percentage of *Neogloboquadrina pachyderma* (s) (de Abreu *et al.,* 2003; Cacho *et al.,* 1999), maxima in the oxygen isotopic composition of the planktonic foraminifera *Globigerina bulloides* (Cayre *et al.,* 1999; Shackleton *et al.,* 2000; Pallier and Bard, 2002; Sánchez Goñi *et al.,* 2008) and reduced SST (Cacho *et al.,* 1999; de Abreu *et al.,* 2003; Pallier and Bard, 2002; Sánchez

Goñi *et al.,* 2008). Temperature reconstructions estimate a winter SST of 0±2°C in the Bay of Biscay during the H4 event (Sánchez Goñi *et al.,* 2008).

Reduction in forest extent (Fletcher and Sánchez Goñi, 2008), particularly a dramatic drop in *Pinus* populations (Roucoux *et al.,* 2005; Sánchez Goñi *et al.,* 2008) and the expansion of semi-desert taxa such as *Artemisia* (Combrourieu Nebout *et al.,* 2002; Roucoux *et al.,* 2005; Sánchez Goñi *et al.,* 2008; Fletcher and Sánchez Goñi 2008) suggest enhanced aridity on the Iberian Peninsula during Heinrich cooling events. Additional evidence from a small vertebrate assemblage from Terrassa Riera dels Canyars established evidence that H4 resulted in cold climatic conditions characterised by significantly harsher and drier climate compared to modern day north-eastern Iberia (López-García *et al.,* 2013). Lacustrine sediments from central Spain have also provided a cold and arid terrestrial signature of H4 on the Iberian Peninsula which is marked by carbonaceous sedimentation, low lake levels, organic matter degradation and an increased percentage of *Juniperus* and steppic taxa (Vegas *et al.,* 2010). A lacustrine record from south-eastern France also identifies H4 as a period of reduced lake levels marked by a hiatus in deposition as a result of the cool and dry conditions of H4 (Wohlfarth *et al.,* 2008; Veres *et al.,* 2009). Evidence for H4 cooling and aridity has also been found in speleothems from Villars Cave. H4 is represented in these records by a decline in speleothem growth rate and a positive excursion in $\delta^{13}C$ values (Wainer *et al.,* 2009; Genty *et al.,* 2010).

The climatic oscillation exhibited in PER10.3 and PER10.4 between 39.4-41.8ka identifies a period of aridity which is coincident with widespread North Atlantic cooling and aridity during H4 (section 6.5.2.3). Although the exact definition of this event in the Cueva de las Perlas speleothem records is complicated by the isotope sampling resolution and dating complexities, speleothem proxies correspond to regional archives recording the H4 event within age error.

7.3.3.2 Two-phased Heinrich event 4

The expression of H4 in marine cores is not straightforward and studies have identified a two-phase hydrological pattern for H4, H2 and H1 in marine sediments. The first phase is marked by wet and very cold atmospheric conditions characterised by low

IRD, high magnetic susceptibility and wet-cold pollen assemblages. In contrast, the second phase is characterised by a shift to extreme continental aridity and cooler climatic conditions illustrated by high IRD and a marked increase in semi-desert taxa (Sánchez Goñi, *et al.,* 2000; Naughton *et al.,* 2007, 2009). A speleothem from Pindal Cave (Northern Iberia) has identified a similar two-phase hydrological pattern during H2 (Moreno *et al.,* 2010). The Cueva de las Perlas speleothem records do not appear to evidence the presence of a two-phase H4 event in NW Iberia because of limitations in the proxy records and lack of a definitive temperature proxy.

7.3.3.3 Summary

The speleothem record from Cueva de las Perlas agrees with the local and regional North Atlantic records identifying widespread aridity on the Iberian Peninsula associated with Heinrich Event 4. Evidence from other studies has identified the H4 event led to differing climatic and environmental conditions across the Iberian Peninsula with the Atlantic region being more humid than the Mediterranean region (Sánchez Goñi *et al.,* 2002; López-García *et al.,* 2013). Speleothem growth appears to continue in the Matienzo depression, albeit reduced, during this event. Therefore, the speleothem records identify a period of aridity associated with H4 cooling in NW Iberia which fit with the proxy data from different archives and also model simulations which demonstrate the H4 event was characterised by cooler temperatures and more arid conditions in the northern Iberian Peninsula (Sepulchre *et al.,* 2007).

7.3.4 Perlas Event 3

The timing of Perlas Event 3 is synonymous with North Atlantic H5. Marine records from the North Atlantic preserve evidence for cooling in relation to H5. The presence of IRD within numerous marine sediment cores acted as a marker to define the H5 event. However, similarly to H3, authors have identified H5 as a relatively less intensive ice-rafting event based upon a smaller IRD peak (Thomson *et al.,* 1999; de Abreu *et al.,* 2003; Schönfeld *et al.,* 2003; Roucoux *et al.,* 2005) and an absence of any volcanic elements (de Abreu *et al.,* 2003). Other authors have classified H5 based upon high planktonic $\delta^{18}O$ values and high percentage *N. pachyderma* (s) (Cayre *et al.,* 1999;

Combourieu Nebout *et al.,* 2002; Sánchez Goñi *et al.,* 2008). Reconstructed SST from the Bay of Biscay have estimated values of ~0±2°C (Sánchez Goñi *et al.,* 2008) whilst further south in the Alboran Sea, alkenone SST reconstructions identify a 4°C fall in temperature during Heinrich Events (Cacho *et al.,* 1999). Terrestrial pollen in marine cores shows a distinct reduction in *Pinus* pollen (Roucoux *et al.,* 2005) and widespread expansion of steppic taxa associated with H5 (Sánchez Goñi *et al.,* 2000; 2002; Combourieu Nebout *et al.,* 2002; Fletcher and Sánchez Goñi, 2008).

Speleothems from Villars Cave have identified a cold period characterised by increased $\delta^{13}C$ values and reduced growth rates (Wainer *et al.,* 2009; Genty *et al.,* 2010). Wainer *et al.* (2009) define this period between 47.8-49.2ka whereas Genty *et al.* (2010) defined the period as 46.68-47.74±0.8ka. Therefore, although different distinctions are given, both periods overlap within error. Additionally, speleothems from Kleegruben Cave in the Austrian Alps express a period of reduced growth between 47.8-51.5ka coincident with low $\delta^{18}O$ values, which are a function of temperature variations (Spötl and Mangini, 2002; Spötl *et al.,* 2006).

Perlas Event 3 within the Cueva de las Perlas speleothem records has proven challenging to define both chronologically and through the geochemical proxies (section 6.5.2.4). However, evidence from the Cueva de las Perlas speleothems suggests a shift to dry conditions between 46.5-51ka as evidenced primarily through changes in growth rate (figure 6.25). The fall in growth rate associated with Perlas event 3 corresponds to the wider evidence for widespread cooling and aridity in the North Atlantic region associated with H5.

7.3.5 Comparison of the different events

Each Heinrich Event appears to have different characteristics as recorded by various terrestrial and marine archives. López-García *et al.* (2013) suggested that H4 was the most abrupt event in comparison with H3 and H5, with H3 being the least cold. Similarly, peaks in IRD within marine cores are reduced for H3 and H5 suggesting smaller/weaker events (Thomson *et al.,* 1999; Roucoux *et al.,* 2005). A larger H4 in

comparison to H3 and H5 may partially explain the difference between the different event signals recorded in the Cueva de las Perlas speleothems. The signal for H4, represented by a significant peak in Mg in the PER10.3 record is much clearer than those for H3 and H5. Widespread aridity related to reduced precipitation in Matienzo during H4 resulted in increased karst-water interactions which subsequently increased Mg concentrations and $\delta^{13}C$ values in speleothem calcite. In contrast, reduced aridity during H3 and H5 compared to H4, may lead to the muted signal expressed within the Cueva de las Perlas speleothem records.

7.3.6 Summary

This section has examined the evidence for millennial-scale events from the North Atlantic including those from Cueva de las Perlas. The events identified from Cueva de las Perlas display a regional signature of the North Atlantic Heinrich Events 3, 4 and 5 and are comparable to other records from the North Atlantic region (figure 7.1). The signature of each of the events is unique, with H4 being represented as the most abrupt and severe within the Cueva de las Perlas speleothem records and in other archives from the Northern Hemisphere. H3 and H5 display a relatively attenuated signal within the Cueva de las Perlas speleothem records in comparison with H4 and this pattern has previously been identified within North Atlantic records (Schönfeld *et al.,* 2003; Roucoux *et al.,* 2005; Naughton *et al.,* 2009, Vegas *et al.,* 2010; López-García *et al.,* 2013). The next section (7.4) will examine the local and regional evidence for millennial-scale variability demonstrated within the Cueva de las Perlas speleothem records and forcing mechanisms for both millennial-scale events and variability are discussed in section 7.7.

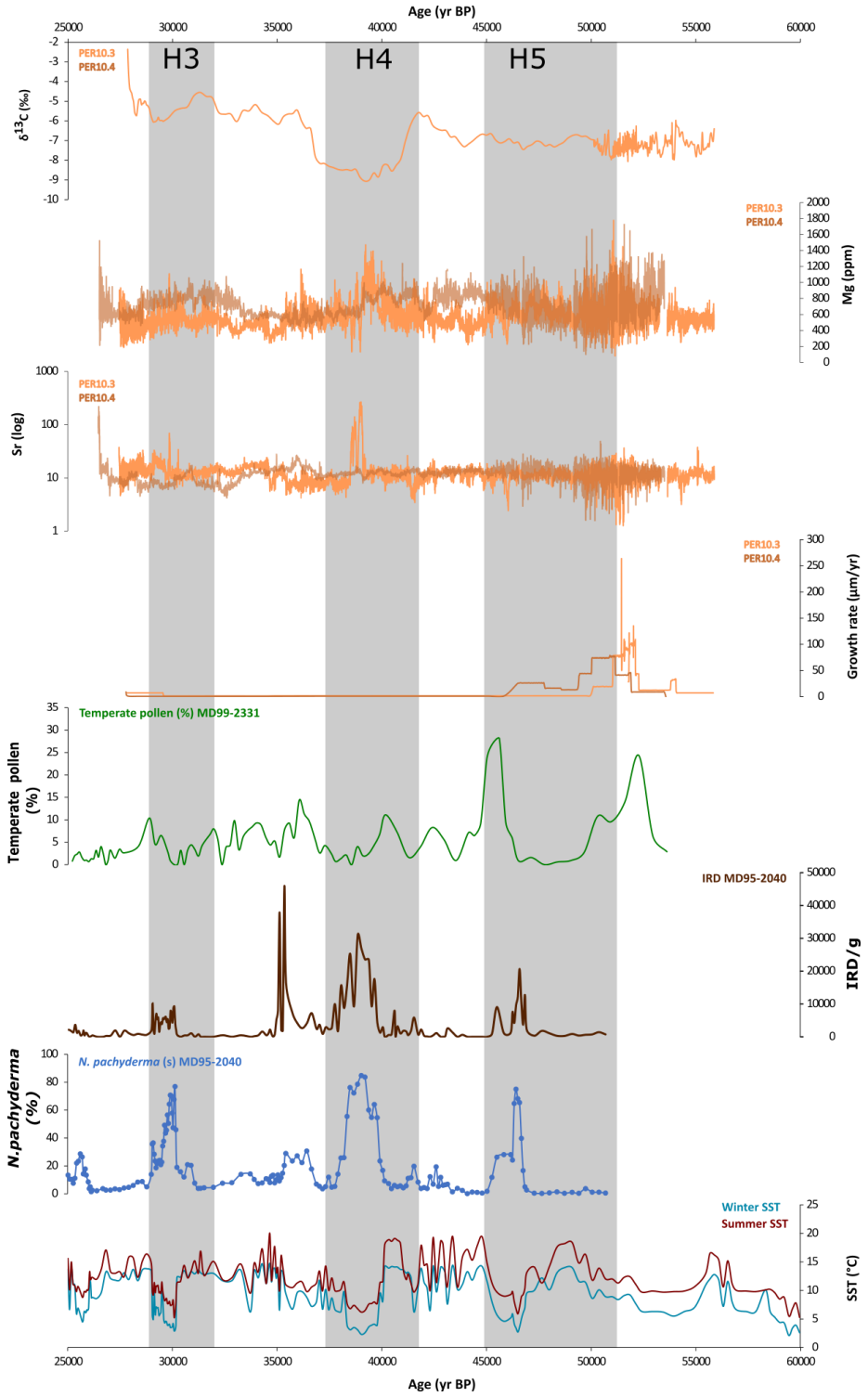

Figure 7.1: Comparison of palaeoclimate records from across the North Atlantic region. Cueva de las Perlas speleothem $\delta^{13}C$ values, Mg and Sr concentrations, temperate pollen from MD99-2331 (ACER Project members, 2017b), IRD and N. pachyderma (s) from MD95-2040 (Eynaud et al., 2009a, data: Eynaud et al., 2009b) and SST from MD95-2040 (Voelker et al., 2011a, data: Voelker et al., 2011b).

7.4 Investigation of the millennial-scale variability recorded in Cueva de las Perlas speleothem records in relation to wider North Atlantic archives

7.4.1 Overview

Section 6.5.3 demonstrated high-frequency abrupt climatic shifts within the Cueva de las Perlas speleothem records and suggested this climatic instability may be coincident with Dansgaard-Oeschger (DO) variability identified in the Greenland ice core records. DO variability in Greenland is defined by abrupt switches in climate from cold stadial conditions to mild interstadial conditions (Dansgaard *et al.,* 1993, Johnsen *et al.,* 1992, Rasmussen *et al.,* 2014) and evidence for millennial-scale variability has been identified across the Northern Hemisphere (Voelker, 2002). This section will present evidence for DO variability from different archives across the Northern Hemisphere and assess how the records from Cueva de las Perlas cohere with the wider North Atlantic evidence.

7.4.2 Evidence for millennial-scale variability from Northern Hemisphere archives

Evidence for millennial-scale variability in marine sediments was identified by Bond *et al.* (1993) through records of past SST from North Atlantic sediments over the past 90ka. Following the work of Bond *et al.* (1993), evidence for such variability has been widely documented in marine cores surrounding the Iberian Peninsula. Proxies used to identify millennial-scale variability in marine archives have included: alkenone SST temperature reconstructions (Cacho *et al.,* 1999; Pailler and Bard, 2002; Sánchez Goñi *et al.,* 2002, 2008), planktonic isotope analyses (Shackleton *et al.,* 2000; Combrourieu Nebout *et al.,* 2002) and pollen (Roucoux *et al.,* 2001, 2005; Sánchez Goñi *et al.,* 2000, 2002, 2008; Combrourieu Nebout *et al.,* 2002). Pollen records have indicated vegetation in Iberia responds rapidly to changes in SST throughout MIS3 and DO cycles are represented by the contraction and expansion of thermophilous tree populations (Roucoux *et al.,* 2005).

Lacustrine records from the Iberian Peninsula demonstrating millennial-scale climatic variability in response to North Atlantic forcing are scarce and most likely attributed to lower sampling resolution in current records and dating constraints (Moreno *et al.,* 2012). However, the Fuentillejo Maar record identifies evidence for close-coupling of the ocean-atmosphere system during MIS3 with variability which corresponds to DO cycles (Vegas *et al.,* 2010). Lacustrine records from across southern Europe have found evidence for shifts between stadial and interstadial conditions. Records include Tenaghi Phillipon, Greece (Müller *et al.,* 2011; Pross *et al.,* 2015), Lago Grande di Montichicco, Italy (Allen *et al.,* 1999; Martin-Puertas *et al.,* 2014) and Les Echets, France (Ampel *et al.,* 2008; Wohlfarth *et al.,* 2008; Veres *et al.,* 2009). Proxies typically express interstadial events in southern Europe as warm and wet whilst stadial events are defined by cold and arid climatic conditions. However, local factors influence the expression of each event in different archives (Sánchez Goñi *et al.,* 2008; Fletcher *et al.,* 2010).

European speleothems have identified the presence of DO cycles. Growth rates from speleothems in northern Iberia have indicated that growth during MIS3 was sporadic and coincided with warm phases of DO events (Stoll *et al.,* 2013). Additionally, speleothems from Sofular Cave, Turkey (Fleitmann *et al.,* 2009) and Austrian caves (Spötl and Mangini, 2002; Moseley *et al.,* 2014) have recognised the presence of DO cycles evidenced through stable isotope analyses.

7.4.3 Comparison of Cueva de las Perlas speleothem records to Northern Hemisphere archives

The Mg/Ca record from PER10.3 demonstrates high frequency oscillations in climate which show a similarity to the Greenland DO interstadial-stadial variability (figure 7.2, also figure 6.27). DO events are marked by abrupt shifts to wetter conditions in the Cueva de las Perlas speleothem records.

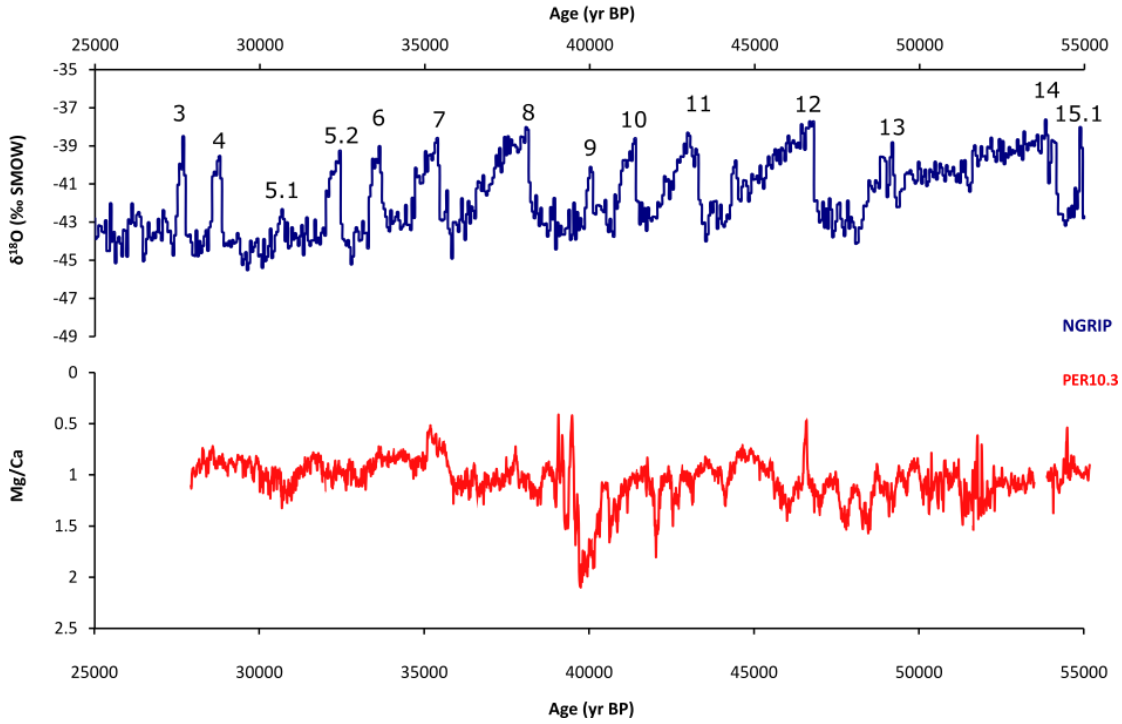

Figure 7.2: Comparison of Cueva de las Perlas speleothem Mg/Ca to ice core data. The ice-core data shown is 50yr averaged $\delta^{18}O$ values from NGRIP and numbers represent Greenland Interstadials (Rasmussen et al., 2014).

Wet conditions in NW Iberia appear to correspond to high temperate forest pollen identified in marine cores from the Iberian margin and Bay of Biscay (figure 7.3). The variability in the Cueva de las Perlas Mg/Ca records corresponds to that exhibited in the marine and ice core records and suggests a close-coupling of the ocean-atmosphere system throughout MIS3 as demonstrated in figure 7.3.

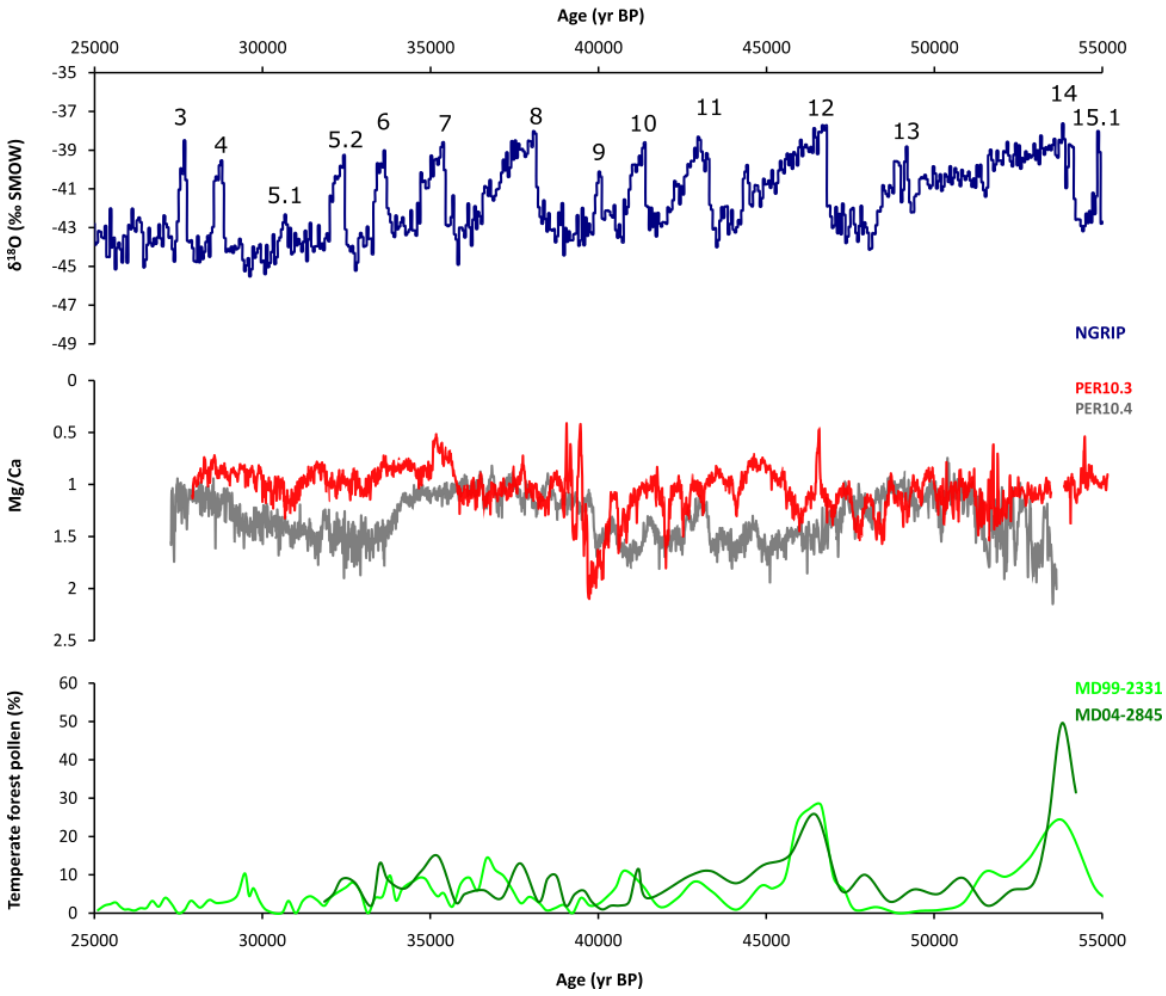

Figure 7.3: Comparison of Cueva de las Perlas speleothem Mg/Ca to ice core and marine pollen data. The ice-core data shown is 50yr averaged $\delta^{18}O$ values from NGRIP and numbers represent Greenland Interstadials (Rasmussen et al., 2014). Marine pollen data show temperate pollen percentages from MD04-2845 (ACER Project Members, 2017a) and MD99-2331 (ACER Project Members, 2017b). Note the reversed scale for the Mg/Ca data from PER10.3 and PER10.4.

7.5 Forcing mechanisms for sub-orbital events and variability

7.5.1 Overview

The identification of DO variability in sections 6.5.3 and 7.4 in Cueva de las Perlas indicates tight coupling of the ocean-atmosphere North Atlantic system throughout

MIS3. This section will discuss forcing mechanisms for stadial-interstadial variability and discuss the potential for latitudinal orbital modulation of abrupt climate variability (Fletcher and Sánchez Goñi, 2008; Sánchez Goñi *et al.,* 2008; Fletcher *et al.,* 2010). Additionally, the timeseries analysis of sub-orbital cyclicity undertaken in section 6.5.4 will be discussed in relation to the wider debate surrounding whether DO events occur cyclically.

7.5.2 Forcing mechanisms during stadials

Heinrich events correspond to the release of mass armadas of icebergs discharged from the Laurentide ice sheet (Bond *et al.,* 1992; Bond and Lotti, 1995) and subsequent melting of icebergs leads to a reduction in SST and reduced salinity across the North Atlantic (Cortijo *et al.,* 1997; Hemming 2004) although the exact mechanism forcing Heinrich events remains debated (e.g. Alvarez-Solas and Ramstein, 2011; Barker *et al.,* 2015). Influx of freshwater as a result of iceberg melting has been shown to influence the thermohaline circulation (Vidal *et al.,* 1997). Evidence has postulated changes in the Atlantic Meridional Overturning Circulation (AMOC) during DO stadials. However, further palaeoclimate records are required in order to further understand the nature and extent of these changes and to clarify the trigger mechanism for AMOC variability (Lynch-Stieglitz, 2017).

Both Heinrich Events and DO stadials are associated with weakening of North Atlantic Deep Water (NADW) formation in the Norwegian Sea and subsequent reduction in the strength of AMOC (Rasmussen *et al.,* 1996; Stocker, 2000; Roucoux *et al.,* 2005). Models have demonstrated a weakening or shutdown of AMOC reduces transport of heat northwards leading to a strengthening of the pole-to-equator mid-latitude temperature gradient (thermal front). In order to compensate and bring more heat to the North Atlantic, the strength of the Azores high and the Hadley cell are intensified resulting in a southward shift of the ITCZ (Kageyama *et al.,* 2009). Modelling agrees with climate proxy archives which have hypothesised that the northward migration of the thermal front and associated northward shift and strengthening of the westerlies led to the enhanced aridity across the Iberian Peninsula during HE and DO stadials. A

similar forcing mechanism has been identified to drive the positive-mode of the NAO and some authors have proposed a prevailing positive-mode NAO-like mechanism was responsible for driving aridity during Heinrich Events (Sánchez Goñi *et al.,* 2002; Naughton *et al.,* 2009).

In summary, the forcing mechanism currently dominant in the literature for extreme aridity and cooling during HE and DO stadials invokes a reduction in the strength of AMOC. As a consequence, SST were lowered, and westerly winds were intensified and shifted to the north. Colder SST, the presence of offshore ice and the close proximity of the polar front led to enhanced aridity and cooling in and around the Iberian Peninsula during Heinrich Events relative to DO stadials (Roucoux *et al.,* 2005).

7.5.3 Forcing mechanisms during interstadials

The relative synchronicity between DO warming events in Greenland and the increase in the SST of waters surrounding the Iberian Peninsula demonstrates a close coupling of the ocean-atmosphere system which has repeatedly undergone rapid reorganisation on relatively short timescales (i.e. centuries) (Bond *et al.,* 1993). The synchronous relationship between the two regions during DO events is most likely propagated through rapid northward migration of the polar front accompanied by reorganisation of the atmospheric circulation (Bond *et al.,* 1993; Shackleton *et al.,* 2000; Roucoux *et al.,* 2001; Fletcher *et al.,* 2010). Rapid reorganisations in atmospheric circulation have been demonstrated to occur within 1-3yrs during the last two abrupt warmings (Steffensen *et al.,* 2008). Evidence from the Bay of Biscay marine core (MD04-2845) has shown the development of *Betula*-*Pinus* deciduous *Quercus* forest in northwestern Iberia and western France during warming phases when summer SST reach 12°C (Sánchez Goñi *et al.,* 2008). Increases in SST associated with North Atlantic warming would enhance evaporation and lead to increased temperatures and precipitation over Iberia (Roucoux *et al.,* 2005).

7.5.4 Potential modulation of DO events through orbital forcing

7.5.4.1 Overview

Marine cores have demonstrated the significance of the Iberian Peninsula and wider Mediterranean region as they lie upon the boundary between obliquity-forced and precession-forced climate variability, particularly during MIS3 (Sánchez Goñi *et al.,* 2018). DO cycles are evident in archives from across the North Atlantic although responses to DO events are region-specific as a result of orbital modulation. Regions below 40°N are suggested to be influenced by precession whilst those above are influenced by obliquity (Sánchez Goñi *et al.,* 2018). This section will summarise the current evidence and investigate potential for orbital modulation within the Cueva de las Perlas speleothems.

7.5.4.2 The influence of precession below 40°N

Analysis of a marine core from the Alboran Sea (MD95-2043) recognised periods of strongest forest development occurred during DO8, 7, 6 and 5 and were coincident with precession minima (Fletcher and Sánchez Goñi, 2008). During precession minima, Mediterranean climate was strengthened through enhanced seasonality resulting in hot-dry summers and wet-cool winters (Fletcher and Sánchez Goñi, 2008; Sánchez Goñi *et al.,* 2018). Precessional influence on forest development has not clearly been demonstrated in marine pollen records from the NW Iberian margin (Roucoux *et al.,* 2005; Sánchez Goñi *et al.,* 2008) or in the Bay of Biscay (Sánchez Goñi *et al.,* 2008). Consequently, it has been proposed that the influence of precession on modulating millennial-scale climate variability is more significant in the western Mediterranean basin as opposed to the northern Iberian Peninsula and higher northern latitudes (Sánchez Goñi *et al.,* 2008; Fletcher and Sánchez Goñi., 2008).

7.5.4.3 Obliquity forcing above 40°N

Marine cores, particularly through pollen analysis, have identified that periods of maximum expansion of Atlantic forest (above 40°N) coincided with obliquity maxima (Sánchez Goñi *et al.,* 2018). The significant expansion of forest during DO14 and 12 occurred during both an obliquity maximum and a precession maximum (Fletcher *et al.,* 2010). An obliquity maximum would lead to preferential warming at high latitudes

and precession maxima would reduce seasonality at lower latitudes (Fletcher *et al.,* 2010; Sánchez Goñi *et al.,* 2018). Both of these parameters combined would result in a reduction of ice sheet extent and encourage forest development at high latitudes associated with warmer and wetter conditions (Fletcher *et al.,* 2010).

7.5.4.4 Orbital modulation of the Cueva de las Perlas speleothem records

Similar to Fletcher and Sánchez Goñi (2008), the length and resolution of the Cueva de las Perlas speleothem record does not permit the full assignment of millennial-scale variability to either precessional or obliquity cycles. However, there is evidence for the modulation of Northern Iberian climate by orbital parameters (figure 7.5).

Section 6.5.4 proposed that decline in Mg/Ca in PER10.3 at 39.5ka may correspond to DO8. If this is true, the Mg/Ca record following DO8 exhibits changes which are relatively muted compared to those preceding DO8 (inclusive) (figure 7.5). Climate variability prior to DO-8 includes abrupt oscillations towards wetter conditions demonstrated by shifts in Mg/Ca of >0.5. Following DO8, millennial-scale variability is less evident, oscillations towards wetter conditions are present but they are less pronounced and distinguished by a gradual shift in Mg/Ca of typically less than 0.5. This distinction between events prior to and including DO8 and those after DO8 coincides with declining obliquity and precession which would inhibit ice sheet reduction and forest expansion through lowered temperatures at high latitudes. This forcing mechanism has the ability to act to complement variations in NHSI at 65°N, which have previously been demonstrated to influence drying trends in northern Iberia (section 6.5.1). The decline of NHSI throughout MIS3 resulted in the expansion of ice sheets and onset of glacial conditions associated with MIS2. Therefore, post-DO8 weaker DO warmings are evident in northern Iberia and are likely to reflect not only NHSI, but also the modulating effects of declining obliquity and precession.

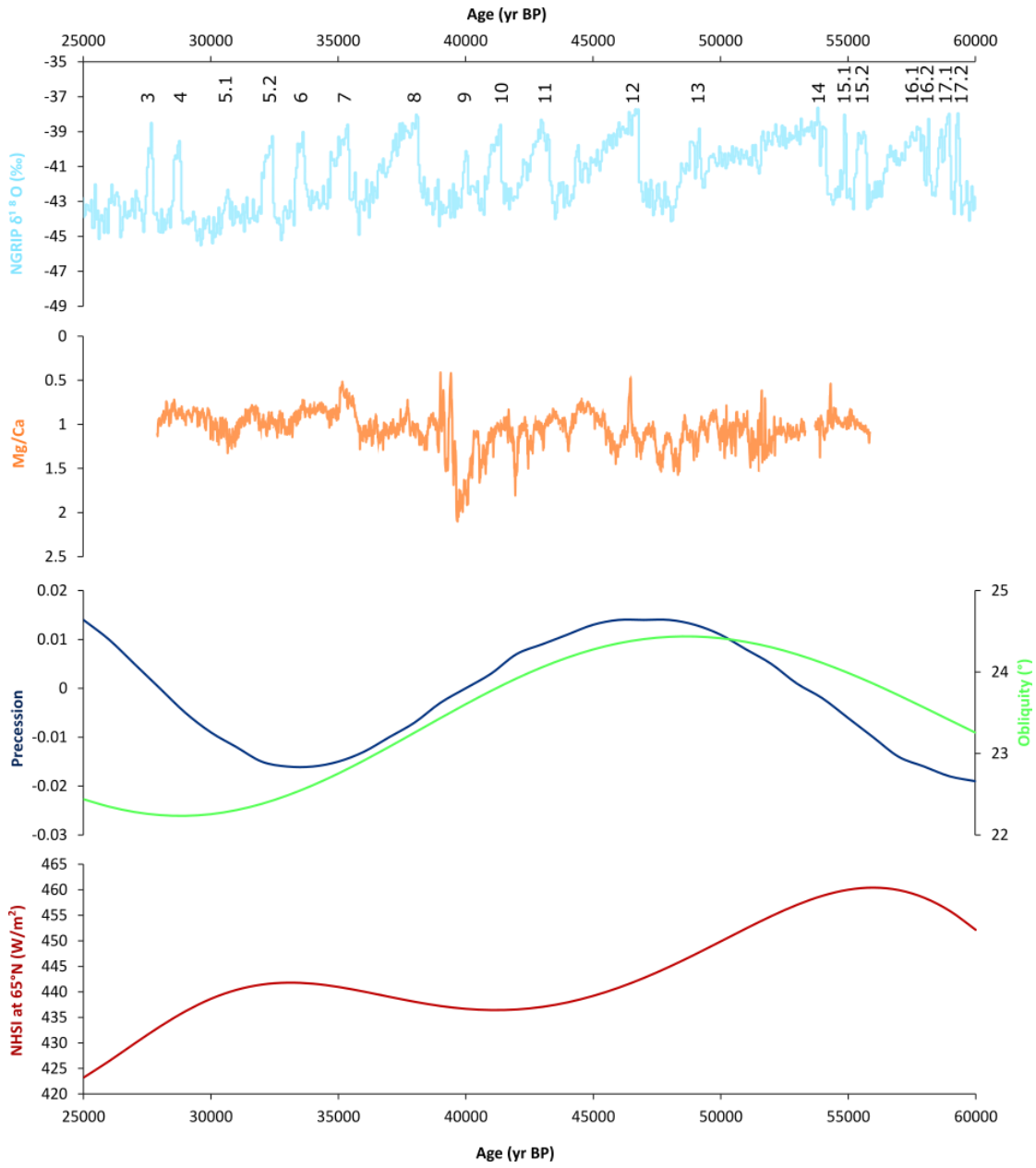

Figure 7.5: Orbital modulation of DO millennial-variability at Cueva de las Perlas. NGRIP 20-yr averaged oxygen isotope data are shown in light blue and numbers represent GI onsets (Rasmussen et al., 2014), PER10.3 Mg/Ca 10-yr averaged data is shown in orange and precession index, obliquity and Northern Hemisphere summer insolation at 65°N are also shown (Berger and Loutre, 1991; data from Berger and Loutre (1999).

7.5.5 Investigation of the ~2000yr periodicity identified in the Cueva de las Perlas speleothem record

Periodicities of ~1500yr have been identified for millennial-scale climate events during the Holocene (Bond *et al.,* 2001; Mayewski *et al.,* 2004). Speleothems from Asiul Cave, Matienzo, have demonstrated a similar pacing for millennial-scale events of ~1500yrs throughout the Holocene (Smith *et al.,* 2016b). Section 6.5.4 identified periodicities of 1900-yr and 2000-yr in the PER10.3 Mg/Ca profile and ~1600yr and ~2000yr in the PER10.4 profile. This periodicity may underlie the cyclic wet-dry events exhibit in the Cueva de las Perlas speleothem records (section 6.5.3).

Previous studies have also identified a lack of ~1500-yr cycles within data from different palaeoclimate archives (Long and Stoy, 2013; Ditlevsen *et al.,* 2007; Thomas *et al.,* 2011; Obrochta *et al.,* 2012). Stable isotope data from Lake Malawi diatoms revealed quasi-periodic dry events occurring ~2300ka coinciding with cooler temperatures in Greenland (Barker *et al.,* 2007). However, investigation into the periodicity within a marine core from the North Atlantic suggested that the ~1500-yr cycle may be a statistical artefact of ~1000-yr and ~2000-yr cycles which were demonstrated throughout glacial periods 2 and 3. These periodicities are postulated to respond to solar forcing (Obrochta *et al.,* 2012).

Spectral analysis of Hulu Cave speleothems and the GRIP and GISP2 ice core records by Clemens (2005) identified that the ~1500-yr cycles are an artefact of the GISP2 age model. Millennial-band cycles were evident in the Hulu record with peaks centred at 1190-yr, 1490-yr and 1667-yr. This pattern was identified in the GISP2 record when it was analysed using the Hulu Cave age model and also in the GRIP record using a radiometric age model. Clemens (2005) postulates these peaks may represent millennial-scale climate variability as a heterodyne response to centennial-scale solar forcing. In order to validate the potential influence of centennial solar cycles on millennial-scale climate variability in the Cueva de las Perlas speleothem records, age models with lower age errors are required.

Timeseries has identified periodicities in the PER10.3 Mg/Ca record of 1900-yr and 2000-yr and in the PER10.4 Mg/Ca record of ~1600yr and ~2000yr for millennial-scale

climate variability thought to relate to DO cycles. However, due to the large age errors associated with the dataset, particularly <50ka, it is difficult to determine the validity of these cycles. Further dating is required in order to fully constrain the chronology and permit a full assessment of cyclic variability within the Cueva de las Perlas speleothem records.

7.5.6 Summary

The speleothem records from Cueva de las Perlas add to the growing literature identifying a strong coupling of the ocean-atmosphere system throughout MIS3, shown through the expression of millennial-scale events comparable to the Greenland ice core records. Cold and dry intervals in northern Iberia are associated with a reduction in the strength of AMOC and subsequent shifts in atmospheric circulation patterns. Of particular significance to this study is the northerly shift in westerly winds, which leads to enhanced aridity on the Iberian Peninsula during Heinrich Events and DO stadials which is clearly evident in the Mg/Ca profiles from Cueva de las Perlas speleothems. Interstadials associated with abrupt DO warmings are forced by rapid movements of the polar front and reorganisation of atmospheric circulation.

Previously, marine proxies have identified the potential for orbital modulation of DO variability (Sánchez Goñi *et al.,* 2008; Fletcher and Sánchez Goñi, 2008; Fletcher *et al.,* 2010; Sánchez Goñi *et al.,* 2018). Although the resolution and length of the Cueva de las Perlas record inhibit full assessment of orbital forcing, there is evidence to suggest obliquity and precession maxima act to influence DO12 in northern Iberia. Additionally, DO events after DO8 coincide with declining obliquity, precession and NHSI which may act to reduce the impact of these events on the Iberian Peninsula.

7.6 Placing the Neanderthal demise in the context of climate and environmental change on the northern Iberian Peninsula 85-30ka BP

7.6.1 Overview

The causes of the Neanderthal extinction remain debated with the leading theories invoking the arrival of anatomically modern humans (AMH) (Banks, 2008; Benazzi *et al.,* 2015; Gilpin *et al.,* 2016) or climate changes (Finlayson and Carrion, 2007; Sepulchre *et al.,* 2007), both directly and indirectly influencing Neanderthal population dynamics. Recent technological advances have allowed sequencing of the Neanderthal genome (Green *et al.,* 2010) and further assessment has shed light on Neanderthals with some evidence suggesting their genetic make-up may have induced their own demise. Castellano *et al.,* (2014) demonstrated Neanderthals had a reduced genetic diversity and populations were typically small and isolated. Evidence for a prolonged population bottleneck would have reduced genetic diversity (Prüfer *et al.,* 2014; Harris and Neilsen, 2016, 2017) which may have contributed to their demise.

The extent to which Neanderthal populations were influenced by climate and environmental changes requires a significant archaeological input from northern Spain. However, the aim of this work was to investigate the terrestrial climatic and environmental variability during MIS5a-3 using speleothems from northern Spain in order to provide a regional climate and environmental background onto which the Neanderthal demise can be placed. Climate change has long been postulated as a cause of the Neanderthal demise (d'Errico and Sánchez Goñi, 2003; Finlayson and Carrion, 2007). However, different events have been attributed to the extinction of Neanderthals for example H5 (Galvan *et al*, 2014; Garralda *et al*, 2014) and H4 (Sepulchre *et al*, 2007, Wolf *et al.,* 2018) and additionally the influence of climatic oscillations has also been proposed (Finlayson and Carrion, 2007; Tzedakis *et al*, 2007).

Prior to the discussion of the influence of climate change on Neanderthal populations, it must be stressed that the dynamics of the Neanderthal population decline which culminated in their extinction remain debated due to ambiguous archaeological

records (Finlayson *et al.,* 2004). Recent re-dating of archaeological sites by Higham *et al.* (2014) proposed that the disappearance of the Mousterian culture associated with the Neanderthals occurred at 42ka and since then studies have identified evidence for an "early" (prior to 42ka) Neanderthal extinction (Galvan *et al.,* 2014; Alcaraz-Castaño *et al.,* 2017; Kehl *et al.,* 2017). Although, some authors argue for the later persistence of Neanderthals on the Iberian Peninsula until 37ka (Zilhão *et al.,* 2017). Discrepancies also lie in the timing of the arrival of modern humans into Iberia. Wood *et al.* (2014) demonstrate AMH arrived in northern Iberia at ~42ka whereas results from Higham *et al.* (2014) suggest an overlap between the two species of *Homo* of 2,600-5,400yrs which allowed for cultural and genetic exchange.

7.6.2 The influence of orbitally-forced climate change on Neanderthals

The speleothem records presented as part of this project have identified the continued drying throughout MIS5a and into MIS4 demonstrated by a hiatus at 65ka-55ka. Nucleation of growth at 55ka indicates a return to wetter conditions, however, the record does continue to show evidence of a long-term drying trend throughout MIS3 and into the MIS2 glacial period where growth terminates. A continued drying throughout the period 85-27ka would have influenced the environment the Neanderthals were occupying, and potentially caused stress on their populations. Dry climates would have resulted in inhospitable conditions for Neanderthals characterised by a reduction in vegetation, bioproductivity and prey (Wolf *et al.,* 2018). As a result, Neanderthals would have restricted resources available.

7.6.3 The influence of sub-orbital driven climate and environmental variability on Neanderthals

High-frequency millennial-scale oscillations in climate are superimposed on the overall drying trend in northern Iberia. As a consequence, these climatic changes would have influenced the environments in which Neanderthals were living on the Iberian Peninsula. The literature emphasises the role of Heinrich events in the extinction of

Neanderthals (Seplulchre *et al.,* 2007; d'Errico and Sachez-Goni 2003; Galvan *et al.,* 2014; Wolf *et al.,* 2018). The severe drying episodes present in the speleothem records from Cueva de las Perlas likely reflect an indirect effect of climate on population dynamics via changes in ecology and food resources (Stewart, 2005). However, recent frameworks have identified the limited influence of Abrupt Environmental Transitions on hominin populations (Davies *et al.,* 2015). Additionally, the frequency and amplitude of these climate oscillations is more likely to drive changes in Neanderthal population dynamics rather than the intensity of each individual event (Finlayson *et al.,* 2004).

Neanderthals had survived previous climatic instability since the divergence of their lineage from AMH. Recent evidence from DNA sequences from Neanderthals estimates their divergence prior to 550ka (Meyer *et al.,* 2016) and the persistence of Neanderthals may suggest that climatic instability did not influence their populations. Evidence from the Sandy Lane Mammal Assemblage Zone demonstrated Neanderthal populations thrived in warm and dry habitats during MIS7 (Schreve, 2017). Habitat preferences of Neanderthals ranged throughout their existence and evidence from Schreve (2017) suggested Neanderthals were not intolerant to the productive steppic habitats associated with warm and dry climate conditions. Nevertheless, as highlighted by Finlayson *et al.,* (2004) it would be naïve to expect an analogous response of populations to similar climatic and environmental perturbations.

The identification of a single forcing mechanism for the Neanderthal population decline is challenging, with multiple strands of evidence invoking a variety of different factors. Rey-Rodríguez *et al.* (2016) concluded by proposing climatic and environmental change cannot alone be held responsible for the Neanderthal extinction, attributing a combination of changing subsistence and territory exploitation strategies and the arrival of the AMH rival populations which may have added to the strain on Neanderthal populations triggering instability and a decline (Rey-Rodríguez *et al.,* 2016).

Speleothems from Cueva de las Perlas have demonstrated an overall drying trend throughout MIS3 as a response to orbital forcing. Additionally, evidence from

speleothem proxies identifies MIS3 as a period characterised by climate instability involving abrupt shifts from dry to wet conditions and extreme aridity during millennial-scale events. These climatic oscillations would have impacted the terrestrial landscapes in which the Neanderthals were inhabiting primarily through changes in prey species and vegetation.

Similar to the conclusions of Rey-Rodriguez *et al.* (2016) and considering the Cueva de las Perlas speleothem record, a combined influence of the arrival of modern humans, indirect terrestrial effects of millennial-scale climate oscillations (including DO instability and Heinrich events) and an overall drying trend throughout MIS3 most likely forced the decline of Neanderthal populations. The impact of these forcing mechanisms would have been exacerbated as a consequence of the low genetic diversity of the Neanderthal populations, making them more susceptible to variations in climate and the additional competition from AMH.

7.6.4 Summary

The Cueva de las Perlas speleothem records have reconstructed palaeoclimate and palaeoenvironments on the northern Iberian Peninsula. It is apparent from these records that high-frequency oscillations in climate occurred throughout MIS3 which led to fluctuations between warm-wet conditions and cold-dry conditions on the Iberia Peninsula, with extensive drying associated with Heinrich Events. The climatic shifts may have added stress to the weakening Neanderthal populations, however it is unlikely that the shifts to arid conditions played a determining role in the Neanderthal demise. An alternative hypothesis proposes the combined effects of the arrival of modern humans and the indirect effects of a changing climate and environment superimposed on a genetically limited population, were responsible for the extinction of the Neanderthals. Additional evidence from the archaeological record is needed in order to understand the Neanderthal and AMH population dynamics during this period and can provide further understanding of the responses of these hominin species to climatic perturbations.

8. Conclusions and suggestions for further research

This thesis has produced the first comprehensive cave monitoring study of Cueva de las Perlas and has developed the first terrestrial palaeoclimate and palaeoenvironmental record from the Matienzo depression spanning 86-27ka. The sections below will act as a summary of key findings and highlight areas for further research.

8.1 Cave monitoring

Cave temperature is seasonal and dependent on density-driven ventilation induced by temperature differences between external and internal air temperatures. This ventilation is moderated by latent bedrock heating which leads to a lag between maximum summer external and internal temperature. Seasonal patterns of cave air temperatures and correspondence to external air temperatures suggest density-driven ventilation; as demonstrated by other cave systems across the globe (Spötl *et al.,* 2005; James *et al.,* 2015; Smith *et al.,* 2016a).

Carbon dynamics within the cave (CO_2 and $\delta^{13}C$ values) do not appear to demonstrate a seasonal cycle but respond rapidly to diurnal oscillations in external temperature. Daily fluctuations in external temperature cross the internal temperature threshold which induces density-driven ventilation within the cave leading to an influx of CO_2-poor external air. As a result, CO_2 concentrations and $\delta^{13}C$ values of cave air remain close to external air all year round. Calcite precipitation is therefore promoted throughout the year as a result of enhanced degassing into the low CO_2 cave void.

Evidence from CO_2 concentrations and electrical conductivity values of drip waters has shown the secondary influence of pressure-induced ventilation on the carbon dynamics within Cueva de las Perlas. Low external pressures enhance draw down of CO_2-rich air from the karst and subsequently increase CO_2 concentrations in the cave. High CO_2 concentrations act to limit degassing of dripwaters and result in an increase

in electrical conductivity. This work acts to support the findings of Smith *et al.* (2015) who identified the secondary influence of pressure on carbon dynamics in nearby Asiul Cave (Matienzo).

Stable isotope analyses of drip waters have found that $\delta^{18}O$ and δD values reflect external precipitation amount and trajectory analysis has identified the North Atlantic ocean as the source region. These isotopes lie towards the winter end of the Local Meteoric Water Line and suggest a homogenised aquifer with primary recharge during the winter months. The carbon isotope composition of the dripwaters is influenced by soil productivity and modified by karst-water interaction processes. Further monitoring is required to clarify the influence of productivity on carbon isotope values. Modern assessment of trace elements in drip waters has indicated Mg and Sr are primarily a function of karst-water interaction processes such as prior calcite precipitation and/or incongruent calcite dissolution. Further study of trace elements e.g. P, Zn, Fe in the waters by ICP-MS would act to constrain the influence of soil and vegetation processes on trace elements in drip waters and subsequent incorporation into speleothem calcite.

Water movement is primarily through matrix flow with a secondary influence of fracture or piston-flow during periods of increased precipitation. Inter-annual isotopic variability in percolating waters related to karst hydrology was assessed using the karst hydrological model of Baker and Bradley (2010). Modelling determined minimal influence of karst-hydrological processes on isotopic variability. This model could be developed by continued monitoring of external and internal climate and drip water chemistry.

Study of modern calcite plates has demonstrated isotopic variability across growth laminae calling into question the validity of the 'Hendy test'. Additionally, these plates have demonstrated the complexities associated with determining "equilibrium deposition" and have suggest modern calcite is forming in quasi-equilibrium with the cave environment. This work supports the hypothesis of Dorale and Liu (2009) which argued that equilibrium fractionation may be occurring along the central growth axis while the speleothem flanks are subject to kinetic fractionation.

8.2 Reconstructing past climate variability between 86-27ka

Three speleothems collected from Cueva de las Perlas were used to assess past climate and environmental variability between 86-27ka. Proxies demonstrated shifts in precipitation amount ($\delta^{18}O$ values) and karst-water interaction processes ($\delta^{13}C$ values, Mg, Sr and Ba). Although, Sr and Ba were also indicative of changes in speleothem growth and $\delta^{13}C$ values can be influenced by soil productivity over long-timescales.

A long-term trend towards arid conditions was evident during MIS5a into MIS4 and throughout MIS3 into MIS2. The long-term aridity trend recorded in the Cueva de las Perlas speleothems is coincident with a contraction of tree populations and ericaceous heathlands (Roucoux *et al.,* 2005; Fletcher and Sánchez Goñi, 2008), declining sea surface temperatures (Cacho *et al.,* 1999) and an expansion of ice sheets (Thomson *et al.,* 1999; Schönfeld *et al.,* 2003; Shackleton *et al.,* 2000). This variability is related to orbital forcing, particularly Northern Hemisphere Summer Insolation. Reductions in insolation drive the Northern Hemisphere ice ages through expansion of ice sheets.

Sub-orbital climate instability is superimposed on the orbital-trends and observed throughout the records. This variability agrees with local Iberian marine and terrestrial archives (Roucoux *et al.,* 2001; 2005; Sánchez Goñi *et al.,* 2000; 2008; Wainer *et al.,* 2009; Moseley *et al.,* 2014) and wider North Atlantic archives (Bond *et al.,* 1993; Dansgaard *et al.,* 1993; Rasmussen *et al.,* 2014) suggesting the presence of Dansgaard-Oeschger cycles and Heinrich events. Therefore, the identification of this pattern in Cueva de las Perlas strengthens the hypothesis for a tightly-coupled ocean-atmosphere system during MIS3.

Timeseries analysis undertaken has identified a periodicity for the wet-dry cycles in the Mg/Ca record of ~2000yrs. This overlaps with the ~1500±500yr periodicity determined by Bond *et al.* (1997). However, the validity of this periodicity has been questioned (Clemens, 2005; Obrochta *et al.,* 2012). Further U-series dating would minimise the age errors associated with the speleothem chronologies. Reduced age errors are required in order to validate the observed periodicity in the Cueva de las Perlas speleothems. Additionally, higher resolution isotope sampling between 25-

50ka would permit analysis of different proxy data, thus evidencing the existence of the cycles in numerous proxies.

A caveat of the present study was the weaker chronology between 25-50ka. This period proved challenging to date and subsequently contained large age errors which made comparison to other records and classification of individual events difficult. Additionally, the fall in growth rate during the same period led to a reduction in isotope sampling resolution. Further dating and isotope analyses on PER10.3 and PER10.4 <50ka would aid the interpretation of the palaeoclimate records greatly.

8.3 The influence of climate change on Neanderthal populations

Dry conditions and abrupt climatic variability has been identified within the Cueva de las Perlas speleothem records. Although climate change has frequently been invoked as a cause for Neanderthal population decline (e.g. Finlayson *et al.,* 2004; d'Errico and Sánchez Goñi, 2003; Sepulchre *et al.,* 2007), the high-frequency climatic perturbations during MIS3 are unlikely to have directly influenced Neanderthals. Climate change and environmental variability combined with the arrival of anatomically modern humans would have increased the strain upon an already genetically weak species. Initial work from Cueva de Cofresnedo has begun to explore the archaeological potential within the Matienzo region and future efforts should aim to constrain the periods of Neanderthal and anatomically modern human occupation of the site. Furthermore, archaeological records from the Iberian Peninsula should constrain the timing of the Neanderthal demise using modern dating techniques (Higham *et al.,* 2014) in order to fully understand the nature of the extinction.

8.4 Potential extension of the Cueva de las Perlas speleothem records to explore climate and environmental change during MIS5e and beyond

Understanding glacial-interglacial transitions remains an important objective for the palaeoclimate community. Glacial terminations are associated with melting ice sheets, reorganisations of atmospheric circulation and increased CO_2 concentrations (Denton *et al.,* 2010). Termination II marks the transition between MIS6 and MIS5e. However, the exact timing of onset remains debated (Muñoz-García *et al.,* 2007). Although palaeoclimate records from speleothems have been used to determine climatic and environmental variability during Termination II, these have primarily focused on variations in stable isotope values (Muñoz-García *et al.,* 2007; Stoll *et al.,* 2015; Moseley *et al.,* 2015) or changes in growth rate (Stoll *et al.,* 2013).

Speleothem palaeoclimate records from Matienzo have demonstrated the sensitivity of the region to past climate variability due to the unique positioning of Northern Iberia on the margin of key air masses and influence of the North Atlantic Ocean. The top of a speleothem from Cueva de las Perlas was dated to 120.06±5.13ka BP as part of the present study. This speleothem has the potential to explore climate variability during MIS5e through geochemical proxies. The basal date for this speleothem is unknown but growth initiation may precede or coincide with Termination II. Trace elements, primarily Mg and Sr, have been crucial indicators of past climate and environmental variability in the present study. There are many other trace elements which can be utilised in speleothem palaeoclimate studies, such as P, Zn and Fe. Assessment of trace element concentrations within speleothem calcite, combined with comprehensive contemporary monitoring of trace element incorporation into drip waters (suggested previously in section 8.1), would provide insight into local and regional climate dynamics across MIS5e and potentially span Termination II.

8.5 Summary

This study was the first to investigate cave dynamics within Cueva de las Perlas, Matienzo, through an extensive cave monitoring programme. In light of this modern monitoring, three speleothems were collected and were used to reconstruct past climate and environmental variability between 86-27ka. Evidence has demonstrated orbital and sub-orbital climate variability throughout MIS5a-MIS3. Sub-orbital variability is similar to Dansgaard-Oeschger cycles recorded in numerous North Atlantic archives. Therefore, it is evident that during the period of Neanderthal population decline climate conditions were fluctuating on the Iberian Peninsula. However, the Neanderthal extinction coincides with the arrival of modern humans. It is probable the Neanderthal demise was related to the arrival of modern humans and climatic and environmental instability superimposed onto an already genetically weak population.

9. Reference list

ACER PROJECT MEMBERS. 2017a. *CLAM age model and biomes of sediment core MD04-2845.* [Online]. PANGAEA. Available: https://doi.org/10.1594/PANGAEA.872808 [Accessed May 2018].

ACER PROJECT MEMBERS. 2017b. *CLAM age model and biomes of sediment core MD99-2331.* [Online]. PANGAEA. Available: https://doi.org/10.1594/PANGAEA.872813 [Accessed May 2018].

ALCARAZ-CASTAÑO, M., ALCOLEA-GONZÁLEZ, J., KEHL, M., ALBERT, R.-M., BAENA-PREYSLER, J., DE BALBÍN-BEHRMANN, R., CUARTERO, F., CUENCA-BESCÓS, G., JIMÉNEZ-BARREDO, F., LÓPEZ-SÁEZ, J.-A., PIQUÉ, R., RODRÍGUEZ-ANTÓN, D., YRAVEDRA, J. & WENIGER, G.-C. 2017. A context for the last Neandertals of interior Iberia: Los Casares cave revisited. *PloS one,* 12**,** e0180823.

ALLEN, J. R., BRANDT, U., BRAUER, A., HUBBERTEN, H.-W., HUNTLEY, B., KELLER, J., KRAML, M., MACKENSEN, A., MINGRAM, J. & NEGENDANK, J. F. 1999. Rapid environmental changes in southern Europe during the last glacial period. *Nature,* 400**,** 740-743.

ALLISON, G. B. 1982. The relationship between 18O and deuterium in water in sand columns undergoing evaporation *Journal of Hydrology,* 55**,** 163-169.

ÁLVAREZ-LAO, D. J. 2014. The Jou Puerta cave (Asturias, NW Spain): A MIS 3 large mammal assemblage with mixture of cold and temperate elements. *Palaeogeography, Palaeoclimatology, Palaeoecology,* 393**,** 1-19.

ÁLVAREZ-LAO, D. J. & GARCÍA, N. 2010. Chronological distribution of Pleistocene cold-adapted large mammal faunas in the Iberian Peninsula. *Quaternary International,* 212**,** 120-128.

ALVAREZ-SOLAS, J. & RAMSTEIN, G. 2011. On the triggering mechanism of Heinrich events. *Proceedings of the National Academy of Sciences,* 108**,** E1359-E1360.

AMPEL, L., WOHLFARTH, B., RISBERG, J. & VERES, D. 2008. Paleolimnological response to millennial and centennial scale climate variability during MIS 3 and 2 as suggested by the diatom record in Les Echets, France. *Quaternary Science Reviews,* 27**,** 1493-1504.

ARIENZO, M. M., SWART, P. K., BROAD, K., CLEMENT, A. C., POURMAND, A. & KAKUK, B. 2017. Multi-proxy evidence of millennial climate variability from multiple Bahamian speleothems. *Quaternary Science Reviews,* 161**,** 18-29.

AUSTIN, W. E. N. & HIBBERT, F. D. 2012. Tracing time in the ocean: a brief review of chronological constraints (60–8 kyr) on North Atlantic marine event-based stratigraphies. *Quaternary Science Reviews,* 36**,** 28-37.

AYALON, A., BAR-MATTHEWS, M. & SASS, E. 1998. Rainfall-recharge relationships within a karstic terrain in the Eastern Mediterranean semi-arid region, Israel: δ 18 O and δD characteristics. *Journal of Hydrology,* 207**,** 18-31.

BAAS, J. H., MIENERT, J., ABRANTES, F. & PRINS, M. A. 1997. Late Quaternary sedimentation on the Portuguese continental margin: climate-related processes and products. *Palaeogeography, Palaeoclimatology, Palaeoecology,* 130**,** 1-23.

BAILEY, S. E. & HUBLIN, J.-J. 2006. Dental remains from the Grotte du Renne at Arcy-sur-Cure (Yonne). *Journal of Human Evolution,* 50**,** 485-508.

BAKER, A. & BRADLEY, C. 2010. Modern stalagmite δ18O: Instrumental calibration and forward modelling. *Global and Planetary Change,* 71**,** 201-206.

BAKER, A. & BRUNSDON, C. 2003. Non-linearities in drip water hydrology: an example from Stump Cross Caverns, Yorkshire. *Journal of Hydrology,* 277**,** 151-163.

BAKER, A., GENTY, D. & FAIRCHILD, I. J. 2000. Hydrological characterisation of stalagmite dripwaters at Grotte de Villars, Dordogne, by the analysis of inorganic species and luminescent organic matter. *Hydrology and Earth System Sciences,* 4**,** 439-449.

BAKER, A., ITO, E., SMART, P. L. & MCEWAN, R. F. 1997. Elevated and variable values of 13C in speleothems in a British cave system. *Chemical Geology,* 136**,** 263-270.

BAKER, A. J., MATTEY, D. P. & BALDINI, J. U. L. 2014. Reconstructing modern stalagmite growth from cave monitoring, local meteorology, and experimental measurements of dripwater films. *Earth and Planetary Science Letters,* 392**,** 239-249.

BALDINI, J. U. L. 2010. Cave atmosphere controls on stalagmite growth rate and palaeoclimate records. *Geological Society, London, Special Publications,* 336**,** 283-294.

BALDINI, J. U. L., MCDERMOTT, F. & FAIRCHILD, I. 2006. Spatial variability in cave drip water hydrochemistry: Implications for stalagmite paleoclimate records. *Chemical Geology,* 235**,** 390-404.

BALDINI, J. U. L., MCDERMOTT, F., HOFFMANN, D. L., RICHARDS, D. A. & CLIPSON, N. 2008. Very high-frequency and seasonal cave atmosphere PCO2 variability: Implications for stalagmite growth and oxygen isotope-based paleoclimate records. *Earth and Planetary Science Letters,* 272**,** 118-129.

BALDINI, L. M., MCDERMOTT, F., BALDINI, J. U., FISCHER, M. J. & MÖLLHOFF, M. 2010. An investigation of the controls on Irish precipitation δ 18 O values on monthly and event timescales. *Climate dynamics,* 35**,** 977-993.

BAN, F., BAKER, A., MARJO, C. E., DUAN, W., LI, X., HAN, J., COLEBORN, K., AKTER, R., TAN, M. & NAGRA, G. 2018. An optimized chronology for a stalagmite using seasonal trace element cycles from Shihua Cave, Beijing, North China. *Scientific Reports,* 8**,** 4551.

BANKS, W. E., D'ERRICO, F., PETERSON, A. T., KAGEYAMA, M., SIMA, A. & SÁNCHEZ-GOÑI, M.-F. 2008. Neanderthal extinction by competitive exclusion. *PLoS One,* 3**,** e3972.

BANNER, J. L., GUILFOYLE, A., JAMES, E. W., STERN, L. A. & MUSGROVE, M. 2007. Seasonal Variations in Modern Speleothem Calcite Growth in Central Texas, U.S.A. *Journal of Sedimentary Research,* 77**,** 615-622.

BAR-MATTHEWS, M., AYALON, A., GILMOUR, M., MATTHEWS, A. & HAWKESWORTH, C. J. 2003. Sea–land oxygen isotopic relationships from planktonic foraminifera and speleothems in the Eastern Mediterranean region and their implication for paleorainfall during interglacial intervals. *Geochimica et Cosmochimica Acta,* 67**,** 3181-3199.

BARKER, S., CHEN, J., GONG, X., JONKERS, L., KNORR, G. & THORNALLEY, D. 2015. Icebergs not the trigger for North Atlantic cold events. *Nature,* 520**,** 333-336.

BARKER, P. A., LENG, M. J., GASSE, F. & HUANG, Y. 2007. Century-to-millennial scale climatic variability in Lake Malawi revealed by isotope records. *Earth and Planetary Science Letters,* 261**,** 93-103.

BARNOSKY, A. D., KOCH, P. L., FERANEC, R. S., WING, S. L. & SHABEL, A. B. 2004. Assessing the causes of Late Pleistocene extinctions on the continents. *science,* 306**,** 70-75.

BASSINOT, F. 2009. SPECMAP. *In:* GORNITZ, V. (ed.) *Encyclopedia of Paleoclimatology and Ancient Environments.* Springer Netherlands.

BENAZZI, S., DOUKA, K., FORNAI, C., BAUER, C. C., KULLMER, O., SVOBODA, J., PAP, I., MALLEGNI, F., BAYLE, P., COQUERELLE, M., CONDEMI, S., RONCHITELLI, A., HARVATI, K. & WEBER, G. W. 2011. Early dispersal of modern humans in Europe and implications for Neanderthal behaviour. *Nature,* 479**,** 525-528.

BENAZZI, S., SLON, V., TALAMO, S., NEGRINO, F., PERESANI, M., BAILEY, S. E., ... & HUBLIN, J.-J. 2015. The makers of the Protoaurignacian and implications for Neandertal extinction. *Science,* 348**,** 793-796.

BENSON, A., HOFFMANN, D. L., BELLA, P., DRURY, A. J., HERCMAN, H. & ATKINSON, T. C. 2018. Building robust age models for speleothems–A case-study using coeval twin stalagmites. *Quaternary Geochronology,* 43**,** 83-90.

BERGER, A. & LOUTRE, M.-F. 1991. Insolation values for the climate of the last 10 million years. *Quaternary Science Reviews,* 10**,** 297-317.

BERGER, A. & LOUTRE, M.-F. 1999. *Parameters of the Earths orbit for the last 5 Million years in 1kyr resolution.* [Online]. PANGAEA. Available: https://doi.pangaea.de/10.1594/PANGAEA.56040 [Accessed March 2018].

BERGER, A. & LOUTRE, M.-F. 2007. Glaciation, Causes: Milankovitch Theory and Palaeoclimate. *In:* ELIAS, S. A. (ed.) *Encyclopedia of Quaternary Science.* Elsevier.

BLAAUW, M. 2010. Methods and code for 'classical'age-modelling of radiocarbon sequences. *quaternary geochronology,* 5**,** 512-518.

BLAAUW, M. 2012. Out of tune: the dangers of aligning proxy archives. *Quaternary Science Reviews,* 36**,** 38-49.

BLACK, B. A., NEELY, R. R. & MANGA, M. 2015. Campanian Ignimbrite volcanism, climate, and the final decline of the Neanderthals. *Geology,* 43**,** 411-414.

BLOCKLEY, S. P. E., LANE, C. S., HARDIMAN, M., RASMUSSEN, S. O., SEIERSTAD, I. K., STEFFENSEN, J. P., SVENSSON, A., LOTTER, A. F., TURNEY, C. S. M. & BRONK RAMSEY, C. 2012. Synchronisation of palaeoenvironmental records over the last 60,000 years, and an extended INTIMATE event stratigraphy to 48,000 b2k. *Quaternary Science Reviews,* 36**,** 2-10.

BOCH, R., SPÖTL, C. & FRISIA, S. 2011. Origin and palaeoenvironmental significance of lamination in stalagmites from Katerloch Cave, Austria. *Sedimentology,* 58**,** 508-531.

BOND, G., BROECKER, W., JOHNSEN, S. J., MCMANUS, J., LABEYRIE, L., JOUZEL, J. & BONANI, G. 1993. Correlations between North Atlantic sediments and Greenland ice. *Nature,* 365**,** 143-147.

BOND, G., HEINRICH, H., BROECKER, W., LABEYRIE, L., MCMANUS, J., ANDREWS, J., HUON, S., JANTSCHIK, R., CLASEN, S., SIMET, C., TEDESCI, K., KLAS, M., BONANI, G. & IVY, S. 1992. Evidence for massive discharges of icebergs into the North Atlantic ocean during the last glacial period. *Nature,* 360**,** 245-249.

BOND, G., KROMER, B., BEER, J., MUSCHELER, R., EVANS, M. N., SHOWERS, W., HOFFMANN, S., LOTTI-BOND, R., HAJDAS, I. & BONANI, G. 2001. Persistent solar influence on North Atlantic climate during the Holocene. *Science,* 294**,** 2130-2136.

BOND, G. & LOTTI, R. 1995. Iceberg discharges into the North Atlantic on millennial time scales during the last glaciation. *Science,* 267**,** 1005-1010.

BOND, G., SHOWERS, W., CHESEBY, M., LOTTI, R., ALMASI, P., DEMENOCAL, P. B., PRIORE, P., CULLEN, H., HAJDAS, I. & BONANI, G. 1997. A Pervasive Millennial-Scale Cycle in North Atlantic Holocene and Glacial Climates. *Science,* 278**,** 1257-1266.

BOND, G., SHOWERS, W., ELLIOT, M., EVANS, M., LOTTI, R., HAJDAS, I., BONANI, G. & JOHNSON, S. 1999. The North Atlantic's 1-2 Kyr Climate Rhythm: Relation to Heinrich Events, Dansgaard/Oeschger Cycles and the Little Ice Age. *In:* CLARK, P. U., WEBB, R. S. & KEIGWIN, L. D. (eds.) *Mechanisms of global climate change at millennial time scales Geophysical Monograph Series Volume 112.* Washington DC: AGU.

BORSATO, A. Dripwater monitoring at Grotta di Ernesto (NE-Italy): a contribution to the understanding of karst hydrology and the kinetics of carbonate dissolution. Proceedings of the 12th International Congress of Speleology, 1997. 57-60.

BORSATO, A., FRISIA, S., FAIRCHILD, I. J., SOMOGYI, A. & SUSINI, J. 2007. Trace element distribution in annual stalagmite laminae mapped by micrometer-resolution X-ray fluorescence: Implications for incorporation of environmentally significant species. *Geochimica et Cosmochimica Acta,* 71**,** 1494-1512.

BORSATO, A., FRISIA, S., WYNN, P. M., FAIRCHILD, I. J. & MIORANDI, R. 2015. Sulphate concentration in cave dripwater and speleothems: long-term trends and overview of its significance as proxy for environmental processes and climate changes. *Quaternary Science Reviews,* 127**,** 48-60.

BOWEN, G. J. & REVENAUGH, J. 2003. Interpolating the isotopic composition of modern meteoric precipitation. *Water Resources Research,* 39**,** n/a-n/a.

BOWEN, G. J. & WILKINSON, B. 2002. Spatial distribution of δ18O in meteoric precipitation. *Geology,* 30**,** 315-318.

BRADLEY, C., BAKER, A., JEX, C. N. & LENG, M. J. 2010. Hydrological uncertainties in the modelling of cave drip-water δ18O and the implications for stalagmite palaeoclimate reconstructions. *Quaternary Science Reviews,* 29**,** 2201-2214.

BRADTMÖLLER, M., PASTOORS, A., WENINGER, B. & WENIGER, G.-C. 2012. The repeated replacement model–rapid climate change and population dynamics in Late Pleistocene Europe. *Quaternary International,* 247**,** 38-49.

BREITENBACH, S., REHFELD, K., GOSWAMI, B., BALDINI, J., RIDLEY, H., KENNETT, D., PRUFER, K., AQUINO, V., ASMEROM, Y. & POLYAK, V. 2012. Constructing proxy records from age models (COPRA). *Climate of the Past,* 8**,** 1765-1779.

BRONK RAMSEY, C. 2008. Deposition models for chronological records. *Quaternary Science Reviews,* 27**,** 42-60.

BRONK RAMSEY, C. 2017. *OxCal online* [Online]. Available: https://c14.arch.ox.ac.uk/oxcal.html [Accessed December 2017].

BRONK RAMSEY, C. 2018. *OxCal 4.3 Manual* [Online]. Available: https://c14.arch.ox.ac.uk/oxcalhelp/hlp_contents.html [Accessed].

BRONK RAMSEY, C. & LEE, S. 2013. Recent and planned developments of the program OxCal. *Radiocarbon,* 55**,** 720-730.

BRYSON, R. A. & HARE, F. K. 1974. Climates of North America. *In:* LANDSBERG, H. E. (ed.) *World Survey of Climatology.* Amsterdam: Elsevier.

BURJACHS, F. & JULIÀ, R. 1994. Abrupt climatic changes during the last glaciation based on pollen analysis of the Abric Romani, Catalonia, Spain. *Quaternary Research,* 42**,** 308-315.

BURNS, S. J., FLEITMANN, D., MUDELSEE, M., NEFF, U., MATTER, A. & MANGINI, A. 2002. A 780-year annually resolved record of Indian Ocean monsoon precipitation from a speleothem from south Oman. *Journal of Geophysical Research,* 107**,** 4434.

CACHO, I., GRIMALT, J. O., PELEJERO, C., CANALS, M., SIERRO, F. J., FLORES, J. A. & SHACKLETON, N. 1999. Dansgaard-Oeschger and Heinrich event imprints in Alboran Sea paleotemperatures. *Paleoceanography,* 14**,** 698-705.

CAI, B., ZHU, J., BAN, F. & TAN, M. 2011. Intra-annual variation of the calcite deposition rate of drip water in Shihua Cave, Beijing, China and its implications for palaeoclimatic reconstructions. *Boreas,* 40**,** 525-535.

CAI, J. 2018. humidity: Calculate Water Vapor Measures from Temperature and Dew Point. R package version 0.1.4.

CARRIÓN, J., MUNUERA, M. & NAVARRO, C. 1998. The palaeoenvironment of Carihuela Cave (Granada, Spain): a reconstruction on the basis of palynological investigations of cave sediments. *Review of Palaeobotany and Palynology,* 99**,** 317-340.

CASTELLANO, S., PARRA, G., SÁNCHEZ-QUINTO, F. A., RACIMO, F., KUHLWILM, M., KIRCHER, M., ... & PÄÄBO, S. 2014. Patterns of coding variation in the complete exomes of three Neandertals. *Proceedings of the National Academy of Sciences,* 111**,** 6666-6671.

CAYRE, O., LANCELOT, Y., VINCENT, E. & HALL, M. A. 1999. Paleoceanographic reconstructions from planktonic foraminifera off the Iberian Margin: temperature, salinity, and Heinrich events. *Paleoceanography,* 14**,** 384-396.

CHENG, H., EDWARDS, R., HOFF, J., GALLUP, C., RICHARDS, D. & ASMEROM, Y. 2000. The half-lives of uranium-234 and thorium-230. *Chemical Geology,* 169**,** 17-33.
CLARK, I. D. & FRITZ, P. 1997. *Environmental Isotopes in Hydrogeology* United States of America, CRC Press.
CLEMENS, S. 2005. Millennial-band climate spectrum resolved and linked to centennial-scale solar cycles. *Quaternary Science Reviews,* 24**,** 521-531.
COLLISTER, C. & MATTEY, D. P. High resolution measurement of water drip rates in caves using an acoustic drip counter. American Geophysical Union, Fall Meeting 2005, abstract, 2005.
COMBOURIEU NEBOUT, N., TURON, J., ZAHN, R., CAPOTONDI, L., LONDEIX, L. & PAHNKE, K. 2002. Enhanced aridity and atmospheric high-pressure stability over the western Mediterranean during the North Atlantic cold events of the past 50 ky. *Geology,* 30**,** 863-866.
CORRIN, J. 2004. Introduction to the Caves of Matienzo. *RRCPC Newsletter,* 41.
CORRIN, J. 2018. *Matienzo Caves* [Online]. Available: http://matienzocaves.org.uk/page1.htm [Accessed March 2018].
CORTIJO, E., LABEYRIE, L., VIDAL, L., VAUTRAVERS, M., CHAPMAN, M., DUPLESSY, J.-C., ELLIOT, M., ARNOLD, M., TURON, J.-L. & AUFFRET, G. 1997. Changes in sea surface hydrology associated with Heinrich event 4 in the North Atlantic Ocean between 40 and 60 N. *Earth and Planetary Science Letters,* 146**,** 29-45.
CRAIG, H. 1957. Isotopic standards for carbon and oxygen and correction factors for mass-spectrometric analysis of carbon dioxide. *Geochimica et cosmochimica acta,* 12**,** 133-149.
CRAIG, H. 1961a. Isotopic variations in meteoric waters. *Science***,** 1702-1703.
CRAIG, H. 1961b. Standard for reporting concentrations of deuterium and oxygen-18 in natural water. *Science,* 133**,** 1833-1834.
CROLL, J. 1864. Climate and time. *Philosophical Magazine,* 28**,** 121-137.
CRUZ, F. W., BURNS, S. J., JERCINOVIC, M., KARMANN, I., SHARP, W. D. & VUILLE, M. 2007. Evidence of rainfall variations in Southern Brazil from trace element ratios (Mg/Ca and Sr/Ca) in a Late Pleistocene stalagmite. *Geochimica et Cosmochimica Acta,* 71**,** 2250-2263.
CRUZ, F. W., BURNS, S. J., KARMANN, I., SHARP, W. D., VUILLE, M., CARDOSO, A. O., FERRARI, J. A., DIAS, P. L. S. & VIANA, O. 2005. Insolation-driven changes in atmospheric circulation over the past 116,000 years in subtropical Brazil. *Nature,* 434**,** 63-66.
D'ERRICO, F. & SÁNCHEZ GOÑI, M. F. 2003. Neandertal extinction and the millennial scale climatic variability of OIS 3. *Quaternary Science Reviews,* 22**,** 769-788.
DALÉN, L., ORLANDO, L., SHAPIRO, B., BRANDSTRÖM-DURLING, M., QUAM, R., GILBERT, M. T. P., DÍEZ FERNÁNDEZ-LOMANA, J. C., WILLERSLEV, E., ARSUAGA, J. L. & GÖTHERSTRÖM, A. 2012. Partial genetic turnover in neandertals: continuity in the east and population replacement in the west. *Molecular biology and evolution,* 29**,** 1893-1897.
DANIAU, A.-L., SÁNCHEZ GOÑI, M. F. & DUPRAT, J. 2009. Last glacial fire regime variability in western France inferred from microcharcoal preserved in core MD04-2845, Bay of Biscay. *Quaternary Research,* 71**,** 385-396.
DANSGAARD, W. 1964. Stable isotopes in precipitation. *Tellus,* 16**,** 436-468.
DANSGAARD, W., CLAUSEN, H. B., GUNDESTRUP, N., HAMMER, C. U., JOHNSEN, S. F., KRISTINSDOTTIR, P. M. & REEH, N. 1982. A New Greenland Deep Ice Core. *Science,* 218**,** 1273-1277.
DANSGAARD, W., JOHNSEN, S. J., CLAUSEN, H. B., DAHL-JENSEN, D., GUNDESTRUP, N. S., HAMMER, C. U., HVIDBERG, C. S., STEFFENSEN, J. P., SVEINBJÖRNSDOTTIR, A. E.,

JOUZEL, J. & BOND, G. 1993. Evidence for general instability of past climate from a 250-kyr ice-core record. *Nature,* 364**,** 218-220.
DAVIES, W. 2014. Palaeoanthropology: The time of the last Neanderthals. *Nature,* 512**,** 260-261.
DAVIES, W., WHITE, D., LEWIS, M. & STRINGER, C. 2015. Evaluating the transitional mosaic: frameworks of change from Neanderthals to Homo sapiens in eastern Europe. *Quaternary Science Reviews,* 118**,** 211-242.
DAY, C. & HENDERSON, G. 2011. Oxygen isotopes in calcite grown under cave-analogue conditions. *Geochimica et Cosmochimica Acta,* 75**,** 3956-3972.
DE ABREU, L., SHACKLETON, N. J., SCHÖNFELD, J., HALL, M. & CHAPMAN, M. 2003. Millennial-scale oceanic climate variability off the Western Iberian margin during the last two glacial periods. *Marine Geology,* 196**,** 1-20.
DEMENOCAL, P. B. & STRINGER, C. 2016. Human migration: Climate and the peopling of the world. *Nature,* 538**,** 49-50.
DENIS, A., LASTENNET, R., HUNEAU, F. & MALAURENT, P. 2005. Identification of functional relationships between atmospheric pressure and CO2 in the cave of Lascaux using the concept of entropy of curves. *Geophysical Research Letters,* 32**,** L05810.
DENNISTON, R. F., GONZÁLEZ, L. A., ASMEROM, Y., BAKER, R. G., REAGAN, M. K. & BETTIS, E. A. 1999. Evidence for increased cool season moisture during the middle Holocene. *Geology,* 27**,** 815-818.
DENTON, G. H., ANDERSON, R. F., TOGGWEILER, J., EDWARDS, R., SCHAEFER, J. & PUTNAM, A. 2010. The last glacial termination. *Science,* 328**,** 1652-1656.
DEWIT, J., FOUBERT, A., EL DESOUKY, H., MUCHEZ, P., HUNT, D., VANHAECKE, F. & SWENNEN, R. 2014. Characteristics, genesis and parameters controlling the development of a large stratabound HTD body at Matienzo (Ramales Platform, Basque–Cantabrian Basin, northern Spain). *Marine and Petroleum Geology,* 55**,** 6-25.
DICKINSON, S. R., HENDERSON, G. & MCGRATH, K. 2002. Controlling the kinetic versus thermodynamic crystallisation of calcium carbonate. *Journal of Crystal Growth,* 244**,** 369-378.
DITLEVSEN, P. D., ANDERSEN, K. K. & SVENSSON, A. 2007. The DO-climate events are probably noise induced: statistical investigation of the claimed 1470 years cycle. *Climate of the Past,* 3**,** 129-134.
DITLEVSEN, P. D. & DITLEVSEN, O. D. 2009. On the stochastic nature of the rapid climate shifts during the last ice age. *Journal of Climate,* 22**,** 446-457.
DOMÍNGUEZ-VILLAR, D., FAIRCHILD, I. J., BAKER, A., CARRASCO, R. M. & PEDRAZA, J. 2013. Reconstruction of cave air temperature based on surface atmosphere temperature and vegetation changes: implications for speleothem palaeoclimate records. *Earth and Planetary Science Letters,* 369**,** 158-168.
DORALE, J. A., EDWARDS, R. L., ALEXANDER JR, E. C., SHEN, C. C., RICHARDS, D. A. & CHENG, H. 2004. Uranium-series dating of speleothems: current techniques, limits and applications. *In:* SASOWSKY, I. D. & MYLROIE, J. (eds.) *Studies of Cave Sediments: Physical and Chemical Records of Paleoclimate.* New York: Kluwer Academic/Plenum Publishers.
DORALE, J. A. & LIU, Z. 2009. Limitations of Hendy test criteria in judging the paleoclimatic suitability of speleothems and the need for replication. *Journal of Cave and Karst Studies,* 71**,** 73-80.
DREYBRODT, W. 1999. Chemical kinetics, speleothem growth and climate. *Boreas,* 28**,** 347-356.
EMILIANI, C. 1955. Pleistocene temperatures. *Journal of Geology* 63**,** 538-578.
EMILIANI, C. 1966. Isotopic palaeotemperatures *Science,* 154**,** 851-857.

EYNAUD, F., DE ABREU, L., VOELKER, A., SCHÖNFELD, J., SALGUEIRO, E., TURON, J. L., PENAUD, A., TOUCANNE, S., NAUGHTON, F. & SÁNCHEZ GONI, M. F. 2009a. Position of the Polar Front along the western Iberian margin during key cold episodes of the last 45 ka. *Geochemistry, Geophysics, Geosystems,* 10**,** Q07U05.

EYNAUD, F., DE ABREU, L., VOELKER, A. H. L., SCHÖNFELD, J., SALGUEIRO, E., TURON, J.-L., PENAUD, A., TOUCANNE, S., NAUGHTON, F., SANCHEZ GOÑI, M. F., MALAIZÉ, B. & CACHO, I. 2009b. *(Appendix 4) Stable oxygen isotope record of Globigerina bulloides and abundances of Neogloboquadrina pachyderma and ice-rafted debris in sediment core MD95-2040.* [Online]. PANGAEA. Available: https://doi.org/10.1594/PANGAEA.738133, [Accessed May 2017].

FAIRCHILD, I., BAKER, A., BORSATO, A., FRISIA, S., HINTON, R. W., MCDERMOTT, F. & TOOTH, A. 2001. Annual to sub-annual resolution of multiple trace element trends in speleothems. *Journal of the Geological Society,* 158**,** 831-841.

FAIRCHILD, I. & BAKER, A. J. 2012. *Speleothem Science: From Process to Past Environments*, Wiley-Blackwell.

FAIRCHILD, I., BORSATO, A., TOOTH, A., FRISIA, S., HAWKESWORTH, C. J., HUANG, Y., MCDERMOTT, F. & SPIRO, B. 2000. Controls on trace element (Sr-Mg) compositions of carbonate cave waters: implications for speleothem climatic records. *Chemical Geology,* 166**,** 255-269.

FAIRCHILD, I., FRISIA, S., BORSATO, A. & TOOTH, A. 2007. Chapter 7: Speleothems. *In:* NASH, D. J. & MCLAREN, S. J. (eds.) *Geochemical Sediments and Landscapes.* Oxford: Blackwells.

FAIRCHILD, I. & HARTLAND, A. 2010. Trace element variations in stalagmites: controls by climate and by karst system processes. *EMU Notes in Mineralogy,* 10**,** 259-287.

FAIRCHILD, I. & MCMILLAN, E. A. 2007. Speleothems as indicators of wet and dry periods. *International Journal of Speleology,* 36**,** 69-74.

FAIRCHILD, I., SMITH, C. L., BAKER, A., FULLER, L., SPÖTL, C., MATTEY, D. & MCDERMOTT, F. 2006a. Modification and preservation of environmental signals in speleothems. *Earth-Science Reviews,* 75**,** 105-153.

FAIRCHILD, I., SPOTL, C., FRISIA, S., BORSATO, A., SUSINI, J., WYNN, P. M. & CAUZID, J. 2010. Petrology and geochemistry of annually laminated stalagmites from an Alpine cave (Obir, Austria): seasonal cave physiology. *Geological Society, London, Special Publications,* 336**,** 295-321.

FAIRCHILD, I. & TREBLE, P. C. 2009. Trace elements in speleothems as recorders of environmental change. *Quaternary Science Reviews,* 28**,** 449-468.

FAIRCHILD, I., TUCKWELL, G. W., BAKER, A. & TOOTH, A. F. 2006b. Modelling of dripwater hydrology and hydrogeochemistry in a weakly karstified aquifer (Bath, UK): implications for climate change studies. *Journal of Hydrology,* 321**,** 213-231.

FEDELE, F. G., GIACCIO, B. & HAJDAS, I. 2008. Timescales and cultural process at 40,000 BP in the light of the Campanian Ignimbrite eruption, Western Eurasia. *Journal of Human Evolution,* 55**,** 834-857.

FERNÁNDEZ-CORTÉS, A., CALAFORRA, J., SÁNCHEZ-MARTOS, F. & GISBERT, J. 2007. Stalactite drip rate variations controlled by air pressure changes: an example of non-linear infiltration processes in the 'Cueva del Agua'(Spain). *Hydrological processes,* 21**,** 920-930.

FINLAYSON, C. & CARRION, J. S. 2007. Rapid ecological turnover and its impact on Neanderthal and other human populations. *Trends in Ecology & Evolution,* 22**,** 213-222.

FINLAYSON, C., FA, D. A., FINLAYSON, G., PACHECO, F. G. & VIDAL, J. R. G. 2004. Did the moderns kill off the Neanderthals? A reply to F. d'Errico and Sánchez Goñi. *Quaternary Science Reviews,* 23**,** 1205-1209.

FLEITMANN, D., BURNS, S. J., MUDELSEE, M., NEFF, U., KRAMERS, J., MANGINI, A. & MATTER, A. 2003. Holocene forcing of the Indian monsoon recorded in a stalagmite from southern Oman. *Science,* 300**,** 1737-1739.

FLEITMANN, D., CHENG, H., BADERTSCHER, S., EDWARDS, R. L., MUDELSEE, M., GÖKTÜRK, O. M., FANKHAUSER, A., PICKERING, R., RAIBLE, C. C., MATTER, A., KRAMERS, J. & TÜYSÜZ, O. 2009. Timing and climatic impact of Greenland interstadials recorded in stalagmites from northern Turkey. *Geophysical Research Letters,* 36**,** L19707.

FLETCHER, W. J., SÁNCHEZ GOÑ GONI, M. F., ALLEN, J. R., CHEDDADI, R., COMBOURIEU-NEBOUT, N., HUNTLEY, B., ... & TZEDAKIS, P. C. 2010. Millennial-scale variability during the last glacial in vegetation records from Europe. *Quaternary Science Reviews,* 29**,** 2839-2864.

FLETCHER, W. J. & SÁNCHEZ GOÑI, M. F. 2008. Orbital- and sub-orbital-scale climate impacts on vegetation of the western Mediterranean basin over the last 48,000 yr. *Quaternary Research,* 70**,** 451-464.

FOHLMEISTER, J., SCHRÖDER-RITZRAU, A., SCHOLZ, D., SPÖTL, C., RIECHELMANN, D. F. C., MUDELSEE, M., WACKERBARTH, A., GERDES, A., RIECHELMANN, S., IMMENHAUSER, A., RICHTER, D. K. & MANGINI, A. 2012. Bunker Cave stalagmites: an archive for central European Holocene climate variability. *Climate of the Past Discussions,* 8**,** 1687-1720.

FORD, D. & WILLIAMS, P. D. 2007. *Karst hydrogeology and geomorphology*, John Wiley & Sons.

FRIEDMAN, I., HARRIS, J. M., SMITH, G. I. & JOHNSON, C. A. 2002. Stable isotope composition of waters in the Great Basin, United States 1. Air-mass trajectories. *Journal of Geophysical Research,* 107**,** 4400.

FRISIA, S. 2015. Microstratigraphic logging of calcite fabrics in speleothems as tool for palaeoclimate studies. *International Journal of Speleology,* 44**,** 1-16.

FRISIA, S. & BORSATO, A. 2010. Chapter 6 Karst. *Developments in Sedimentology,* 61**,** 269-318.

FRISIA, S., BORSATO, A., FAIRCHILD, I. J. & MCDERMOTT, F. 2000. Calcite fabrics, growth mechanisms, and environments of formation in speleothems from the Italian Alps and southwestern Ireland. *Journal of Sedimentary Research,* 70**,** 1183-1196.

FRISIA, S., BORSATO, A., FAIRCHILD, I. J. & SUSINI, J. 2005. Variations in atmospheric sulphate recorded in stalagmites by synchrotron micro-XRF and XANES analyses. *Earth and Planetary Science Letters,* 235**,** 729-740.

FRISIA, S., FAIRCHILD, I. J., FOHLMEISTER, J., MIORANDI, R., SPÖTL, C. & BORSATO, A. 2011. Carbon mass-balance modelling and carbon isotope exchange processes in dynamic caves. *Geochimica et Cosmochimica Acta,* 75**,** 380-400.

FRUMKIN, A. & STEIN, M. 2004. The Sahara–East Mediterranean dust and climate connection revealed by strontium and uranium isotopes in a Jerusalem speleothem. *Earth and Planetary Science Letters,* 217**,** 451-464.

FULLER, L., BAKER, A., FAIRCHILD, I., SPÖTL, C., MARCA-BELL, A., ROWE, P. & DENNIS, P. 2008. Isotope hydrology of dripwaters in a Scottish cave and implications for stalagmite palaeoclimate research. *Hydrology and Earth System Sciences Discussions,* 5**,** 547-577.

GABITOV, R. & WATSON, E. 2006. Partitioning of strontium between calcite and fluid. *Geochemistry, Geophysics, Geosystems,* 7**,** Q11004.

GALVAN, B., HERNANDEZ, C. M., MALLOL, C., MERCIER, N., SISTIAGA, A. & SOLER, V. 2014. New evidence of early Neanderthal disappearance in the Iberian Peninsula. *Journal of human evolution,* 75**,** 16-27.

GARRALDA, M. D., GALVÁN, B., HERNÁNDEZ, C. M., MALLOL, C., GÓMEZ, J. A. & MAUREILLE, B. 2014. Neanderthals from El Salt (Alcoy, Spain) in the context of the latest Middle

Palaeolithic populations from the southeast of the Iberian Peninsula. *Journal of human evolution,* 75**,** 1-15.
GAT, J. R. 1996. Oxygen and hydrogen isotopes in the hydrologic cycle. *Annual Review of Earth and Planetary Sciences,* 24**,** 225-262.
GAT, J. R., BOWSER, C. J. & KENDALL, C. 1994. The contribution of evaporation from the Great Lakes to the continental atmosphere: estimate based on stable isotope data. *Geophysical Research Letters,* 21**,** 557-560.
GENTY, D. 2008. Palaeoclimate Research in Villars Cave (Dordogne, SW-France). *International Journal of Speleology,* 37**,** 173-191.
GENTY, D., BLAMART, D., OUAHDI, R., GILMOUR, M., BAKER, A., JOUZEL, J. & VAN-EXTER, S. 2003. Precise dating of Dansgaard–Oeschger climate oscillations in western Europe from stalagmite data. *Nature,* 421**,** 833-837.
GENTY, D., COMBOURIEU-NEBOUT, N., PEYRON, O., BLAMART, D., WAINER, K., MANSURI, F., GHALEB, B., ISABELLO, L., DORMOY, I. & VON GRAFENSTEIN, U. 2010. Isotopic characterization of rapid climatic events during OIS3 and OIS4 in Villars Cave stalagmites (SW-France) and correlation with Atlantic and Mediterranean pollen records. *Quaternary Science Reviews,* 29**,** 2799-2820.
GENTY, D. & DEFLANDRE, G. 1998. Drip flow variations under a stalactite of the Père Noël cave (Belgium). Evidence of seasonal variations and air pressure constraints. *Journal of Hydrology,* 211**,** 208-232.
GILPIN, W., FELDMAN, M. W. & AOKI, K. 2016. An ecocultural model predicts Neanderthal extinction through competition with modern humans. *Proceedings of the National Academy of Sciences,* 113**,** 2134-2139.
GOEDE, A., MCCULLOCH, M., MCDERMOTT, F. & HAWKESWORTH, C. 1998. Aeolian contribution to strontium and strontium isotope variations in a Tasmanian speleothem. *Chemical Geology,* 149**,** 37-50.
GONFIANTINI, R. 1986. Environmental isotopes in lake studies. *In:* FRITZ, P. & FONTES, J., -CH (eds.) *Handbook of Environmental Isotope Geochemistry.* Amsterdam: Elsevier.
GONZÁLEZ-SAMPÉRIZ, P., VALERO-GARCÉS, B., MORENO, A., JALUT, G., GARCÍA-RUIZ, J., MARTÍ-BONO, C., DELGADO-HUERTAS, A., NAVAS, A., OTTO, T. & DEDOUBAT, J. 2006. Climate variability in the Spanish Pyrenees during the last 30,000 yr revealed by the El Portalet sequence. *Quaternary Research,* 66**,** 38-52.
GREEN, R. E., KRAUSE, J., BRIGGS, A. W., MARICIC, T., STENZEL, U., KIRCHER, M., ... & PÄÄBO, S. 2010. A draft sequence of the Neandertal genome. *Science,* 328**,** 710-722.
GRIFFITHS, M. L., DRYSDALE, R. N., GAGAN, M. K., FRISIA, S., ZHAO, J.-X., AYLIFFE, L. K., HANTORO, W. S., HELLSTROM, J. C., FISCHER, M. J. & FENG, Y.-X. 2010. Evidence for Holocene changes in Australian–Indonesian monsoon rainfall from stalagmite trace element and stable isotope ratios. *Earth and Planetary Science Letters,* 292**,** 27-38.
GRIFFITHS, M. L., DRYSDALE, R. N., GAGAN, M. K., ZHAO, J. X., AYLIFFE, L. K., HELLSTROM, J. C., HANTORO, W. S., FRISIA, S., FENG, Y. X., CARTWRIGHT, I., PIERRE, E. S., FISCHER, M. J. & SUWARGADI, B. W. 2009. Increasing Australian–Indonesian monsoon rainfall linked to early Holocene sea-level rise. *Nature Geoscience,* 2**,** 636-639.
GROOTES, P. & STUIVER, M. 1997. Oxygen 18/16 variability in Greenland snow and ice with 10− 3-to 105-year time resolution. *Journal of Geophysical Research: Oceans,* 102**,** 26455-26470.
GROOTES, P., STULVER, M., WHITE, J., JOHNSEN, S. F. & JOUZEL, J. 1993. Comparison of oxygen isotope records from the GISP2 and GRIP Greenland ice cores. *Nature,* 366**,** 552-554.
HARMON, R. S. 1979. An isotopic study of groundwater seepage in the central Kentucky karst. *Water Resources Research,* 15**,** 476-480.

HARRIS, K. & NIELSEN, R. 2016. The genetic cost of Neanderthal introgression. *Genetics,* 203**,** 881-891.
HARRIS, K. & NIELSEN, R. 2017. Q&A: Where did the Neanderthals go? *BMC biology,* 15**,** 73.
HARTLAND, A., FAIRCHILD, I. J., LEAD, J. R., BORSATO, A., BAKER, A., FRISIA, S. & BAALOUSHA, M. 2012. From soil to cave: Transport of trace metals by natural organic matter in karst dripwaters. *Chemical Geology,* 304-305**,** 68-82.
HARTMANN, A. & BAKER, A. 2017. Modelling karst vadose zone hydrology and its relevance for paleoclimate reconstruction. *Earth-Science Reviews,* 172**,** 178-192.
HARVATI, K. 2010. Neanderthals. *Evolution: Education and Outreach,* 3**,** 367-376.
HAYASHI, R., TAKAHARA, H., HAYASHIDA, A. & TAKEMURA, K. 2010. Millennial-scale vegetation changes during the last 40,000yr based on a pollen record from Lake Biwa, Japan. *Quaternary Research,* 74**,** 91-99.
HAYS, J. D., IMBRIE, J. & SHACKLETON, N. J. 1976. Variations in the Earth's Orbit: Pacemaker of the Ice Ages. *Science,* 194**,** 1121-1131.
HELLSTROM, J. 2006. U–Th dating of speleothems with high initial 230Th using stratigraphical constraint. *Quaternary Geochronology,* 1**,** 289-295.
HELLSTROM, J. & MCCULLOCH, M. 2000. Multi-proxy constraints on the climatic significance of trace element records from a New Zealand speleothem. *Earth and Planetary Science Letters,* 179**,** 287-297.
HEMMING, S. R. 2004. Heinrich events: Massive late Pleistocene detritus layers of the North Atlantic and their global climate imprint. *Reviews of Geophysics,* 42**,** RG1005.
HENDERSON, G. M. 2006. Climate. Caving in to new chronologies. *Science (New York, NY),* 313**,** 620-622.
HENDY, C. H. 1971. The isotopic geochemistry of speleothems—I. The calculation of the effects of different modes of formation on the isotopic composition of speleothems and their applicability as palaeoclimatic indicators. *Geochimica et cosmochimica Acta,* 35**,** 801-824.
HIGHAM, T., COMPTON, T., STRINGER, C., JACOBI, R., SHAPIRO, B., TRINKAUS, E., CHANDLER, B., GRÖNING, F., COLLINS, C. & HILLSON, S. 2011. The earliest evidence for anatomically modern humans in northwestern Europe. *Nature,* 479**,** 521-524.
HIGHAM, T., DOUKA, K., WOOD, R., RAMSEY, C. B., BROCK, F., BASELL, L., ... & JACOBI, R. 2014. The timing and spatiotemporal patterning of Neanderthal disappearance. *Nature,* 512**,** 306-309.
HÖBIG, N., WEBER, M. E., KEHL, M., WENIGER, G.-C., JULIÀ, R., MELLES, M., FÜLÖP, R.-H., VOGEL, H. & REICHERTER, K. 2012. Lake Banyoles (northeastern Spain): A Last Glacial to Holocene multi-proxy study with regard to environmental variability and human occupation. *Quaternary International,* 274**,** 205-218.
HOFFECKER, J. F. 2009. The spread of modern humans in Europe. *Proceedings of the National Academy of Sciences,* 106**,** 16040-16045.
HORI, M., ISHIKAWA, T., NAGAISHI, K., LIN, K., WANG, B.-S., YOU, C.-F., SHEN, C.-C. & KANO, A. 2013. Prior calcite precipitation and source mixing process influence Sr/Ca, Ba/Ca and 87Sr/86Sr of a stalagmite developed in southwestern Japan during 18.0–4.5ka. *Chemical Geology,* 347**,** 190-198.
HU, C., HENDERSON, G., HUANG, J., CHEN, Z. & JOHNSON, K. 2008. Report of a three-year monitoring programme at Heshang Cave, Central China. *International Journal of Speleology,* 37**,** 143-151.
HUANG, Y. & FAIRCHILD, I. J. 2001. Partitioning of Sr2+ and Mg2+ into calcite under karst-analogue experimental conditions. *Geochimica et Cosmochimica Acta,* 65**,** 47-62.
HUANG, Y., FAIRCHILD, I., BORSATO, A., FRISIA, S., CASSIDY, N. J., MCDERMOTT, F. & HAWKESWORTH, C. J. 2001. Seasonal variations in Sr, Mg and P in modern speleothems (Grotta di Ernesto, Italy). *Chemical Geology,* 175**,** 429-448.

HUBLIN, J. 2015. The modern human colonization of western Eurasia: when and where? *Quaternary Science Reviews,* 118**,** 194-210.
HURRELL, J. W. 1995. Decadal trends in the North Atlantic Oscillation: regional temperatures and precipitation. *Science,* 269**,** 676-679.
IAEA/WMO. 2018. *Global Network of Isotopes in Precipitation. The GNIP Database.* [Online]. Available: http://www.iaea.org/water [Accessed March 2018].
IMBRIE, J., HAYS, J. D., MARTINSON, D. G., MCINTYRE, A., MIX, A. C., MORELEY, J. J., PISIAS, W. L., PRELL, W. L. & SHACKLETON, N. J. 1984. The orbital theory of Pleistocene climate: Support from a revised chronology of the marine δ18O record. *In:* BERGER, A. (ed.) *Milankovitch and Climate, Part 1.* New York: Springer.
IMBRIE, J. Z., IMBRIE-MOORE, A. & LISIECKI, L. E. 2011. A phase-space model for Pleistocene ice volume. *Earth and Planetary Science Letters,* 307**,** 94-102.
JAMES, E. W., BANNER, J. L. & HARDT, B. 2015. A global model for cave ventilation and seasonal bias in speleothem paleoclimate records. *Geochemistry, Geophysics, Geosystems,* 16**,** 1044-1051.
JAMES, J. M. 1977. Carbon dioxide in the cave atmosphere. *Transactions of the British Cave Research Association,* 4**,** 417-429.
JOCHUM, K. P., WEIS, U., STOLL, B., KUZMIN, D., YANG, Q., RACZEK, I., JACOB, D. E., STRACKE, A., BIRBAUM, K. & FRICK, D. A. 2011. Determination of reference values for NIST SRM 610–617 glasses following ISO guidelines. *Geostandards and Geoanalytical Research,* 35**,** 397-429.
JOHNSEN, S., CLAUSEN, H. B., DANSGAARD, W., FUHRER, K., GUNDESTRUP, N., HAMMER, C. U., IVERSEN, P., JOUZEL, J., STAUFFER, B. & STEFFENSEN, J. P. 1992. Irregular glacial interstadials recorded in a new Greenland ice core. *Nature,* 359**,** 311-313.
JOHNSON, K., HU, C., BELSHAW, N. & HENDERSON, G. 2006. Seasonal trace-element and stable-isotope variations in a Chinese speleothem: The potential for high-resolution paleomonsoon reconstruction. *Earth and Planetary Science Letters,* 244**,** 394-407.
JONES, I. C., BANNER, J. L. & HUMPHREY, J. D. 2000. Estimating recharge in a tropical Karst Aquifer. *Water Resources Research,* 36**,** 1289-1299.
JURIC, I., AESCHBACHER, S. & COOP, G. 2016. The strength of selection against Neanderthal introgression. *PLoS genetics,* 12**,** e1006340.
KAGEYAMA, M., MIGNOT, J., SWINGEDOUW, D., MARZIN, C., ALKAMA, R. & MARTI, O. 2009. Glacial climate sensitivity to different states of the Atlantic Meridional Overturning Circulation: results from the IPSL model. *Climate of the Past,* 5**,** 551-570.
KAUFMAN, A., WASSERBURG, G., PORCELLI, D., BAR-MATTHEWS, M., AYALON, A. & HALICZ, L. 1998. U-Th isotope systematics from the Soreq cave, Israel and climatic correlations. *Earth and Planetary Science Letters,* 156**,** 141-155.
KEHL, M., ÁLVAREZ-ALONSO, D., DE ANDRÉS-HERRERO, M., DÍEZ-HERRERO, A., KLASEN, N., ROJO-HERNÁNDEZ, J. & WENIGER, G.-C. Dating the last Neanderthals in Central Iberia-New evidence from Abrigo del Molino, Segovia, Spain. EGU General Assembly Conference Abstracts, 2017. 6402.
KENDALL, C. 2004. *Resources on Isotopes* [Online]. USGS. Available: http://wwwrcamnl.wr.usgs.gov/isoig/period/h_iig.html [Accessed 18.2.15 2015].
KIM, S.-T. & O'NEIL, J. R. 1997. Equilibrium and nonequilibrium oxygen isotope effects in synthetic carbonates. *Geochimica et Cosmochimica Acta,* 61**,** 3461-3475.
KINDLER, P., GUILLEVIC, M., BAUMGARTNER, M., SCHWANDER, J., LANDAIS, A., LEUENBERGER, M., SPAHNI, R., CAPRON, E. & CHAPPELLAZ, J. 2014. Temperature reconstruction from 10 to 120 kyr b2k from the NGRIP ice core. *Climate of the Past,* 10**,** 887-902.
KOSTER, R. D., DE VALPINE, D. P. & JOUZEL, J. 1993. Continental water recycling and H218O concentrations. *Geophysical Research Letters,* 20**,** 2215-2218.

LACEY, J. H., LENG, M. J., HÖBIG, N., REED, J. M., VALERO-GARCÉS, B. & REICHERTER, K. 2016. Western Mediterranean climate and environment since Marine Isotope Stage 3: a 50,000-year record from Lake Banyoles, Spain. *Journal of paleolimnology,* 55**,** 113-128.

LACHNIET, M. S. 2009. Climatic and environmental controls on speleothem oxygen-isotope values. *Quaternary Science Reviews,* 28**,** 412-432.

LACHNIET, M. S. & PATTERSON, W. P. 2006. Use of correlation and stepwise regression to evaluate physical controls on the stable isotope values of Panamanian rain and surface waters. *Journal of Hydrology,* 324**,** 115-140.

LANGGUT, D., ALMOGI-LABIN, A., BAR-MATTHEWS, M. & WEINSTEIN-EVRON, M. 2011. Vegetation and climate changes in the South Eastern Mediterranean during the Last Glacial-Interglacial cycle (86 ka): new marine pollen record. *Quaternary Science Reviews,* 30**,** 3960-3972.

LANGMUIR, D. 1978. Uranium solution-mineral equilibria at low temperatures with applications to sedimentary ore deposits. *Geochimica et Cosmochimica Acta,* 42**,** 547-569.

LANGMUIR, D. 1997. *Aqueous Environmental Geochemistry,* Upper Saddle River, NJ, Prentice Hall.

LANGMUIR, D. & HERMAN, J. S. 1980. The mobility of thorium in natural waters at low temperatures. *Geochimica et Cosmochimica Acta,* 44**,** 1753-1766.

LAURITZEN, S.-E. 2014. Chapter 17: Reconstructing Holocene Climate Records from Speleothems. *In:* BIRKS, J., BATTARBEE, R., MACKAY, A. & OLDFIELD, F. (eds.) *Global Change in the Holocene.* revised ed. New York: Routledge (Taylor and Francis).

LEGRANDE, A. N. & SCHMIDT, G. A. 2006. Global gridded data set of the oxygen isotopic composition in seawater. *Geophysical Research Letters,* 33**,** L12604.

LISIECKI, L. E. & RAYMO, M. E. 2005. A Pliocene-Pleistocene stack of 57 globally distributed benthic δ18O records. *Paleoceanography,* 20**,** PA1003.

LONG, J. A. & STOY, P. C. 2013. Quantifying the periodicity of Heinrich and Dansgaard–Oeschger events during marine oxygen isotope stage 3. *Quaternary Research,* 79**,** 413-423.

LÓPEZ-GARCÍA, J., BLAIN, H.-A., BENNASAR, M., SANZ, M. & DAURA, J. 2013. Heinrich event 4 characterized by terrestrial proxies in southwestern Europe. *Climate of the Past,* 9**,** 1053-1064.

LORENS, R. B. 1981. Sr, Cd, Mn and Co distribution coefficients in calcite as a function of calcite precipitation rate. *Geochimica et Cosmochimica Acta,* 45**,** 553-561.

LOWE, J., BARTON, N., BLOCKLEY, S., RAMSEY, C. B., CULLEN, V. L., DAVIES, W., ... & TZEDAKIS, P. C. 2012. Volcanic ash layers illuminate the resilience of Neanderthals and early modern humans to natural hazards. *Proceedings of the National Academy of Sciences,* 109**,** 13532-13537.

LYNCH-STIEGLITZ, J. 2017. The Atlantic meridional overturning circulation and abrupt climate change. *Annual review of marine science,* 9**,** 83-104.

MAGNIEZ, P. & BOULBES, N. 2014. Environment during the Middle to Late Palaeolithic transition in southern France: the archaeological sequence of Tournal Cave (Bize-Minervois, France). *Quaternary International,* 337**,** 43-63.

MAHER, B. A. & THOMPSON, R. 2012. Oxygen isotopes from Chinese caves: records not of monsoon rainfall but of circulation regime. *Journal of Quaternary Science,* 27**,** 615-624.

MARTÍN-CHIVELET, J., MUÑOZ-GARCÍA, M. B., EDWARDS, R. L., TURRERO, M. J. & ORTEGA, A. I. 2011. Land surface temperature changes in Northern Iberia since 4000 yr BP, based on δ13C of speleothems. *Global and Planetary Change,* 77**,** 1-12.

MARTIN-PUERTAS, C., BRAUER, A., WULF, S., OTT, F., LAUTERBACH, S. & DULSKI, P. 2014. Annual proxy data from Lago Grande di Monticchio (southern Italy) between 76 and 112 ka: new chronological constraints and insights on abrupt climatic oscillations. *Climate of the Past,* 10**,** 2099-2114.

MARTINSON, D. G., PISIAS, N. G., HAYS, J. D., IMBRIE, J., MOORE JR, T. C. & SHACKLETON, N. J. 1987. Age dating and the orbital theory of the ice ages: development of a high-resolution 0 to 300,000-year chronostratigraphy. *Quaternary Research,* 27**,** 1-29.

MARTRAT, B., GRIMALT, J. O., SHACKLETON, N. J., DE ABREU, L., HUTTERLI, M. A. & STOCKER, T. F. 2007. Four climate cycles of recurring deep and surface water destabilizations on the Iberian margin. *Science,* 317**,** 502-507.

MATTEY, D., LOWRY, D., DUFFET, J., FISHER, R., HODGE, E. & FRISIA, S. 2008. A 53 year seasonally resolved oxygen and carbon isotope record from a modern Gibraltar speleothem: Reconstructed drip water and relationship to local precipitation. *Earth and Planetary Science Letters,* 269**,** 80-95.

MATTEY, D. P. & COLLISTER, C. 2008. Acoustic Drip Counters for Environmental Monitoring. *BCRA Cave Radion and Electronics Group,* 70**,** 14-17.

MATTEY, D. P., FAIRCHILD, I. J., ATKINSON, T. C., LATIN, J. P., AINSWORTH, M. & DURELL, R. 2010. Seasonal microclimate control of calcite fabrics, stable isotopes and trace elements in modern speleothem from St Michaels Cave, Gibraltar. *Geological Society, London, Special Publications,* 336**,** 323-344.

MAYEWSKI, P. A., ROHLING, E. E., STAGER, J. C., KARLÉN, W., MAASCH, K. A., MEEKER, L. D., MEYERSON, E. A., GASSE, F., VAN KREVELD, S. & HOLMGREN, K. 2004. Holocene climate variability. *Quaternary research,* 62**,** 243-255.

MCDERMOTT, F. 2004. Palaeo-climate reconstruction from stable isotope variations in speleothems: a review. *Quaternary Science Reviews,* 23**,** 901-918.

MCDERMOTT, F., FRISIA, S., HUANG, Y., LONGINELLI, A., SPIRO, B., HEATON, T. H., HAWKESWORTH, C. J., BORSATO, A., KEPPENS, E. & FAIRCHILD, I. J. 1999. Holocene climate variability in Europe: evidence from δ18O, textural and extension-rate variations in three speleothems. *Quaternary Science Reviews,* 18**,** 1021-1038.

MCDERMOTT, F., SCHWARCZ, H. & ROWE, P. J. 2005. 5. Isotopes in Speleothems. *In:* LENG, M. J. (ed.) *Isotopes in Palaeoenvironmental Research.* Dordrecht, The Netherlands: Springer.

MCDERMOTT, F., ATKINSON, T., FAIRCHILD, I. J., BALDINI, L. M. & MATTEY, D. P. 2011. A first evaluation of the spatial gradients in δ18O recorded by European Holocene speleothems. *Global and Planetary Change,* 79**,** 275-287.

MCDONALD, J., DRYSDALE, R., HILL, D., CHISARI, R. & WONG, H. 2007. The hydrochemical response of cave drip waters to sub-annual and inter-annual climate variability, Wombeyan Caves, SE Australia. *Chemical Geology,* 244**,** 605-623.

MCKINNEY, C. R., MCCREA, J. M., EPSTEIN, S., ALLEN, H. & UREY, H. C. 1950. Improvements in mass spectrometers for the measurement of small differences in isotope abundance ratios. *Review of Scientific Instruments,* 21**,** 724-730.

MCMILLAN, E. A., FAIRCHILD, I. J., FRISIA, S., BORSATO, A. & MCDERMOTT, F. 2005. Annual trace element cycles in calcite-aragonite speleothems: evidence of drought in the western Mediterranean 1200-1100 yr BP. *Journal of Quaternary Science,* 20**,** 423-433.

MELLARS, P. 1998. The fate of the Neanderthals. *Nature,* 395**,** 539-540.

MEYER, M., ARSUAGA, J.-L., DE FILIPPO, C., NAGEL, S., AXIMU-PETRI, A., NICKEL, B., ... & PÄÄBO, S. 2016. Nuclear DNA sequences from the Middle Pleistocene Sima de los Huesos hominins. *Nature,* 531**,** 504.

MICKLER, P. J., STERN, L. A. & BANNER, J. L. 2006. Large kinetic isotope effects in modern speleothems. *Geological Society of America Bulletin,* 118**,** 65-81.

MILANKOVITCH, M. 1941. Kanon der Erdbastrahlung und seinse Anwendung auf des Eiszeitenproblem. *Royal Serbian Sciences, Special Publication 132 Section of Mathematical and Natural Sciences,* 33.

MILLS, L. D. J. & WALTHAM, A. C. 1981. Geomorphology of the Matienzo Caves. *Transactions of the British Cave Research Association,* 8**,** 63-84.

MINDHAM, D. & TYCH, W. 2018. Arbitrary Sampling in Dynamic Harmonic Regression. *In Preparation*.

MIORANDI, R., BORSATO, A., FRISIA, S., FAIRCHILD, I. J. & RICHTER, D. K. 2010. Epikarst hydrology and implications for stalagmite capture of climate changes at Grotta di Ernesto (NE Italy): results from long-term monitoring. *Hydrological Processes,* 24**,** 3101-3114.

MORENO, A., GONZÁLEZ-SAMPÉRIZ, P., MORELLÓN, M., VALERO-GARCÉS, B. L. & FLETCHER, W. J. 2012. Northern Iberian abrupt climate change dynamics during the last glacial cycle: A view from lacustrine sediments. *Quaternary Science Reviews,* 36**,** 139-153.

MORENO, A., VALERO-GARCÉS, B. L., JIMÉNEZ-SÁNCHEZ, M., DOMÍNGUEZ-CUESTA, M. J., MATA, M. P., NAVAS, A., GONZÁLEZ-SAMPÉRIZ, P., STOLL, H., FARIAS, P., MORELLÓN, M., CORELLA, J. P. & RICO, M. 2010. The last deglaciation in the Picos de Europa National Park (Cantabrian Mountains, northern Spain). *Journal of Quaternary Science,* 25**,** 1076-1091.

MORSE, J. W. & BENDER, M. L. 1990. Partition coefficients in calcite: Examination of factors influencing the validity of experimental results and their application to natural systems. *Chemical Geology,* 82**,** 265-277.

MOSELEY, G. E., SPÖTL, C., CHENG, H., BOCH, R., MIN, A. & EDWARDS, R. L. 2015. Termination-II interstadial/stadial climate change recorded in two stalagmites from the north European Alps. *Quaternary Science Reviews,* 127**,** 229-239.

MOSELEY, G. E., SPOTL, C., SVENSSON, A., CHENG, H., BRANDSTATTER, S. & EDWARDS, R. L. 2014. Multi-speleothem record reveals tightly coupled climate between central Europe and Greenland during Marine Isotope Stage 3. *Geology,* 42**,** 1043-1046.

MÜHLINGHAUS, C., SCHOLZ, D. & MANGINI, A. 2009. Modelling fractionation of stable isotopes in stalagmites. *Geochimica et Cosmochimica Acta,* 73**,** 7275-7289.

MÜLLER, U. C., PROSS, J., TZEDAKIS, P. C., GAMBLE, C., KOTTHOFF, U., SCHMIEDL, G., WULF, S. & CHRISTANIS, K. 2011. The role of climate in the spread of modern humans into Europe. *Quaternary Science Reviews,* 30**,** 273-279.

MÜLLER, W., SHELLEY, M., MILLER, P. & BROUDE, S. 2009. Initial performance metrics of a new custom-designed ArF excimer LA-ICPMS system coupled to a two-volume laser-ablation cell. *Journal of Analytical Atomic Spectrometry,* 24**,** 209-214.

MUÑOZ-GARCÍA, M., MARTÍN-CHIVELET, J., ROSSI, C., FORD, D. C. & SCHWARCZ, H. P. 2007. Chronology of Termination II and the Last Interglacial Period in North Spain based on stable isotope records of stalagmites from Cueva del Cobre (Palencia)/Cronología de la Terminación II y del Último Periodo Interglacial en el norte de España a partir de los registros de isótopos estables de estalagmitas procedentes de la Cueva del Cobre (Palencia). *Journal of Iberian Geology,* 33**,** 17-30.

NAKAGAWA, T., GOTANDA, K., HARAGUCHI, T., DANHARA, T., YONENOBU, H., BRAUER, A., YOKOYAMA, Y., TADA, R., TAKEMURA, K., STAFF, R. A., PAYNE, R., BRONK RAMSEY, C., BRYANT, C., BROCK, F., SCHLOLAUT, G., MARSHALL, M., TARASOV, P. & LAMB, H. 2012. SG06, a fully continuous and varved sediment core from Lake Suigetsu, Japan: stratigraphy and potential for improving the radiocarbon calibration model and understanding of late Quaternary climate changes. *Quaternary Science Reviews,* 36**,** 164-176.

NAUGHTON, F., SÁNCHEZ GOÑI, M., DESPRAT, S., TURON, J.-L., DUPRAT, J., MALAIZÉ, B., JOLI, C., CORTIJO, E., DRAGO, T. & FREITAS, M. 2007. Present-day and past (last 25

000 years) marine pollen signal off western Iberia. *Marine Micropaleontology,* 62**,** 91-114.
NAUGHTON, F., SÁNCHEZ GOÑI, M., KAGEYAMA, M., BARD, E., DUPRAT, J., CORTIJO, E., DESPRAT, S., MALAIZÉ, B., JOLY, C. & ROSTEK, F. 2009. Wet to dry climatic trend in north-western Iberia within Heinrich events. *Earth and Planetary Science Letters,* 284**,** 329-342.
NEFF, U., BURNS, S., MANGINI, A., MUDELSEE, M., FLEITMANN, D. & MATTER, A. 2001. Strong coherence between solar variability and the monsoon in Oman between 9 and 6 kyr ago. *Nature,* 411**,** 290-293.
NGRIPMEMBERS 2004. High-resolution record of Northern Hemisphere climate extending into the last interglacial period. *Nature* 431**,** 147-151.
NOAA ARL. 2017. *HYSPLIT transport and dispersion model and/or READY website* [Online]. Available: https://ready.arl.noaa.gov/HYSPLIT_traj.php [Accessed May 2017].
OBROCHTA, S. P., MIYAHARA, H., YOKOYAMA, Y. & CROWLEY, T. J. 2012. A re-examination of evidence for the North Atlantic "1500-year cycle" at Site 609. *Quaternary Science Reviews,* 55**,** 23-33.
ORLAND, I. J., BURSTYN, Y., BAR-MATTHEWS, M., KOZDON, R., AYALON, A., MATTHEWS, A. & VALLEY, J. W. 2014. Seasonal climate signals (1990–2008) in a modern Soreq Cave stalagmite as revealed by high-resolution geochemical analysis. *Chemical Geology,* 363**,** 322-333.
ORTIZ, J. E., TORRES, T., DELGADO, A., JULIÀ, R., LUCINI, M., LLAMAS, F. J., REYES, E., SOLER, V. & VALLE, M. 2004. The palaeoenvironmental and palaeohydrological evolution of Padul Peat Bog (Granada, Spain) over one million years, from elemental, isotopic and molecular organic geochemical proxies. *Organic Geochemistry,* 35**,** 1243-1260.
PAILLER, D. & BARD, E. 2002. High frequency palaeoceanographic changes during the past 140 000 yr recorded by the organic matter in sediments of the Iberian Margin. *Palaeogeography, Palaeoclimatology, Palaeoecology,* 181**,** 431-452.
PARKHURST, D. L. 1995. User's guide to PHREEQC: A computer program for speciation, reaction-path, advective-transport, and inverse geochemical calculations. US Geological Survey, Water Resources Investigations Report US Geological Survey.
PÈREZ-OBIOL, R. & JULIÀ, R. 1994. Climatic change on the Iberian Peninsula recorded in a 30,000-yr pollen record from Lake Banyoles. *Quaternary Research,* 41**,** 91-98.
PONS, A. & REILLE, M. 1988. The Holocene-and Upper Pleistocene pollen record from Padul (Granada, Spain): a new study. *Palaeogeography, Palaeoclimatology, Palaeoecology,* 66**,** 243-263.
PROSS, J., KOUTSODENDRIS, A., CHRISTANIS, K., FISCHER, T., FLETCHER, W. J., HARDIMAN, M., KALAITZIDIS, S., KNIPPING, M., KOTTHOFF, U. & MILNER, A. M. 2015. The 1.35-Ma-long terrestrial climate archive of Tenaghi Philippon, northeastern Greece: Evolution, exploration, and perspectives for future research. *Newsletters on Stratigraphy,* 48**,** 253-276.
PROUTY, N. G., SAHY, D., RUPPEL, C. D., ROARK, E. B., CONDON, D., BROOKE, S., ROSS, S. W. & DEMOPOULOS, A. W. 2016. Insights into methane dynamics from analysis of authigenic carbonates and chemosynthetic mussels at newly-discovered Atlantic Margin seeps. *Earth and Planetary Science Letters,* 449**,** 332-344.
PRÜFER, K., RACIMO, F., PATTERSON, N., JAY, F., SANKARARAMAN, S., SAWYER, S., ... & PÄÄBO, S. 2014. The complete genome sequence of a Neanderthal from the Altai Mountains. *Nature,* 505**,** 43-49.
QUIN, A. 2010. Matienzo Geomorphology. *In:* CORRIN, J. & SMITH, P. (eds.) *Matienzo 50 years of speleology.*
RASMUSSEN, S. O., BIGLER, M., BLOCKLEY, S. P., BLUNIER, T., BUCHARDT, S. L., CLAUSEN, H. B., ... & WINSTRUP, M. 2014. A stratigraphic framework for abrupt climatic changes

during the Last Glacial period based on three synchronized Greenland ice-core records: refining and extending the INTIMATE event stratigraphy. *Quaternary Science Reviews,* 106**,** 14-28.

RASMUSSEN, T. L., THOMSEN, E., WEERING, T. C. & LABEYRIE, L. 1996. Rapid changes in surface and deep water conditions at the Faeroe Margin during the last 58,000 years. *Paleoceanography,* 11**,** 757-771.

RAVBAR, N. & KOSUTNIK, J. 2013. Variations of karst underground air temperature induced by various factors (Cave of Županova jama, Central Slovenia). *Theoretical and Applied Climatology,* 116**,** 327-341.

REGATTIERI, E., ZANCHETTA, G., DRYSDALE, R. N., ISOLA, I., HELLSTROM, J. C. & DALLAI, L. 2014. Lateglacial to Holocene trace element record (Ba, Mg, Sr) from Corchia Cave (Apuan Alps, central Italy): paleoenvironmental implications. *Journal of Quaternary Science,* 29**,** 381-392.

REIMER, P. J., BARD, E., BAYLISS, A., BECK, J. W., BLACKWELL, P. G., RAMSEY, C. B., BUCK, C. E., CHENG, H., EDWARDS, R. L., FRIEDRICH, M., GROOTES, P. M., GUILDERSON, T. P., HAFLIDASON, H., HAJDAS, I., HATTÉ, C., HEATON, T. J., HOFFMANN, D. L., HOGG, A. G., HUGHEN, K. A., KAISER, K. F., KROMER, B., MANNING, S. W., NIU, M., REIMER, R. W., RICHARDS, D. A., SCOTT, E. M., SOUTHON, J. R., STAFF, R. A., TURNEY, C. S. M. & VAN DER PLICHT, J. 2013. IntCal13 and Marine13 radiocarbon age calibration curves 0–50,000 years cal BP. *Radiocarbon,* 55**,** 1869-1887.

REY-RODRÍGUEZ, I., LÓPEZ-GARCÍA, J.-M., BENNASAR, M., BAÑULS-CARDONA, S., BLAIN, H.-A., BLANCO-LAPAZ, Á., ... & FÁBREGAS-VALCARCE, R. 2016. Last Neanderthals and first Anatomically Modern Humans in the NW Iberian Peninsula: climatic and environmental conditions inferred from the Cova Eirós small-vertebrate assemblage during MIS 3. *Quaternary Science Reviews,* 151**,** 185-197.

RICHARDS, D. A. & DORALE, J. A. 2003. Uranium-series chronology and environmental applications of speleothems. *Reviews in Mineralogy and Geochemistry,* 52**,** 407-460.

RIECHELMANN, D. F. C., SCHRÖDER-RITZRAU, A., SCHOLZ, D., FOHLMEISTER, J., SPÖTL, C., RICHTER, D. K. & MANGINI, A. 2011. Monitoring Bunker Cave (NW Germany): A prerequisite to interpret geochemical proxy data of speleothems from this site. *Journal of Hydrology,* 409**,** 682-695.

ROEBROEKS, W. 2008. Time for the Middle to Upper Paleolithic transition in Europe. *Journal of Human Evolution,* 55**,** 918-926.

ROLPH, G., STEIN, A. & STUNDER, B. 2017. Real-time environmental applications and display system: Ready. *Environmental Modelling & Software,* 95**,** 210-228.

ROUCOUX, K. H., DE ABREU, L., SHACKLETON, N. J. & TZEDAKIS, P. C. 2005. The response of NW Iberian vegetation to North Atlantic climate oscillations during the last 65kyr. *Quaternary Science Reviews,* 24**,** 1637-1653.

ROUCOUX, K. H., SHACKLETON, N. J., DE ABREU, L., SCHÖNFELD, J. & TZEDAKIS, P. C. 2001. Combined marine proxy and pollen analyses reveal rapid Iberian vegetation response to North Atlantic millennial-scale climate oscillations. *Quaternary Research,* 56**,** 128-132.

ROUSSEAU, D. D., SIMA, A., ANTOINE, P., HATTÉ, C., LANG, A. & ZÖLLER, L. 2007. Link between European and North Atlantic abrupt climate changes over the last glaciation. *Geophysical Research Letters,* 34**,** L22713.

ROZANSKI, K., ARAGUÁS-ARAGUÁS, L. & GONFIANTINI, R. 1993. Isotopic patterns in modern global precipitation. *Climate change in continental isotopic records***,** 1-36.

ROZANSKI, K., SONNTAG, C. & MÜNNICH, K. 1982. Factors controlling stable isotope composition of European precipitation. *Tellus,* 34**,** 142-150.

RUDDIMAN, W. F. 2006. Orbital changes and climate. *Quaternary Science Reviews,* 25**,** 3092-3112.

RUIZ COBO, J. *The Matienzo Valley* [Online]. Matienzo Caves. Available: http://matienzocaves.org.uk/science/web_matienzo/pdfs/Matienzo%20Environment.pdf [Accessed March 2018].

SAINI-EIDUKAT, B. 2018. *WEB-PHREEQ* [Online]. Available: https://www.ndsu.edu/webphreeq/ [Accessed February 2018].

SAINI-EIDUKAT, B. & YAHIN, A. 1999. Web-phreeq: a WWW instructional tool for modeling the distribution of chemical species in water. *Computers & Geosciences,* 25**,** 347-353.

SALGUEIRO, E., NAUGHTON, F., VOELKER, A. H. L., DE ABREU, L., ALBERTO, A., ROSSIGNOL, L., DUPRAT, J., MAGALHÃES, V. H., VAQUEIRO, S. & TURON, J.-L. 2014. Past circulation along the western Iberian margin: a time slice vision from the Last Glacial to the Holocene. *Quaternary Science Reviews,* 106**,** 316-329.

SALGUEIRO, E., VOELKER, A. H. L., DE ABREU, L., ABRANTES, F., MEGGERS, H. & WEFER, G. 2010. Temperature and productivity changes off the western Iberian margin during the last 150 ky. *Quaternary Science Reviews,* 29**,** 680-695.

SÁNCHEZ GOÑI, M. F. 2013. *North Atlantic SST, Foraminifera, Isotope and Ice-Rafted Debris Data during the last interglacial and glacial.* [Online]. NOAA. Available: https://www.ncdc.noaa.gov/paleo-search/study/14650 [Accessed May 2018].

SÁNCHEZ GOÑI, M. F., BARD, E., LANDAIS, A., ROSSIGNOL, L. & D'ERRICO, F. 2013. Air–sea temperature decoupling in western Europe during the last interglacial–glacial transition. *Nature Geoscience,* 6**,** 837-841.

SÁNCHEZ GOÑI, M. F., CACHO, I., TURON, J.-L., GUIOT, J., SIERRO, F., PEYPOUQUET, J., GRIMALT, J. & SHACKLETON, N. 2002. Synchroneity between marine and terrestrial responses to millennial scale climatic variability during the last glacial period in the Mediterranean region. *Climate dynamics,* 19**,** 95-105.

SÁNCHEZ GOÑI, M. F., DESPRAT, S., FLETCHER, W. J., MORALES DEL MOLINO, C., NAUGHTON, F., OLIVEIRA, D., URREGO, D. H. & ZORZI, C. 2018. Pollen from the deep-sea: a breakthrough in the mystery of the Ice Ages. *Frontiers in Plant Science,* 9**,** 38.

SÁNCHEZ GOÑI, M. F., LANDAIS, A., FLETCHER, W. J., NAUGHTON, F., DESPRAT, S. & DUPRAT, J. 2008. Contrasting impacts of Dansgaard–Oeschger events over a western European latitudinal transect modulated by orbital parameters. *Quaternary Science Reviews,* 27**,** 1136-1151.

SÁNCHEZ GOÑI, M. F., TURON, J.-L., EYNAUD, F. & GENDREAU, S. 2000. European Climatic Response to Millennial-Scale Changes in the Atmosphere–Ocean System during the Last Glacial Period. *Quaternary Research,* 54**,** 394-403.

SCHMIDT, G. A., LEGRANDE, A. N. & HOFFMANN, G. 2007. Water isotope expressions of intrinsic and forced variability in a coupled ocean-atmosphere model. *Journal of Geophysical Research: Atmospheres,* 112**,** D10103.

SCHOLZ, D. & HOFFMANN, D. 2008. 230Th/U-dating of fossil corals and speleothems. *Eiszeitalter und Gegenwart Quaternary Science Journal,* 57**,** 52-76.

SCHOLZ, D. & HOFFMANN, D. L. 2011. StalAge–An algorithm designed for construction of speleothem age models. *Quaternary Geochronology,* 6**,** 369-382.

SCHOLZ, D., HOFFMANN, D. L., HELLSTROM, J. & RAMSEY, C. B. 2012. A comparison of different methods for speleothem age modelling. *Quaternary Geochronology,* 14**,** 94-104.

SCHÖNFELD, J., ZAHN, R. & DE ABREU, L. 2003. Surface and deep water response to rapid climate changes at the Western Iberian Margin. *Global and Planetary Change,* 36**,** 237-264.

SCHRAG, D. P., ADKINS, J. F., MCINTYRE, K., ALEXANDER, J. L., HODELL, D. A., CHARLES, C. D. & MCMANUS, J. F. 2002. The oxygen isotopic composition of seawater during the Last Glacial Maximum. *Quaternary Science Reviews,* 21**,** 331-342.

SCHREVE, D. 2017. Neither hot nor cold but dry. *In:* POPE, M., MCNABB, J. & GAMBLE, C. (eds.) *Crossing the Human Threshold: Dynamic Transformation and Persistent Places During the Middle Pleistocene.* London and New York: Routledge.

SCHULZ, M. 2002. On the 1470-year pacing of Dansgaard-Oeschger warm events. *Paleoceanography and Palaeoclimatology,* 17**,** 1014.

ŠEBELA, S. & TURK, J. 2011. Local characteristics of Postojna Cave climate, air temperature, and pressure monitoring. *Theoretical and Applied Climatology,* 105**,** 371-386.

SEIERSTAD, I. K., ABBOTT, P. M., BIGLER, M., BLUNIER, T., BOURNE, A. J., BROOK, E., ... & VINTHER, B. M. 2014. Consistently dated records from the Greenland GRIP, GISP2 and NGRIP ice cores for the past 104 ka reveal regional millennial-scale δ18O gradients with possible Heinrich event imprint. *Quaternary Science Reviews,* 106**,** 29-46.

SEPULCHRE, P., RAMSTEIN, G., KAGEYAMA, M., VANHAEREN, M., KRINNER, G., SÁNCHEZ GOÑI, M. F. & D'ERRICO, F. 2007. H4 abrupt event and late Neanderthal presence in Iberia. *Earth and Planetary Science Letters,* 258**,** 283-292.

SEVERINGHAUS, J. P. & BROOK, E. J. 1999. Abrupt climate change at the end of the last glacial period inferred from trapped air in polar ice. *Science,* 286**,** 930-934.

SHACKLETON, N. J. 1967. Oxygen isotope analyses and Pleistocene temperatures re-assessed. *Nature,* 215**,** 15-17.

SHACKLETON, N. J., HALL, M. A. & VINCENT, E. 2000. Phase relationships between millennial-scale events 64,000–24,000 years ago. *Paleoceanography,* 15**,** 565-569.

SHARP, Z. 2007. *Principles of stable isotope geochemistry,* United State of America, Pearson Education Inc.

SINCLAIR, D. J. 2011. Two mathematical models of Mg and Sr partitioning into solution during incongruent calcite dissolution: implications for dripwater and speleothem studies. *Chemical Geology,* 283**,** 119-133.

SINCLAIR, D. J., BANNER, J. L., TAYLOR, F. W., PARTIN, J., JENSON, J., MYLROIE, J., GODDARD, E., QUINN, T., JOCSON, J. & MIKLAVIČ, B. 2012. Magnesium and strontium systematics in tropical speleothems from the Western Pacific. *Chemical Geology,* 294-295**,** 1-17.

SMART, P. & FRIEDRICH, H. Water movement and storage in the unsaturated zone of a maturely karstified aquifer, Mendip Hills, England. Proceedings, Conference on Environmental Problems in Karst Terrains and their Solution, Bowling Green, Kentucky, 1987. National Water Well Association, 57-87.

SMERDON, J. E., POLLACK, H. N., CERMAK, V., ENZ, J. W., KRESL, M., SAFANDA, J. & WEHMILLER, J. F. 2006. Daily, seasonal, and annual relationships between air and subsurface temperatures. *Journal of Geophysical Research: Atmospheres,* 111**,** D07101.

SMITH, A. 2014. *Speleothem Climate Capture - A Holocene Reconstruction of Northern Iberian Climate and Environmental Change.* PhD, Lancaster University.

SMITH, A. C., WYNN, P. M., BARKER, P. A. & LENG, M. J. 2015. Drip water electrical conductivity as an indicator of cave ventilation at the event scale. *Science of the Total Environment,* 532**,** 517-527.

SMITH, A. C., WYNN, P. M., BARKER, P. A., LENG, M. J., NOBLE, S. R. & STOTT, A. 2016a. Cave monitoring and the potential for palaeoclimate reconstruction from Cueva de Asiul, Cantabria (N. Spain). *International Journal of Speleology,* 45**,** 1-9.

SMITH, A. C., WYNN, P. M., BARKER, P. A., LENG, M. J., NOBLE, S. R. & TYCH, W. 2016b. North Atlantic forcing of moisture delivery to Europe throughout the Holocene. *Scientific Reports,* 6**,** 24745.

SMITH, C. L., FAIRCHILD, I. J., SPÖTL, C., FRISIA, S., BORSATO, A., MORETON, S. G. & WYNN, P. M. 2009. Chronology building using objective identification of annual signals in trace element profiles of stalagmites. *Quaternary Geochronology,* 4**,** 11-21.

SMITH, P. 2006. *Cave Archaeology in the Matienzo Area* [Online]. Available: http://matienzocaves.org.uk/archaeol.htm [Accessed May 2018].

SMITH, P. 1998. *Cueva de las Perlas Cave Survey* [Online]. Available: http://matienzocaves.org.uk/indexnf.htm [Accessed April 2017].

SODEMANN, H., SCHWIERZ, C. & WERNLI, H. 2008. Interannual variability of Greenland winter precipitation sources: Lagrangian moisture diagnostic and North Atlantic Oscillation influence. *Journal of Geophysical Research: Atmospheres,* 113**,** D03107.

SPÖTL, C., FAIRCHILD, I. J. & TOOTH, A. F. 2005. Cave air control on dripwater geochemistry, Obir Caves (Austria): Implications for speleothem deposition in dynamically ventilated caves. *Geochimica et Cosmochimica Acta,* 69**,** 2451-2468.

SPÖTL, C. & MANGINI, A. 2002. Stalagmite from the Austrian Alps reveals Dansgaard–Oeschger events during isotope stage 3: Implications for the absolute chronology of Greenland ice cores. *Earth and Planetary Science Letters,* 203**,** 507-518.

SPÖTL, C., MANGINI, A. & RICHARDS, D. A. 2006. Chronology and paleoenvironment of Marine Isotope Stage 3 from two high-elevation speleothems, Austrian Alps. *Quaternary Science Reviews,* 25**,** 1127-1136.

STAUBWASSER, M., DRĂGUȘIN, V., ONAC, B. P., ASSONOV, S., ERSEK, V., HOFFMANN, D. L. & VERES, D. 2018. Impact of climate change on the transition of Neanderthals to modern humans in Europe. *Proceedings of the National Academy of Sciences,* 115**,** 9116-9121.

STEFFENSEN, J. P., ANDERSEN, K. K., BIGLER, M., CLAUSEN, H. B., DAHL-JENSEN, D., FISCHER, H., GOTO-AZUMA, K., HANSSON, M., JOHNSEN, S. J., JOUZEL, J., MASSON-DELMOTTE, V., POPP, T., RASMUSSEN, S. O., RÖTHLISBERGER, R., RUTH, U., B, S., SIGGAARD-ANDERSEN, M.-L., SVEINBJÖRNSDÓTTIR, A. E., SVENSSON, A. & WHITE, J. W. C. 2008. High-resolution Greenland ice core data show abrupt climate change happens in few years. *Science,* 321**,** 680-684.

STEIN, A., DRAXLER, R. R., ROLPH, G. D., STUNDER, B. J., COHEN, M. & NGAN, F. 2015. NOAA's HYSPLIT atmospheric transport and dispersion modeling system. *Bulletin of the American Meteorological Society,* 96**,** 2059-2077.

STEWART, J. R. 2005. The ecology and adaptation of Neanderthals during the non-analogue environment of Oxygen Isotope Stage 3. *Quaternary International,* 137**,** 35-46.

STEWART, J. R. 2007. Neanderthal extinction as part of the faunal change in Europe during Oxygen Isotope Stage 3. *Acta Zoologica Cracoviensia-Series A: Vertebrata,* 50**,** 93-124.

STOCKER, T. F. 2000. Past and future reorganizations in the climate system. *Quaternary Science Reviews,* 19**,** 301-319.

STOLL, H., MENDEZ-VICENTE, A., GONZALEZ-LEMOS, S., MORENO, A., CACHO, I., CHENG, H. & EDWARDS, R. L. 2015. Interpretation of orbital scale variability in mid-latitude speleothem δ18O: Significance of growth rate controlled kinetic fractionation effects. *Quaternary Science Reviews,* 127**,** 215-228.

STOLL, H. M., MORENO, A., MENDEZ-VICENTE, A., GONZALEZ-LEMOS, S., JIMENEZ-SANCHEZ, M., DOMINGUEZ-CUESTA, M. J., EDWARDS, R. L., CHENG, H. & WANG, X. 2013. Paleoclimate and growth rates of speleothems in the northwestern Iberian Peninsula over the last two glacial cycles. *Quaternary Research,* 80**,** 284-290.

STŘEDA, T., STŘEDOVÁ, H. & VYSOUDIL, M. 2012. Temperature regime of Kateřinská Cave. *Contributions to Geophysics and Geodesy,* 42**,** 243-254.

STUIVER, M. 1968. Oxygen-18 content of atmospheric precipitation during last 11,000 years in the Great Lakes region. *Science,* 162**,** 994-997.
TANG, K. & FENG, X. 2001. The effect of soil hydrology on the oxygen and hydrogen isotopic compositions of plants' source water. *Earth and Planetary Science Letters,* 185**,** 355-367.
TAYLOR, C. J., PEDREGAL, D. J., YOUNG, P. C. & TYCH, W. 2007. Environmental time series analysis and forecasting with the Captain toolbox. *Environmental Modelling & Software,* 22**,** 797-814.
THOMAS, A. M., RUPPER, S. & CHRISTENSEN, W. F. 2011. Characterizing the statistical properties and interhemispheric distribution of Dansgaard-Oeschger events. *Journal of Geophysical Research: Atmospheres,* 116**,** D03103.
THOMSON, J., NIXON, S., SUMMERHAYES, C., SCHÖNFELD, J., ZAHN, R. & GROOTES, P. 1999. Implications for sedimentation changes on the Iberian margin over the last two glacial/interglacial transitions from $(^{230}Th_{excess})_0$ systematics. *Earth and Planetary Science Letters,* 165**,** 255-270.
THORNTHWAITE, C. W. 1948. An approach toward a rational classification of climate. *Geographical review,* 38**,** 55-94.
TIMMERMANN, A. & FRIEDRICH, T. 2016. Late Pleistocene climate drivers of early human migration. *Nature,* 538**,** 92-95.
TOOTH, A. F. 2000. *Controls on the geochemistry of speleothem-forming karstic drip waters.* PhD, Keele University.
TREBLE, P., CHAPPELL, J., GAGAN, M., MCKEEGAN, K. & HARRISON, T. 2005a. In situ measurement of seasonal δ18O variations and analysis of isotopic trends in a modern speleothem from southwest Australia. *Earth and Planetary Science Letters,* 233**,** 17-32.
TREBLE, P., SHELLEY, J. M. G. & CHAPPELL, J. 2003. Comparison of high resolution sub-annual records of trace elements in a modern (1911–1992) speleothem with instrumental climate data from southwest Australia. *Earth and Planetary Science Letters,* 216**,** 141-153.
TREBLE, P. C., CHAPPELL, J. & SHELLEY, J. M. G. 2005b. Complex speleothem growth processes revealed by trace element mapping and scanning electron microscopy of annual layers. *Geochimica et Cosmochimica Acta,* 69**,** 4855-4863.
TREMAINE, D. M. & FROELICH, P. N. 2013. Speleothem trace element signatures: a hydrologic geochemical study of modern cave dripwaters and farmed calcite. *Geochimica et Cosmochimica Acta,* 121**,** 522-545.
TREMAINE, D. M., FROELICH, P. N. & WANG, Y. 2011. Speleothem calcite farmed in situ: Modern calibration of δ18O and δ13C paleoclimate proxies in a continuously-monitored natural cave system. *Geochimica et Cosmochimica Acta,* 75**,** 4929-4950.
TRIGO, R. M., POZO-VÁZQUEZ, D., OSBORN, T. J., CASTRO-DÍEZ, Y., GÁMIZ-FORTIS, S. & ESTEBAN-PARRA, M. J. 2004. North Atlantic Oscillation influence on precipitation, river flow and water resources in the Iberian Peninsula. *International Journal of Climatology,* 24**,** 925-944.
TZEDAKIS, P., HUGHEN, K., CACHO, I. & HARVATI, K. 2007. Placing late Neanderthals in a climatic context. *Nature,* 449**,** 206-208.
TZEDAKIS, P. C., FROGLEY, M. R., LAWSON, I. T., PREECE, R. C., CACHO, I. & DE ABREU, L. 2004. Ecological thresholds and patterns of millennial-scale climate variability: The response of vegetation in Greece during the last glacial period. *Geology,* 32**,** 109-112.
VAN ANDEL, T. H. & DAVIES, W. 2003. *Neanderthals and modern humans in the European landscape during the last glaciation: archaeological results of the Stage 3 Project*, McDonald Institute for Archaeological Research monographs.

VAN CALSTEREN, P. & THOMAS, L. 2006. Uranium-series dating applications in natural environmental science. *Earth-Science Reviews,* 75**,** 155-175.

VEGAS, J., RUIZ-ZAPATA, B., ORTIZ, J. E., GALÁN, L., TORRES, T., GARCÍA-CORTÉS, Á., GIL-GARCÍA, M. J., PÉREZ-GONZÁLEZ, A. & GALLARDO-MILLÁN, J. L. 2010. Identification of arid phases during the last 50 cal. ka BP from the Fuentillejo maar-lacustrine record (Campo de Calatrava Volcanic Field, Spain). *Journal of Quaternary Science,* 25**,** 1051-1062.

VERES, D., LALLIER-VERGÈS, E., WOHLFARTH, B., LACOURSE, T., KÉRAVIS, D., BJÖRCK, S., PREUSSER, F., ANDRIEU-PONEL, V. & AMPEL, L. 2009. Climate-driven changes in lake conditions during late MIS 3 and MIS 2: a high-resolution geochemical record from Les Echets, France. *Boreas,* 38**,** 230-243.

VERHEYDEN, S., GENTY, D., DEFLANDRE, G., QUINIF, Y. & KEPPENS, E. 2008. Monitoring climatological, hydrological and geochemical parameters in the Père Noël cave (Belgium): implication for the interpretation of speleothem isotopic and geochemical time-series. *International Journal of Speleology,* 37**,** 221-234.

VIDAL, L., LABEYRIE, L., CORTIJO, E., ARNOLD, M., DUPLESSY, J., MICHEL, E., BECQUE, S. & VAN WEERING, T. 1997. Evidence for changes in the North Atlantic Deep Water linked to meltwater surges during the Heinrich events. *Earth and Planetary Science Letters,* 146**,** 13-27.

VIETEN, R., WINTER, A., WARKEN, S. F., SCHRÖDER-RITZRAU, A., MILLER, T. E. & SCHOLZ, D. 2016. Seasonal temperature variations controlling cave ventilation processes in Cueva Larga, Puerto Rico. *International Journal of Speleology,* 45**,** 259-273.

VOELKER, A. H. 2002. Global distribution of centennial-scale records for Marine Isotope Stage (MIS) 3: a database. *Quaternary Science Reviews,* 21**,** 1185-1212.

VOELKER, A. H. & DE ABREU, L. 2011a. A review of abrupt climate change events in the Northeastern Atlantic Ocean (Iberian Margin): Latitudinal, longitudinal, and vertical gradients. *In:* RASHID, H., POLYAK, L. & MOSLEY-THOMPSON, E. (eds.) *Abrupt Climate Change: Mechanisms, Patterns, and Impacts.* Geophysical Monograph Series (AGU, Washington D.C.).

VOELKER, A. H. L. & DE ABREU, L. 2011b. *Reconstruction of sea surface temperatures of sediment core MD95-2040.* [Online]. PANGAEA. Available: https://doi.org/10.1594/PANGAEA.737142, [Accessed May 2018].

VOELKER, A. H. L. & DE ABREU, L. 2011c. *Stable oxygen and carbon isotope ratios of Globigerina bulloides of sediment core MD95-2040.* [Online]. PANGAEA. Available: https://doi.org/10.1594/PANGAEA.737413 [Accessed May 2018].

WAINER, K., GENTY, D., BLAMART, D., HOFFMANN, D. & COUCHOUD, I. 2009. A new stage 3 millennial climatic variability record from a SW France speleothem. *Palaeogeography, Palaeoclimatology, Palaeoecology,* 271**,** 130-139.

WALDRON, S., SCOTT, E. M. & SOULSBY, C. 2007. Stable isotope analysis reveals lower-order river dissolved inorganic carbon pools are highly dynamic. *Environmental science & technology,* 41**,** 6156-6162.

WALTHAM, A. 1981. The karstic evolution of the Matienzo depression, Spain. *Zeitschrift fur Geomorphologie,* 25**,** 300-312.

WANG, Q., WANG, Y., ZHAO, K., CHEN, S., LIU, D., ZHANG, Z., HUANG, W., YANG, S. & LIANG, Y. 2018. The transfer of oxygen isotopic signals from precipitation to drip water and modern calcite on the seasonal time scale in Yongxing Cave, central China. *Environmental Earth Sciences,* 77**,** 474.

WANG, Y., CHENG, H., EDWARDS, R. L., AN, Z. S., WU, J. Y., SHEN, C. C. & DORALE, J. A. 2001. A high-resolution absolute-dated late Pleistocene Monsoon record from Hulu Cave, China. *Science,* 294**,** 2345-2348.

WANG, Y., CHENG, H., EDWARDS, R. L., HE, Y., KONG, X., AN, Z., WU, J., KELLY, M. J., DYKOSKI, C. A. & LI, X. 2005. The Holocene Asian monsoon: links to solar changes and North Atlantic climate. *Science,* 308**,** 854-857.

WEBB, M., BARKER, P. A., WYNN, P. M., HEIRI, O., VAN HARDENBROEK, M., PICK, F., RUSSELL, J. M., STOTT, A. W. & LENG, M. J. 2016. Interpretation and application of carbon isotope ratios in freshwater diatom silica. *Journal of Quaternary Science,* 31**,** 300-309.

WEBB, M., DREDGE, J., BARKER, P., MUELLER, W., JEX, C., DESMARCHELIER, J., HELLSTROM, J. & WYNN, P. 2014. Quaternary climatic instability in south-east Australia from a multi-proxy speleothem record. *Journal of Quaternary Science,* 29**,** 589-596.

WELKER, J. 2000. Isotopic (δ18O) characteristics of weekly precipitation collected across the USA: an initial analysis with application to water source studies. *Hydrological Processes,* 14**,** 1449-1464.

WHITE, W. B. 2004. Paleoclimate records from speleothems in limestone caves. *In:* SASOWSKY, I. D. & MYLROIE, J. (eds.) *Studies of Cave Sediments: Physical and Chemical Records of Paleoclimate.* New York: Kluwer Academic/Plenum Publishers.

WOHLFARTH, B., VERES, D., AMPEL, L., LACOURSE, T., BLAAUW, M., PREUSSER, F., ANDRIEU-PONEL, V., KÉRAVIS, D., LALLIER-VERGÈS, E., BJÖRCK, S., DAVIES, S. M., DE BEAULIEU, J.-L., RISBERG, J., HORMES, A., KASPER, H. U., POSSNERT, G., REILLE, M., THOUVENY, N. & ZANDER, A. 2008. Rapid ecosystem response to abrupt climate changes during the last glacial period in western Europe, 40–16 ka. *Geology,* 36**,** 407-410.

WOILLEZ, M.-N., KRINNER, G., KAGEYAMA, M. & DELAYGUE, G. 2012. Impact of solar forcing on the surface mass balance of northern ice sheets for glacial conditions. *Earth and Planetary Science Letters,* 335**,** 18-24.

WOLF, D., KOLB, T., ALCARAZ-CASTAÑO, M., HEINRICH, S., BAUMGART, P., CALVO, R., SÁNCHEZ, J., RYBORZ, K., SCHÄFER, I. & BLIEDTNER, M. 2018. Climate deteriorations and Neanderthal demise in interior Iberia. *Scientific Reports* 8**,** 7048.

WOLFF, E. W., CHAPPELLAZ, J., BLUNIER, T., RASMUSSEN, S. O. & SVENSSON, A. 2010. Millennial-scale variability during the last glacial: The ice core record. *Quaternary Science Reviews,* 29**,** 2828-2838.

WOOD, R. E., ARRIZABALAGA, A., CAMPS, M., FALLON, S., IRIARTE-CHIAPUSSO, M.-J., JONES, R., ... & HIGHAM, T. 2014. The chronology of the earliest upper palaeolithic in northern Iberia: new insights from L'Arbreda, Labeko Koba and La Viña. *Journal of human evolution,* 69**,** 91-109.

WU, J. Y., WANG, Y. J., CHENG, H., KONG, X. G. & LIU, D. B. 2012. Stable isotope and trace element investigation of two contemporaneous annually-laminated stalagmites from northeastern China surrounding the "8.2 ka event". *Climate of the Past,* 8**,** 1497-1507.

WUNSCH, C. 2000. On sharp spectral lines in the climate record and the millennial peak. *Paleoceanography,* 15**,** 417-424.

WYNN, P. M., BORSATO, A., BAKER, A., FRISIA, S., MIORANDI, R. & FAIRCHILD, I. J. 2013. Biogeochemical cycling of sulphur in karst and transfer into speleothem archives at Grotta di Ernesto, Italy. *Biogeochemistry,* 114**,** 255-267.

WYNN, P. M., FAIRCHILD, I. J., BAKER, A., BALDINI, J. U. & MCDERMOTT, F. 2008. Isotopic archives of sulphate in speleothems. *Geochimica et Cosmochimica Acta,* 72**,** 2465-2477.

WYNN, P. M., FAIRCHILD, I. J., FRISIA, S., SPÖTL, C., BAKER, A. & BORSATO, A. 2010. High-resolution sulphur isotope analysis of speleothem carbonate by secondary ionisation mass spectrometry. *Chemical Geology,* 271**,** 101-107.

WYNN, P. M., FAIRCHILD, I. J., SPÖTL, C., HARTLAND, A., MATTEY, D., FAYARD, B. & COTTE, M. 2014. Synchrotron X-ray distinction of seasonal hydrological and temperature patterns in speleothem carbonate. *Environmental Chemistry,* 11**,** 28-36.

ZHAO, J.-X., YU, K.-F. & FENG, Y.-X. 2009. High-precision 238U–234U–230Th disequilibrium dating of the recent past: a review. *Quaternary Geochronology,* 4**,** 423-433.

ZILHÃO, J., ANESIN, D., AUBRY, T., BADAL, E., CABANES, D., KEHL, M., ... & ZAPATA , J. 2017. Precise dating of the Middle-to-Upper Paleolithic transition in Murcia (Spain) supports late Neandertal persistence in Iberia. *Heliyon,* 3**,** e00435.

ZIMMERMAN, U., EHHALT, D. & MUNNICH, K. O. Soil water movement and evaporation: changes in the isotopic composition of the water. IAEA Symposium on Isotope Hydrology, 1967 Vienna.

ZUMAQUE, J., EYNAUD, F., ZARAGOSI, S., MARRET, F., MATSUZAKI, K. M., KISSEL, C., ROCHE, D. M., MALAIZÉ, B., MICHEL, E., BILLY, I., RICHTER, T. & PALIS, E. 2012. An ocean–ice coupled response during the last glacial: a view from a marine isotopic stage 3 record south of the Faeroe Shetland Gateway. *Climate of the Past,* 8**,** 1997-2017.

10. Supplementary materials

The following appendices can be found on the accompanying CD-R.

- Appendix A: Temperature
- Appendix B: Carbon dioxide
- Appendix C: Air samples
- Appendix D: Pressure
- Appendix E: Precipitation and drip rates
- Appendix F: Water chemistry
- Appendix G: Electrical conductivity
- Appendix H: U-series ages
- Appendix I: OxCal P-sequences
- Appendix J: Geochemical data from PER0
- Appendix K: Geochemical data from PER10.3
- Appendix L: Geochemical data from PER10.4
- Appendix M: Cueva de Cofresnedo preliminary archaeological investigations